Dissertation zur Erlangung des Doktorgrades
der Fakultät für Chemie und Pharmazie
der Ludwig-Maximilians-Universität München

ILLUMINATING NOVEL ASPECTS IN VIRUS-HOST INTERACTIONS BY TAILORED QUANTITATIVE PROTEOMICS ANALYSES

PHILIPP HUBEL

AUS
DACHAU, DEUTSCHLAND

2019

Erklärung

Diese Dissertation wurde im Sinne von § 7 der Promotionsordnung vom 28. November 2011 von Herrn Professor Dr. Matthias Mann betreut.

Eidesstattliche Versicherung

Diese Dissertation wurde eigenständig und ohne unerlaubte Hilfe erarbeitet.

München, den 01.08.2019

.....

Philipp Hubel

Dissertation eingereicht am: 01.08.2019

1. Gutachter: Prof. Dr. Matthias Mann

2. Gutachter: Prof. Dr. Andreas Pichlmair

Mündliche Prüfung am: 10.12.2019

ABSTRACT

The arms race between host and pathogens through evolution shaped a tightly connected and complex defense network. The innate immune system provides essential mechanisms capable to efficiently inhibit invading pathogens. Central mechanisms of the innate immune system, such as pathogen recognition and regulation of defense responses, require complex systems to be balanced, fast responding and effective. The interferon system consisting of pattern recognition receptors, signaling molecules and cytokines, is a defense system that gets activated very early after virus infection and proved to be extremely powerful to inhibit virus replication and spread. Interferons induce the expression of a whole arsenal of specific proteins called Interferon stimulated genes (ISGs), which serve a wide array of different activities, including direct inhibition of viruses and initiation of upstream defense mechanisms that facilitate long lasting adaptive immune responses. However, viruses frequently target the interferon system to block cellular defense responses and thereby evade the immune system. In recent years antiviral properties of ISGs were mainly studied by gain and lack of function experiments, which allowed insights into their specificity and effectivity to inhibit viruses. However, only a few antiviral ISGs were studied in detail on the molecular level so far and the mode of action of the majority of ISGs remained enigmatic.

During my PhD, I worked on different projects which focused on host-pathogen interactions. I used large scale affinity enrichment followed by mass spectrometry (AE-LC-MS/MS) experiments to study protein-protein interactions between cellular proteins and more than 100 functionally well-defined ISGs. The generated data allowed me to functionally validate and mechanistically explain the mode of action of several ISGs including the novel negative innate immune regulator LGALS3BP, the G-protein coupled nucleotide cell surface receptor P2RY6, and the ISG ANXA2R which unexpectedly engages the CCR4-NOT complex to fulfil its antiviral activity. I also investigated the functional consequence of the association between the ISG IFIT1 and the 2'O unmethylated RNA cap structure, which is a key element in the antiviral potential of IFIT1. Furthermore, I contributed to the identification of a novel type of cell death, called oxeiptosis, which is induced by reactive oxygen species (ROS) and commonly generated during intoxications or pathogen encounter. In an additional collaborative project, I revealed the function of the immune-regulating E3 ubiquitin ligase FBXO3 in RVFV infection and identified the cellular cofactor GBF1, which is required for the antiviral activity of the ISG viperin against flaviviruses. My work, as shown in this thesis, significantly contributed to our understanding of virus-host interactions in regards to virus infections and pathology.

Contents

ABBREVIATIONS

5′-ppp RNA	5′triphosphate RNA
AE	Affinity enrichment
AE-LC-MS/MS	Affinity enrichment followed by mass spectrometry
AIM2	Absent in Melanoma 2
ALR	AIM2-like receptor
ANXA2R	Annexin-2 receptor
AP-1	Activator protein 1
APC	Antigen presenting cell
APEX	Absolute protein expression measurement
AP-LC-MS/MS	Affinity purification followed by mass spectrometry
AQUA	Absolute quantification
BioID	Proximity-dependent biotin identification
BST2	Bone marrow stromal antigen 2
BUNV	Bunyamwera virus
CAA	Chloroacetamide
CARD	Caspase recruitment domain
cGAS	Cyclic GMP-AMP synthase
CCHFV	Crimean-Congo hemorrhagic fever virus
CID	Collision induced dissociation
CPSF30	Cleavage and polyadenylation specific factor-30
CREB	cAMP response element-binding protein
DAMP	Danger associated molecular pattern
DC	Direct current
DNA	Deoxyribonucleic acid
dsDNA	Double stranded DNA
dsRNA	Double strand RNA
DTT	Dithiothreitol
EBV	Epstein–Barr virus
ECD	Electron capture dissociation
EIF2AK2	Eukaryotic translation initiation factor 2-alpha kinase2
ER	Endoplasmic reticulum
ESI	Electrospray ionization
ETD	Electron transfer dissociation
FASP	Filter assisted sample preparation
FDPS	Farnesyl diphosphate synthase
FDR	False discovery rate
FFPE	Formalin-fixed paraffin-embedded
FluAV	Influenza A virus
FMDV	Foot- and mouth disease virus
GAF	IFN-γ-activated factor
GAS	γ-activated sequences
GPI	Glycosylphosphatidylinositol
haESC	Haploid embryonic stem cell
HBV	Hepatitis B virus
HCD	Higher-energy C-trap dissociation

HCMV	Human cytomegalovirus
HCV	Hepatitis C virus
HIV	Human immunodeficiency virus
HPLC	High Pressure Liquid Chromatography
HPV	Human papillomavirus
HRSV	Human Respiratory syncytial virus
HTLV	Human T-lymphotrophic virus
IAA	Iodoacetamide
iBAQ	Intensity-based absolute quantification
IFIT	Interferon-induced protein with tetratricopeptide repeats
IFN	Interferon
IFNAR	IFN-α receptor
IFNGR	IFN-γ receptor
IL-1	Interleukin-1
IRAK	IL-1 receptor-associated kinase
IRES	Internal ribosome entry site
IRF2	Interferon Regulatory Factor 2
IRF3	Interferon regulatory factor 3
ISG	Interferon stimulated gene
ISGF3	IFN-stimulated gene factor 3
JAK1	Janus kinase 1
JEV	Japanese encephalitis virus
JNK	c-Jun amino-terminal kinase
KSHV	Kaposi's sarcoma-associated herpesvirus
LACV	La Cross virus
LC	Liquid chromatography
LC-MS/MS	Liquid chromatography coupled to mass spectrometry
LFQ	Label-Free Quantification
LGALS3BP	Lectin galactoside-binding soluble 3-binding protein
LGV	Langat virus
LIT	Linear ion traps
LPS	Lipopolysaccharides
LTβR	Lymphotoxin β receptor
m/z	Mass to charge ratio
MALDI	Matrix-assisted laser desorption ionization
MAPK	Mitogen-activated protein kinase
MAVS	Mitochondrial antiviral-signaling
MDA5	Melanoma differentiation-associated gene 5
MHC	Major histocompatibility complex
MS	Full scan
MS/MS	Fragmentation scan
Mx	Murine myxovirus resistance gene
MyD88	Myeloid differentiation primary response
NF-κB	Nuclear factor kappa B
NGS	Next-generation-sequencing
NIK	NF-κB-inducing kinase
NK cell	Natural killer cell
NLR	Nod-like receptor

NLRP3	NACHT, LRR and PYD domains-containing protein 3
NS5A	Non-structural protein 5A
NSs	Non-structural small
OAS	Oligoadenylate synthase
P2RY6	P2Y purinoceptor 6
PABP	Poly(A)-binding protein
PAI	Protein abundance index
PAMP	Pathogen associated molecular pattern
PCD	Programmed cell death
pDC	Plasmacytoid dendritic cell
PKR	Protein kinase R
Pol-II	Polymerase II
PPI	Protein-protein-interaction
PrEST	Protein Epitope Signature Tag
ProCASP8	Pro-caspase 8
PRR	Pattern recognition receptor
PTM	Post-translational modifications
RdRp	RNA-dependent RNA polymerase
RF	Radio frequency
RIG-I	Retinoic acid inducible gene I
RIPK	Receptor-interacting serine/threonine-protein kinases
RLR	RIG-I-like receptor
RNA	Ribonucleic acid
ROS	Reactive oxygen species
RVFV	Rift valley fever virus
SDS	Sodium dodecylsulfate
SEC-MS	Size-exclusion chromatography coupled to mass spectrometry
SeV	Sendai virus
shRNA	Small hairpin RNA
SILAC	Stable-isotope labeling by amino-acids in cell culture
siRNA	Small interfering RNA
SOCS	Suppressor of cytokine signaling
SOD1	Superoxide Dismutase 1
SP3	Single-pot solid-phase-enhanced sample preparation
ssRNA	Single strand RNA
STAT	Signal transducer and activator of transcription
STING	Stimulator of interferon genes
TAK1	TGFβ- activated kinase 1
TCEP	Tris(2-carboxyethyl)phosphine
TCR	T-cell receptor
TGN	Trans-Golgi network
TICAM-1	TIR domain-containing adapter molecule 1
TLR	Toll-like receptor
TMT	Tandem mass tags
TNF	Tumor necrosis factor
TOF	Time-of-flight
TYK2	Tyrosine kinase 2
USP18	Ubl carboxyl-terminal hydrolase 18

VACV	Vacciniavirus
VAP-A	Vesicle-associated membrane protein-associated protein A
vBCL2	Viral BCL2
vFLIP	Viral FLIP
vIRA	Viral inhibitor of RIP activation
vORF	Viral open reading frame
vRNP	Viral ribonucleotide protein complex
VSV	Vesicular stomatitis virus
WNV	West Nile virus

1 INTRODUCTION

The constant and ubiquitous presence of pathogens forced organisms to acquire a diverse range of defense mechanisms in order to combat these confrontations through evolution. Although modern medicine provides effective drugs and vaccination strategies to control a number of different pathogens, most viruses cannot be targeted by therapeutic treatments. This is in part due to insufficient knowledge on how to target viruses in general but also complicated by the ability of viruses to adapt specific mutations, which cause structural rearrangements at the drug-target interphase [1,2]. Therefore, effective and long lasting medical protection against many viruses still remains challenging. Current strategies focus on targeting host cell machineries, which are essentially required for virus replication [3].

Evolutionary shaped host defense systems provide a whole arsenal of different inhibitors that viruses could not completely overcome by their mutational evasion strategies. Among these immune derived defense mechanisms is the Interferon (IFN) system, which represents one of the most central cellular components that determines the success to control virus infections. As part of the innate immune system, the IFN induced defense mechanisms inhibit a broad range of different pathogens. Successful application of IFN based therapies against persistent virus infections, as for example hepatitis C virus (HCV) infection, highlighted the efficiency of this system to fight virus infections [4]. However, severe side effects limit the applicability of IFN based therapies [5].

This thesis illuminates recent advances in the dynamic field of host-pathogen interactions and focuses on the molecular interplay between viruses and the innate immune system. The first part of the introduction discusses the innate immune system with emphasis on the IFN mediated defense response and its basic roles in context of viral infections. Virus-host interactions and their contribution to virus replication are highlighted in the second part. The third part of the introduction emphasizes state of the art technologies and mass spectrometry based approaches applied to study the innate immune system on a global level. These technologies contributed significantly to study the complex network of virus-host interactions in recent years.

1.1 THE IMMUNE SYSTEM

The immune system includes cellular processes that protect organisms from foreign substances in toxins, particles, small organisms or pathogens. The immune response encompasses two major systems, namely the innate- and the adaptive immunity. Both systems go hand in hand and execute a variety of different tightly regulated, time coordinated defense responses that act in concert to guarantee a fast, long lasting and highly specific protection against invading pathogens. The innate immune system covers passive physical defense barriers such as epithelial monolayers or secreted body fluids and specified innate immune cell types, cytokines and signal pathways that act early during infection [6]. It tightly interacts with the adaptive immune system and significantly contributes to its initiation and activation. The adaptive immune system involves cellular components that aim to elicit a highly specific defense response against pathogen-characteristic structures, so-called antigens. It is responsible for the elimination of pathogens at the late stage of infections and to establish long-term protection (Figure 1) [7].

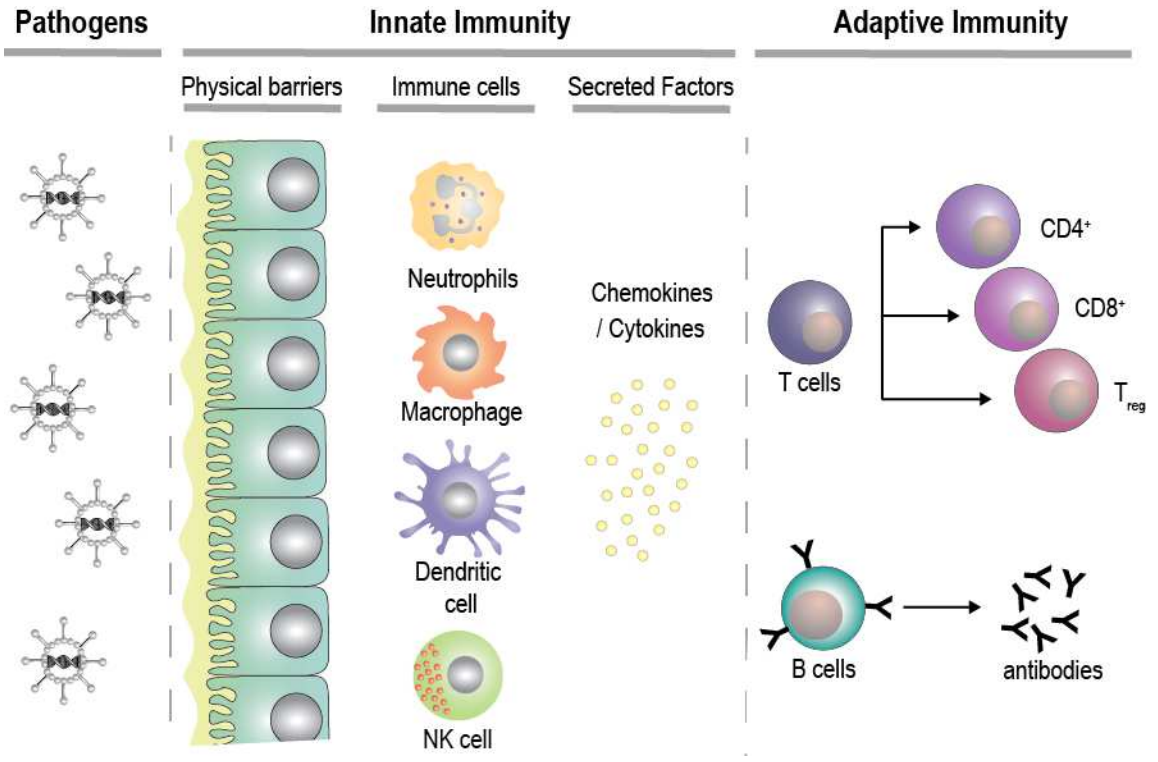

Figure 1: Structure of the immune system. The scheme represents the immune system consisting of innate and adaptive immune processes. The innate immune system serves as the first-line of defense against invading pathogens by physical barriers and innate immune cells. The adaptive immune system delivers highly specific defense responses against pathogen-specific antigens and is responsible for the establishment of long term resistance. Secreted chemokines and cytokines act as immune messengers which coordinate and activate the immune cells.

Immune cells originate from pluripotent stem cells in the bone marrow and differentiate into various cell types with specific functions. These immune cell populations encompass cells of the innate and adaptive immune system which closely interact with each other. The following paragraphs briefly describe immune cell types with important functions in antiviral defense responses.

1.1.1 Cells of the immune system

All nucleated cells are capable to execute basic innate immune functions and participate in antiviral defense responses by either releasing or responding to soluble paracrine and endocrine acting factors such as chemokines and cytokines during infections. However, specialized immune cells exist that exert tailored regulatory or executing immune functions, too. The following paragraphs briefly describe selected immune cells of the innate and adaptive immune system that contribute significantly to defense responses against viruses.

Neutrophils are the most frequent immune cell types in the blood. They exhibit a highly characteristic segmented structure of the nucleus and are among the first immune cell species at the site of infection. They limit virus infection by phagocytosis and by releasing anti-microbial factors at the infected site through degranulation. Additionally, these cells form specific extracellular structures capable to bind and trap foreign species [8].

Macrophages represent key players in the complex system of immune cells. These cells infiltrate infected tissue through leukocyte extravasation in response to chemotaxis and perform phagocytosis of virus-infected cells. During this process, macrophages synthesize and secrete massive amounts of IFN and other cytokines, leading to signal amplification and activation of further innate and adaptive immune responses. Moreover, macrophages also serve as antigen presenting cells (APCs). They activate T-cells by presenting foreign antigens on major histocompatibility complex (MHC) class II molecules at their cell surface. Additionally, specialized macrophage subsets such as M2 macrophages exhibit important functions that control and resolve inflammation after infection [9,10].

Dendritic cells belong to innate immune cells and execute a central communication function by presenting antigens to T-cells. Dendritic cells capture, process and present antigens and subsequently migrate to the lymph nodes to activate T-cells [11]. Specialized matured dendritic cells, such as plasmacytoid dendritic cells (pDCs), contribute significantly to cytokine levels, especially IFNs during viral infection [12]. Additionally, dendritic cells interact closely with natural killer (NK) cells and contribute to the expansion of antiviral acting NK cells during viral infection [13].

Natural killer (NK) cells are lymphocytes and exhibit a pivotal cytotoxic function against infected cells. Hence, they contribute significantly to the inhibition of virus replication during infection. NK cells can be divided into two major groups, namely (i) the cytotoxic NK cells expressing CD56 as well as CD16 and (ii) the regulatory NK cells expressing CD56 exclusively. The regulatory NK cells, as the name intends, secrete cytokines upon virus detection and act regulatory thereby [14]. In humans, about 90 % of the NK cell population represents cytotoxic NK cells. In contrast to cytotoxic CD8+ T-cells, cytotoxic NK cells are capable to lyse infected cells independent of specific antigens presented by MHC class I on the cell surface of virus-infected cells. However, to prevent random NK cell mediated lysis, NK cell activation requires a combination of molecular signals in order to guarantee specificity. Commonly, it necessitates the absence of inhibitory proteins such as HLA-A and HLA-B proteins and the presence of NK cell activators such as receptors and several co-stimulatory proteins at the cell surface [15,16,17].

T-cells are lymphocytes and belong to the adaptive immune system. They have the ability to recognize specific immunogenic peptide structures, so called antigens, presented at the cell surface by MHC molecules through their T-cell receptor (TCR). The somatic recombination of the variable antigen binding TCR domain and a highly specific selection process in the Thymus determines the T-cell specificity to the presented antigen and prevents the recognition of self-antigens. This complex process allows the generation of an almost unlimited arsenal of differently expressed and exposed TCRs with potential binding affinities to antigens of foreign origin. Dependent on the affinity of the TCR to either MHC class I or MHC class II presented antigens and the expression of respective co-receptors at the cell surface, T-cells can be categorized into CD8+ cytotoxic- , CD4+ inflammatory- or helper-T-cells.

CD8+ cytotoxic T-cells bind to antigens presented on MHC class I molecules. Co-activation of CD8+ cytotoxic T-cell relies on CD3 and CD8 dependent signaling, which in turn triggers the release of cytotoxic substances (granzymes) towards the infected cell. The released granzymes in turn lead to the induction of apoptosis of the targeted virus-infected cell.

In contrast to CD8+ T-cells, CD4+ T-cell activation requires the presentation of foreign antigens by MHC class II molecules. APCs, such as dendritic cells and macrophages, take up foreign molecular structures of pathogens and offer these at the cell surface. The APC mediated presentation process includes the uptake of foreign proteins by phagocytosis, processing of the peptides in the lysosome, loading of pathogen-derived antigens to MHC class II molecules and their presentation on the cell surface. These APCs migrate to lymph nodes to present their antigens.

Subsequent recognition of these MHC class II presented antigens by CD4+ T-cells lead to the secretion of cytokines and to the activation of antigen presenting B-cells.

Similar to T-cells, also B-cells are part of the adaptive immune system. They depend on pathogen-derived antigens to establish their long lasting immune memory function. Immune memory by B-cells encompasses the detection of the respective antigen either by binding through the B-cells itself or through the presentation by APCs. In response to the antigen binding, B-cells proliferate and generate two B-cell populations, namely antibody producing plasma cells and B-memory cells. During this process, B-cells require additional support by T-helper cells, which provide essential cytokines for their co-activation and the subsequent production and secretion of immunoglobulins [18].

1.1.2 The innate immune system

The immune system encompasses and links several multi-layered and tightly regulated processes to protect from foreign pathogenic species as described above. Within this system, the adaptive immune system depends on the activation of the T- and B-cells in an antigen dependent manner, a time consuming process that guarantees the correct differentiation of self- from foreign-molecular structures in order to prevent autoimmune reactions. Contrary to that, the innate immune system represents the first line of defense against pathogens such as viruses, bacteria and fungi. Its major task is to control infections until the adaptive immune system has acquired the power to specifically target and eliminate the pathogen [18]. The innate immune system consists of three essential key steps, namely (i) activation of the innate immune system, (ii) signal transduction and amplification and (iii) initiation of early cellular antiviral responses. The following paragraphs briefly describe these three topics.

1.1.2.1 Activation of the innate immune system

Activation of the innate immune system requires several consecutive molecular processes. These include the binding and sensing of pathogen associated molecular patterns (PAMPs) and danger associated molecular patterns (DAMPs), the activation of signaling cascades through cellular adapter proteins and expression and secretion of pro-inflammatory cytokines or the induction of cell death. The following chapters focus on the activation of the innate immune system through viruses in humans and will briefly describe the associated molecular processes.

Sensing of viruses

A critical task of the innate immune system represents the initial differentiation between self- and foreign molecular structures. Therefore, specific cellular pattern recognition receptors (PRRs) bind to their respective PAMPs. These PAMPs represent unique molecular structures present in the host during the replication process of the pathogen. In most cases, recognition of specific genomic structures by the host cell facilitates the detection of viruses during infection [19]. These genomic structures do naturally not occur in the host cell or are at least inaccessible for the respective PRR through cellular compartmentation under normal conditions [20,19]. For example, single stranded DNA or DNA-RNA hybrid structures are not present in the cytosol of uninfected cells as synthesis of ribonucleic acid sequences commonly occurs in the nucleus, thereby isolated from the cytosol through compartmentation. Hence, cytosolic PRRs cannot directly face such nucleotide sequence species, although they regularly appear temporarily during replication and transcription in the nucleus. In line with DNA-, also RNA-synthesis follows highly ordered rules, as in the transcription by Polymerase II (Pol-II) that generates precursor transcripts with a 5' triphosphate (5' PPP) modification in the initial step. 5' PPP RNA structures serve as preferred binding target for PRRs such as Retinoic acid-inducible gene I protein (RIG I). These PRRs would induce the auto-activation of the innate immune system in case of mislocalized 5' PPP-RNA that leaks into the cytosol [21,22]. However, under normal conditions, consecutive modifications of the cellular 5' PPP RNA precursors by the capping process prevents the recognition of such RNA species by RIG-I in the cytosol. Capping of mRNA precursors is performed by fusing a guanosine nucleotide to the triphosphates 5' end. Further chemical modifications include the methylation of the guanosine and the first two ribose molecules at the N7 and the 2' O position [23]. These co-transcriptional modifications are prerequisites for the export of matured 5' capped RNA from the nucleus into the cytosol and limits the presence of host cell derived 5' PPP-RNA in the cytosol. In turn, exported capped transcripts remain unrecognized by cytosolic localized PRRs after nuclear export. In contrast, as mentioned before, viruses regularly expose genomic sequences which lack one or multiple characteristics of their cellular counterparts during replication in the host. Hence, cells commonly exhibit a variety of different PRRs against such viral PAMPS [20,24,25]. The following table provides an overview of cellular PRRs, their localization and binding target of virus derived molecular patterns.

Table 1: Common PRRs that sense virus derived PAMPs [26,27,28]

Sensor Family	PRRs	Cellular Location	Target structure
TLRs	**TLR3**	Endolysosome	dsRNA
	TLR4	Plasma membrane	Viral Glycoproteins
	TLR7	Endolysosome	ssRNA
	TLR8	Endolysosome	ssRNA
	TLR9	Ensolysosome	CpG-DNA
RLRs	**RIG-I**	Cytoplasm	5´triphospate RNA, short dsRNA
	MDA5	Cytoplasm	Long dsRNA
	LGP2	Cytoplasm	dsRNA
ALRs	**AIM2**	Cytoplasm	dsDNA
	DAI	Cytoplasm	DNA sequence specific
	cGAS	Cytoplasm	DNA sequence specific
	IFI16	Nucleus	dsDNA

This thesis focuses on virus-host interaction; hence, the following section mainly depicts the sensing of viruses through Toll-like receptors (TLRs), RIG-I-like receptors (RLRs) and AIM2-like receptors (ALRs).

PRR – dependent induction of cell death

Sacrificing infected cells for the benefit of the cellular community represents a popular defense strategy to limit infection. Induction of cell death is especially effective in viral infections, as the replication of viruses completely depends on the host cell. Nod-like receptors (NLRs) such as the cytosolic double stranded DNA (dsDNA) sensing Absent in Melanoma 2 (AIM2) protein and the viral RNA sensor NACHT, LRR and PYD domains-containing protein 3 (NLRP3) are potent activators of the inflammasome. This high-molecular multi-protein complex leads to cell death by pyroptosis and converts the inactive Interleukin-1 (IL-1) precursor pro-IL-1β into its bioactive form by a caspase-1 dependent process [29,30,31,32]. The inflammasome is also sensitive to indirect, virus-mediated stimuli such as elevated levels of reactive oxygen species (ROS) that are generated during virus infections [31,33].

Another strategy that can results in cell death of virus infected cells is cellular interference with protein synthesis. Members of the oligoadenylate synthase (OAS) family act directly by activating RNase L. OAS proteins catalyze the second messengers 2'-5'-oligoadenylates in response to dsRNA binding, which in turn activates RNase L. The endoribonuclease activity of RNase L mediates cleavage of viral and cellular transcripts, inhibits translation and leads to apoptosis of the infected cell [34,35].

Another PRR that affects the cell's translation machinery in response to PAMP sensing is the eukaryotic translation initiation factor 2-alpha kinase2 (EIF2AK2, also known as PKR). Its binding to dsRNA in the cytosol results in the phosphorylation of the alpha subunit of the eukaryotic initiation factor 2 and causes the inhibition of the translation initiation which finally leads to the breakdown of the cellular translation machinery [36]. Comparable to the translation inhibition through OAS proteins, activation of PKR results in cell death of the host cell and to the restriction of virus replication on an organismal level.

PRR mediated secretion of cytokines

Sensing of viruses by PRRs, as described above, results either in cell death and/or in the inhibition of host cell molecular processes that are essential for viral replication. However, effective defense responses against viruses require the activation of antiviral programs in order to limit virus spread and to control infection in the host organism. Therefore, messengers and signaling pathways are of central importance to transduce the signal elicited by activation of PRRs through incoming viruses. These messengers and signaling pathways are essential for the expression and subsequent secretion of pro-inflammatory cytokines. Cellular adaptor proteins, such as MyD88, MAVS, STRING and TRIFs, link PRRs to signaling cascades of the innate immune system. The following paragraphs summarize several pivotal signaling pathways, which are essential for the innate immune defense against virus infections.

MyD88 and TRIF mediated innate immune activation through Toll-like receptors (TLRs)

TLRs are transmembrane domain containing PRRs localized at either the plasma- or the endosomal membrane. Binding of specific ligands to the outward facing leucine-rich repeat domains leads to receptor dimerization and initiate the formation of signaling complexes that assemble around adaptor proteins. TLR3 for example, senses double strand RNA (dsRNA) present in the endosome and initiates signaling through binding and subsequent oligomerization of the adaptor protein TIR domain-containing adapter molecule 1 (TICAM-1, also known as TRIF) to its TIR domain (Figure.2). The oligomerized TRIF proteins are capable to interact with three proteins to distribute signals by three distinct pathways. Association of RIPK1 to the oligomerized TRIF adaptor, for example, activates a caspase dependent cell death pathway. Interaction with TNF receptor-associated factor (TRAF3) protein, in contrast, results in phosphorylation, dimerization and subsequent translocation of IRF3 into the nucleus. Finally, association of TRAF6 to TRIF oligomers activates the transcription factors Nuclear factor kappa B (NF-κB), Activator protein 1 (AP-1) and cAMP response element-binding protein (CREB) through both, the Mitogen-activated protein kinase (MAPK) and TAK1/IKK pathway. Other members of the TLR family also trigger pro-inflammatory responses through NF-κB, AP1 and CREB pathways.

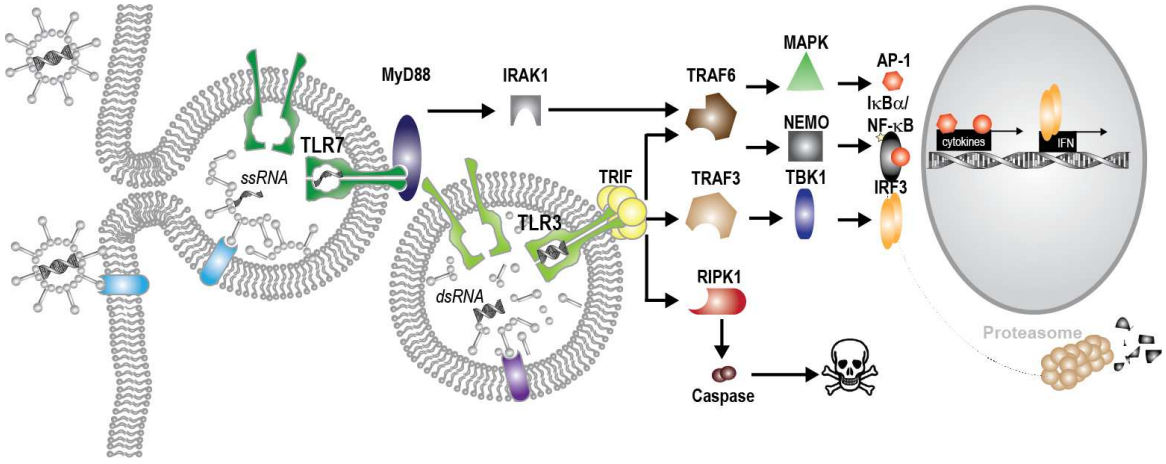

Figure 2: Sensing of foreign virus-derived nucleotide structures through TLR signaling. Binding of viral ssRNA and dsRNA to TLR7 and TLR3, respectively, initiates the associated downstream signaling through MyD88 and TRIF, resulting in the transcription and subsequent induction of IFN and cytokines in the cell (adapted from: [37,38]).

Contrasting to TLR3 however, these TLR family members signal mainly through the adaptor protein Myeloid differentiation primary response (MyD88), which forms, together with IL-1 receptor-associated kinase (IRAK) 1, IRAK2 and IRAK4, the Myddosome, a large signaling complex attached to the cytosolic TIR domain of TLRs that assembles after PAMP binding [39]. Virus

sensing through TLRs include several different TLR family members, which commonly lead to the induction and secretion of IFN-β and pro-inflammatory cytokines during virus infection.

MAVS mediated innate immune activation by RIG-I like receptors

RIG-I like receptors (RLRs) are virus RNA sensors located in the cytoplasm. They exhibit a characteristic domain structure composed of two N-terminal caspase recruitment domains (CARDs), a central DEAD box helicase/ATPase domain and the regulatory domain located at the C-terminus of the proteins. The RLR family covers three members, melanoma differentiation-associated gene 5 (MDA5), Probable ATP-dependent RNA helicase DHX58 (also known as LGP2) and RIG-I. RIG-I binds viral genomic RNA or viral derived RNA intermediates present during replication (Figure 3). It recognizes PPP-RNA and short dsRNA motives at the 5' end [21,22]. After binding of respective PAMPs, RIG-I requires additional modification of the N-terminal CARD domains by K63-linked poly-ubiquitination through the E3 ubiquitin ligases TRIM25 and RNF135 [40]. After activation, RIG-I re-localizes to the mitochondria and interacts with its adaptor protein Mitochondrial antiviral-signaling (MAVS) protein. The association of the exposed CARD domain of RIG-I to the CARD domain of the adaptor protein stabilizes the interaction and induces the formation of a signaling platform by clustering of multiple MAVS proteins. In a subsequent step, the MAVS signaling platform attracts TRAF proteins, which in turn activates Interferon regulatory factor 3 (IRF3), NF-κB and MAPK. These activations result in the expression and secretion of IFN-β and pro-inflammatory cytokines.

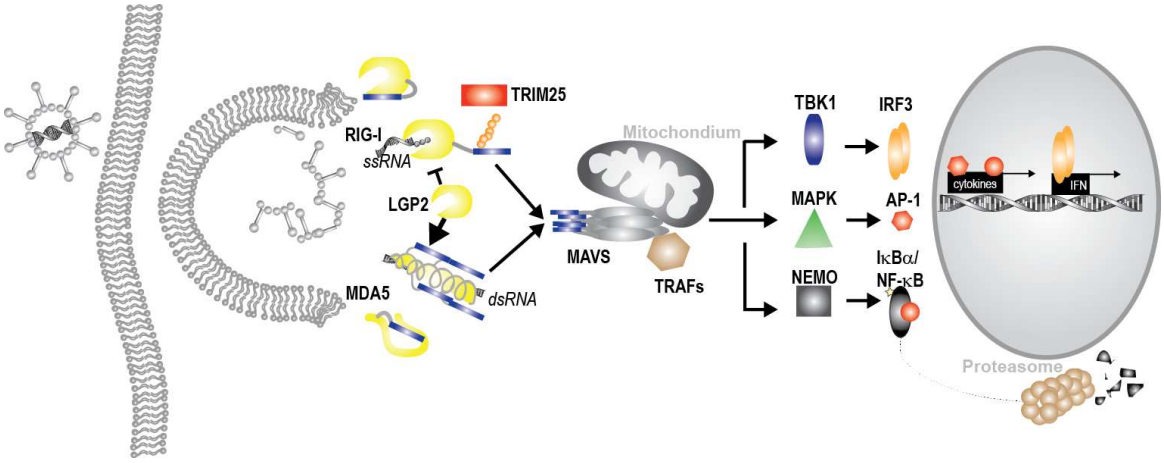

Figure 3: Activation of the innate immune system through RIG-I like receptors. Binding of viral RNA to RIG-I and MDA5 activates the downstream signaling cascade through MAVS. This leads to the expression of IFN and pro-inflammatory cytokines. LGP2 regulates the activities of RIG-I and MDA5 in the initial PAMP recognition step (adapted from: [37, 38]).

MDA5 also signals through MAVS to activate the innate immune system. MDA5 binds to long dsRNA species present in the cytosol during infection of positive-strand RNA viruses. It forms long oligomerized, filament-like structures along the bound dsRNA ligand. During binding, MDA5 exposes its CARD domain which subsequently interacts and activates MAVS [41,42,43].

In contrast to RIG-I and MDA5, LGP2 lacks the characteristic CARD domains and is therefore not able to trigger MAVS mediated signaling directly. However, recent studies clearly showed an important regulatory function of LGP2 in RLR signaling by boosting MDA5 activity while inhibiting RIG-I in the presence of long viral dsRNA. It binds dsRNAs at the 5' end and potentially competes with RIG-I binding. At the same time, however, it still allows MDA5 to bind along the dsRNA sequence to form its activated oligomerized, filament-like structure [44].

Innate immune activation through the cGAS-STING pathway

The cGAS-STING pathway activates the innate immune system in response to dsDNA. cGAS is localized in the cytosol and acts as PRR that catalyzes the synthesis of cGAMP, a 2'-5' linked ATP/GTP dinucleotide second messenger [45]. The synthesized 2'-5' cGAMP second messenger subsequently binds to the stimulator of interferon genes (STING) protein, a transmembrane protein localized in the ER (Figure 4). After cGAMP binding, STING translocates to the Golgi and serves as a potent signaling platform that activates serine/threonine-protein kinase TBK1. TBK1 activation results in IRF3-mediated induction of IFN-β and expression of pro-inflammatory cytokines via NF-κB activation through the IKK complex. Interestingly, innate immune activation through the cGAS-STING pathway is not limited to the infected cell only, as cGAMP is capable to shuttle to neighboring cells through gap junctions [46]. This allows the activation of the signaling pathway downstream of STING in cells in close proximity to the infected site.

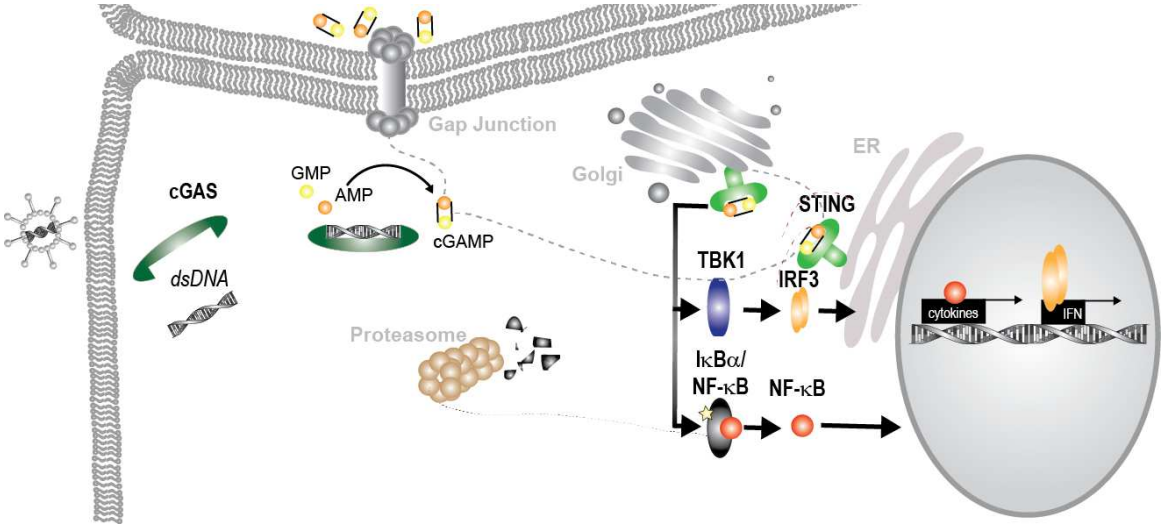

Figure 4: Activation of the innate immune system through the cGAS STING pathway. The binding of viral dsDNA to cGAS results in the synthesis of the secondary messenger cGAMP in the cytosol. cGAMP binds and activates STING in the cell, leading to the expression of IFN and pro-inflammatory cytokines through IRF3 and NF-κB, or it exits the cell via Gap junctions resulting in STING activation and subsequent secretion of IFN and pro-inflammatory cytokines in the cells in close proximity to the infection (adapted from: [37,38]).

Activation of the innate immune system through PRRs results in a surprisingly small number of activated transcription factors (NF-κB, IRFs, and AP1) and consequences in the induction of pro-inflammatory genes and IFN. The next chapter briefly describes the signal amplification and how antiviral signals spread from the site of infection to the whole host organism. It focuses mainly on IFN and its role during virus infection, as this is the central aspect in this thesis.

1.1.2.2 Antiviral signal transduction and amplification

Virus infected cells release a cocktail of immunologically active factors early after recognition of the pathogen. Among some directly acting proteins, such as members of the complement system, most factors attract and coordinate several different, highly specialized immune cells to the site of infection. Chemokines, for example, are secreted small factors which mediate immune cell infiltration into the tissue by leukocyte extravasation and guide immune cells such as macrophages, dendritic- and NK cells to the site of infection [47]. Through the phagocytic uptake of infected material, macrophages secrete massive amounts of immune modulatory molecules such as pro-inflammatory cytokines, chemokines and IFNs (Figure 5). At this stage, these cells amplify the defense signals and boost the immune system. Furthermore, they cross-activate other immune cells, most importantly cells of the adaptive immune system. The communication between signal sending

and receiving cells forms a complex inter cellular information network, which coordinates the antiviral defense response in the host [48].

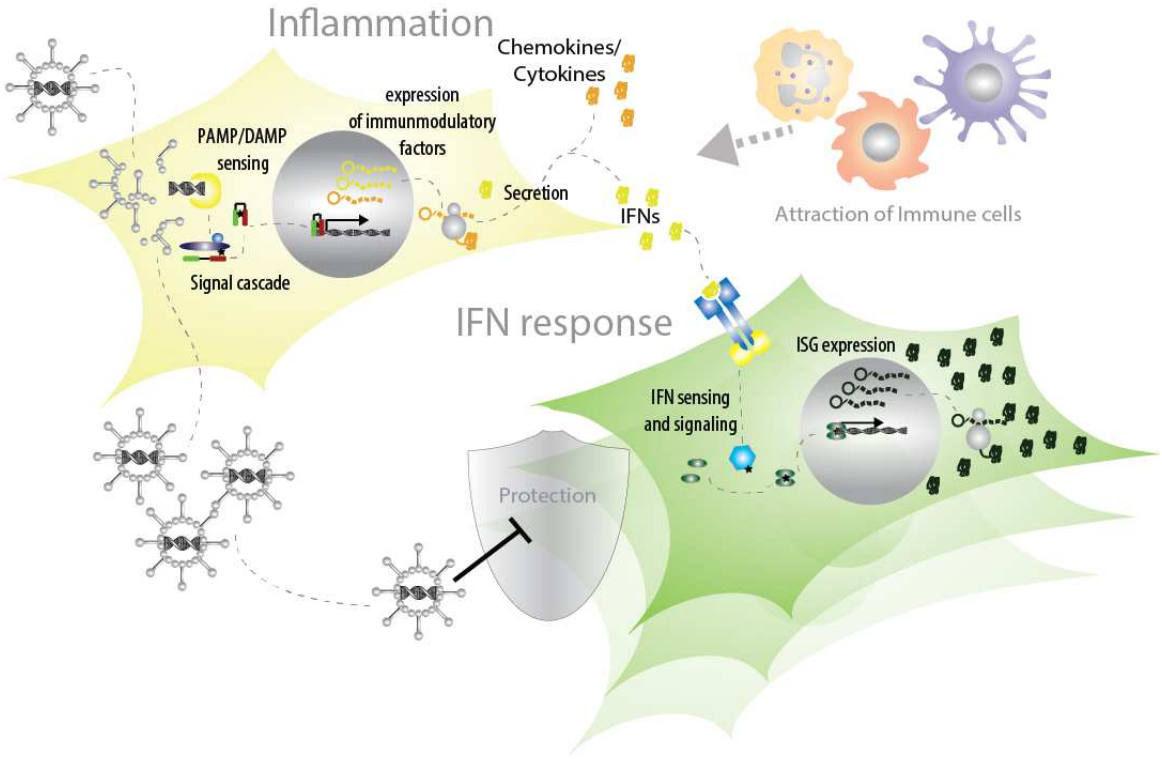

Figure 5: Activation of the innate immune system. Schematic representation of virus-induced innate immune activation and resulting defense responses. Innate immune activation encompasses the initial sensing of PAMPs or virus infection associated DAMPs, expression and secretion of pro-inflammatory cytokines and IFNs, activation and attraction of immune cells through cytokines and chemokines as well as signal activation and expression of ISGs through binding of IFNs to their respective receptors of signal receiving cells during infection.

Several released factors act as warning signals for uninfected cells in an autocrine and paracrine manner. They boost the expression of antiviral acting proteins and trigger processes that successfully limit virus replication in the host. Of central importance are pro-inflammatory cytokines and members of the IFN-family. The following paragraphs describe both, the inflammation processes and the initiation of early cellular antiviral responses by IFNs, with the primary focus on the IFN system.

Inflammation during virus infection

Recognition of PAMPs by PRRs triggers inflammation during virus infection. However, inflammation also appears in response to DAMP sensing. Such DAMPs often originate indirectly during virus infection and are potent pro-inflammatory stimuli. Lytic virus replication for example locally increases the amount of free nucleotides present in the extra-cellular space at the site of infection. These free extracellular localized nucleotides serve as bioactive molecules capable to trigger inflammation through specific receptors present on the surface of surrounding cells [49].

Typically, virus infection activates the NF-κB pathway and results in secretion of pro-inflammatory cytokines, such as TNFα, TGFβ, IL-1β and IL-6 [50,51]. The NF-κB family consists of the five structural related transcription factors NF-κB1 p50, NF-κB2 p52, RELA p65, RELB and c-REL [52]. NF-κB signaling occurs through two distinct pathways called "the canonical" and or "the non-canonical" pathway (Figure 6). The canonical pathway acts downstream of PRRs and results in rapid but only short lasting NF-κB activation [52,53]. Initial activation occurs through TGFβ-activated kinase 1 (TAK1), which in turn induces the formation of the trimeric IκB kinase (IKK) complex (IKKα, IKKβ and IKKγ) by phosphorylation. The activated complex subsequently ubiquitinates the REL-p50 inhibitory complex subunit IκBα, causes its degradation through the proteasome and thereby releases the p50-p65 heterodimeric transcription factor. The released transcription factor shuttles into the nucleus, binds its consensus κB elements in the genome and induces the expression of target genes [54]. In contrast, members of the TNF receptor superfamily, activate the non-canonical NF-κB pathway. Receptors such as lymphotoxin β receptor (LTβR), RANK and CD40 activate the heterodimer complex RELB-p52 transcription factor to mediate the expression of target genes. This signaling pathway uses NF-κB-inducing kinase (NIK) to phosphorylate the RELB inhibitory IκB-like molecule p100. In turn, p100 ubiquitination and proteasomal degradation releases RELB, which forms the heterodimeric RELB-p52 transcription factor, subsequently [55,56,57].

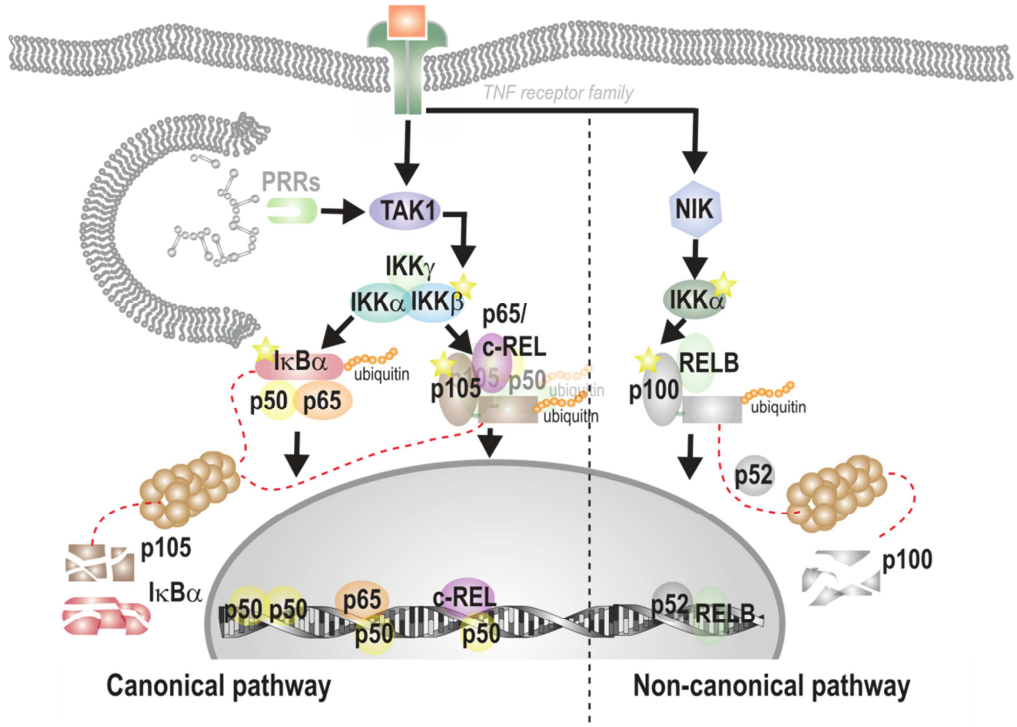

Figure 6: Canonical and non-canonical NF-κB activation. Schematic representation of NF-κB activation and canonical / non-canonical signaling cascade downstream of TNF receptors and PRRs.

Central mediators in both, the canonical and non-canonical NF-κB pathway, are members of the TRAF family. This protein family consists of seven family members (TRAF1-TRAF7), which interact with receptors and signaling mediators through their TRAF domains. In addition, all TRAFs, except of TRAF1, exhibit E3 ubiquitin ligase RING domains that are essential for signal transduction downstream of the receptors. They serve as a group of high variable proteins capable to link several different PRRs to a relative small number of conserved inflammatory signaling pathways. For example, TRAFs regulate the level of NIK through ubiquitination and subsequent proteasome degradation and contribute directly to a balanced inflammation response during non-canonical NF-κB activation [58]. Interestingly, the canonical and non-canonical NF-κB pathways do not act independently. Crosstalk at several steps leads to the activation of both NF-κB pathways during virus infection and results in a strong inflammation response that results in the secretion of pro-inflammatory cytokines and chemokines such as IL-1β, IL-6 and TNFα [51,59].

Interferons

The Interferon (IFN) system is among the best-studied and most effective defense response system against viruses in the early stage of infection. Its activation starts with the secretion of IFNs into the periphery of infected cells. IFNs bind to their corresponding, cell surface exposed receptors which subsequently trigger the JAK-STAT pathway, resulting in the expression of IFN-stimulated genes (ISGs) [60]. These ISGs represent a group of hundreds of genes which encode for proteins with direct antiviral and essential regulatory function in the innate immune system.

IFNs represent a distinct family of secreted messengers that can be classified in three types according to their corresponding receptor at the cell surface (Type-I, II and III IFNs). Type-I IFNs are the most prominent innate immune messengers during antiviral response. They bind to the heterodimeric receptor complex consisting of the IFN-α receptor 1 (IFNAR1) and the IFN-α receptor 2 (IFNAR2) chain (Figure 7). The binding of type-I IFNs (such as IFN-α, IFN-β, IFN-ε, IFN-τ, IFN-κ, IFN-ω and IFN-ζ) through IFNAR2 at the cell surface induces dimerization of both receptor chains and forms the IFNAR1/2 receptor complex. During dimerization, the tyrosine kinase 2 (TYK2) and Janus kinase 1 (JAK1), which are both attached to the cytosolic domains of the IFNAR1 and IFNAR2 respectively, get in close proximity to each other which causes their reciprocal activation through phosphorylation. The activated kinases in turn phosphorylate the signal transducer and activator of transcription (STAT) 1 and 2. Upon phosphorylation, STAT1 and STAT2 dimerize, attract the interferon regulatory factor 9 (IRF9) and form the heterotrimeric transcription factor complex IFN-stimulated gene factor 3 (ISGF3) thereby. ISGF3 in turn, shuttles into the nucleus, binds to ISRE motives in the genome and activates gene expression [61,62,63]. In parallel, type-I IFN also mediates phosphorylation and dimerization of STAT1, which results in phosphorylation of the IFN-γ-activated factor (GAF) and mediates its binding to γ-activated sequences (GASs) in the nucleus [64]. In addition, dimerization of the IFNAR2 chains activates the mitogen-activated protein kinase / c-Jun amino-terminal kinase (MAPK/JNK) pathway [65].

Type-II IFN signaling is activated downstream of the IFN-γ receptor (IFNGR) by its respective ligand IFN-γ. Binding of IFN-γ results in dimerization and subsequent phosphorylation of STAT1 through IFNAGR1 and IFNAGR2 bound JAK1 and JAK2. Phosphorylated STATs form the transcriptional regulatory complex GAF after dimerization and activate gene expression [66].

Type-III IFNs (IFN-λ1-4) signal through the IFN-λ receptor 1 composed of the low-affinity receptor subunit IL-10R2 and the high-affinity type-III IFN receptor subunit (IFNLR1). Similar to

the IFNAR1 receptor in response to type-I IFN, IFN-λ signals through the JAK-STAT in a TYK2 and JAK1 dependent manner [67,68].

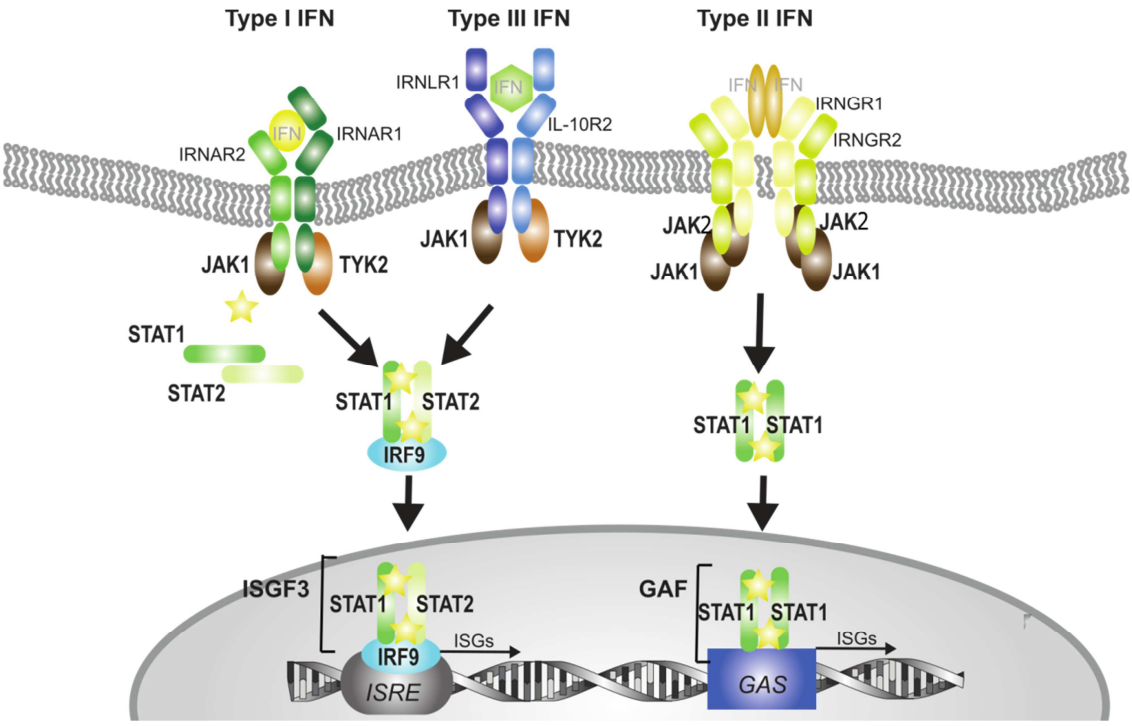

Figure 7: IFN signaling. Binding of IFNs (type I, II and III) through their respective cell surface receptors results in the activation of the downstream JAK-STAT pathways and induces the expression of ISGs through binding of the activated transcription factor complexes ISGF3 and GAF to their respective promotor elements (ISRE and GAS) in the nucleus (adapted from [66]).

1.1.2.3 Interferon stimulated genes

Interferon stimulated genes (ISGs) encompass a group of 300-400 genes which are expressed to elevated levels in response of IFN. Depending on their function, ISGs and their corresponding protein products can be categorized into three main groups: (i) ISGs with IFN-sensitization and co-activating function, (ii) ISGs with direct effector functions against pathogens and (iii) ISGs, which balance or down-regulate the IFN system.

ISGs with IFN-sensitization and co-activating function

Many ISGs encode for proteins with key regulatory functions within the IFN-system or other defense response processes such as inflammation. Prominent members of this group are PRRs, such as RIG, MDA5, TLRs, and signaling proteins that transmit signals elicited by PRRs as for example MyD88, STATs, JAK and IRFs [66]. Most cells express these factors at baseline levels, which enable cells to sense and activate the innate immune system in case of a virus infection. In response to IFN,

these factors are significantly up-regulated in the cell, which results in higher overall sensitivity against pathogens. ISGs belonging to this group share the ability to reinforce and co-activate defense pathways of the host to inhibit pathogen replication early after infection [66]. Systematic functional studies based on overexpression of single ISGs, revealed that a considerable number of ISGs in this group exhibit broad antiviral activity and are therefore of central importance for innate immune mediated antiviral defense strategies [69]. Expression and subsequent activation of IRF1, for example, was shown to occur in parallel to PRR mediated PAMP/DAMP sensing in cells and directly induces expression of selected ISGs independently of the JAK-STAT pathway. This IRF1-mediated ISG expression is believed to act as an emergency system to activate ISG expression even if JAK-STAT signaling is inhibited through pathogen induced evasion strategies [66,70].

ISGs with direct effector functions against pathogens

Another group of ISGs represents a class of IFN-induced effector proteins, which directly inhibit viruses. Functional overexpression studies of individual ISGs of this group showed high antiviral activity against viruses with similar molecular and structural properties. This points towards a highly selective, evolutionary shaped adaption of such antiviral factors to inhibit specific virus classes [69]. The following paragraphs briefly describe selected ISGs with pivotal protective functions against virus infections.

Among the longest and best-studied ISGs are members of the murine myxovirus (Mx) resistance gene family, namely Mx1 and Mx2. Both are present in the cytoplasm of human cells after IFN stimulation and share structural homology with proteins of the dynamine and dynamine-like GTPase family. Although Mx1 inhibits numerous different viruses such as Rift valley fever virus (RVFV), La Cross virus (LACV), Hepatitis B virus (HBV) and Crimean-Congo hemorrhagic fever virus (CCHFV), its antiviral function is best studied in the context of infection with Influenza A virus (FluAV), a member of the *orthomyxoviridiae* family. During FluAV infection, Mx1 interacts with the nucleoprotein complex during the viral uncoating process and prevents the import of the viral ribonucleotide protein complex (vRNP) into the nucleus, which leads to an efficient block of FluAV replication [71–73].

Interestingly, characterization of Mx2 revealed only limited activity against Mx1 targets. Instead, Mx2 exhibits highly specific inhibitory functions against herpesviruses and HIV at a pre-nuclear entry step. Mutational analysis of the HIV-1 capsid protein suggests that the antiviral activity of Mx2 against HIV-1 depends on the Mx2 interaction property to the capsid structure of HIV-1 virus particles. This hypothesis is in line with the observation that Mx2 fails to inhibit HIV-1 with mutated capsid structures [74,75]. In contrast, the pan-herpesvirus restriction by Mx2 depends on the

GTPase function of Mx2 as shown by inhibition experiments of herpes simplex virus 1 and 2 (HSV-1/-2) with intact and mutated, GTPase inactive Mx2 variants [76,77].

The interferon-induced protein with tetratricopeptide repeats (IFIT) protein family is highly diverse in mammals and contains four members IFIT1, -2, -3 and 5 in humans. They are localized in the cytosol and are among the highest induced ISGs in response to IFN stimulation. IFITs exhibit antiviral activity against numerous viruses including VSV, RFVF, West Nile virus (WNV) and HCV [78–80]. The antiviral activities of IFIT proteins rely on two major mechanisms. IFIT proteins inhibit HCV, a positive-stranded RNA virus, by targeting viral mRNA translation. Translation of HCV mRNA through its viral internal ribosome entry site (IRES) is strictly dependent on the recruitment of the cap-independent translation initiation complex. Human IFIT1 and IFIT2 interact with eIF3E and eIF3C. This interaction in turn blocks the assembly of the cap-independent translation initiation complex at the IRES motives present on viral mRNA and thereby prevent its translation [81–83]. Similar to RLRs, IFITs bind to virus-specific structures on the 5′prime end of viral RNA with high affinity as for example to 5′-ppp RNA [79]. During this binding process, IFIT1 recruits IFIT2 and IFIT3, which subsequently results in the 5′-ppp RNA IFIT1/-3 complex formation. Antiviral activity of IFITs is dependent on the complex formation, as depletion, but not the ectopic expression of individual IFIT proteins affects the IFN mediated inhibition of virus replication in cells. Interestingly, antiviral activity of IFIT1 against the human papillomavirus (HPV), a DNA virus, has also been reported. In contrast to the antiviral mechanisms against RNA viruses described before, a direct interaction of IFIT1 with the viral E1 helicase causes inhibition of HPV replication, which results in the local depletion of this essential HPV factor from the viral replication site [84,85].

The virus-inhibitory protein, endoplasmic reticulum-associated interferon-inducible (viperin) protein inhibits various RNA and DNA viruses. Viperin is highly evolutionary conserved and associates to ER-derived lipid droplets under normal conditions in the cell [86]. It limits replication of numerous enveloped viruses by different molecular mechanisms. During FluAV and HIV-1 infection, for example, viperin inhibits the enzyme activity of farnesyl diphosphate synthase (FDPS) and reduces membrane fluidity at the plasma membrane, which in turn limits the release of the newly synthesized virus particles [87,88]. Antiviral activity against HCV relies on viperin′s interaction to the HCV non-structural protein 5A (NS5A) and to the cellular vesicle-associated membrane protein-associated protein A (VAP-A). The interaction of viperin to VAP-A disturbs HCV replication complexes on lipid droplets and causes the inhibition of viral replication thereby [89,90].

Bone marrow stromal antigen 2 (BST2, also known as Tetherin) is a membrane-associated ISG that inhibits a variety of different enveloped viruses. BST2 associates to membranes through its two GPI-anchors. One of the two GPI-anchors integrates into the lipid layer covering the newly formed enveloped virus particles while the second GPI-anchor remains attached to the lipid layer of the plasma membrane. Thereby, BST2 tethers the infectious particle to the cell and prevents virus release. Hence, BST2 functions as a biological trap and mediates the formation of long chain-like structures that consist of interconnected, non-released virus particles [91]. More recently, BST2 was shown to activate the NF-κB pathway during virus replication. Although, the exact molecular mechanism that links BST2 to the NF-κB pathway remains speculative so far, this finding characterizes BST2 as a direct antiviral acting ISG with an additional immune-stimulatory function [92].

Beside the selected ISGs descripted above, numerous less well characterized ISGs with potent antiviral activity against specific viruses were identified in several ISG overexpression studies [69,93–95]. Notably, the diverse distribution of ISGs in cells indicates that these proteins are able to face viruses at different subcellular localizations and act at several stages of the viral replication cycle.

ISGs which balance and down-regulate the IFN system

Constant activation of the innate immune system correlates with various autoimmune phenotypes and overshooting, harmful reactions. To limit such negative effects, the immune system needs to be balanced carefully. Therefore, it requires mechanisms capable to reverse inflammation and to down-regulate the IFN system after pathogen elimination.

IFN de-sensitization occurs immediately after activation of the IFN system by endocytosis and subsequent lysosomal degradation of the IFN receptor [66]. However, some ISGs also contribute actively to the IFN desensitization processes by inhibiting JAK-STAT signaling. The suppressor of cytokine signaling (SOCS) proteins, for example, binds to JAK proteins and IFN receptors at phosphorylated tyrosine residues and efficiently blocks STAT phosphorylation. Another negative regulator of the IFN system is Ubl carboxyl-terminal hydrolase 18 (USP18) protein. It is the major de-ISGylation enzyme and balances the pool of free and covalently bound ISG15, a ubiquitin-like modifier with various known regulatory innate immune functions [96–98]. Interestingly it was shown, that USP18 inhibits activation of the IFN system in a de-ISGylation independent mechanism, by interacting with the IFNAR2 receptor and competing with JAK1 binding sites. Thereby USP18 blocks downstream JAK-STAT signaling and downregulates the activation of the innate immune system [99].

1.2 VIRUSES

Viruses are among the most abundant class of pathogens on earth and strictly depend on host organisms for their own replication [100]. Viruses are known to infect highly diverse lifeforms ranging from prokaryotes to plants and mammals. In human, virus infections are responsible for a huge proportion of the overall diseases worldwide. These virus infections lead to various disease forms in infected individuals including relatively harmless outcomes such as a common cold but also life-threatening reactions such as hemorrhagic fever and encephalitis [101–103]. Furthermore, several persistent virus infections such as for example by human papillomavirus (HPV), human T-lymphotrophic virus (HTLV), Epstein-Barr virus (EBV) and hepatitis C virus (HCV), are known to cause cancer in human and are estimated to be responsible for approximately 15 % of all cases worldwide [104]. Additionally seasonal recurring virus infections and pandemics such as by influenza virus are accountable for high numbers of deaths and economical losses worldwide [105,106]. Especially immune suppressed individuals suffer from severe viral infections which are commonly well controlled in healthy, immune competent individuals. This highlights the central importance of the immune system during virus infections. Unfortunately, only a limited number of antiviral treatment options are available, which inhibit specific viral infections efficiently. A pan antiviral drug that inhibits a broad range of different viruses still remains elusive.

Their ability to adapt to their environment resulted in an incredible versatility of diverse viruses. Viruses can be categorized into numerous groups and families dependent on their genome structure (e.g. negative and positive stranded RNA, DNA, segmented genomes), structural properties (e.g. enveloped and un-enveloped) and their degree of genome similarity. Viruses per definition rely on the molecular machineries of their hosts, which provide and support obligate processes for virus replication. This dependency is a consequence of the limited viral genome capacity and necessitates sophisticated manipulation strategies to conquer the molecular machineries of their hosts. Viruses commonly encode for proteins that secure the successful formation of infectious, replication-competent particles. It includes structural proteins and viral polymerases that are required for viral genome replication. Additionally, viruses encode for highly variable proteins that serve as adaptor proteins and interact with cellular machineries to control and manipulate the host. A typical viral replication cycle includes three steps: i) viral entry, ii) viral genome replication, protein synthesis and assembly and iii) maturation and budding of the new infectious viral particle.

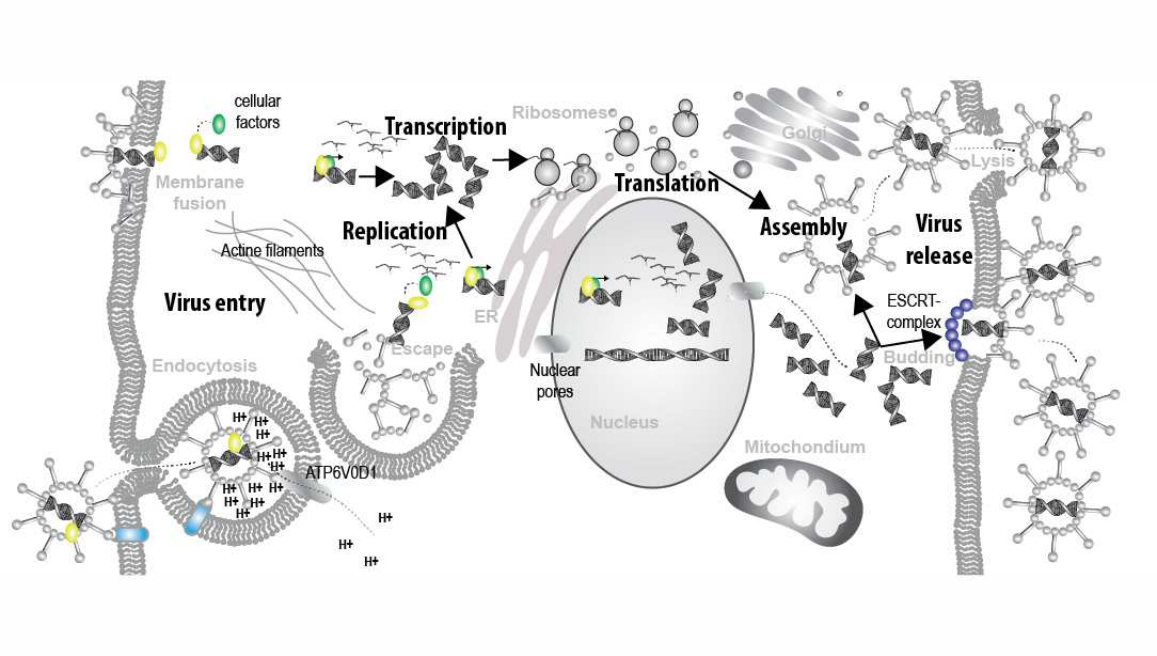

Figure 8: Virus replication cycle during infection. Schematic representation of key steps during virus replication. Viruses enter the host by attaching to specific cell-surface factors and enter the cell by membrane fusion or by endocytosis. Virus particles escape the endosome during the acidification process by structural rearrangements of pH sensitive viral proteins. Alternatively, virus derived ribonucleoprotein (vRNPs) complexes are directly released into the cytosol after membrane fusion. After uncoating of viral genome-associated structures in the cytosol, cellular factors (green) attach to the viral polymerase (yellow) and genome structure to support genome replication and transcription of virus encoded open reading frames. Virus transcripts are supplied to the cellular translation machinery and assemble with their newly synthesized genomes at different subcellular compartments or directly at the plasma membrane of the cell. Finally, virus particles are released through a budding process or by lysis of the host cell.

1.2.1 Virus entry

Viruses commonly enter their hosts through exposed viral structures which attach to the surface receptors of their host cells. This process subsequently triggers the uptake of the infectious particle through endocytosis or fusion of the viral coating lipid layer at the plasma membrane. Several post-uptake processes occur, which include escape strategies from endosomal vesicles, uncoating of viral capsid structures and the translocation of the viral genome to its preferred replication site. During this entry process, the virus relies on several supportive host factors and protein complexes. Essential host factors in this regard encompass cell-surface receptors that are highly specific to individual viruses, viral classes or – families and are required for the initial attachment of the viral particle [107,108]. Several viruses enter the host cell by endocytosis and require V-type proton ATPase pumps such as ATP6AP1 to escape from the endosome. These proton pumps facilitate the influx of hydrogen ions into the endosome and lead to endosomal acidification, which in turn causes structural rearrangements of viral glycoproteins, disrupts the endosome-covering lipid layer thereby

and delivers the viral capsid into the cytoplasm. This escape process is important to prevent subsequent lysosomal degradation of the infectious particle [109,110].

1.2.2 Viral genome replication, protein synthesis and assembly

Replication and transcription of the viral genome occurs at defined sites within the cell. Some viruses such as members of the *orthomyxoviridae*, *herpesviridae* and *retroviridae*, replicate in the nucleus and depend on the active transport through the nuclear pore complex or on the breakdown of the nuclear structure during cell division to enter the nucleus. Other viruses, such as the *flaviviridae* family members, replicate in specified structures at the endoplasmic reticulum (ER) or directly in the cytosol such as *filoviridae* and *hantaviridae* [111–113]. Although viruses encode for their own polymerases, they depend on cellular proteins which support replication and transcription of their genetic information by adding specific modifications or even misuse whole cellular complexes like the spliceosome [114–116]. Additionally, all viruses strictly depend on the host's translation machinery for protein synthesis. Therefore, viruses evolved multiple strategies to feed-in their transcripts into the cellular system. They either use internal ribosomal entry site (IRES) elements or modify their transcripts accordantly to the demands of the translation machinery[117,118]. Viruses also make use of cellular factors that support correct folding by co- or posttranslational processes to ensure functionality of their proteins [119–121]. To complete their replication cycle, viruses need to form new infectious virus particles to leave their host cell. Therefore, viruses recruit cellular machineries that transport viral genomes and proteins to distinct cellular sites [122]. At these sites, the high concentration of virus-encoded proteins and virus-derived nucleic sequences result in a self-assembly process, which is supported by cellular factors [119,123].

1.2.3 Maturation and budding of new viral particles

Viruses utilize two mayor release strategies to leave the cell after their replication cycle. They either rely on the lysis of the host cell or bud from the cell surface into the extracellular space [124–127]. The release mechanism is dependent on the virus type. Enveloped viruses for example predominately bud from cellular membranes in order to generate their coating lipid layer and initiate their release. Hence, many enveloped viruses require the support of cellular factors such as the ESCRT complex to efficiently separate from the lipid bilayer of their hosts [128]. Interestingly, virus budding is not limited to the cell surface. Viruses of the *flaviviridae* family for example bud into the ER to mature and to subsequently leave the cell through the trans-Golgi network (TGN)

[129,130]. Other viruses such as members of the *herpesviridae* family bud from the nucleus into the perinuclear space before they finally leave the host cell through exocytosis [131].

1.2.4 Viral innate immune evasion strategies

Extensive recruitment of cellular factors at multiple steps during replication is characteristic for virus infections. Among others, viruses control gene expression, cell cycle, energy metabolism and cell death pathways in host cells to optimize their replication efficiency [107,132]. Cellular defense strategies are particularly in the focus of viral manipulation strategies as they determine significantly to the success of the viral replication. In fact, all viruses capable to infect and replicate in humans, exhibit a multitude of different virus-specific strategies that aim to limit the host′s defense system. Central targets of viral proteins are cellular proteins and pathways that are involved in antiviral defense systems such as the innate and adaptive immunity [132–134]. These acquired strategies operate in a collaborative manner and manage to prevent virus recognition and subsequent immune activation. The following paragraphs provide a brief overview of such virus-mediated strategies capable to control the IFN response during infection.

1.2.4.1 Viral immune evasion through mutation and adaption

Viruses commonly adapt quickly to their environment due to their high mutation rates and short replication times. This enables most viruses to escape neutralization through antibodies or to escape the activity of therapeutic drugs by acquiring mutations in the drug target site [135,136]. Therefore, viruses with particularly high mutation rates such as HIV and FluAV manage to evade medical treatment and/or vaccination strategies in short time. FluAV for example is able to escape neutralizing antibodies by rapidly changing the molecular patterns of its accessible glycoproteins exposed at the surface of the virus particle by gene drift and shift strategies [137]. Other viruses such as HIV-1 for example, evolved strategies to keep exposed proteins variable in order to reduce recognition and elimination by neutralizing antibodies [138]. Additionally, viruses regularly mask huge parts of their protein- and genome-structures by their lipid bilayers and form capsid structures which effectively shield potential immune targets from their respective cellular sensors. However, after entering their host cells, viruses disassemble and their genomes become accessible during replication. Consequently, viral genes encode for proteins that are dedicated to suppress the immune system of the host. These proteins exhibit direct or indirect immune modulatory functions to guarantee efficient production of new infectious virus particles. Common viral targets of the

innate immune system represent sensing of PAMPs by PRRs, inhibition of signaling pathways downstream of PRRs, cellular transcription, translation and cell death pathways. The following paragraphs focus on these frequently targeted processes and describe representative viral strategies to inhibit innate immune responses.

1.2.4.2 Virus modulation to disrupt pathogen sensing by PRRs

Sensing of viruses through PRRs is a key process in the activation of the innate immune system. Therefore, many viruses target this early step to evade recognition. They interact directly with the PRRs or inhibit signal transduction of the associated downstream signaling pathways.

Protein kinase R (PKR) and oligoadenylate synthase (OAS) represent cellular sensors that recognize dsRNA in the cytosol. The FluAV encoded NS1 protein interacts with both, PKR and OAS, to inhibit RNaseL and eif2α activation, respectively, which in turn prevents inhibition of translation and guarantees continuous synthesis of virus-derived proteins during infection. To suppress PKR activation even more, NS1 additionally binds and blocks the association of PKR to dsRNA structures in the cytosol [139,140]. Interestingly, viruses target PKR regularly, which points towards an evolutionally highly conserved antiviral mechanism. For example, RVFV encoded NSs, E3L of Vaccinia virus (VACV) and TSR1 of Human Cytomegalovirus (HCMV) prevent PKR activation during infection. The RVFV derived NSs protein for example recruits the F-box proteins FBXW11 and βTRCP1, which fuse ubiquitin to PKR and facilitate its degradation through the proteasome [141,142]. In contrast, VACV E3L binds and sequesters dsRNA to prevent PKR activation and HCMV TSR1 inhibits PKR activation by trapping it in the nucleus of the cell [143,144]. Additionally, VACV K3L, sigma3 protein of Reovirus and NS5A of HCV are also potent viral effectors which effectively inhibit PKR activation [145–147].

Viral factors often interact with members of the RLR- and TLR-pathways to control virus sensing. The Z protein of Arenavirus and NS2 of the Human Respiratory syncytial virus (HRSV) inhibit RLR signaling by preventing the interaction of RIG-I with MAVS [148,149]. The NS1 of FluAV was also shown to inhibit activation of the RIG-I. It prevents the TRIM25 mediated ubiquitination of the CARD domain, a process that is essential for the interaction of RIG-I with its adapter protein MAVS [150]. Several other viral factors such as PB1-F2 of FluAV, HBX of HBV, NS3/4A of HCV act downstream of RIG-I and interact directly with MAVS or with cellular factors downstream in the signaling cascade to prevent innate immune activation. For example, they block phosphorylation, dimerization and nuclear translocation of IRFs such as by the Ebola virus encoded VP35 protein to

disrupt downstream signal transduction [151–155]. Notably, targeting of IRFs by viruses also affect other PAMP sensing pathways such as TLRs and cGAS. Therefore, it represents an attractive, central target for viral immune modulatory strategies. Further virus proteins that interfere with the function of IRF family members include BGLF4 of EBV and NSP1 of Rotavirus for example. Both initiate IRF3 and IRF7 degradation by the proteasome to inhibit innate immune activation [156,157].

A viral target of the TLR pathway represents its central adaptor protein TRIF. The HAV encoded 3CD and the VACV encoded A46R proteins both induce the degradation of TRIF by binding and cleaving this central TLR adapter protein [158,159]. Additionally, numerous viral proteins were identified recently, that target and inhibit selective steps of the cGAS/STING pathway. These virus-mediated cGAS/STING inhibition strategies include the disruption of ligand binding, blockage of protein interactions and inhibition of posttranslational modifications which are required along the signaling pathway [160].

1.2.4.3 Viral modulation of cell death pathways

Programmed cell death (PCD) pathways are capable to sacrifice cells for the benefit of the remaining cell community within an organism. PCD pathways, which include apoptosis, necroptosis, necrosis and pyroptosis, act in response to a number of different cellular events such as DNA damage caused by radiation or other mutagenic substances, external signals such as by Tumor necrosis factors (TNFs) or in response to pathogen sensing during virus infection. Viruses commonly inhibit PCD in order to gain time to complete their replication cycles. However, some viruses also profit from cell death and even promote the activation of PCD pathways [161]. In both cases, viruses try to influence cell death programs by manipulating key mechanisms within PCD pathways.

Viruses manipulate PCD at the levels of regulatory factors such as for example caspases, RIPs and mitochondria associated processes [161]. These factors function as central platforms for signal transduction and determine the progression of cell death to a large extent. One common strategy represents the expression of virus encoded proteins with high sequence similarity to central regulatory apoptosis factors such as viral BCL2 (vBCL2) and viral FLIP (vFLIP) proteins. They mimic the properties of their cellular counterparts and modulate apoptosis for the demand of the virus. The viral FLIP homolog for example, potently inhibits the cleavage of the inactive pro-caspase 8 (ProCASP8) precursor into its processed, activated form and prevents caspase induced apoptosis [162,163]. Other viral mimetics such as vBCL2s block the cytochrome C release by affecting the mitochondrial membrane permeability, which also prevents the caspase-mediated cell death

activation. Kaposi's sarcoma-associated herpesvirus (KSHV), VACV and adenoviruses for example express such homologs during infection to prevent cell death [164–166]. Caspases are among the most frequently targeted cell death factors during virus infection, pointing towards their central function during virus infection. The HCMV encoded vICA protein, for example, binds to the ProCASP8 and prevents its cleavage-mediated activation. In contrast to the vFLIP protein described before, vICA does not show high sequence homology to the cellular FLIP protein and is likely to represent an independent evolutionally shaped HCMV strategy to inhibit caspase dependent activation during infection [167]. Additionally, viral proteins of the *poxviridae* family were shown to inhibit apoptosis by preventing caspase 8 activation, too [168,169]. Although CASP8 represents a major target for viruses in cell death regulation, other viral proteins like KSHV encoded K7 and the VACV encoded BCL2 homolog F1L prevent caspase-mediated cell death by inhibiting CASP3 and 9 [170,171]. In contrast, HIV, LGV (Langat virus) and HPV express proteins that directly activate caspases. This enhanced activation of the host´s cell death program is highly regulated and was shown to support the release of newly synthesized viral particles at a late stage of infection [172–174].

Another important PCD pathway that affects virus replication is necroptosis. This PCD pathway relies on signal transduction through the Receptor-interacting serine/threonine-protein kinases (RIPK) RIPK3, RIPK1 as well as through MLKL proteins and represents a caspase-independent cell death pathway [175]. Herpesviruses inhibit necroptosis during infection through their viral inhibitor of RIP activation (vIRA) protein. The vIRA protein binds to RIPK3 and prevents its polymerization and subsequent activation [176]. Further cell death inducing factors represent reactive oxygen species (ROS). Elevated ROS levels are regularly observed during virus infection and result from an imbalanced cellular redox environment during infection [179,178]. Although the molecular mechanism of ROS induced PCD is not yet examined in detail, a recent study points towards a central function of the Superoxide Dismutase 1 (SOD1) protein, an enzyme which is capable to reduce ROS in cells during FluAV infection [179].

1.2.4.4 Virus modulation of NF-κB and Interferon signaling

According to their central importance in pathogen sensing and initiation of defense responses, viruses inhibit IFN signaling and the NF-κB pathway through a whole arsenal of different mechanisms. For example, viruses modulate NF-κB activity by preventing IKK degradation. They encode for IKK like proteins, which directly inhibit NF-κB activation and block the translocation of the activated NF-κB complex into the nucleus [180,181]. The Epstein-Barr virus-encoded EBNA1

protein for example inhibits IKK phosphorylation and prevents its ubiquitination and subsequent degradation by the proteasome thereby [182]. The Rotavirus nonstructural protein NSP1 also antagonizes NF-κB activation. It stabilizes IKK by forcing beta-transducin repeat containing protein (β-TrCP) into proteasomal degradation. β-TrCP is a central component of an E3 ubiquitin ligase complex, which mediates ubiquitination and subsequent degradation of IKK [183].

Although several specialized virus proteins inhibit NF-κB activation, some viruses activate NF-κB to prevent apoptosis during infection. The human respiratory syncytial virus (HRSV) protein M2-1 for example associates with RELA and activates NF-κB to evade death of the host cell during HRSV replication [184–186].

IFN triggers the major defense response against viruses during early stages of infection. Viruses developed diverse strategies to suppress IFN activation and subsequent IFN regulated genes (ISG) expression in their hosts. Therefore, viruses inhibit IFN signaling either by interacting directly with their respective PRRs or by interfering with the signal transduction along the associated downstream signaling cascades. The KHSV encoded K3 and K5 proteins for example downregulate the gamma interferon receptor from the cell surface during infection [187]. Other viral factors such as VP40 of Marburg virus, EBV encoded LMP1 and the NS5 protein of Japanese encephalitis virus (JEV) interact with the kinases JAK1 and TYK2 to prevent IFN signaling [188–191]. Other viral factors modulate JAK/STAT signaling further downstream by interfering with the phosphorylation, dimerization and translocation of STAT proteins and by inducing the degradation of other essential cellular signaling factors required for signal transduction along the JAK/STAT pathway[192–196]. All these strategies aim to avoid the expression of the restrictive ISGs. The next paragraph encompasses common molecular mechanisms that allow viruses to prevent the expression of ISGs.

1.2.4.5 Viral modulation of the host´s gene expression

Although viruses affect NF-κB and IFN signaling as described before, these viral strategies are not sufficient to suppress innate immune responses effectively along the whole time of infection. Hence, viruses acquired mechanisms which potently shutoff the gene expression in the host. They successfully modulate protein expression at different levels such as transcription, mRNA transport, splicing and translation [197–199].

Viruses affect the function of the RNA polymerase II (RNAP II) to modulate the gene transcription in the host. The non-structural small (NSs) proteins of the *bunyaviridae* family

members RVFV and Bunyamwera virus (BUNV) for example target the RNAP II complex by initiating the degradation of the TFIIH subunit p62 [200,201]. This TFIIH subunit is an essential component of the transcription factor 2 and recruits RNAP II to the promotor region of genes. Other viral strategies include the disruption of the pre-initiation complex by the immediate early protein 63 of VZV (IE63) and the ubiquitination and degradation of the cellular RNAP II by the FluAV polymerase [202,203]. These viral interventions in transcription efficiently suppress host protein expression and prevent elevated levels of ISGs that would accelerate an effective antiviral response in the cell.

Several virus-encoded proteins interfere with the cellular mRNA transport mechanisms to control the host's gene expression on a post-transcriptional level. Among the best-studied viral proteins in this regard is NS1 of FluAV. It inhibits mRNA polyadenylation and nuclear export of host cell transcripts. The structure of NS1 contains an N-terminal RNA-binding domain as well as an effector domain located at its C-terminus of the protein [204,205]. The effector domain interacts with the cellular cleavage and polyadenylation specific factor-30 (CPSF30) and inhibits pre-mRNA processing. This in turn traps cellular transcripts in the nucleus, stops the translation of host transcripts and suppresses the expression of defense response genes like ISGs during infection [206–208]. Notably, FluAV performs polyadenylation of transcripts by its own viral RNA-dependent RNA polymerase (RdRp) and is therefore not affected by the NS1-mediated mRNA export blockage [209,210]. This mechanism effectively reduces the amount of competing host mRNA for translation and efficiently blocks the expression of cytokines and antiviral proteins such as ISGs at the same time [211]. Interestingly, FluAV mediated mRNA export blockage seems to exclude selected transcripts of housekeeping genes. These selected transcripts encompass cellular factors which contribute to oxidative phosphorylation and are believed to maintain the required high energy level in the cell for effective FluAV replication [209]. Other viruses, such as members of the *picornaviridae* and *rhabdoviridae*, mainly inhibit host protein expression by controlling nuclear export through the nuclear pore complexes [212–214]. The M protein of VSV, for example, interacts with Rae1, a central mRNA export factor and disturbs Rea1-Nup98 interaction. This in turn blocks the nuclear Rae1/mrnp41 mRNA export pathway [215,216].

Herpesviruses such as HHV1 and HHV2 control protein expression through their ICP27 proteins at the posttranscriptional splicing step. ICP27 interacts with cellular spicing factors and affects pre-mRNA processing which results in reduced host protein translation [217–219]. The HIV-1 encoded accessory protein VPR highjacks the pre-spliceosome in a comparable process [220]. Both viral proteins bind to the essential splicing factor SAP145 and disturb the subsequent complex

formation steps which lead to the blockage of the pre-spliceosome and results in incomplete pre-mRNA processing. Alternatively, several *herpesviridae* family members encode for proteins, which lead to the degradation of the host′s mRNA through their RNase activity. These viral factors include the VHS protein of HSV, the SOX protein of KSHV and the Epstein–Barr virus (EBV) encoded BGLF5 protein [221–223].

Next to the alteration of splicing mentioned above, viruses also interact and inhibit translation directly at the eukaryotic translation machinery [224]. Eukaryotes require a set of additional, supportive proteins to initiate, elongate and terminate translation. The high molecular weight translation initiation complex provides essential functions during this process and serves as target for several viruses. Among other picornaviruses, the Foot- and mouth disease virus (FMDV) encodes for a protease which specifically cleaves eIF4G, a central component of the cap binding complex eIF4F, which is responsible for the recruitment of mRNA to the ribosome during translation initiation [225,226]. Commonly, viruses that target eIF4G rely on alternative translation initiation strategies, such as internal ribosomal entry sites (IRES), to be independent of the eIF4F complex-mediated cap-binding function during the translation of viral proteins.

Another viral target represents the canonical translation initiation factor poly(A)-binding protein (PABP). Depletion of PABP in cellular extracts revealed dramatically reduced translation rates, which were rescued by adding wt PARP but not by adding a mutated PARP variant that is incapable of interacting with eIF4G [227]. Viral factors such as 3C Proteases of *picornaviridae* family members cleave PABPs enzymatically. This prevents PABP binding to the polyadenylated sequences at the 3′end of host transcripts and causes inhibition of host protein translation [228–230]. Protease 3C cleaves several other cellular factors with central function within the eukaryotes' translation machinery which underlines the importance of the translation control for the replication of *picornaviridae* family members [230,231].

In summary, viruses and their host cells are highly interconnected and virus replication necessitates a variety of different cellular processes. Detailed knowledge about this complex virus-host interplay is pivotal for the understanding of the virus-host relationship and could provide important novel information that could help to develop more efficient treatments of viral infections in the future. Improvements of assays and screening technologies already helped to gain momentum in resolving this high complexity in the host-pathogen interaction field. The next chapter focuses on tools, strategies and methods, which contributed significantly to the understanding of the molecular interplay between viruses and their hosts in recent years.

1.3 RECENT ADVANCES IN VIRUS-HOST INTERACTION STUDIES

For a long time, molecular virus-host interaction studies were limited to hypothesis-driven approaches and relied on elaborate *in vitro* and *in vivo* experiments. Recombinant virus systems enabled the manipulation or even deletion of viral open reading frames (vORFs) with high efficiency, which facilitated the characterization of viral proteins and their functions during infection. However, the identification of relevant host factors for virus infections was still limited, as complementary genetic technologies for mammalian cells were still not available. More recently, improvements in "omics" technologies and genome wide screens revolutionized the virus-host interactions research field. The following paragraphs concentrate on approaches that contributed to the current understanding of the virus-host interaction system.

1.3.1 Genome wide functional screen applications to study virus-host interactions

Genetic screens allow a detailed view of virus replication required and restricting host factors. Initially, genome wide studies were based on gain of function screens as availability of appropriate reverse technology for loss of function studies was inaccessible for a long time. The following paragraphs describe recent *in vitro* methods, which are used to study and link genes to their function in virus replication. In these screens, gene functionality is commonly assessed by the observed virus replication rate in presence or absence of a specific host gene. Traditional methods that evaluate virus growth such as plaque counting depend on time-consuming and work-extensive protocols that are not suitable for genome-wide applications. Consequently, genome-wide functional screens are commonly limited to recombinant reporter virus systems. Such viruses typically encode fluorescent proteins or enzymes, which accumulate during infection and directly correlate with viral replication rates [232]. Detection of such signals can be performed in highly parallelized and automated formats capable to deal with genome wide applications.

1.3.1.1 Gain of function studies to analyze virus-host interactions

Gain of function studies rely on the overexpression of single genes in the host cell. Traditionally, cDNA libraries of virus-permissive cell lines were transferred to cell lines, which resisted virus infection. Assessing virus replication in these modified cells enabled the identification of crucial

cellular factors such as receptors that are used by viruses to enter the cell [233–235]. This approach was also extensively used to study the function of ISGs. Almost 400 different ISGs were expressed individually in cells and replication rates of different viruses were monitored subsequently. These experiments contributed significantly to our understanding of the function of ISGs during virus infections [69,94,95]. Moreover, cDNA library based gain of function screens were of central importance for the discovery and characterization of key innate immune factors such as RIG-I [236]. Gain of function screens can be also applied in a pooled format. However, pooled screens necessitate a traceable system to reliable quantify the genotypes of the surviving cells after virus infection. Additionally, pooled gain of function screens are biased towards identification of cellular restriction factors, since overexpression of restriction factors potently inhibit virus infection which results in prolonged overall survival of these cells.

1.3.1.2 Loss of function screens to study virus-host interactions

Loss of function screens require the depletion of selected proteins in the host cell to connect gene function to replication phenotypes during virus infection. During recent years, the following techniques were applied to study virus-host interactions.

RNA interference (RNAi) is regularly used to deplete selected proteins in cells in order to study gene function. Two technologies are commonly applied, which use either small hairpin RNA (shRNA) or small interfering RNAs (siRNA) to direct the mRNA-cleaving RISC complex to its target transcript. In a genome wide format, this strategy allows to identify three categories of proteins: restriction factors, essential host factors and proteins that do not alter virus replication. Within the last decade, numerous research groups used RNAi knock down screens to define such protein groups for different viruses. These screens provided hundreds of candidates per studied virus, including flaviviruses such as HCV and WNV, VSV-G pseudotyped HIV and several FluAV strains among others [107,237–240]. Interestingly, most siRNA screens tend to identify considerable more virus-essential host factors compared to virus restriction factors. This trend is a consequence from the applied assay formats and from the nature of antiviral acting genes, which often are regulated in their expression levels during virus replication and therefore might not be depleted sufficiently [241]. Additionally, RNAi screens of different research groups commonly result in a low overlap of identified candidates. Low standardization of assay designs and data analyses contributed to this low conformity between different RNAi screens. Analyzing such screens in a combined format, however, significantly increases overlaps of the identified candidate groups [107,242]. RNAi screens identified multiple cellular factors with central importance for the replication of viruses. For

example, several studies identified a group of vATPases as essentially required host factors for FluAV replication [107]. Additionally, RNAi screens contributed valuable information about the uptake of HCV into its host cell. EGFR and EphA2 were identified as cell surface proteins that are required for this initial step in HCV infection [243].

In contrast to RNAi based knock-down screens, other assays rely on gene knock-out technologies to study the interplay between viruses and their hosts. Such technologies generate phenotypes that are more pronounced and exhibit a better signal-to-noise ratio compared to conventional knock-down screens [244]. Two major technologies were extensively used to study virus-host biology in recent years.

Screens in haploid cell lines rely in the knock-out of target genes by lenti- or retroviral gene traps, which insert splice acceptor sites into the host genome. This process leads to truncated mRNA transcripts and loss of gene function. Screens are commonly performed in a pooled format by applying retroviral gene traps to a population of haploid cells. These gene traps integrate into the genome of cells and lead to the loss of gene function. Infection of such a mutated mixed cell population results in the relative enrichment of cells that resist virus induced death. Subsequent sequencing allows to map and quantify these respective cells [245]. So far, genome wide screens in haploid cell lines identified several host factors, which are essentially required for virus replication. A prominent example is Niemann-Pick C1, a cholesterol transporter protein essential for the entry of Ebola virus into its host cell [246]. Haploid screens also identified several other entry receptors. These include important proteins for adeno-associated-, Lassa- and Rift-valley fever virus entry processes [247–249]. However, these assays are limited as only a few haploid or near-haploid cell lines are available that guarantee reliable knock-out efficiency by lenti- or retroviral gene traps. This limits its application to viruses that are capable to replicate within these cells lines. Recently however, gamete manipulation resulted in the generation of human haploid embryonic stem cell (haESC). These haESCs exhibit characteristics comparable to human pluripotent stem cells which makes them a perfect cell system for loss of function studies that are very close to the physiological condition in human [250,251]. Furthermore, the high number of gene traps that hit a single gene in this kind of screens result into studies with statistical power that commonly outperforms alternative genetic approaches.

CRISPR-Cas9 gene editing technology enjoys increasing popularity in the host-pathogen interaction research field recently. Its high efficiency and broad application spectrum makes CRISPR-Cas9 gene editing perfectly suitable for genome-wide loss of function screens. The technology is derived from the prokaryotic CRISPR-Cas defense system and was reengineered to

knock-out genes in almost any mammalian cell type [252,253]. CRISPR-Cas9 requires a designed single guide RNA (sgRNA) to align and direct the endonuclease Cas9 to its target site in the genome. It introduces double-strand breaks at its target site in the genome, which is repaired by non-homologous end joining (NHEJ). The double-strand repair process frequently causes frameshift mutations that result in the expression of non-functional or truncated proteins [252–254]. Recent CRISPR-Cas9 based screens focused on the *flaviviridae* family. These studies resulted in a comprehensive and detailed understanding of the biological processes that drive replication of flaviviruses in cells [255–258]. Other examples include the identification of CLM1 as an entry receptor of the murine Norovirus and the identification of cellular factors important for early steps in the infection process of CD4+ T-cell lines by HIV-1 [259,260]. Other CRISPR-Cas9 applications include the identification of cellular factors with functional relevance for Toll-like receptor signaling [261]. This study revealed several so far unknown cellular factors, which contribute to TLR 4 signaling.

Another regularly used technology in the virus-host interaction field is mass spectrometry based proteomics. The following paragraphs describe its applications in this research field, including a brief introduction into the basic principles of the technology with focus on recent advances.

1.4 APPLIED MASS SPECTROMETRY BASED PROTEOMICS IN HOST-PATHOGEN INTERACTIONS

The ability to identify and reliably quantify a broad range of cellular products made mass spectrometry the technology of choice to study complex biological systems. Although the basic principle of mass spectrometry is known since decades, the analyses of complex samples such as cell extracts remained challenging. These limitations were overcome by key technological improvements, such as soft ionization methods as for example by electrospray ionization (ESI) and matrix-assisted laser desorption ionization (MALDI) [262,263]. Another necessity that improved tremendously is the availability of genome sequence data, which is essentially required for mass spectra interpretation by software algorithms [264,265]. Proteins, as the major executing molecular unit in the cell, are of particular interest as they determine most phenotype-relevant processes [266]. Mass spectrometry based proteomics allows to access this central step directly and in an unbiased way. Furthermore, it can analyze proteins on multiple molecular levels, including investigation of protein abundance, post-translational modifications (PTMs), protein interactions, protein stability and even structural properties of proteins [267–269].

However, even after huge advances in recent years, acquisition of high quality mass spectrometry spectra and identification of the entire proteome is still challenged by the incredible high complexity and dynamic range present in the samples [270,271]. This high complexity leads to technical challenges in practice. High identification rates and reliable quantification by bottom-up proteomics makes it the method of choice to study such complex proteome samples [272].

1.4.1 Bottom-up proteomics

Bottom-up proteomics relies on the detection of proteolytic digested peptides. The enzymatic activity of trypsin for example, a highly active and specific protease which is commonly used in bottom-up proteomics, results in a pattern of pre-defined peptide fragments [267]. A typical bottom-up proteomics workflow consists of the following consecutive steps: i) experimental design and sample preparation, ii) mass spectrometry based data acquisition and iii) data analysis and interpretation. All these individual steps contribute to the performance and quality of a proteomic study.

1.4.1.1 Experimental design and sample preparation

The success of a scientific study depends on the experimental design. Most proteomic studies rely on the relative quantification between experimental- and control conditions. Therefore, proteomic experiments require a set of suitable references. The required amount of starting material needs to be considered, too. Analysis of post-translational modifications (PTMs) for example often relies on elaborative enrichment steps and requires relatively high amounts of starting material. Therefore, the minimum amount of material for each experimental setting needs to be considered, which can be a limiting factor in particular when analysis of primary cells or tissues should be performed. Furthermore, a sufficiently high number of independent replicates needs to be considered for the analysis to gain enough statistical power in order to discriminate real proteome changes from random noise.

Detergents like sodium dodecylsulfate (SDS) or strong chaotropic reagents such as Urea or Guanidinium–hydrochlorid are commonly used to destabilize the structure of cells [273,274]. For some experiments, including affinity enrichment (AE) and affinity purification (AP) analyses, mild detergents such as NP40 or digitonine are used to preserve the structural conformation of proteins and the integrity of protein complexes [275,276]. The addition of dithiothreitol (DTT) or tris(2-carboxyethyl)phosphine (TCEP) to the lysate reduces disulfide bonds. The subsequent incubation of the reduced peptide mixture with iodoacetamide (IAA) or chloroacetamide (CAA) chemically modifies the reactive cysteine side chains by alkylation and prevents the formation of disulfide bonds in the sample lysate [277]. Proteases, like Trypsin and LysC, digest the proteins by proteolysis into defined peptides [278]. These peptides carry a positive charge at the N-terminus and an additional positive charge at the amino acid side chain of either arginine or lysine located at the C-terminus. The charge-state of peptides can be used to distinguish contaminants from digested peptides. Therefore, uncharged and single charged signals are commonly excluded from subsequent mass spectrometry analysis. Furthermore, the double charged state of the peptides is favorable as it results in highly informative MS/MS spectra after peptide fragmentation [275]. However, different chemicals, such as detergents, interfere with subsequent steps in the analytical workflow and have to be removed completely. This can be achieved by protein precipitation, filter assisted sample preparation (FASP) and affinity based single-pot solid-phase-enhanced sample preparation (SP3) protocols [279]. Before applying the sample to the LC-MS/MS system, peptides have to be desalted, enriched and eluted into small volumes which can be loaded onto the small diameter analytical column of the LC system [280].

1.4.1.2 Mass spectrometry based data acquisition

Bottom-up proteomics analyses require three online-coupled units to fulfill the following basic processes: i) separation of sample complexity, ii) transition of ionized analytes into the gas phase and iii) identification and quantification of the peptides. The following sections focus on these three basic processes and describe common instrumental solutions.

The separation of the peptides in time and space is essential for high quality and reproducible results. This is especially important for complex proteome samples, which exceed the scan capacities, even of modern mass spectrometers [281,282]. Peptides are commonly separated at the front end of the mass spectrometer by coupled units [283,284]. Most state of the art systems use online-coupled High Pressure Liquid Chromatography (HPLC) columns, which elute and separate peptides by linear gradients over time [267]. Ideally, these HPLC units de-complex the peptides to an extend that the mass spectrometers can analyze the eluting peptides without exceeding their technical limitation.

Separation efficiency of liquid chromatography methods depends on several parameters such as column length, column diameter, resin bead diameter and several other physical properties of the stationary phase such as its specific affinity to the analytes. Mobile phase parameters like viscosity, flow rate as well as environmental factors, such as the temperature and pressure in the system, also affect peptide separation [285]. C18 resin packed analytical columns are most commonly used for bottom-up proteomics applications. The bead size of the C18 resin and the diameter of the analytical column correlate reversely with the separation efficiency of the peptide mixture. A small column diameter limits vertical diffusion events and a small bead size leads to an overall increased accessible interaction surface area. The column length correlates directly with the separation efficiency since a longer stationary phase increases the possible interaction surface between the stationary phase and the peptides in solution [285]. However, longer columns increase the dead volume and the back pressure dramatically and lateral diffusion events along the analytical column can lead to peak broadening that impairs peptide separation efficiency. Heated, tightly controlled temperature regulating devices such as column ovens help to keep the backpressure of the analytical columns in a tolerable range even at high flow rates [286,287]. They additionally increase the reproducibility of methods by keeping the analytical column temperature in a defined narrow range. The increasing concentration of organic volatile liquids such as acetonitrile in the mobile phase leads to the elution of peptides along the gradient.

At the interface of modern LC-MS/MS systems, the electrospray ionization (ESI) unit links the LC to the mass spectrometer. ESI is capable to ionize peptides in solution and is therefore applicable

to LC coupled mass spectrometry systems. Ionization is performed by applying a high electrostatic potential to the tip of the analytical column. The analytes elute from the LC column and form highly dispersed liquid droplets as a consequence of the electrostatic repulsion between the liquid droplets [288]. The ionization of the solubilized analytes occurs during the evaporation process before and within the initial entry step into the mass spectrometer. During this process, the charges distribute equally along the surface area of the spray droplets until a maximal electronic charge density, the so called Rayleigh-limit, is reached. Liquid evaporation over time increases the charge density of the droplets until the Rayleigh-limit is exceeded which leads to the formation of smaller droplets. This increases the relative droplet surface area and relaxes the charge density again. Repetition of this cycle finally transfers the electrostatic potential to the analyte [262]. An alternative ionization method is matrix-assisted laser desorption/ionization (MALDI). However, in contrast to ESI, MALDI cannot ionize peptides in solution efficiently and is therefore preferentially used to analyze low complex samples [263].

Mass spectrometers have to guide, fragment, analyze and detect peptides in bottom-up proteomics applications. Guidance of ionized peptides in bottom-up proteomics needs to be fast, efficient and gentle. Therefore, mass spectrometers use different kinds of ion optics to direct ionized analytes through the high vacuum space and to ensure fast and gentle transmission. By using electromagnetic fields, ions can be guided similar to light by optical devices.

In the widely used bench top Exactive systems (Thermo Fisher Scientific) for example, the so called s-lens gradually focuses ions to a defined ion beam at the front end of the instrument. The injection flatapole transfers the ion beam to the bent flatapole. The bent flatapole forces ions into a 90° curved trajectory and separates ionized analytes from uncharged contaminations that co-transmit into the system [263]. Subsequently, the ions enter the Quadrupole which stabilizes specific ions according to their mass to charge (m/z) ratio. Therefore, the Quadrupole changes its radio frequency (RF) potential and applies a direct current (DC) potential along the rods. Opposing rod pairs of the Quadrupole exhibit the same electrostatic potential, while the neighboring opposing rod pair exhibits an electrostatic potential in the opposite charge state. Changing these pairwise settings periodically between the rod pairs stabilizes ions in a narrow m/z range, which depends on the applied RF and DC potential [289]. Therefore, Quadrupoles can serve as extremely versatile mass filters. Finally, specific peptide species are collected and stored in the C-trap before they are distributed into the higher-energy C-trap dissociation (HCD) collision cell [272,290].

In bottom-up proteomics, identification of peptides relies on the detection of characteristic atomic masses derived from fragmented peptides by so called MS/MS scans. The peptide fragmentation follows the Roepstorff-Fohlmann-Biemann nomenclature and represents a series of a, b, c and x, y, z-ions [288,291,292]. In Orbitrap instruments, collision induced dissociation (CID) and the related HCD are commonly used. They predominately generate peptide fragments according to the lowest energy pathway, which results in the cleavage of the amino bonds along the peptide backbone [288]. The collision with an inert gas phase, such as nitrogen, causes a series of fragment derived, highly informative, singly charged b- and y-ions which bear positive charges at the N-or C-terminal sites from the parental peptide [293].

An alternative fragmentation method represents electron transfer dissociation (ETD). In contrast to CID and HCD, ETD primarily generates c- and z-ions and induces fragmentation by transferring electrons from radical ions to the peptide in the fragmentation cells. Although ETD, and its parental method electron capture dissociation (ECD), provide less peptide fragmentation efficiency at small double-positively charged peptides, it outperforms collision-based fragmentation methods when analyzing long and multiple charged peptides and preserves labile posttranscriptional modifications (PTMs). It is therefore the method of choice for top-down proteomic approaches [294].

Detection of peptides and corresponding peptide fragments is carried out in the mass analyzer. Mass analyzers can be separated according to their basic working principle into two groups, namely the beam- and the trap-based analyzer types. Time-of-flight (TOF) and Quadrupole analyzers belong to beam-type analyzers as both continuously scan incoming ions. Ion trap analyzer, Fourier-transform ion cyclotron resonance and Orbitrap mass analyzer belong to trap-type analyzers, which determine m/z ratios of captured ion species. The individual mass analyzers differ significantly in regards to their scan speed, sensitivity, resolution and mass accuracy. Orbitrap instruments commonly use Orbitrap mass analyzers alone, in combination with linear ion traps or make use of the incredible scan speed of a selection Quadrupole such as in the state of the art Exactive system [295,296].

Linear ion traps (LIT) are regularly used in mass spectrometers as they are capable to trap, select, fragment and analyze the masses of ions directly. LITs deduce m/z values based on the ion trajectory stability in oscillating electric fields and consist of hyperbolic Quadrupoles with a central section that is flanked by trapping units at both ends. In contrast to Quadrupoles, which periodically scan through the mass range and stabilize ions with specific m/z ratios, LITs operate on the principle of resonance ion ejection and subsequently detect the ejected ions by electron multipliers [297]. LITs exhibit high sensitivity and relatively high sequencing speed but are limited in

the resolution and mass accuracy compared to other mass analyzers. Hence, LITs are commonly used in modern hybrid mass spectrometry instruments to complement their functions and increase the flexibility of the analytical platform [289].

The highest resolving-power of mass analyzers is achieved by using Fourier-transformation for the interpretation of oscillating ion signals [298–300]. This Fourier-transformation based principle is used in Orbitrap analyzer to deduce mass information from the ionized analytes. The Orbitrap analyzer work-principle is based on an electrostatic trap and provides high resolution (~ 150.000), high mass accuracy (2-5 ppm) combined with a high dynamic range [301]. Basically, the Orbitrap cell consists of a spindle-like shaped inner and outer electrode. The special orientation and shape of the electrodes as well as the electrostatic field inside the Orbitrap forces ions into an orbital trajectory around the inner electrode. The ions are accelerated to high kinetic energies in an ion trap unit called C-trap before they are pulse-injected asymmetrically into the Orbitrap cell. The applied electronic fields on each side in the Orbitrap initiate the oscillation of the injected ions along the spindle-shaped inner electrode, while attraction of the inner electrode counter-balances the centrifugal forces of the ions and stabilizes the orbital trajectory around it. The frequency of the axial ion oscillation across the neutral area between the axial electrostatic fields in the center of the Orbitrap depends on the m/z ratios of the ions. The oscillating signal is measured by the outer electrodes and is interpreted by a fast Fourier-transformation algorithm to deduce the m/z values of the circulating ions [289].

1.4.1.3 Data analysis and interpretation in mass spectrometry based bottom-up proteomics

With the advances in mass spectrometry based proteomics applications, the increased complexity and quantity of the generated data require automated workflows, which are able to deal with the increasing amount of acquired data. These computational pipelines need to fulfill certain criteria to successfully link the information of the observed mass spectra to the corresponding peptides.

Implemented algorithms in these computational pipelines need to interpret peptide signals which appear as peaks along the elution gradient. These peaks are defined by the m/z ratio of the peptide and by the signal intensity which represents the abundance of a peptide or peptide derived fragment at a given time. Algorithms need to find and define these peaks and must be capable to separate peptide derived signals from background noise. During peptide identification, the signals are interpreted. Therefore, the sequence information is deduced on the basis of the obtained mass

spectra from the fragmented peptides (MS/MS) [302]. Mapping of the MS/MS spectra to its corresponding peptide is performed through a target-decoy principle. Therefore, an implemented search engine compares the observed MS/MS spectra to a set of expected theoretical fragment ions. These expected theoretical fragment ions are deduced from reference proteomes of the respective organism as for example provided by UniProt FASTA files. The algorithm compares the theoretical fragment ions to the observed mass spectra and calculates the probability for their match based on the signal characteristics. These probabilities are controlled by a false discovery rate (FDR) threshold based on the nonsense peptide sequence information which is commonly deduced from the reversed amino acid sequences of the used reference proteome from a decoy database [288,303,304]. Search engines such as Mascot, SEQUEST and the MaxQuant embedded Andromeda algorithm perform these calculations and match spectral information to the best fitting peptide in the reference database. Subsequently, algorithms map identified peptides to their corresponding proteins. This protein assembly step is particularly challenging in case of non-unique peptides, which regularly occur during the proteolytic digest. This is especially difficult in case of closely related proteins and protein isoforms. Therefore, software solutions, such as offered by MaxQuant, generate protein groups, which contain identifiers of multiple protein isoforms and of closely related proteins. Finally, algorithms calculate the protein intensities by integrating and summarizing the peptide signals over the elution time [305,306]. However, several different protein quantification strategies can be applied. These differ substantially from each other and are briefly described in the following section.

1.4.1.4 Protein quantification by mass spectrometry

Reliable quantification methods are essential for the interpretation of most biological experiments. Depending on the application, protein quantification by mass spectrometry needs to fulfill certain requirements and can be separated into label-dependent or label-free methods [307].

In label-dependent methods, quantification necessitates either metabolic or chemical labeling of the analytes to compare different experimental settings [308,309]. In classical SILAC based experiments for example, cells grow in medium that contains fully substituted 13C-labeled lysine and arginine amino acids. These stable isotope substituted amino acids differ in their mass from their natural occurring counterparts and integrate into the newly synthesized protein pool of cells over time. This results in synthesis of protein species, which exhibit peptides with defined mass shifts in their mass spectra [306,310,311]. In the classic experimental design, each labeled sample represents a defined experimental condition. At the beginning of the sample preparation process the differently labeled

samples are pooled and processed together to prevent introduction of variation by sample handling in subsequent steps. During bioinformatics analysis, the samples are distinguished by their respective mass shifts in the observed mass spectra [310]. However, despite of low sample variation and high reproducibility, SILAC based methods face some limitations. Multiplexing capacity of this method for example, is strictly dependent on the number of available isotope labeled amino acids. Additionally, sample complexity multiplies with the number of used SILAC channels. The increased sample complexity commonly results in less overall identification rates compared to analogous label-free experimental designs. Finally, and most importantly, classical SILAC experiments require complete label efficiency in cells, which limits its applications mainly on fast proliferating cell lines. However, special adapted workflows such as Super-SILAC and Absolute-SILAC approaches serve as alternative SILAC-based quantification strategies, which overcome these limitations for primary cells and tissues [312,313].

In contrast to metabolic labeling, chemical labeling relies on coupling of traceable mass-tags to reactive sites along the amino acid sequence of proteins by highly specific chemical reactions [314]. Recent advances in chemical labeling strategies encompass different molecules with overall equal masses. These molecules however, differ in terms of their chemical structure and can be used to label proteins and peptides by a unique mass-tag per experimental condition principle. After the chemical labeling of several samples, the different reaction mixtures are pooled and analyzed in one combined LC-MS/MS run. During fragmentation, these so called isobaric mass-tags break into characteristic reporters which are distinguishable through MS/MS [315]. This information is subsequently used to compare the different samples with each other [316]. The major drawback of most chemical labeling methods remains the ratio compression phenomenon. This phenomenon describes signals of co-eluting peptides contaminating the MS/MS spectra, which co-fragment and thereby impair quantification. Especially in complex samples, this phenomenon can lead to severe over- and under-estimation of the real values [317,318].

Label-free methods, in comparison, use computational based approaches to quantify peptides and proteins measured by mass spectrometry. Applications of label-free quantification methods do not depend on any pre-requirement on the sample side and are therefore particularly suitable to study the proteomes of primary tissue and cells. Especially for discovery-based experiments, recent methods provide sufficient quantification accuracy to reliable identify changes in protein levels of different experimental settings. Spectral count based methods, for example, simply rely on the number of observed peptide-specific MS/MS events during the analysis [319,320]. However, such methods provide only a rough estimate of the actual protein abundance levels [316]. Recent label-free

quantification methods commonly use more accurate signal-intensity-based approaches to relatively quantify different experimental conditions. These methods monitor the peptide signals along the LC gradient and deduce intensities by determining the area under the curve of the individual peptide profiles over the elution time. Label-Free Quantification (LFQ) by the MaxQuant software package, for example, by default considers at least two peptide pairs per protein group to compare and relatively quantify proteins between different mass spectrometry runs. Additionally, the algorithm assumes equal amounts of the overall protein concentration in the samples and accounts for it by normalization [321]. Theoretically, label-free quantification methods can compare an almost indefinite number of different conditions. However, the computational demand increases dramatically with the sample size and limits the number of conditions that can be analyzed in parallel in practice. Furthermore, label-free methods necessitate highly reproducible workflows to minimize variations introduced by sample preparation and during LC-MS/MS analysis. However, even highly optimized protocols until now do not reach comparable mass accuracy that can be achieved by label-based methods. Hence, label-free quantification based experiments commonly need more replicates to allow a comparable statistical power in the subsequent data analysis [322].

An alternative to relative quantification methods represent absolute quantification strategies. Several different approaches such as absolute quantification (AQUA), Protein Epitope Signature Tag (PrEST) and FlexiQuant are available, which rely on reference peptides or proteins which are spiked into the sample during the sample preparation process. Absolute quantification is mainly used in context of pharmaceutical- and clinical applications, which require high quantification accuracy for the interpretation and are less common in discovery based experimental settings [316]. Some label-free algorithms like absolute protein expression measurements (APEX), protein abundance index (PAI), intensity-based absolute quantification (iBAQ) and the 'proteomic ruler' also provide estimates for the absolute protein quantification [323–325].

1.4.2 Applications of mass spectrometry based proteomics in virus-host interactions and innate immunity

The unbiased quantitative analysis of several thousand proteins and its high application flexibility makes bottom-up proteomics the method of choice to study complex molecular systems in biology. In recent years this technique contributed significantly to the understanding of virus-host interactions.

Most cellular responses to environmental changes and stimuli affect the proteome in the cell. A prototype example of such characteristic changes represents the cellular response to IFN. The detection of IFN at the cell surface results in increased levels of a defined group of proteins, the so called ISGs. However, during infection, viruses rearrange the host's proteome massively through transcriptional, posttranscriptional and posttranslational mechanisms. Especially virus caused interference of the proteome homeostasis by posttranslational mechanisms cannot be studied by transcriptome based approaches, such as microarray of next-generation-sequencing (NGS). Therefore, bottom-up proteomics remains the method of choice to reliably detect such alterations on the molecular level. It allows to evaluate time resolved virus-mediated proteome changes when several selected time-points are considered [326–328]. The observed changes between the different time points or in comparison to an uninfected control represent a blueprint of the virus-mediated manipulation strategies during infections and can pave the way for so far undiscovered viral alterations. Such proteome changes can be identified by protein profiles that show characteristic trends along the replication cycle of the virus and form clusters of co-regulated protein groups.

As a response to virus infection, cells commonly secrete cytokines and chemokines to distribute warning signals within the host organism. These essential mediators regulate, coordinate and balance immune responses to achieve effective pathogen restriction and to prevent overshooting and harmful reactions at the same time. Studying the communication between different immune cells remains a key challenge to understand the immune system. Mass spectrometry based proteomics can reliable identify and quantify secreted proteins by analyzing the supernatant of cells in culture or in the blood plasma during infection [329–331]. LC-MS/MS analyses identified several cellular factors that accumulated dynamically in the supernatant of isolated macrophages in response to lipopolysaccharide (LPS) treatment [332]. Although the functional role of the majority of these identified secreted factors have still to be confirmed, these group of proteins might contain important novel key factors that coordinate immune regulation. A complementary study recently elucidated the communication between cells of the immune system by generating and mining information about the expression of immune receptors and immune messengers among different immune cell populations. This study contributed significantly to our understanding of underlying intercellular communication networks between different primary immune cell types [333].

Many innate immune response mechanisms and virally encoded proteins target the cellular translation machinery and affect protein synthesis to limit virus protein production or to escape the IFN response [330,334]. Pulse experiments are the methods of choice to study protein synthesis by mass spectrometry [335,336]. These methods rely on the incorporation of metabolically labeled amino acids

such as arginine and lysine used for SILAC experiments. Transferring cells into medium containing 'heavy' or 'medium' labeled amino acids results in the incorporation of the traceable amino acids into the newly synthesized proteins. In pulse chase labelling experiments, the cells are challenged with different labels, which allow to deduce protein stability [337]. Among several studies which elucidated protein turnover rates in cells, a SILAC pulse chase approach was also used to monitor the effects of LPS on the protein turn over in dendritic cells [324,338,339]. The data revealed that approximately half of the observed proteome changes originate from impaired translation or by degradation in dendritic cells during LPS induced stimulation [338]. Another recent study investigated the degradation of cellular proteins during human cytomegalovirus infection by a quantitative pulsed SILAC/TMT approach and identified 35 actively degraded restriction factors [327]. The observed data indicated for example, that HCMV induces degradation of HLTF, a helicase-like transcription factor that potently inhibits HCMV gene expression early during infection.

Many proteins act in concert with other proteins or execute their functions as part of high molecular weight complexes [340]. Mass spectrometry based proteomics provides different strategies, which help to elucidate protein interactions. Classical affinity purification coupled to LC-MS/MS analysis (AP-LC-MS/MS) uses specific antibodies or affinity-tags fused to the protein of interest to facilitate binding, enrichment and purification of the targeted protein (called bait) and associated factors (called preys) at immobilized stationary phases such as protein G sepharose or magnetic beads. In a subsequent step, prey proteins sticking at the bait are identified by LC-MS/MS based bottom-up analysis.

This method was extensively used to detect interactions between proteins and other cellular products such as nucleotide sequences. Recent methods use sophisticated statistical models to identify specific enriched proteins based on the signal intensities observed in the experiment. Such approaches were used to study protein-protein interactions between viruses and the host cell and led to a detailed understanding of host proteins and protein complexes as viral targets [341,342]. A comprehensive AP-MS/MS study for example, which included 70 different viral open reading frames (vORFs) revealed that viruses predominantly interact with cellular targets at central positions in cellular signaling pathways. Several of these targets were associated with key signaling pathways that initiate antiviral defense response in cells [132]. However, AP-LC-MS/MS is not limited to determine protein-protein interactions only. It can be used to study interactions between different biological structures and proteins. For example, it was successfully used to identify novel protein interactions to viral genome structures such as triphosphates at the 5′end of viral RNA (pppRNA) genomes. This experiment identified relevant host defense factors such as IFIT proteins

which interact with viral pppRNA species [79,343]. An extension of the AP-LC-MS/MS analysis represents affinity enrichment coupled to LC-MS/MS analysis (AE-LC-MS/MS). This approach benefits from less stringent washing conditions and preserves even low affinity interactions. It identifies interacting proteins based on the relative intensity-based enrichment compared to unspecific-bound background proteins in a statistically controlled analysis strategy [344]. Recently, this approach was applied in an orthogonal proteomic study in the context of Zika virus infection. This data was complemented with deep proteome and phospho proteomics data to form a comprehensive integrated network, which represents the molecular nature of Zika virus infection in neuronal cells [345]. A thematically related study combined AP-LC-MS/MS with interaction data derived by proximity-dependent biotin identification (BioID) to characterize the global Zika virus interactome[346]. Both studies provided important information regarding the Zika virus-mediated targeting strategies of cellular factors and organelles.

Taking together, mass spectrometry provides a powerful toolbox to delineate complex biological systems such as in virus-host interactions. It helps to understand signaling pathways by elucidating protein abundance, stability, interactions and post-translational modifications. Recent studies integrate data from different proteomics and other "omics" applications to generate blueprints of the virus-host biology at different molecular levels [330]. This might help to identify so far unknown key players in cellular defense responses and factors which are essentially required for the replication of respective viruses.

1.5 AIMS OF THE THESIS

Recent comparative loss and gain of function screens revealed numerous cellular factors with high relevance for virus replication. Especially the characterization of ISGs and their ability to counteract viral infections elucidated many candidates with broad and highly-specific antiviral activities. However, the molecular functions of these factors largely remain poorly understood and further information about these factors might be of high value for novel broad antiviral strategies in the future.

The aim of my thesis was to expand these functional screens by molecular protein-protein interactions and to link these antiviral active host factors to their underlying molecular processes in the cell. With this, I intended to illuminate novel molecular interactions and processes which control virus infections and the innate immune response. Therefore, I used state of the art bottom-up proteomic approaches to identify novel key factors in the virus-host interplay. Based on the observed proteomic results, I deduced hypotheses and proofed their value by tailored functional tests in targeted experiments. Thereby, I systematically generated proteomics data, mined relevant information and further characterized proteins, complexes and pathways that I could link to the innate immune system and to viral perturbation strategies.

I elucidated protein-protein interactions of 104 functionally predefined ISGs, studied the binding capacity of IFIT1 to nucleic acid sequences, actively supported the characterization of a novel ROS induced cell death pathway, identified a cellular factor that supports the antiviral activity of viperin against tick-borne encephalitis virus and studied the function of SCF ubiquitin ligases in the RVFV NSs induced innate immune control.

2 RESULTS

2.1 PUBLICATION 1: A PROTEIN INTERACTION NETWORK OF INTERFERON STIMULATED GENES EXTENDS THE INNATE IMMUNE SYSTEM LANDSCAPE

In my main project I elucidated the cellular protein-protein-interaction (PPI) network of ISGs relevant for the replication of a diverse set of different viruses. I collaborated with the "Laboratory of Virology and Infectious Disease" headed by Prof. Charles Rice at Rockefeller University (New York, USA), a pioneering research group, which extensively uses gain of function screens to systematically characterize the relevance of individual ISGs in the context of virus infections. Based on the data of their two most comprehensive studies, I selected 104 ISGs with high virus specific, pan-antiviral or pro viral functions.

I generated stable cell lines expressing tagged, functional active ISGs and investigated their interactions by a tailored AE-LC-MS/MS workflow. Based on this data, I was able to generate a representative ISG interaction network. This ISG PPI network links ISGs to their underlying, potential functional relevant cellular factors in the cell. Through the integration of functional data from external sources, this ISG interaction network serves as a valuable starting point for targeted hypothesis-driven experiments in the future.

I tested the value of these combined information together with the laboratory of Prof. Martin Schwemmle (Institute of Virology, Medical Center University of Freiburg). We identified cellular proteins that interact with FluAV particles in an early post entry step. Therefore, we infected cells with a recombinant PB1 Flag-tagged FluAV strain and identified the viral ribonucleoprotein (vRNP) associated cellular proteins by AE-LC-MS/MS. Comparing these vRNP associated proteins with the ISG interactome resulted in an unexpected high number of matching cellular factors. These shared factors potentially link ISGs to the virus derived structures during infection and might contribute to an early cellular response during infection. This hypothesis is supported by an overall increased antiviral activity of these indirectly linked ISGs against FluAV compared to the remaining set of ISGs studied in this project.

Among several hundreds of novel interactions, I focused on the interaction of the interferon stimulated gene ANXA2R with the CCR4-NOT complex, investigated the regulatory function of the highly connected LGALS3BP protein within the IFN response and studied the P2RY6 mediated NF-κB activation.

nature immunology

RESOURCE

https://doi.org/10.1038/s41590-019-0323-3

A protein-interaction network of interferon-stimulated genes extends the innate immune system landscape

Philipp Hubel[1], Christian Urban[2], Valter Bergant[2], William M. Schneider[3], Barbara Knauer[1], Alexey Stukalov[1,2], Pietro Scaturro[1,2], Angelika Mann[1], Linda Brunotte[4,5], Heinrich H. Hoffmann[3], John W. Schoggins[3,6], Martin Schwemmle[7], Matthias Mann[8], Charles M. Rice[3] and Andreas Pichlmair[1,2,9*]

Interferon-stimulated genes (ISGs) form the backbone of the innate immune system and are important for limiting intra- and intercellular viral replication and spread. We conducted a mass-spectrometry-based survey to understand the fundamental organization of the innate immune system and to explore the molecular functions of individual ISGs. We identified interactions between 104 ISGs and 1,401 cellular binding partners engaging in 2,734 high-confidence interactions. 90% of these interactions are unreported so far, and our survey therefore illuminates a far wider activity spectrum of ISGs than is currently known. Integration of the resulting ISG-interaction network with published datasets and functional studies allowed us to identify regulators of immunity and processes related to the immune system. Given the extraordinary robustness of the innate immune system, this ISG network may serve as a blueprint for therapeutic targeting of cellular systems to efficiently fight viral infections.

Defense against viral infections relies on rapid and massive engagement of cellular proteins with antiviral properties. Germline-encoded pattern-recognition receptors sense the presence of pathogens and initiate a signaling cascade leading to the induction of antiviral cytokines, including type-I interferons (IFN-α/β). IFN-α/β bind to the IFN-α/β receptor (IFNAR), initiating signaling that culminates in the expression of interferon-stimulated genes (ISGs). In summary, viral infection triggers the expression of several hundred proteins covering a wide range of biological activities. Among these proteins are pattern-recognition receptors (for example RIG-I, MDA5 and Toll-like receptors), signaling molecules (for example, MYD88 and MAVS), transcription factors (for example members of the interferon-regulatory family (IRFs) and members of the signal transducer and activator of transcription family (STATs)) and proteins with direct antiviral functions (for example, Mx proteins and interferon-induced proteins with tetratricopeptide repeats (IFITs)), as well as negative regulators of immune responses (for example suppression of cytokine signaling proteins, DAPK1) that prevent overshooting of immune reactions. ISGs are thus a heterogeneous group of proteins that serve different purposes related to direct antiviral defense and immune regulation.

Although some ISGs have been studied in detail, the modes of action of a large majority of ISGs are still unknown. Much knowledge on their functional activities has been gained from overexpression screens in which single ISGs were expressed and their antiviral activity was tested against different viruses[1,2]. Even though these studies identified antiviral effects for individual ISGs, most of the underlying molecular mechanisms remained unknown. It is accepted that many proteins must interact with one or more other cellular factors to achieve full activity. In line with this notion, some ISGs form multiprotein complexes to attain optimal antiviral efficiency. Examples are IFIT1, IFIT2 and IFIT3, which show only marginal antiviral activity when individually expressed. However, co-expression of IFITs leads to the formation of large heteroprotein complexes that recruit additional cellular proteins and together confer potent antiviral effect. Similarly, interferon-induced E3 ubiquitin ligases, such as the RIG-I activating protein TRIM25, require constitutively expressed E2 and E1 ubiquitin ligases. In addition, TRIM25 requires ZC3HAV1 (ZAP) to efficiently mediate RIG-I ubiquitination and activation[3,4]. Although the importance of ISGs for the antiviral response of the host is well accepted, the cellular cofactors associating with ISGs have not yet been systematically studied. Here we conduct a survey on the basis of affinity proteomics to systematically chart the ISGs protein-interaction network. We aim to illuminate the molecular mechanisms underlying their antiviral potential and to identify additional cellular factors that are critically required by the innate immune system.

Results

Identification of novel ISG binding partners using mass spectrometry. To select ISGs that represent a wide range of antiviral activities, we performed a meta-analysis of single ISG overexpression studies conducted in 5 cell types that covered 20 viruses from 9 virus classes (Supplementary Table 1). We identified proteins that

[1]Innate Immunity Laboratory, Max-Planck Institute of Biochemistry, Munich, Germany. [2]Institute of Virology, School of Medicine, Technical University of Munich, Munich, Germany. [3]Laboratory of Virology and Infectious Disease, The Rockefeller University, New York, NY, USA. [4]Institute of Virology, Westfaelische Wilhelms-University Muenster, Muenster, Germany. [5]Cluster of Excellence 'Cells in Motion', Westfaelische Wilhelms-University Muenster, Muenster, Germany. [6]Department of Microbiology, University of Texas Southwestern Medical Center, Dallas, TX, USA. [7]Institute of Virology, Medical Center University of Freiburg, Freiburg, Germany. [8]Department of Proteomics and Signal Transduction, Max-Planck Institute of Biochemistry, Munich, Germany. [9]German Center for Infection Research (DZIF) Munich Partner Site, Munich, Germany. *e-mail: andreas.pichlmair@tum.de

have antiviral activity against a wide range of viruses (for example IRF2, IRF7 and MAP3K14) as well as proteins specific to a single virus class (for example TCF7L2 and DDX60) (Supplementary Table 1). Among these proteins, we selected 104 ISGs with diverse antiviral properties (Supplementary Fig. 1a), expressed them as Strep-II-Hemagglutinin (SH)-tagged fusion proteins in doxycycline-inducible HeLa-FlpIn or HEK-FlpIn TREX cells and validated their expression by immunoblotting. We confirmed that this expression system preserves functionality of the ISGs by testing the antiviral activity of MxA and MAP3K14 in comparison to an inactive MxA (M527D) mutant for their ability to impair vesicular stomatitis virus (VSV) replication (Supplementary Fig. 1b).

To determine binding partners for these 104 ISGs, we established an affinity enrichment with quantitative liquid chromatography–tandem mass spectrometry (AE–LC–MS/MS) workflow that allowed identification of proteins associating to ISGs (Supplementary Fig. 2a). By combining 439 mass-spectrometry runs we identified 2,734 high-confidence interactions between 104 ISG baits and 1,401 cellular proteins (Fig. 1a and Supplementary Table 2). The majority of the ISGs (70 out of 104) formed a connected network (Fig. 1a). Ten percent of the interactions identified here were already reported in public databases (Supplementary Fig. 2b). As well as confirming many reported ISG interactors (for example FBOX6, PSMB9 and JADE2), we additionally characterized the cellular interactomes of a number of ISGs that have not yet been comprehensively studied (for example IRF2, IRF7 and NOD2) (Supplementary Fig. 2c). We confirmed the reliability of this approach further by validating a subset of these novel interactions through co-immunoprecipitation with immunoblotting. OASL interacted with the helicase LARP7, known for its ability to unwind RNA and its involvement in RNA degradation (Supplementary Fig. 2d). The RNA helicase LGP2 co-precipitated the DNA sensor IFI16. Interferon stimulatory protein C14ORF166 bound RTCB, a protein involved in tRNA splicing and eIF3e interacted with the ISGs DDX60 and CD74 (Supplementary Fig. 2d).

On a global level, these data allowed us to infer previously undescribed ISG-related biological processes. Only 30% of the Gene Ontology (GO) terms enriched in our network were directly or indirectly associated to the analyzed ISGs, according to semantic-similarity clustering[5] (Fig. 1b and Supplementary Table 3). In particular, many of the new ISG interactors identified here are involved in apoptotic processes, NF-κB regulation and the innate immune response (Fig. 1c).

Among cellular proteins that were specifically targeted by ISGs, we identified proteins involved in innate defense mechanisms, cell cycle, and protein metabolism (Fig. 1d and Supplementary Table 3). In particular, this analysis confirmed known interactions but also revealed novel interactions between ISGs and proteins involved in NF-κB regulation (Fig. 1c and Supplementary Fig. 2e). Moreover, a prominent group of ISGs associated with proteins involved in intracellular transport (Fig. 1d), indicating that ISGs have a major effect on intracellular trafficking. We also found unexpected interactions between ISGs and proteins involved in energy metabolism, suggesting that ISGs influence cellular metabolic activity (Fig. 1d and Supplementary Fig. 2f). For instance, apoptosis facilitator Bcl-2-like protein 14 (BCL2L14) associated with succinate dehydrogenase (SDHB) and succinate–Co-A ligase complex members (SUCLG1, SUCLG2, SUCLA2), as well as members of the ubiquinone oxidoreductase complex (NDUFAF4, NDUFS2), suggesting regulation of complex-II activity in mitochondria (Supplementary Fig. 2f).

This comprehensive analysis allowed us to evaluate the overall organization of the ISG protein–protein interaction network. Nearly half of the interactors identified (694 proteins) were found to interact with one individual ISG, while 707 proteins interacted with more than one ISG bait (Figs. 1a and 2a and Supplementary Table 2). Strikingly, two proteins were interacting with as many as nine baits: LGALS3BP and COPB1. This analysis uncovered interactions between ISGs mediated by cellular proteins (Fig. 2b), as well as direct interactions between ISGs (Supplementary Fig. 3a and Supplementary Table 2). For instance, we could confirm previously described IFIT1–IFIT3 and ATF3–JUNB interactions (Supplementary Fig. 3a). Of particular interest are novel interactions, such as IRF2–TRIM25, which point towards a role for ubiquitination in IRF2-mediated gene transcription (Supplementary Fig. 3a). Furthermore, our data identified a novel interaction between BST2 (also known as tetherin) and the NF-κB modulator NOD2 (Supplementary Fig. 3a,b), which may explain reports describing BST2-mediated NF-κB regulation[4,6,7].

Proteins connected to multiple ISGs were implicated in protein folding, endoplasmic reticulum (ER)-to-Golgi transport, neutrophil degranulation as well as viral processes (Fig. 2c (red) and Supplementary Table 4). Notable examples of highly connected proteins, recently described as host-dependency factors critically required by diverse viruses[8–10], are the transport protein COPB1 and UBR4, which is involved in protein degradation (Supplementary Fig. 3c). ISGs also prominently engage members of the nuclear pore complex that are reported to have antiviral activity, these include XPO1 (also known as CRM1), NUP210 and NUP155. We validated CSE1L (also known as exportin-2) and KPNB1 (importin-β1) binding to five and six individual ISGs, respectively (Supplementary Fig. 3d,e).

Notably, proteins specifically binding to a single ISG bait were often associated with signaling pathways related to immune system modulation (TNF signaling pathway, T cell signaling pathway, C-type lectin signaling pathway, MAPK cascade) (Fig. 2c (blue) and Supplementary Table 4). The data from the ISGs tested here, indicate that some ISGs have a particular role in regulation of the antiviral immune response.

ISGs associate with viral ribonucleocomplexes through cellular factors. ISGs are the frontline of cellular antiviral responses, thus they have to directly or indirectly associate with viral components to limit viral spread. To study whether ISGs or their interactors associate with viral proteins, we used a recombinant influenza A virus (FluAV) expressing an affinity-tagged PB2 subunit, a central component of the viral ribonucleoprotein (vRNP) complex. AE–LC–MS/MS analysis identified 58 proteins bound to the FluAV vRNP complex during the initial phase of infection (Fig. 3a, Supplementary Fig. 3f and Supplementary Table 5). Although we did not identify direct interactions between ISGs and the vRNP, 34 of the 58 vRNP interactors were part of the ISG interactome (Fig. 3a). These 34 vRNP binders associated with 26 ISGs, which showed significantly higher antiviral activity against FluAV compared with the remaining 78 ISGs in our study (Fig. 3b and Supplementary Table 1). These 26 ISGs included five (IFITM3, MX1, NOD2, DDX60 and TCF7L2) of the six ISGs that showed highest specific anti-influenza activity in previous overexpression studies[1] (Fig. 3c and Supplementary Table 1). This suggests that to target vRNP complexes, ISGs use proteins that are not necessarily regulated by type-I interferons. These data might explain the specificity of some ISGs, such as DDX60, which are active against FluAV but not against other viruses upon overexpression (Supplementary Table 1). DDX60 and FluAV–vRNP both interact with PPP6R3, a subunit of the cellular serine/threonine protein phosphatase 6 (PP6) complex that is required for influenza virus replication and vRNA nuclear export[11]. Similarly, TCF7L2 shares six proteins interacting with influenza vRNPs, including ANP32B, PDCD6, STUB1, which have known functions in either virus replication or immune processes[12–14]. Therefore besides the reported ability of some ISGs to directly interact with viral structures, our data suggest that ISGs engage cellular proteins that are important for virus replication.

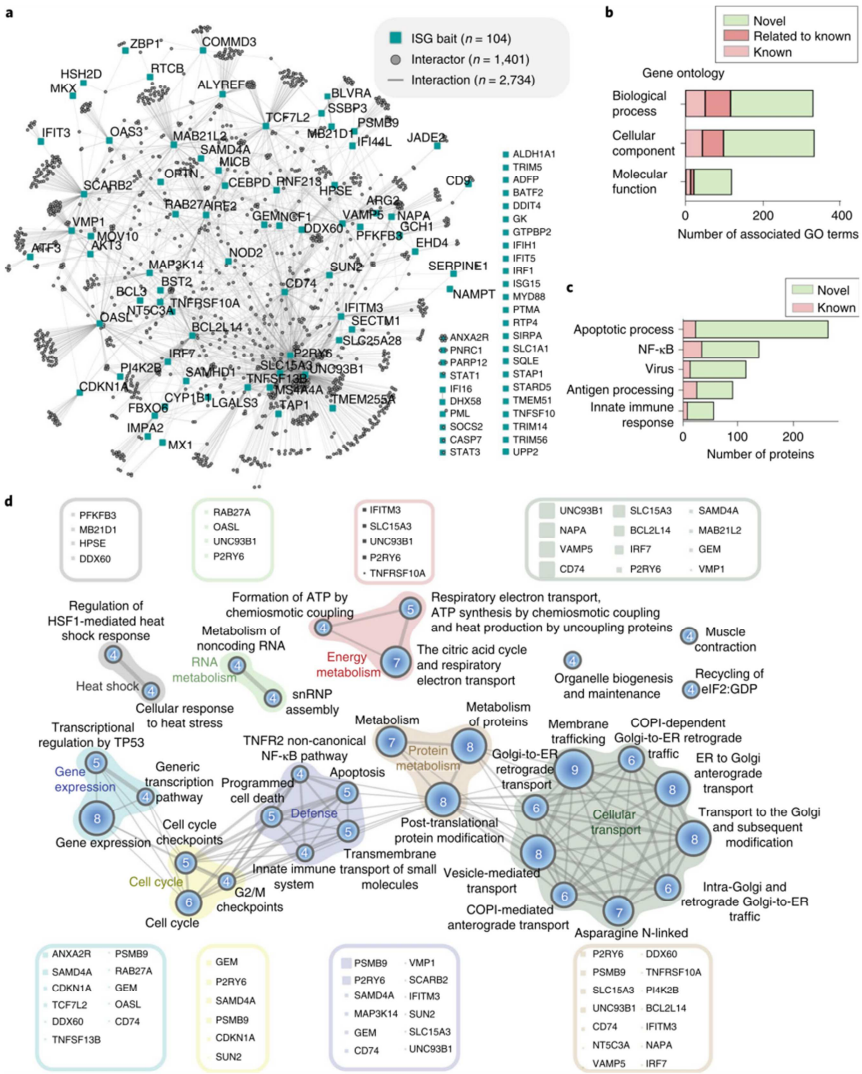

Fig. 1 | Identifying interactions between ISGs and cellular proteins using mass spectrometry. a, ISG network derived from AE-LC-MS/MS experiments in this study. **b**, GO terms enriched among ISG interactors: matching to the terms of ISG bait (known), similar to the terms of the bait (related to known) or novel. **c**, Interactions between ISGs and proteins implicated in the specified processes and pathways. Known, published interactions (BioGrid) between ISGs and cellular proteins of the respective GO term. Novel, newly identified interactions. **d**, Pathways most frequently targeted by ISG baits (top 33 Reactome pathways). Each node represents a specific pathway, node size indicates the number of interactions to individual ISGs. Edge thickness between nodes represents the number of ISG-interacting proteins shared by both pathways. Halos group closely related pathways. Boxes show ISGs targeting at least one pathway in the respective group, and square size correlates with the number of targeted pathways. For **b**,**d**, Fisher's exact test using Benjamini–Hochberg FDR < 0.05 and enrichment factor of at least twofold was set as a threshold. Only pathways significantly enriched among the interactors of at least four individual ISGs and baits with at least three interacting proteins were considered.

Data intersection identifies the lectin-binding protein LGALS3BP as an immune regulator. Intersecting our ISG network with complementary immunity-related datasets revealed a strong enrichment of cellular proteins targeted by viral immune-modulatory open reading frames (vORFs) (Fisher's exact test unadjusted $P = 2.92 \times 10^{-83}$)[15] and influenza A virus replication

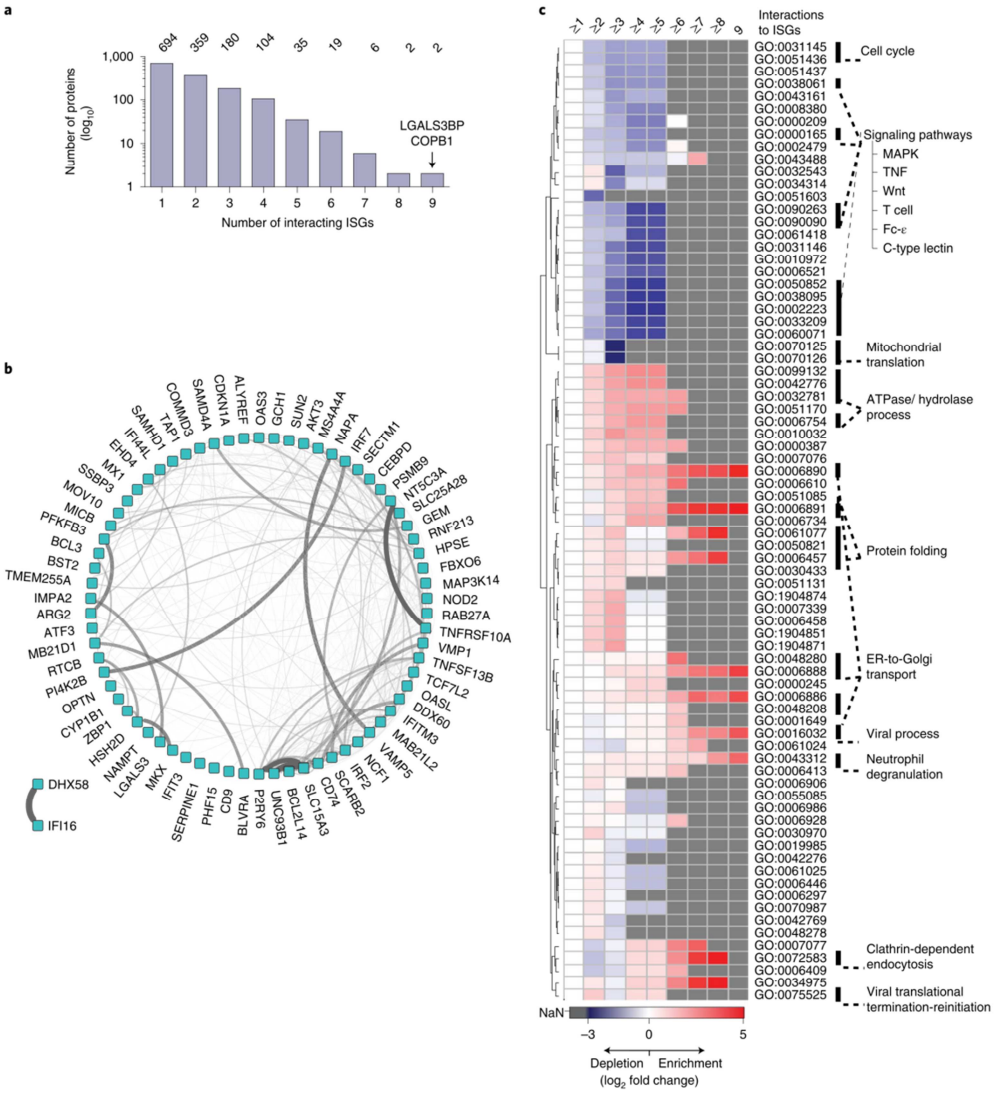

Fig. 2 | Analysis of the ISGs interaction network. a, Distribution of proteins by the number of ISG baits they interact with. **b**, Similarity of ISGs interaction profiles. Edge thickness corresponds to the number of shared prey proteins between the two linked ISGs. ISGs with at least three identified interacting proteins or directly binding to another ISG were considered. **c**, GO biological processes (GOBP) that are enriched among the proteins interacting with the indicated number of ISG baits. Heat map shows significantly enriched GOBP terms ($P \leq 0.05$ on the basis of a Fisher's exact test with Bejamini–Hochberg adjustment, enrichment factor ≥ 2) with reduced (blue) or increased (red) relative enrichment depending on the number of ISGs the annotated proteins are interacting with.

factors previously identified by functional genome-wide RNA interference knockdown screens (Fisher's exact test unadjusted $P = 8.01 \times 10^{-44}$)[9], whereas the other ISGs were represented not so prominently (Fisher's exact test unadjusted $P = 0.00392$)[16] (Fig. 4a and Supplementary Table 6). Overall, the ISG interactome was significantly enriched with the proteins reported in these public datasets compared with the remaining human proteome (Fig. 4b,c). Six proteins (KPNB1, LGALS3BP, MYH10, NAP1L1, TUBB2A and

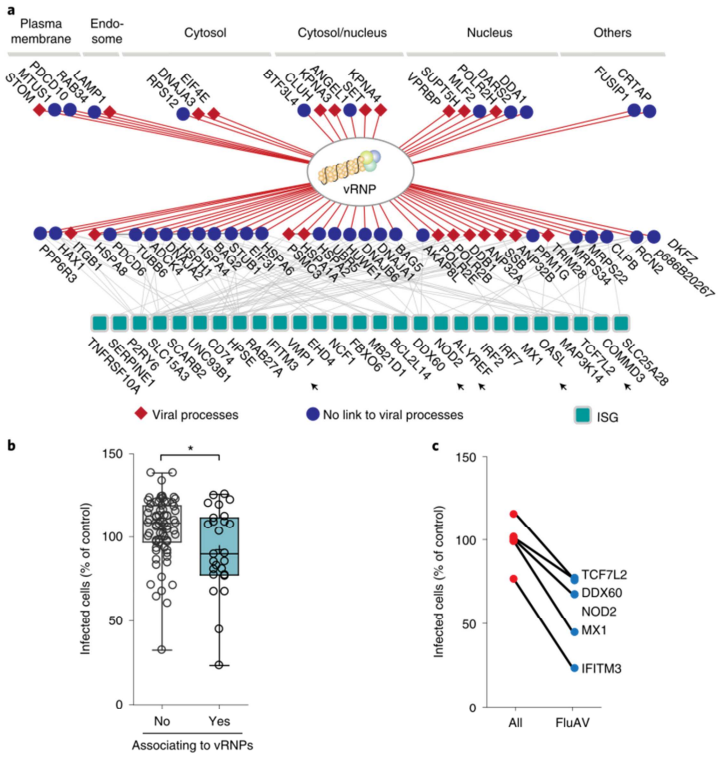

Fig. 3 | ISGs associate with influenza A virus RNPs through cellular proteins a, Intersection of the ISG network and the interactome of FluAV–vRNPs. The red edges connect proteins significantly enriched in anti-SII-tagged AE–LC–MS/MS analysis of A549 cells infected for 4 h with FluAV (multiplicity of infection (m.o.i.) = 30) expressing SII-tagged PB2. Proteins are grouped according to GOCC annotations. The five ISGs with highest anti-FluAV activity (Supplementary Table 1) are highlighted with black arrowheads. Red diamonds, proteins associated to viral processes according to GOBP. **b**, Antiviral activity of ISGs that associate to FluAV–vRNPs (yes; 26 ISGs) compared with the remaining ISG population in this study (no; 78 ISGs). *$P < 0.027$ on the basis of a two-sided Mann–Whitney test; box and whisker plot, boxes indicate the median and interquartile range, whiskers indicate the range. **c**, Antiviral activity of the indicated ISGs against FluAV compared to the mean antiviral activity of all other tested viruses (data are derived from refs. [1,2]).

VCP) were present in all four independent datasets (ISG network, vORF interactome, siRNA screens and Interferome DB), suggesting a central role in antiviral immunity (Fig. 4c and Supplementary Table 6). LGALS3BP, a protein that exists both in secreted and non-secreted forms[17–19], was highly connected in the ISG interactome (Figs. 2a and 4c). Importantly, we validated binding of LGALS3BP to six intracellular proteins by co-immunoprecipitation assay (Supplementary Fig. 4a). Furthermore, LGALS3BP depletion in different cell lines reduced FluAV–driven renilla luciferase (Ren) and VSV–driven firefly luciferase (Luc) expression to a similar extent as ATP6V0D1, a subunit of the ATP proton pump absolutely required for productive FluAV entry (Fig. 4d and Supplementary Fig. 4b,c). An influenza A virus replicon system, which selectively tests for the activity of the viral polymerase and reporter gene expression, was also affected by LGALS3BP depletion, suggesting a mechanism of inhibition that is independent from virus entry or assembly and does not produce significant cytotoxic effects (Supplementary Fig. 4d,e). To gain additional insights into LGALS3BP antiviral activity, we compared the total proteomes of FluAV-infected and non-infected HeLa cells lacking LGALS3BP. LGALS3BP knockdown led to a significant upregulation of proteins linked to antiviral immunity, most notably ISGs (Fig. 4e, Supplementary Fig. 4f,g and Supplementary Table 7). Short interfering RNA (siRNA)-mediated depletion of LGALS3BP, but not of control proteins, led to spontaneous expression of IFIT3 (Fig. 4f), and positively stimulated ISGs expression, as indicated by global analysis of proteome expression (Supplementary Fig. 4h,i and Supplementary Table 7). Collectively, these data suggest that LGALS3BP negatively regulates the interferon response, explaining its broad antiviral activity on diverse virus genera. This example shows how integration of the ISG interactome with other datasets can accelerate the search for novel proteins critically required for virus growth and immune regulation.

Cell-death modulating ANXA2R interacts with the RNA-degrading CCR4–NOT complex. Proteins assemble into functional complexes to form operative units. Therefore we mined the ISG interactome for protein complexes that are enriched by individual or multiple ISGs (Fig. 5a and Supplementary Table 3).

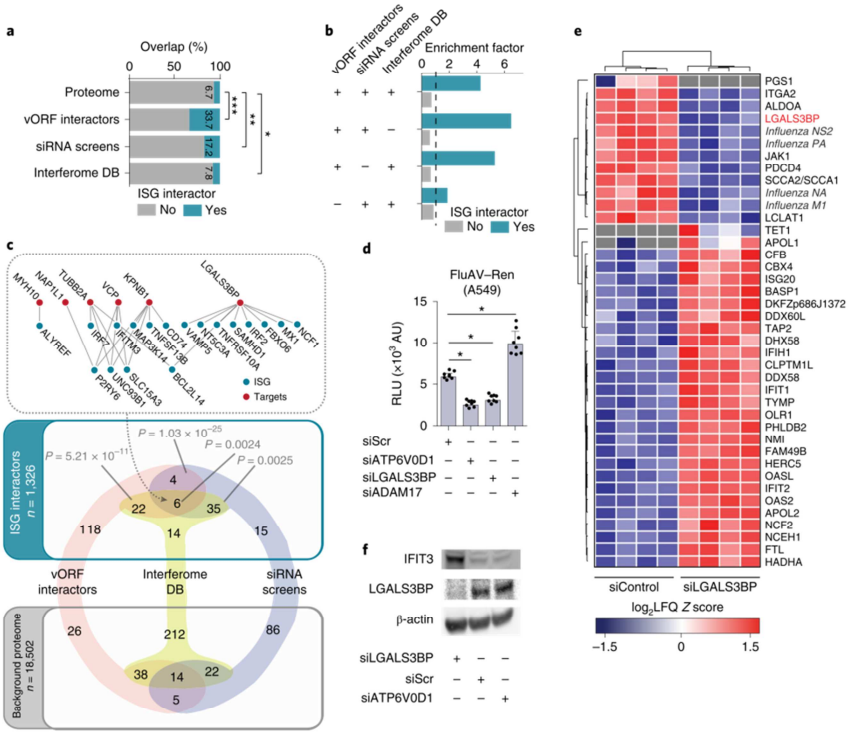

Fig. 4 | Intersection of the ISG interaction network with complementary published datasets. a, Occurrence of ISG interactors within the whole proteome and the other datasets. vORF interactors, proteins associating with viral immune regulators[15]; siRNA screens, proteins modulating FluAV replication as determined by genome-wide gene depletion experiments[9]; interferome DB, proteins reported to be induced by type-I interferon. $^{*}P = 0{,}004$, $^{**}P = 8 \times 10^{-44}$, $^{***}P = 3 \times 10^{-84}$ on the basis of Fisher's exact tests with Benjamini–Hochberg. **b**, Enrichment factors for the intersections of the indicated datasets in the ISG network (turquoise) and in the background proteome (gray). **c**, Venn diagram of ISG interactors (turquoise frame, 1,326 proteins), vORF interactors (orange), FluAV host and restriction factors (siRNA screens, blue), IFN-regulated proteins (fold change ≥ 2 in at least three independent experiments in interferome DB, yellow) and the background proteome of the ISG network (gray frame, 18,502 proteins). The labels indicate the number of proteins in the overlaps of the dataset. **d**, A549 cells were treated with the indicated siRNAs for 24 h and subsequently infected with FluAV expressing renilla luciferase (FluAV–Ren; m.o.i. = 0.05). The histogram shows renilla activity (mean ± s.d.) 24 h after infection ($n = 8$ independent samples; one representative experiment of three is shown). $^{*}P < 1 \times 10^{-5}$ on the basis of a one-way ANOVA with Tukey's multiple comparisons test . **e**, HeLa cells treated with either LGALS3BP or control siRNAs (siScr) were infected with FluAV (m.o.i. = 0.05) and 24 h after infection the total proteome of infected cells was analyzed using mass spectrometry. The heat map shows significantly regulated cellular and viral proteins (two-sided Welch's *t*-test, permutation-based FDR = 0.01, $S_0 = 0.1$, $n = 4$ independend samples). **f**, Immunoblot of IFIT3 and LGALS3BP in HeLa cells 24 h after treatment with siRNA targeting LGALS3BP or ATP6V0D1 or control siRNA.

In summary, we identified 80 protein complexes. Although the proteasome complex, the eukaryotic translation initiation factor complex and the spliceosomal complex were targeted by two or more ISGs, other complexes predominantly bound individual ISGs. MAP3K14, TNFSF13B and ATF3, for instance, very specifically co-precipitated protein complexes related to their described functions (Fig. 5b). A subset of ISGs associated with cellular complexes that were not previously linked to innate immunity (Fig. 5c and Supplementary Fig. 5a). Notable examples within this dataset were annexin-2 receptor (ANXA2R), GCH1 and OASL. Among these, the largely unstudied ANXA2R was unique in its specific enrichment for components of the CCR4–NOT complex (Fig. 5c), a key player in RNA degradation. We confirmed the potent interaction between ANX2R and CNOT1, a core component of the CCR4–NOT complex, using co-immunoprecipitation with immunoblotting (Supplementary Fig. 5b). Furthermore, as predicted by our meta-analysis (Supplementary Fig. 1a), ANXA2R exhibited strong antiviral activity in virus replication assays using a doxycycline-inducible cell line (Supplementary Fig. 5c). In line with previous publications[20], persistent ANXA2R expression led to cytotoxic effects (Supplementary Fig. 5d), a phenotype that has also been reported in cell lines that were depleted for CNOT1, a critical component of the CCR4–NOT complex[21]. To rule out possible pleiotropic effects resulting from cell death, we induced ANXA2R expression for very short time frames, using conditions that had no detectable detrimental effects on cell viability. Under

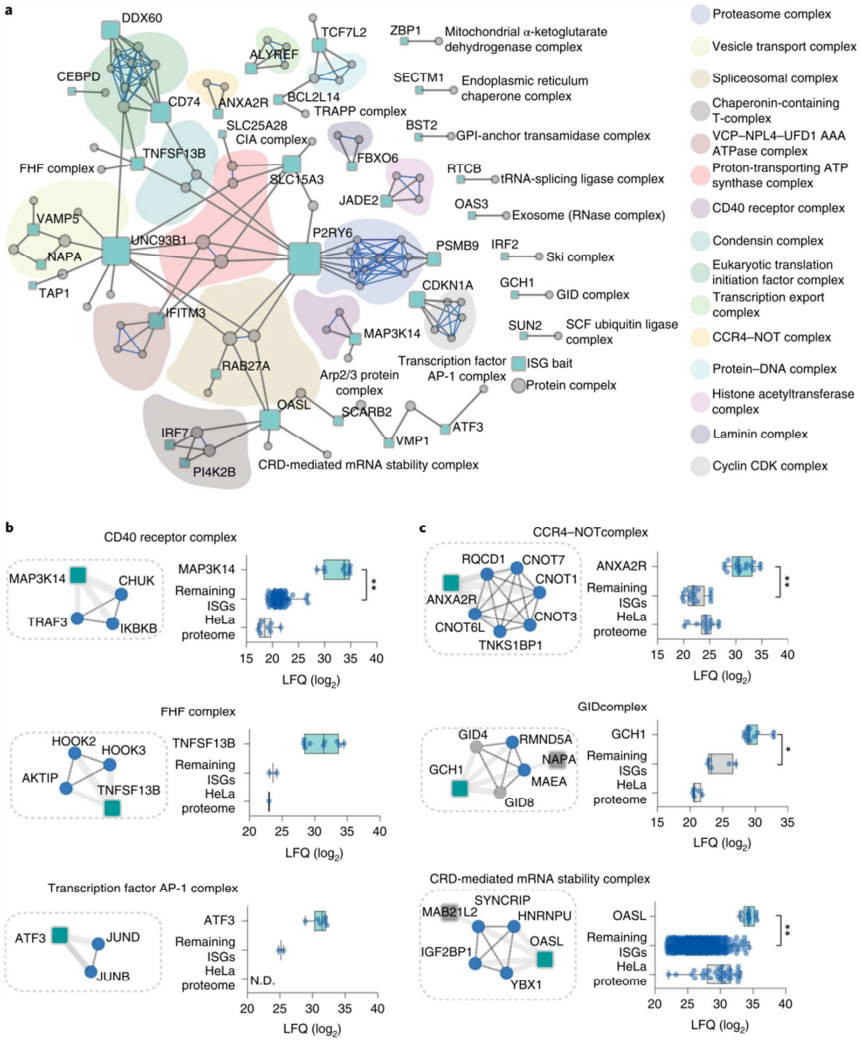

Fig. 5 | ISG interactions with protein complexes. a, Interactions of ISG baits (turquoise squares) with protein complexes (gray circles). Only significantly enriched protein complexes annotated in GOCC are shown (Fisher's exact test; Benjamini-Hochberg FDR ≤ 0.001, enrichment factor > 3). The node size is proportional to the number of connections in this network. Gray edges represent interactions found in the ISG network, and blue edges connect related subcomplexes. Halos group together related protein complexes (representative complex names are shown). **b**,**c**, Isolated subnetworks with known (**b**) or novel (**c**) ISG interactions to individual complex members. Circles represent protein complex subunits annotated in GOCC (blue) or extrapolated from yeast (gray) that were found in the ISG network. Turquoise squares represent ISGs specifically targeting the complex, whereas gray squares denote ISGs that specifically associate to one of the complex subunits. The corresponding box plots show the abundance of the given complex members in the pulldowns of the interacting ISG bait, of the other ISG baits and in the HeLa proteome. $^{*}P < 0.002$, $^{**}P < 0.0001$ on the basis of a two-sided Mann–Whitney test for the LFQ values; box and whisker plots, boxes indicate the median and interquartile range, whiskers indicate the range.

these conditions, replication of VSV was significantly reduced, confirming a direct antiviral role of ANXA2R (Supplementary Fig. 5e,f). The CCR4–NOT complex regulates expression of a subset of genes[21–23]. Notably, ANXA2R expression specifically led to a prominent re-distribution of CNOT1 to perinuclear areas, suggesting a potential perturbation of CCR4–NOT activity in

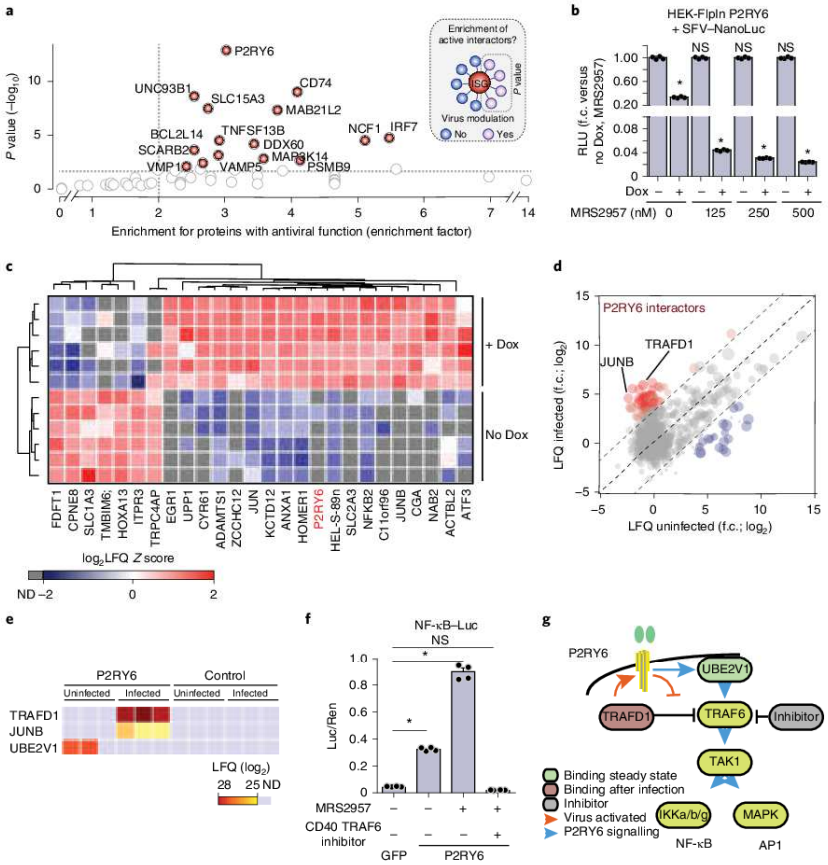

Fig. 6 | ISG interactome reveals functional interactions. a, The enrichment of host and restriction factors of FluAV[9] among the interactors of ISG baits. Each point represents one ISG bait. The axes correspond to the enrichment factor of FluAV-modulating proteins (compared with the proteome background) and the corresponding *P* value (Fisher's exact test, Benjamini–Hochberg-corrected). The activity of the ISG itself was not considered. ISG baits with enrichment factor ≥2 and $P \leq 0.01$ are highlighted (red). **b**, HEK-FlpIn TREX P2RY6 cells were treated or not treated with doxycycline (Dox) for 20 h and an additional 8 h with the P2RY6 ligand MRS2957, as indicated. Cells were infected with SFV-NanoLuc (m.o.i. = 0.01) for 24 h and luciferase activity was measured. The histogram shows fold change (f.c., y axis)) of luciferase activity relative to the non-induced control (mean ± s.d.; $n = 4$ independent samples, one representative experiment of three independent biological repeats is shown). *$P < 0.0001$ and NS, not significant on the basis of two-way ANOVA with Tukey's multiple comparisons test. **c**, HEK-FlpIn TREX P2RY6 cells were treated or not treated with doxycycline for 24 h, and total proteomes were analyzed by LC–MS/MS. The heat map shows proteins with significant doxycycline-dependent changes in total levels of expression (see Supplementary Fig. 5d). Two-tailed *t*-test permutation-based FDR < 0.01, $S_0 = 0.5$, $n = 6$ independent samples. ND, not detected. **d**,**e**, Control HEK-FlpIn TREX cells and HEK-FlpIn TREX P2RY6 cells were infected with RVFV Clone 13 for 18 h (m.o.i. = 0.1) or not infected and used for AE–LC–MS/MS analysis. **d**, Enrichment of P2RY6-associated proteins in uninfected (*x* axis) and infected conditions (*y* axis) relative to the background. Dashed lines correspond to $\pm 3.5 \times \log_2$(fold change of association strength between the infected and non-infected conditions) and define the proteins that, upon RVFV infection, associate more strongly (red) or more weakly (blue) to P2RY6. Dot size corresponds to the significance of infection-dependent association changes. Two-tailed Welch's *t*-test, permutation-based FDR = 0.05, $S_0 = 1$, $n = 3$. **e**, LFQ intensities of the selected proteins in the affinity enrichments using non-infected or RVFV (Clone 13)-infected P2RY6-expressing or empty control cells. **f**, HEK293 cells were co-transfected with a NF-κB–Luc reporter construct, an EIF1a–Ren control and a plasmid expressing P2RY6 for 20 h. Where indicated, cells were either treated with the P2RY6-specific ligand MRS2957 (250 nM) alone or in combination with a CD40–RAF6 specific inhibitor (3-[(2,5-dimethylphenyl)amino]-1-phenyl-2-propen-1-one, 1 μM) for an additional 8 h. Shown are luciferase/renilla activity ratios (mean ± s.d., $n = 4$ in relation to GFP control transfection; one representative experiment of three is shown). *$P < 0.0001$ on the basis of a one-way ANOVA with Dunnett's multiple comparisons test. **g**, The proposed mechanism of P2RY6-mediated NF-κB and AP1 activation through TRAF6.

the presence of ANXA2R (Supplementary Fig. 5g). To investigate this hypothesis further, we used LC–MS/MS analysis of control or CNOT1 siRNA-depleted cells to identify the subset of proteins that are regulated in a CNOT1-dependent manner. This analysis led to the identification of 95 significantly up- and 36 downregulated proteins (Supplementary Fig. 5h and Supplementary Table 7). We compared these data with time-resolved proteome expression analysis of ANXA2R-expressing HeLa cells (Supplementary Fig. 5i,j and Supplementary Table 7). Notably, proteins upregulated by CNOT1 depletion were generally also upregulated upon ANXA2R induction (Supplementary Fig. 5h–j). Conversely, CNOT1-dependent proteins—including CNOT1 itself—were specifically downregulated in the presence of ANXA2R (Supplementary Fig. 5i,j). Altogether, these data indicate that ANXAR2 expression leads to impairment of CCR4–NOT function. Moreover, these findings exemplify that the ISG interactome can resolve targeting of individual complexes engaged in the innate antiviral response, thereby expanding our current knowledge of the innate-immune-regulated cellular machinery.

ISG interaction partners suggest antiviral functions. Although most of the ISG interactors we identified are not interferon-stimulated, ISGs could interact with these proteins to modulate their activity. To test this hypothesis, we asked whether ISGs target proteins that have been reported to modulate influenza virus growth in genome-wide siRNA knockdown screens (Fig. 6a, gray inset). We identified 15 ISGs, which showed a significant enrichment of FluAV modulatory proteins (Fisher's exact test unadjusted $P \leq 0.01$; P2RY6, CD74, UNC93B1, SLC15A3 and MAB21L2 showed the highest *P*-value) (Fig. 6a and Supplementary Table 6). We focused our attention on P2RY6, a plasma-membrane-bound G-protein-coupled nucleotide receptor, which has not been studied in detail in the context of antiviral immunity. In line with ISG overexpression studies, doxycycline-driven expression of P2RY6 in HEK-FlpIn TREX cells potently inhibited replication of Semliki forest virus (SFV), VSV and FluAV (Fig. 6b and Supplementary Fig. 6a,b). Antiviral activity could be further boosted by the specific P2RY6 agonist MRS2957 (Fig. 6b and Supplementary Fig. 6c). To assess the potential function of P2RY6 and its agonist, we performed total proteome analysis in P2RY6-expressing cells. These data indicated that P2RY6 expression leads to differential expression of a subset of proteins (Fig. 6c, Supplementary Fig. 6d and Supplementary Table 7), which were associated with AP1 and NF-κB signaling (Supplementary Fig. 6e). Indeed, the activation of NF-κB by P2RY6 expression could be confirmed by reporter assays (Supplementary Fig. 6f) as previously suggested[24]. The ISG interactome data suggested binding of P2RY6 to ubiquitin-conjugating enzyme E2 variant 1 (UBE2V1) (Supplementary Fig. 2e and Supplementary Table 2), which is a central component for K63-dependent ubiquitination of TRAF proteins in response to pathogen sensing and inflammatory signal amplification[25]. To assess potential molecular mechanisms of P2RY6-dependent inflammatory signaling we performed AE–LC–MS/MS experiments in virus-infected cells. Using MAP3K14 as a prototypic case confirmed feasibility of this approach; infection with a cytokine-inducing clone 13 of Rift Valley fever virus (RVFV)[26] led to a dissociation of NF-κB inhibitory components from MAP3K14 precipitates (Supplementary Fig. 6g and Supplementary Table 8). Similar experiments with P2RY6 as bait identified JUNB, an AP1-specific transcription factor, and TRAFD1, which is involved in TRAF6-mediated NF-κB signaling, as RVFV infection-dependent P2RY6 interactors (Fig. 6d,e). Conversely, P2RY6 lost its interaction to UBE2V1 in presence of RVFV (Fig. 6e and Supplementary Table 8). Therefore, these data corroborated that P2RY6 directly triggers NF-κB activation through regulation of TRAF6-mediated signaling. To test this hypothesis we used a TRAF6 inhibitor and tested its influence on P2RY6-dependent NF-κB activation. Notably, inhibition of TRAF6 completely abrogated P2RY6-dependent NF-κB activation (Fig. 6f). Altogether, the data indicate engagement of a specific signaling pathway in response to P2RY6 activation. P2RY6 engages the E3 ubiquitin ligase UBE2V1 under steady-state conditions, and virus infection drives binding of the negative regulator TRAFD1 to P2RY6, which might facilitate TRAF6-mediated activation of NF-κB and AP1 signaling (Fig. 6g). Collectively, these data demonstrate that the ISG interactome provides entry points for hypothesis-driven characterization of specific signaling events that are activated during virus infections.

Discussion

The evolutionarily shaped antiviral immune system is highly efficient and relies on the function of ISGs that employ multiple pathways and act together to control a wide variety of pathogens. However, the influence of ISGs on the cellular landscape and their engagement of cellular proteins is only partially defined. The ISG interactome presented here allows several considerations regarding the organization of the innate immune system. For instance, some of the ISG interactors were previously found to be relevant for virus replication. The affinity to such proteins may allow ISGs to target viral replication hotspots, and would enable the cells to neutralize a wide variety of pathogens with a limited set of ISGs. Conversely, integrating interaction data from other pathogens with the ISG interactome might prove an effective strategy to pinpoint ISGs with specific antiviral activity. Diverse ISGs share a few common interactors, suggesting a central role for these proteins in ISG-mediated antiviral functions. For instance, LGALS3BP—the most connected protein in the network—functions as a potent negative regulator of the interferon response. Such highly connected proteins in key positions of the innate immune network may have as-yet-unappreciated roles in regulating the antiviral immune response. In summary, the combination of pleiotropic and specific interactions within the antiviral defense system might provide an extraordinary flexibility, enabling high efficacy against a broad range of pathogens. Furthermore, multiple interconnections with pre-existing cellular machinery reduce energy limitations, allowing the response to proceed more rapidly than if new molecular infrastructure were required[1,2].

The ISG interactome complements functional data from overexpression and genome-wide gene-depletion studies, facilitating the identification of activities and functions of individual ISGs and their binding partners. Integration of diverse datasets highlights central hubs with particular antiviral potency. For instance, the identification of P2RY6 and the downstream pathway signaling through NF-κB and AP1, demonstrates how this resource could be used to guide further functional and mechanistic studies on individual ISGs. ISG activity often depends on cellular proteins, which serve as essential co-factors for viral replication or are themselves targets of ISGs. Since susceptibility to ISGs varies between viruses, the data presented here may allow identifying vulnerability hotspots for pathogen-centric therapies. In personalized medicine, the individual susceptibility is taken into account to maximize therapeutic efficiency of drugs. By analogy, considering the ISG interactome and activities of ISGs against specific viruses should help the development of pathogen-centric therapies providing highly specific and efficient treatment against individual viruses and virus classes.

Online content

Any methods, additional references, Nature Research reporting summaries, source data, statements of data availability and associated accession codes are available at https://doi.org/10.1038/s41590-019-0323-3.

Received: 8 June 2018; Accepted: 16 January 2019;
Published online: 4 March 2019

References

1. Schoggins, J. W. et al. Pan-viral specificity of IFN-induced genes reveals new roles for cGAS in innate immunity. *Nature* **505**, 691–695 (2014).
2. Schoggins, J. W. et al. A diverse range of gene products are effectors of the type I interferon antiviral response. *Nature* **472**, 481–485 (2011).
3. Hayakawa, S. et al. ZAPS is a potent stimulator of signaling mediated by the RNA helicase RIG-I during antiviral responses. *Nat. Immunol.* **12**, 37–44 (2011).
4. Li, M. M. et al. TRIM25 enhances the antiviral action of zinc-finger antiviral protein (ZAP). *PLoS Pathog.* **13**, e1006145 (2017).0
5. Supek, F., Bosnjak, M., Skunca, N. & Smuc, T. REVIGO summarizes and visualizes long lists of gene ontology terms. *PLoS One* **6**, e21800 (2011).
6. Tokarev, A. et al. Stimulation of NF-κB activity by the HIV restriction factor BST2. *J. Virol.* **87**, 2046–2057 (2013).
7. Galao, R. P., Le Tortorec, A., Pickering, S., Kueck, T. & Neil, S. J. Innate sensing of HIV-1 assembly by tetherin induces NFκB-dependent proinflammatory responses. *Cell Host Microbe* **12**, 633–644 (2012).
8. Wang, I. H., Burckhardt, C. J., Yakimovich, A., Morf, M. K. & Greber, U. F. The nuclear export factor CRM1 controls juxta-nuclear microtubule-dependent virus transport. *J. Cell Sci.* **130**, 2185–2195 (2017).
9. Tripathi, S. et al. Meta- and orthogonal integration of influenza "OMICs" data defines a role for UBR4 in virus budding. *Cell Host Microbe* **18**, 723–735 (2015).
10. de Wilde, A. H. et al. A kinome-wide small interfering RNA screen identifies proviral and antiviral host factors in severe acute respiratory syndrome coronavirus replication, including double-stranded RNA-activated protein kinase and early secretory pathway proteins. *J. Virol.* **89**, 8318–8333 (2015).
11. York, A., Hutchinson, E. C. & Fodor, E. Interactome analysis of the influenza A virus transcription/replication machinery identifies protein phosphatase 6 as a cellular factor required for efficient virus replication. *J. Virol.* **88**, 13284–13299 (2014).
12. Ma, J. et al. Structural and functional study of apoptosis-linked gene-2-heme-binding protein 2 interactions in HIV-1 production. *J. Biol. Chem.* **291**, 26670–26685 (2016).
13. Long, J. S. et al. Species difference in ANP32A underlies influenza A virus polymerase host restriction. *Nature* **529**, 101–104 (2016).
14. Zhao, K. et al. Cytoplasmic STAT4 promotes antiviral type I IFN production by blocking CHIP-mediated degradation of RIG-I. *J. Immunol.* **196**, 1209–1217 (2016).
15. Pichlmair, A. et al. Viral immune modulators perturb the human molecular network by common and unique strategies. *Nature* **487**, 486–490 (2012).
16. Rusinova, I. et al. Interferomev2.0: an updated database of annotated interferon-regulated genes. *Nucleic Acids Res.* **41**, D1040–D1046 (2013).
17. Goffinet, C. Cellular antiviral factors that target particle infectivity of HIV-1. *Curr. HIV Res.* **14**, 211–216 (2016).
18. Fogeron, M. L. et al. LGALS3BP regulates centriole biogenesis and centrosome hypertrophy in cancer cells. *Nat. Commun.* **4**, 1531 (2013).
19. White, M. J., Roife, D. & Gomer, R. H. Galectin-3 binding protein secreted by breast cancer cells inhibits monocyte-derived fibrocyte differentiation. *J. Immunol.* **195**, 1858–1867 (2015).
20. Xiong, Y. et al. Annexin II receptor induces apoptosis independent of Annexin II. *Apoptosis* **18**, 925–939 (2013).
21. Ito, K., Takahashi, A., Morita, M., Suzuki, T. & Yamamoto, T. The role of the CNOT1 subunit of the CCR4–NOT complex in mRNA deadenylation and cell viability. *Protein Cell* **2**, 755–763 (2011).
22. Rodriguez-Gil, A. et al. The CCR4–NOT complex contributes to repression of major histocompatibility complex class II transcription. *Sci. Rep.* **7**, 3547 (2017).
23. Chapat, C. et al. hCAF1/CNOT7 regulates interferon signalling by targeting STAT1. *EMBO J.* **32**, 688–700 (2013).
24. Bar, I. et al. Knockout mice reveal a role for P2Y6 receptor in macrophages, endothelial cells, and vascular smooth muscle cells. *Mol. Pharmacol.* **74**, 777–784 (2008).
25. Hacker, H., Tseng, P. H. & Karin, M. Expanding TRAF function: TRAF3 as a tri-faced immune regulator. *Nat. Rev. Immunol.* **11**, 457–468 (2011).
26. Le May, N. et al. TFIIH transcription factor, a target for the Rift Valley hemorrhagic fever virus. *Cell* **116**, 541–550 (2004).

Acknowledgements

We acknowledge the innate immunity laboratory for critical discussions and suggestions. We thank K. Mayr, I. Paron and G. Sowa for maintaining mass spectrometers and the MPI-B core facility for support. We further thank G. Kochs for the FluAV mini replicon and A549 cells, G. Zimmer for VSV-Luc and A. Merits for SFV-gLuc and SFV-NanoLuc. We also thank M. Feulner for technical assistance. The work in the authors' laboratories was supported by the Max-Planck Free Floater program, ERC starting grant (ERC-StG iVIP, 311339), ERC consolidator grant (ERC-CoG ProDAP, 817798), Infect-Era and the German Federal Ministry of Education and Research (ERASE), the German Research Foundation (PI 1084/2, PI 1084/3, P1083/4 TRR179 and TRR237) to A.P. and (MS 632/15) to M.S. This work was also supported by NIH grant R01-AI091707 (to C.M.R.).

Author contributions

P.H., C.U., V.B. B.K., W.M.S., P.S., L.B., H.H.H and A.M. conducted experiments. P.H. and A.S. analyzed data. M.S. and J.W.S. contributed critical reagents. P.H., M.S., M.M., C.M.R., A.S, P.S. and A.P. designed the experiments and wrote the paper.

Competing interests

The authors declare no competing interests.

Additional information

Supplementary information is available for this paper at https://doi.org/10.1038/s41590-019-0323-3.

Reprints and permissions information is available at www.nature.com/reprints.

Correspondence and requests for materials should be addressed to A.P.

© The Author(s), under exclusive licence to Springer Nature America, Inc. 2019

Methods

Cells, plasmids, viruses and reagents. HEK293T, HeLa, HEK-FlpIn TREX, HeLa-FlpIn TREX, Vero E6 cells were described previously[15,27,28], A549 cells were a kind gift from G. Kochs. Cell lines were maintained in DMEM medium (PAA Laboratories) supplemented with 10% fetal calf serum (GE Healthcare) and antibiotics (100 U ml^{-1} penicillin, 100 µg ml^{-1} streptomycin) and regularly tested to be free of *Mycoplasma* contamination. Doxycycline-inducible cell lines were generated as described[15]. Expression constructs for N-terminal SII-HA tagged ISGs were generated by Gateway cloning of ISGs cDNA into pTO-SII-HA-GW[15]. The NF-κB reporter assay was performed as described before[15]. The FluAV mini replicon system (based on WSN strain) was provided by G. Kochs. Reporter assays were normalized to a co-transfected pBS EF1a–Ren construct kindly provided by E. Gürlevik. siRNAs were purchased from Qiagen or Dharmacon (see Supplementary Table 9). A/SC35M–NS1–2A–Renilla–2A–NEP (FluAV–Ren)[29] and VSV–Luc were gifts from G. Zimmer, SFV–NanoLuc and SFV–gLuc were gifts from A. Merits. Generation of Influenza A virus (WSN strain) encoding an N-terminal SII-tagged PB2 was described earlier[30]. Streptavidin beads were purchased from IBA (2-1201-010, Strep-Tactin Sepharose). The following antibodies were used: rabbit anti-IFIT3[28], rabbit anti-LGALS3BP was a kind gift form A. Ullrich, mouse anti-actin antibody (Santa Cruz; sc-47778), anti-HA-tag from rabbit (Cell Signaling; 3724), horseradish peroxidase (HRP)-coupled mouse antibody against HA (Sigma-Aldrich; H6533), mouse anti-VSV-G (Santa Cruz Biotechnology; sc-66180), HRP-coupled mouse against c-myc (Roche; 11814150001), rabbit anti-CSE1L (Proteintech; 22219-1-AP), mouse anti-KPNB1 (Abcam; ab2811), rabbit anti-CNOT1 (Cell Signaling Technology; 44613), HRP-coupled secondary antibody against mouse IgG (Sigma-Aldrich; RABHRP2) and against rabbit IgG (Cell Signaling Technology; 7074). Transfection of nucleic acids was performed using Metafectene Pro (Biontex). Dual-luciferase reporter assay system, cell viability assay (CellTiter-Glo) and Luciferase substrate d-Luciferin (E1602) were from Promega. Resazurin reduction assay was performed as described earlier[31]. The renilla substrate Coelenterazine (no. C2230) and the CD40 TRAF6 Inhibitor (3-[(2,5-dimethylphenyl)amino]-1-phenyl-2-propen-1-one; no. SML1160) were obtained from Sigma-Aldrich, while the MRS2957 was obtained from Tocris (no. 4260).

AE-LC–MS/MS analysis. Expression of ISGs in HeLa- and HEK-FlpIn TREX cells was induced by doxycycline (1 µg ml^{-1}) treatment for 48 h. For affinity enrichment, two 15 cm dishes per replicate were used. Cells were scraped off, washed in PBS, precipitated, and pellets were lysed on ice using TAP lysis buffer (50 mM Tris pH 7.5, 100 mM NaCl, 5% (v/v) glycerol, 0.2 % (v/v) Nonidet-P40, 1.5 mM $MgCl_2$, 1 µg ml^{-1} Avidin (2-0204-015; IBA) and protease inhibitor cocktail (EDTA-free, cOmplete; Roche)) for 15 min followed by a 5 min sonication step at 4 °C. Strep-Tactin agarose was added to the clarified cell lysates and incubated for 3 h at 4 °C on a rotary wheel. Beads were washed four times in TAP lysis buffer to reduce the concentration of unspecific proteins and to separate specific binders from background ones. Samples were washed five additional times with TAP washing buffer (50 mM Tris pH 7.5, 100 mM NaCl, 5% (v/v) glycerol, 1.5 mM $MgCl_2$) to eliminate remaining detergents. Beads were resuspended in 20 µl guanidinium chloride buffer (6 M GdmCl, 10 mM TCEP, 40 mM CAA, 100 mM Tris/HCl pH 8), boiled at 95 °C for 5 min and digested by adding 20 µl LysC-Protease-Mix (100 mM Tris/HCl pH 8 and 0.5 µg LysC (WAKO Chemicals)) for 3 h at 30 °C. Samples were diluted 1:5 with Trypsin-Protease-Mix (100 mM Tris/HCl pH 8 and 1 µg trypsin) (Promega) and incubated for 12 h at room temperature. TFA and acetonitrile was added to a final concentration of 0.6% and2 %, respectively. Peptides were desalted and concentrated using C18 Empore filter discs (3 M)[32]. After elution, peptides were analyzed using an EASY-nanoLC system (Thermo Fisher Scientific), which was directly coupled to a LTQ-Orbitrap XL mass spectrometer (Thermo Fisher Scientific). Peptides were loaded on an analytical 15 cm C18 column (Reprosil-Pur 120 C10-AQ, 3 µM; Dr. Maisch) and eluted using an 115 min acetonitrile gradient starting with 5% to 30% (85 min), 30% to 95% (15 min), a wash out period of 5 min at 95% and a re-adjustment phase to 5% of organic acetonitrile buffer (80% acetonitrile, 0.1% formic acid) (10 min) at a constant flow of 250 nl min^{-1}. Proteomic analysis was performed as described earlier[33]. In brief, the mass spectrometer was used in a data-dependent acquisition mode with one full mass-spectrometry scan at a resolution of 60,000 at 400 m/z in the Orbitrap, followed by 10 tandem-mass-spectrometry scans in the linear ion trap (target ion value = 1,000, isolation width = 2 m/z, CID fragmentation mode with normalized collision energy = 40) of the highest reported peaks obtained in the full MS scan before. Raw files were processed with MaxQuant version 1.5.3.34 or 1.6.0.15, using label-free quantification (LFQ) and match between run options and searched against forward and reverse sequences of the human proteome (UniprotKB, release 03.2016) by the built-in Andromeda search engine[34]. Carbamidometylation was set as fixed, methionine oxidation and N-acetylation as variable modification. Precursor ions with a mass tolerance of 6 ppm and fragmented ions with a mass tolerance of 0.5 Da were accepted. Peptide and protein identification was controlled by a False Discovery Rate (FDR) of 0.01. Perseus version 1.5.3.0 or 1.6.0.7 was used to analyze the output of MaxQuant[35]. Protein groups identified as known contaminants or reverse sequence matches were excluded from the analysis. Only proteins with a minimum of two LFQ quantifications in at least one group of replicate experiments (n = 3) for a specific ISG bait were considered for the analysis. Missing values were imputed using normal distribution, whose standard deviation was defined as 30% and the mean was offset by −1.8 s.d. of the data distribution of the real intensities observed in the corresponding mass-spectrometry run, respectively. To identify true interactors of ISG baits and eliminate unspecific (false positive) binders, statistical data analysis was performed as follows: on the basis of the similarity of their protein content, mass-spectrometry runs were classified into 7 groups of 15 ISG baits each and complemented with a fixed set of control experiments (see Supplementary Table 10, 'ISG bait groups'). Within each resulting subset, the significance of the protein enrichment in the pulldowns of a specific ISG bait versus the other baits and control experiments was determined using a t-test (two sided, equal variance, S_0 = 0.5) and corrected for multiple hypothesis testing using permutation-based FDR statistics (FDR = 0.05, 250 permutations) as described previously[36,37]. The groups of ISG baits were determined by co-cluster analysis using the Spearman's ranked correlation of protein abundance (LFQ) profiles as the similarity measure. The complemented set of control experiments included AE–LC–MS/MS experiments of tagged GFP, and experiments defining precipitated background binders obtained in cell lysate without tagged protein, measured in parallel with the AE–LC–MS/MS runs for ISG baits.

FluAV vRNP interactions: A549 cells were infected with a recombinant FluAV (strain WSN) expressing SII-tagged PB2 for 3 h at m.o.i. = 30 and affinity enrichment was performed as described above. Results are shown in Supplementary Table 2 and Supplementary Table 5 (FluAV vRNP interactors) and selected AE–LC–MS/MS experiments were blotted as volcano plots by using Perseus and R (https://www.r-project.org, version 3.3).

We performed direct comparison of protein interactions to ISGs in uninfected and RVFV clone 13 infected HEK293T FlpIn TREX cells. Cells were infected 30 h after doxycycline induction with RVFV clone 13 for 18 h at m.o.i. =0.1. Affinity enrichment, sample preparation, LC–MS/MS analysis and processing of raw data were performed as described before. Statistical analysis was performed as follows: for the comparison, only the experiments from infected and non-infected samples of a specific ISG bait and the controls were considered. In a first step, we excluded infection-induced changes in a background proteome. For this, the dataset was separated into two groups. The first group covered AE–LC–MS/MS runs of infected samples and controls, the second group consisted of the same set of samples and controls, which were not infected with RVFV clone 13. These two groups were compared to each other by multiple equal variance t-tests with permutation-based FDR statistics. Protein groups that changed significantly (FDR < 0.0001) were identified as common RVFV clone 13-mediated changes and excluded from the subsequent analysis steps (830 protein groups were identified and excluded). In a second step, we addressed ISG-specific, significant interactors in infected versus non-infected cells by performing multiple equal variance t-tests with permutation-based FDR statistics of the individual infected or non-infected replicate experiments of a specific ISG bait against the entire pre-filtered data matrix (as described in the previous step). Results of differential binding profiles were combined and direct comparisons are accessible in Supplementary Table 8, and selected comparisons were plotted using R.

Total proteome analysis. After depletion of LGALS3BP in HeLa cells or CNOT1 depletion in HeLa-FlpIn TREX IFIT3 cells or doxycycline-induced expression of P2RY6 in HEK FlpIn TREX or HeLa FlpIn TREX ANXA2R cells, the total cellular proteome was measured and compared to the proteome of control cells. For each replicate, 10^6 cells were used. Cells were washed with PBS, lysed in 200 µl SDS lysis buffer (4% SDS, 10 mM DTT, 55 mM IAA, 50 mM Tris/HCl pH 7.5) and boiled at 95 °C for 5 min. Samples were sonicated until a homogeneous suspension was achieved (20 min at 4 °C; Bioruptor). Protein concentration was determined by DC Protein Assay (BioRad) and protein concentration was adjusted accordingly to a final concentration of 1 µg $µl^{-1}$ with SDS lysis buffer. Per replicate, 200 µg of protein was precipitated using pre-chilled acetone (−20 °C) at a final concentration of 80% acetone (v/v) and incubated for 3 h at −20 °C. Precipitates were pelleted and washed once with 80% acetone. Pellets were air dried at room temperature and resolubilized by adding 80 µl thiourea buffer (6 M urea, 2 M thiourea (U/T) in 10 mM HEPES, pH 8.0) followed by subsequent sonication until a homogeneous suspension was achieved (10 min at 4 °C; Bioruptor). For protein digestion, 25% of the resolubilized protein mixture was used and digested with LysC and trypsin as described above. After peptide clean up on C18 stage tips, purified peptides were loaded onto a 50 cm reverse-phase analytical column (75 µm column diameter; ReproSil-Pur C18-AQ 1.9 µm resin; Dr. Maisch) and separated using a 120 min (P2RY6) or 180 min (LGALS3BP) gradient (80% acetonitrile, 0.1% formic acid) (120 min gradient: 5% to 30% (90 min), 30% to 95% (20 min), wash out at 95% for 5 min, readjustment to 5% in 5 min; 180 min gradient: 5% to 30% (150 min), 30% to 95% (20 min), wash out at 95% for 5 min, readjustment to 5% in 5 min) at a flow rate of 350 nl min^{-1} using the EASY-nLC 1200 system (Thermo Fisher Scientific). Separated peptides were analysed on a Q Exactive HF mass spectrometer (Thermo Fisher Scientific). The MS instrument was set to a data-dependent acquisition mode with repeating cycles of one MS1 full scan (300–1,600 m/z, R = 60,000 at 200 m/z) at an ion target of 3×10^6, followed by 15 MS2 scans of the highest abundant isolated and higher-energy collisional dissociation (HCD) fragmented peptide precursors (15,000 at 200 m/z). For MS2 scans, collection of isolated

peptide precursors in the C-Trap was limited by a ion target of 1×10^5 and a maximum injection time of 120 ms to ensure high quality MS2 spectra and the dynamically adaption to the sample complexity. In-line repeated isolation and fragmentation of the same peptide precursor was eliminated by dynamic exclusion for 20 s. The isolation window of the quadrupole was set to 1.4 m/z and HCD was set to NCE to 27% and underfill ratio of 20%. Identified spectra were analyzed using MaxQuant as described for AE–LC–MS/MS experiments.

The analysis of proteins differentially regulated between HeLa-FlpIn TREX ANXA2R and control (IFIT3) cells was performed in R (version 3.5.1) and Rstudio (version 1.1.456) using a generalized random effects linear model: $\log_2(\text{intensity}) \propto \text{doxcycline} \times \text{time} \times \text{cell line}$.

The significance of ANXA2R induction contribution and the significance of the difference between ANXA2R and IFIT3 induction contribution were estimated by the general linear hypothesis test using the glht function from the multcomp R package (version 1.4-8)[36]. A protein was considered specifically regulated, if it was both significantly regulated by ANXA2R induction (estimate $k2$ in Supplementary Table 7) and this effect was significantly different than upon IFIT3 induction (estimate $k1$ in Supplementary Table 7) (two-sided P values were adjusted using the Benjamini–Yekutieli method[39] with $P = 0.001$ significance cut-off). For visualization purposes, P values of zero were replaced with 0.5 of minimal finite P value.

Bioinformatics analysis. The list of specific ISG–protein interactions identified at the previous step was imported into Cytoscape (version 3.3.0) for further analysis. The resulting interaction network consisted of 104 ISG baits and 1401 binding partners. The connectivity between the two ISG baits was defined as the fraction of shared interactors among all interacting proteins of the ISG pair. The number of novel interactions was defined by intersecting interactions in the ISG network with the interactions reported in BioGrid (release August2017). GO Terms and Reactome pathways enrichment analysis was performed using Fisher's exact tests (Benjamini–Hochberg-adjusted $P \leq 0.05$, minimum twofold enrichment of the annotated genes in comparison to the remaining background) using the annotations of interactors (http://www.pantherdb.org, May 2017) of individual ISGs. The enrichments were calculated against the set of all proteins previously identified as interactors in comparable AE–LC–MS/MS experiments[15,36] and background binders identified in this study. In case of total proteome analysis, functional annotation enrichments were calculated against all the proteins identified in a given experiment, using Fisher's exact tests or by one-dimensional annotation enrichment analysis[40].

Functional annotation of ISG network. The enriched functional annotations of every individual ISG interactome were compared to functional annotations of the corresponding ISG bait itself (QuickGO database, release July 2017). We used the REViGO analysis platform to estimate the relation between the two groups of annotations: interactome GO terms that matched exactly to the reported GO terms of the ISG bait were classified as 'Known', interactome GO terms that formed a defined cluster with the bait GO terms were defined as 'Related to known' (REViGO, allowed similarity threshold = 0.5; Supplementary Table 3), the remaining interactome GO terms could not be associated with the GO terms of the ISG bait and were classified as 'Novel'.

To determine the frequently targeted pathways we counted how often individual Reactome pathways were enriched in the interactomes of individual ISGs. We isolated Reactome pathways, which were targeted by at least three different ISGs. Then we connected the selected pathways to each other, weighting each pair of pathways proportionally to the number of ISG interactors they shared. Highly connected modules were clustered according to their weighted connections and manually defined into functional modules.

To evaluate which functional annotations correlate with the number of ISG baits interacting with the given protein, we first identified annotations significantly enriched among all ISG interactors in comparison to the background set of proteins defined above (Fisher's exact test, Benjamini–Hochberg-corrected $P \leq 0.05$). We then subsequently reduced the group of ISG interactors, considering only the ones interacting with two, three or more ISG baits. At each step we calculated the relative enrichment factor of the term against the set of all interactors in the ISG network (Supplementary Table 4).

Intersecting ISG network with the public data. To intersect the ISG-interaction network with functionally relevant datasets, the proteins identified in this study, confirmed candidates of siRNA screens[9], identified vORF interactors[15] and genes dynamically regulated by the interferon system[16] (fold change ≥ 2 in at least three independent experiments) were mapped using ENSEMBL database to the UniProt accession codes of reviewed human protein sequences. Proteins were classified into three groups: 'ISG interactors', 'ISG baits' and 'Background'. Significance of the overlap between one of the defined groups and the external sets was determined by Fisher's exact test and corrected for multiple hypotheses using a Benjamini–Hochberg FDR against the remaining human proteome background. The overlap between the interactomes of individual ISG baits and the confirmed candidates of siRNA screens was analyzed similarly.

Protein complexes targeted by specific ISGs. Significantly enriched protein complexes were isolated on basis of their Gene Ontology cellular compartment annotations (GO CC) and the numbers of ISGs, which interact with at least one complex member in the ISG network, were determined. In a second step, the LFQ intensities of the complex members in the pulldown experiments of a specific ISG bait were compared to their intensities in the rest of the dataset. The subnetworks of the six complexes showing high specificity to a single ISG bait were generated (see Fig. 5b,c).

Overlapping the ISG network and vRNP interactors. Interactions between ISG binders and influenza vRNP-associated proteins were grouped according to their cellular localization (GOCC) and their overlap with the ISG network. For subsequent analysis, ISGs that bind one or more vRNP-associated proteins were defined as one group and the remaining ISGs in the network as the second group. We mapped the information about ISG-mediated effects on influenza virus replication[1,2] to these two groups and compared these two populations by Mann–Whitney test.

RNA interference knockdown, overexpression, virus replication and luciferase assays. HeLa or A549 cells were transfected with siRNA (30 pmol per 2×10^5 cells) for 48 h using Metafectene Pro (Biontex) according to the manufacturer's instructions. HeLa FlpIn and HEK-FlpIn T-REX cells were treated with doxycycline to induce ISG expression for 24 h. Cells were infected with reporter viruses, which express either renilla or luciferase as reporter genes. Infected cells (1×10^5 to 2×10^5 cells) were lysed 20 h to 24 h after infection and enzyme activity was measured using an Infinite 200 PRO micro plate reader (Tecan). To determine the impact of the protein depletion on FluAV replication, we treated cells with siRNAs for 48 h and transfected a mini replicon system for 36 h. Replication capacity was determined by calculating firefly luciferase/renilla luciferase activity using a dual-luciferase reporter assay system (Promega). To assess the influence of ISGs on NF-κB activity, we co-transfected ISGs (100 ng) with pNFκB-luc (100 ng) and pBS EF1a–Ren (15 ng) in 1×10^5 HEK293T cells and cultured cells for additional 16 h. Cell pellets were lysed in passive lysis buffer and firefly luciferase/renilla luciferase activity ratios were determined as described above.

Where indicated, CD40–TRAF6 specific inhibitor (3-[(2,5-dimethylphenyl) amino]-1-phenyl-2-propen-1-one) (1 μM) was added to cells together with the P2RY6 Ligand MRS2957 8 h before lysis. Cell viability was tested by CellTiter-Glo or resazurin reduction assay[27].

Co-immunoprecipitation and immunofluorescence experiments. For validation of ISG interaction partners, HEK293T cells were seeded at 5×10^6 cells per 10 cm dish and transfected with plasmids for the expression of SII-HA-tagged bait proteins. Twenty-four hours after transfection, cells were collected in 1 ml lysis buffer (50 mM Tris-HCl pH 7.5, 0.2% NP-40, 5% glycerol, 100 mM NaCl, 1.5 mM MgCl2 and protease inhibitor cocktail (cOmplete, Roche)) and clarified lysates were incubated with 20 μl Strep-Tactin agarose for 3 h at 4 °C. After three washing steps with lysis buffer, co-immunoprecipitated proteins were analyzed by immunoblot analysis. LGALS3BP interaction partners were validated using a LUMIER assay. HEK293T cells were seeded at 6×10^5 cells per well in six-well plates and the next day plasmids expressing SII-HA-tagged bait proteins were co-transfected with a Renilla–LGALS3BP fusion protein expressing plasmid. Lysis in 250 μl lysis buffer and co-immunoprecipitation was carried out as described above, followed by two additional washing steps with lysis buffer lacking NP-40. Suspension of the washed agarose in renilla-substrate-buffer (100 mM K3PO4 pH 7.6, 500 mM NaCl, 1 mM EDTA, 25 mM thiourea, 0.01 mM coelenterazine) enabled the quantification of LGALS3BP binding via luminescence following coelenterazine conversion by the renilla enzyme.

For immunofluorescence analysis HeLa FlpIN TREX cells expressing Strep-HA-tagged IFIT3 or ANXAR2 were seeded in 24-well plates (5×10^4 cells per well) and 24 hours later treated with doxycycline (1 μg ml^{-1}) for another 24 h. Cells were fixed with 4% PFA, permeabilized with 0.1% (v/v) Triton X-100 in PBS and unspecific binding sites were blocked with PBS containing 5% BSA for 1 h at room temperature. Cells were then subjected to immunofluorescence staining using anti-HA and anti-CNOT1 antibodies. Secondary staining was performed with donkey anti-mouse Alexa568-conjugated and goat anti-rabbit Alexa488-conjugated antibodies. Nuclear DNA was stained with 4′,6-diamidino-2-phenylindole (DAPI) (Molecular Probes). Coverslips were mounted in Fluoromount-G mounting medium (Southern Biotechnology Associates). Fluorescence images were acquired with a FluoView1000 confocal microscope (Olympus, Hamburg, German) using a 63× water objective.

Reporting Summary. Further information on research design is available in the Nature Research Reporting Summary linked to this article.

Data availability

The MS-based proteomics data were deposited at the ProteomeXchange consortium (http://proteomecentral.proteomexchange.org) via the PRIDE partner repository under following accession codes: PXD012274, PXD012275, PXD012276, PXD012277 and PXD012278. The protein interactions from this publication have been submitted to the IMEx consortium (http://www.imexconsortium.org) through IntAct and has been assigned the identifier IM-26691.

References

27. Holze, C. et al. Oxeiptosis, a ROS-induced caspase-independent apoptosis-like cell-death pathway. *Nat. Immunol.* **19**, 130–140 (2018).
28. Pichlmair, A. et al. IFIT1 is an antiviral protein that recognizes 5′-triphosphate RNA. *Nat. Immunol.* **12**, 624–630 (2011).
29. Reuther, P. et al. Generation of a variety of stable Influenza A reporter viruses by genetic engineering of the NS gene segment. *Sci. Rep.* **5**, 11346 (2015).
30. Chase, G. P. et al. Influenza virus ribonucleoprotein complexes gain preferential access to cellular export machinery through chromatin targeting. *PLoS Pathog.* **7**, e1002187 (2011).
31. Riss, T. L. & Moravec, R. A. Use of multiple assay endpoints to investigate the effects of incubation time, dose of toxin, and plating density in cell-based cytotoxicity assays. *Assay Drug Dev. Technol.* **2**, 51–62 (2004).
32. Gebhardt, A. et al. mRNA export through an additional cap-binding complex consisting of NCBP1 and NCBP3. *Nat. Commun.* **6**, 8192 (2015).
33. Hubner, N. C. et al. Quantitative proteomics combined with BAC TransgeneOmics reveals in vivo protein interactions. *J. Cell Biol.* **189**, 739–754 (2010).
34. Tyanova, S., Temu, T. & Cox, J. The MaxQuant computational platform for mass spectrometry-based shotgun proteomics. *Nat. Protoc.* **11**, 2301–2319 (2016).
35. Tyanova, S. et al. The Perseus computational platform for comprehensive analysis of (prote)omics data. *Nat. Methods* **13**, 731–740 (2016).
36. Hein, M. Y. et al. A human interactome in three quantitative dimensions organized by stoichiometries and abundances. *Cell* **163**, 712–723 (2015).
37. Keilhauer, E. C., Hein, M. Y. & Mann, M. Accurate protein complex retrieval by affinity enrichment mass spectrometry (AE–MS) rather than affinity purification mass spectrometry (AP-MS). *Mol. Cell Proteomics* **14**, 120–135 (2015).
38. Hothorn, T., Bretz, F. & Westfall, P. Simultaneous inference in general parametric models. *Biom. J.* **50**, 346–363 (2008).
39. Benjamini, Y. & Yekutieli, D. The control of the false discovery rate in multiple testing under dependency. *Ann. Stat.* **29**, 1165–1188 (2001).
40. Cox, J. & Mann, M. 1D and 2D annotation enrichment: a statistical method integrating quantitative proteomics with complementary high-throughput data. *BMC Bioinformatics* **13**, S12 (2012).

nature immunology

SUPPLEMENTARY INFORMATION

https://doi.org/10.1038/s41590-019-0323-3

In the format provided by the authors and unedited.

A protein-interaction network of interferon-stimulated genes extends the innate immune system landscape

Philipp Hubel[1], Christian Urban[2], Valter Bergant[2], William M. Schneider[3], Barbara Knauer[1], Alexey Stukalov[1,2], Pietro Scaturro[1,2], Angelika Mann[1], Linda Brunotte[4,5], Heinrich H. Hoffmann[3], John W. Schoggins[3,6], Martin Schwemmle[7], Matthias Mann[8], Charles M. Rice[3] and Andreas Pichlmair[1,2,9]*

[1]Innate Immunity Laboratory, Max-Planck Institute of Biochemistry, Munich, Germany. [2]Institute of Virology, School of Medicine, Technical University of Munich, Munich, Germany. [3]Laboratory of Virology and Infectious Disease, The Rockefeller University, New York, NY, USA. [4]Institute of Virology, Westfaelische Wilhelms-University Muenster, Muenster, Germany. [5]Cluster of Excellence 'Cells in Motion', Westfaelische Wilhelms-University Muenster, Muenster, Germany. [6]Department of Microbiology, University of Texas Southwestern Medical Center, Dallas, TX, USA. [7]Institute of Virology, Medical Center University of Freiburg, Freiburg, Germany. [8]Department of Proteomics and Signal Transduction, Max-Planck Institute of Biochemistry, Munich, Germany. [9]German Center for Infection Research (DZIF) Munich Partner Site, Munich, Germany. *e-mail: andreas.pichlmair@tum.de

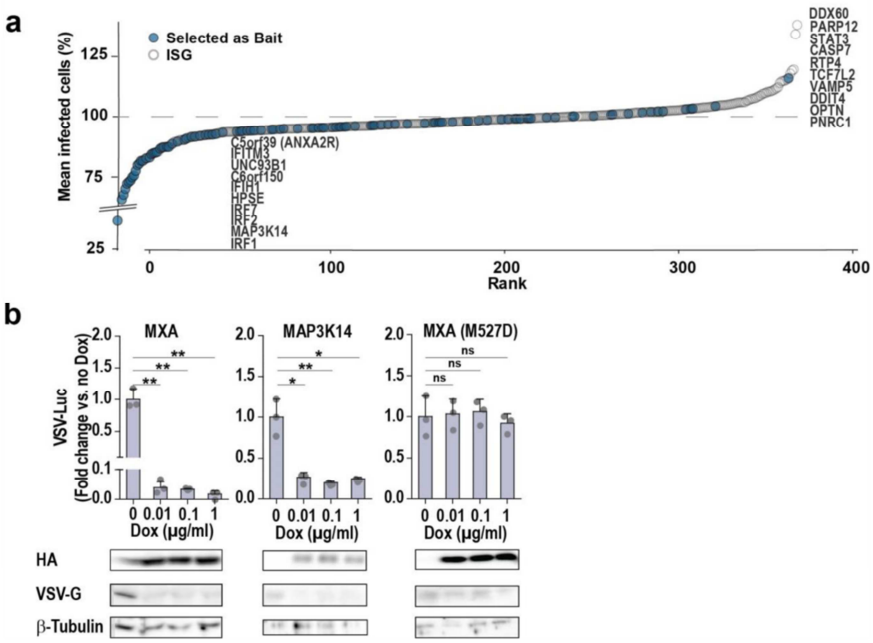

Supplementary Figure 1

Bait selection and testing bait functionality.

(a) ISG proteins ranked by average antiviral activity in published gain of function virus replications studies. ISGs selected for AE-LC-MS/MS experiments are highlighted (blue circles). Top 10 ISGs showing highest and lowest antiviral activity are listed. **(b)** Validation of antiviral activity of selected ISGs in HEK-FlpIn TREX cells. ISG expression was induced by increasing concentrations of doxycycline (Dox) for 24h followed by infection with VSV-expressing firefly luciferase (VSV-Luc; MOI=0.01). Graphs show luciferase activity 18h post infection. Lysates were used to determine protein expression levels of the ISG transgene (HA), VSV-G and β-Tubulin by immunoblot analysis. The histogram shows average luciferase activity ±s.d. n = 3 independent samples, one representative experiment of three is shown. * *p*-value ≤ 0,0002, ** *p*-value ≤ 0,0001, ns: not significant. One-way ANOVA with Dunnett's multiple comparisons test. One representative experiment of three is shown.

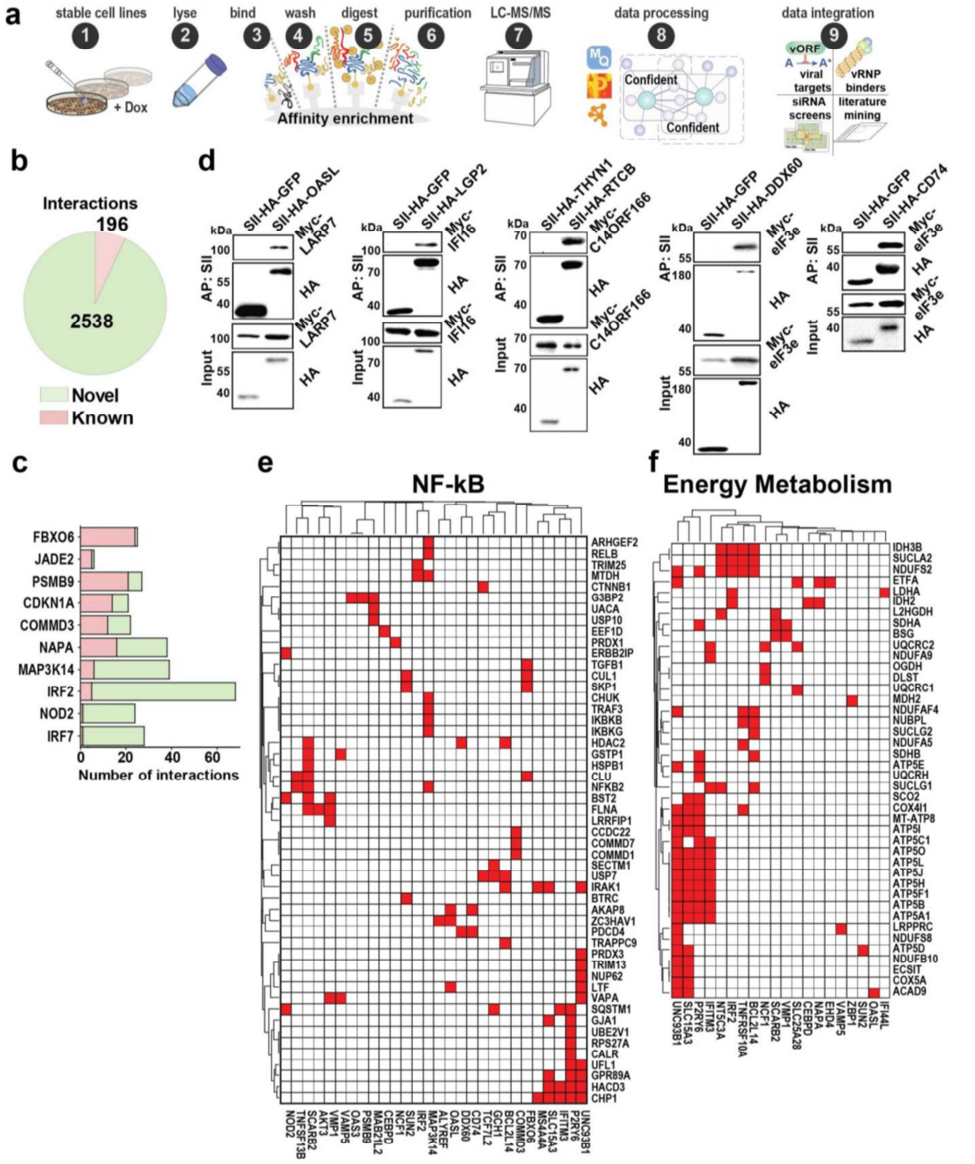

Supplementary Figure 2

AE-LC-MS/MS procedure and identified interactions.

(a) AE-LC-MS/MS workflow and data analysis strategy. **(b)** The number of already reported and novel interactions identified by AE-LC-MS/MS experiments in this study. **(c)** The number of known and novel interactions for selected ISG baits, colors as in (b). **(d)** 293T cells were transfected for plasmids expressing SII-HA-tagged control (GFP, THYN1) or bait proteins (OASL, LGP2, RTCB, DDX60, CD74) together with Myc-tagged prey proteins (LARP7, IFI16, C14ORF166, eIF3e). Cell lysates of HEK293T cells were used for SII-immunoprecipitation and probed with antibodies against HA or Myc. One representative blot of three is shown. **(e, f)** Binary matrix of interactions between ISG baits (columns) and proteins (rows) with reported functions in NF-kB signaling **(e)** and in energy metabolism **(f)**.

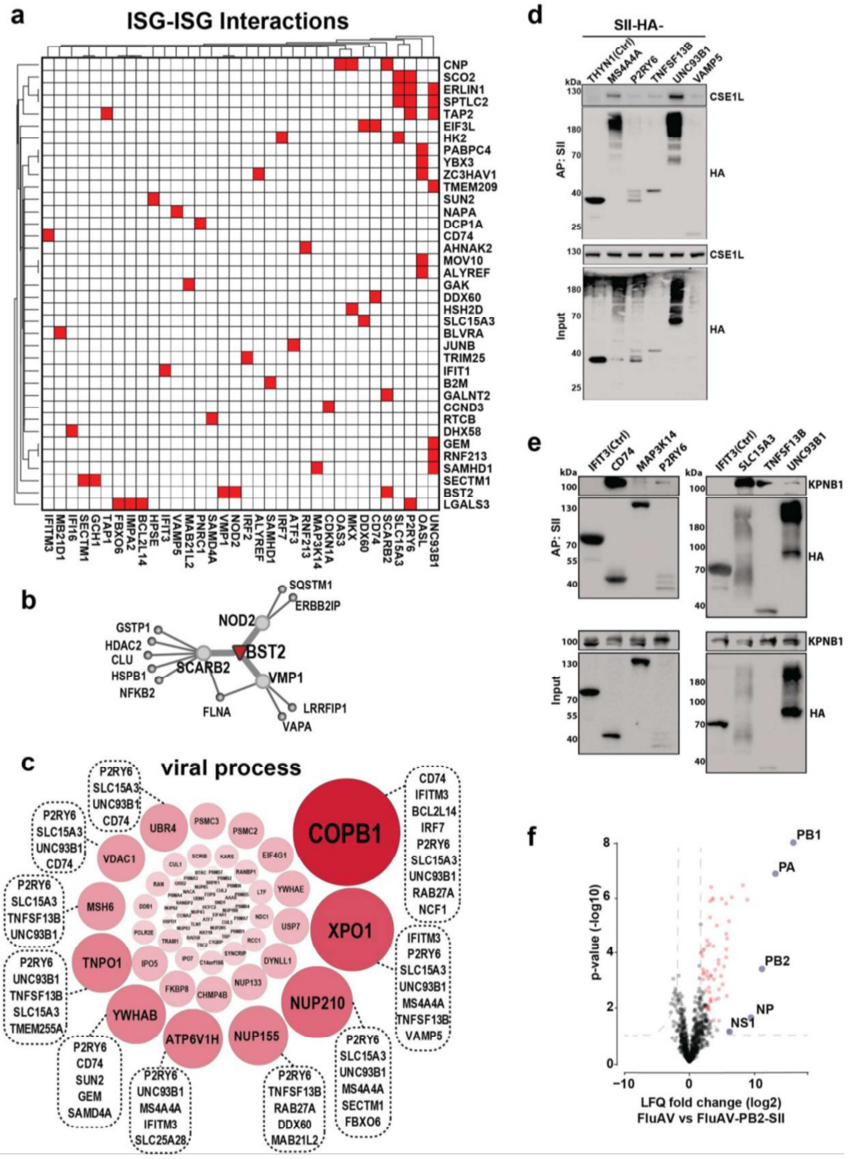

Supplementary Figure 3

Identification of ISG–ISG interactions and FluAV vRNP interactors.

(a) Binary matrix of ISG-ISG interactions identified in this study. Only ISGs listed in Supplementary Table 1 were considered. Bait ISG (columns), Prey ISG (rows). **(b)** BST2-centric NF-kB subnetwork. ISG baits (large circles) interacting with BST2 (red triangle) plus the other bait interactors (small balls) implicated in NF-kB signaling (based on GO BP annotations). **(c)** Identified ISG interactors with known functions in viral processes. Size and color intensity correspond to the number of interacting ISG baits (shown in callout boxes). **(d, e)** Co-immunoprecipitation of SII-HA-tagged control (THYN1, IFIT3) or bait proteins (NS4A4A, P2RY6, TNFSF13B, UNC93B1, VAMP5, CD74, and MAP3K14) and endogenous proteins (CSE1L, KPNB1). Cell lysates of 293T cells were used for SII-immunoprecipitation and probed with antibodies against HA-tag, CSE1L or KPNB1. One representative blot of three is shown. **(f)** Identification of FluAV vRNP-binding proteins by AE-LC-MS/MS analysis. A549 cells were infected with SII-tagged viral polymerase subunit 2 (PB2) expressing FluAV or untagged virus and anti-SII precipitates were analyzed by AE-LC-MS/MS. Volcano plot shows the average enrichment of a protein in PB2 pulldown compared to the control enrichments and the corresponding *p*-value (N = 4, two tailed *t*-test, unadjusted) with significantly enriched cellular (red) and viral (blue) proteins (permutation-based FDR = 0.05, S_0 = 1, n = 4)

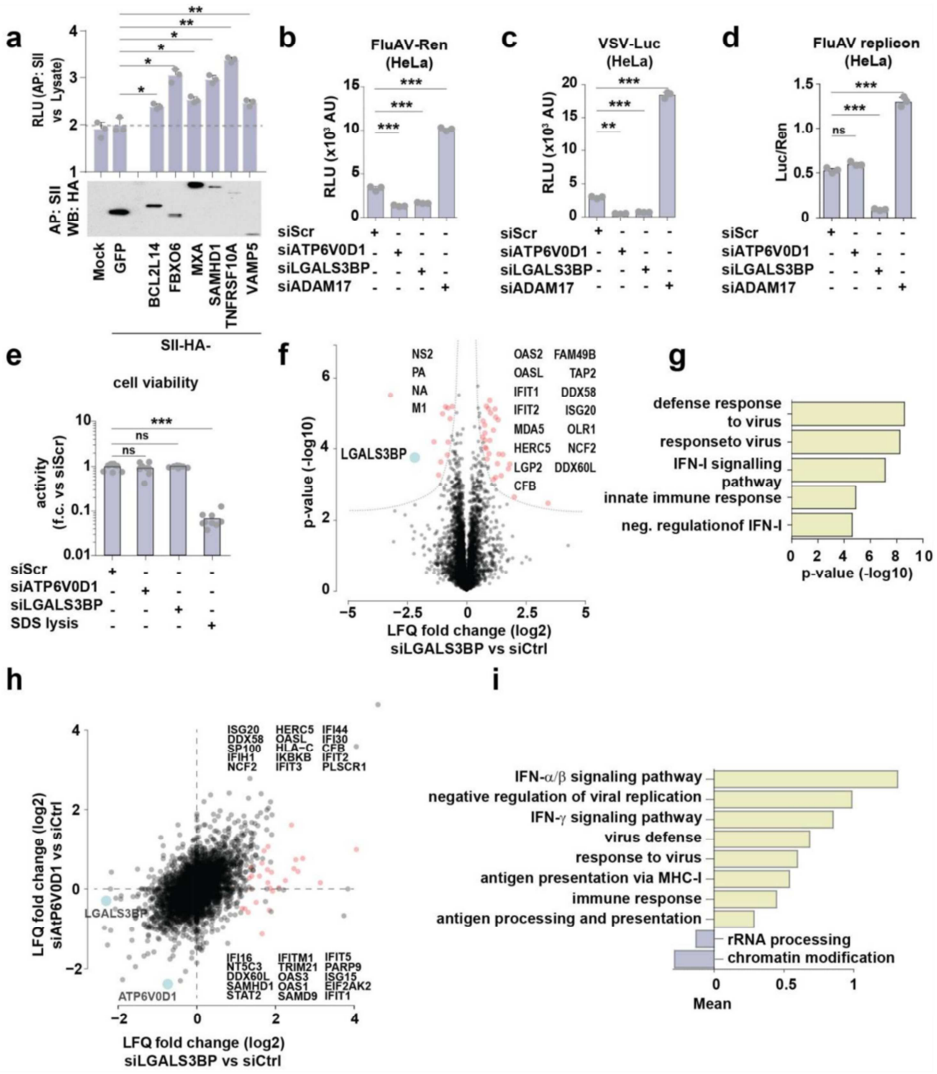

Supplementary Figure 4

Identification of LGALS3BP as an immunomodulatory protein.

(a) Co-immunoprecipitation of N-terminal-renilla-tagged LGALS3BP with non-transfected control (Mock), SII-HA-tagged control (GFP), or bait proteins (BCL2L14, FBXO6, MXA, SAMHD1, TNFRSF10A, VAMP5) in 293T cells. The graph shows mean ±s.d. relative luminescence unites (RLU) of streptavidin co-immunoprecipitated renilla-LGALS3BP normalized to the corresponding input renilla expression. Graph is based on technical triplicates (dots) of one representative biological repeat of three. * *p*-value < 0.01, ** *p*-value ≤ 0.001. Immunoblot analysis shows the enrichment of SII-HA-tagged proteins following SII-immunoprecipitation, probed with a HA-specific antibody. **(b-e)** HeLa cells were treated with siRNA against LGALS3BP, ATP6V0D1, ADAM17 or control siRNA (siCtrl) for 24h. The cells were **(b)** infected with FluAV-Ren (MOI=0.05), **(c)** infected with VSV expressing firefly luciferase (VSV-Luc), **(d)** transfected with plasmids that encode for the FluAV replication complex driving luciferase expression, **(e)** left untreated. (b, c, e) 24h , (c) 36h later (b) renilla, (c, d) firefly luciferase or (e) cell titer glow activity were measured. Histograms show average ±s.d. of three (b-d) or nine (e) technical replicates, representative experiments of at least three independent biological experiments are shown. ** *p*-value < 0.001, *** *p*-value < 0.0001, ns: not significant based on one way ANOVA with Dunnett's multiple comparisons test. **(f, g)** Proteome analysis of HeLa cells treated with siRNA targeting LGALS3BP or Control (siScr) for 24h and subsequently infected with FluAV (MOI=0.05). (f) Protein expression in siLGALS3BP-treated FluAV-infected HeLa cells in comparison to siScr. Significantly enriched proteins are highlighted in red (two-tailed Welch's *t*-test, FDR ≤ 0.01, S0 = 0.1, n = 4 independent measurements). (g) Top 5 GOBP terms enriched among the proteins significantly changed in (f) (Fisher's exact test, Benjamini-Hochberg FDR ≤ 0.05, enrichment factor ≥ 2). **(h)** Proteome changes in LGALS3BP- (X axis) and ATP6V0D1- (Y axis) depleted HeLa cells in comparison to the non-targeting siRNA control (siScr). Red dots: ISGs upregulated in LGALS3BP-depleted cells. **(i)** Top 10 GOBP terms enriched among the proteins changed in (h). Histogram displays enrichment factors representing the mean LFQ based protein abundance distribution for each significant category, relative to the overall LFQ abundance distribution in the proteome. (Benjamini-Hochberg FDR ≤ 0.05).

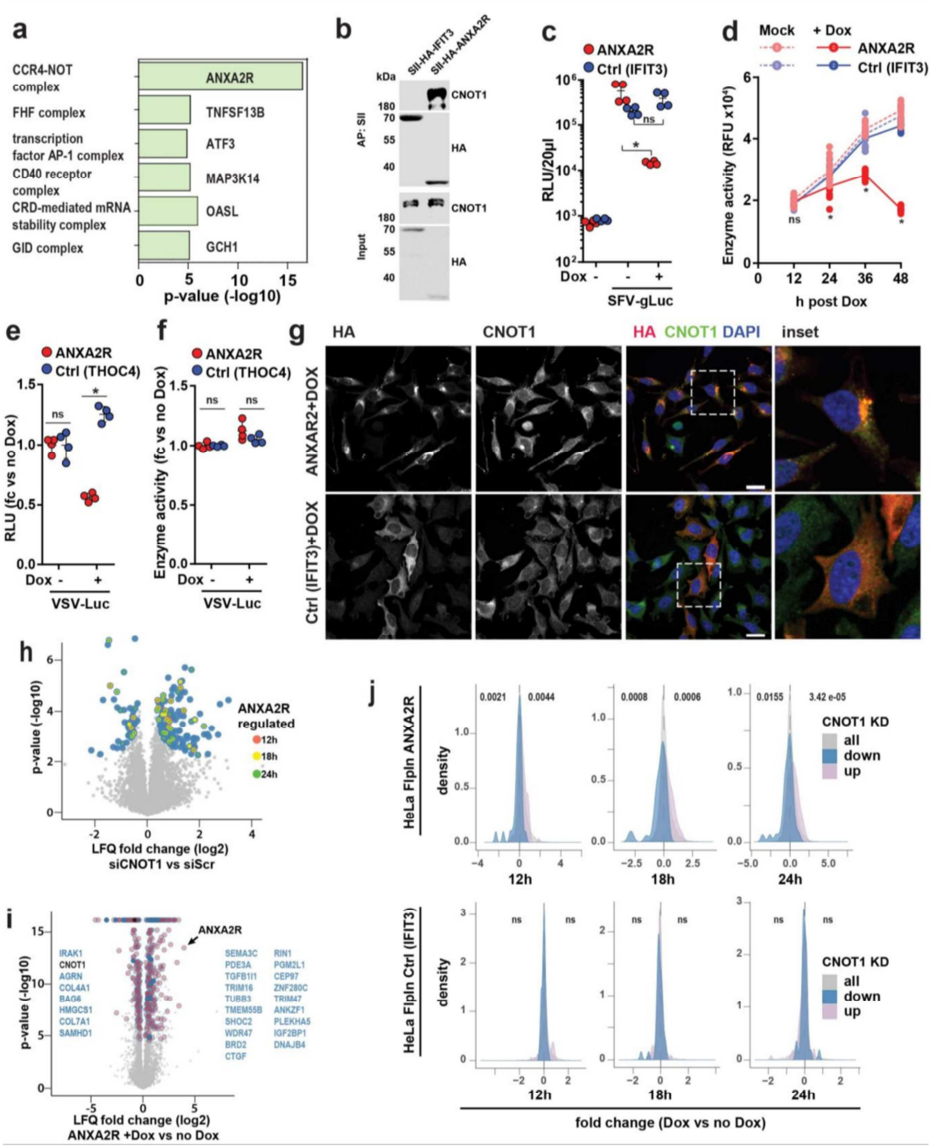

Supplementary Figure 5

Functional effects of protein complex targeting.

(a) Selected protein complexes (based on GOCC) targeted by individual ISGs (Fisher's exact test, Benjamini-Hochberg FDR ≤ 0.001, enrichment factor > 3). Shown protein complexes have ≤ 1 interactions of protein complex members to other ISGs in the network. Bar shows $-\log_{10}$ *p*-value of enrichment of the protein complex by the ISG against the background. **(b)** SII co-immunoprecipitation of endogenous CNOT1 with transfected SII-HA-tagged IFIT3 (control) or ANXA2R in 293T cells. One representative blot of three is shown. **(c)** HeLa-FlpIn TREX cells expressing the indicated transgene were left untreated or treated with doxycycline (1µg/ml) and at the same time infected with SFV-gLuc (MOI: 0.2). The graph shows mean luciferase activity ±s.d. of four independent samples 36h after infection. One representative experiment of three independent biological repeats is shown. *p*-values: Two way ANOVA with Tukey's multiple comparisons test. * $p < 0.0001$, ns: not significant. **(d)** HeLa FlpIn TREX ANXA2R or Ctrl (IFIT3) cells were treated with doxycycline or not and cell viability was tested by resazurin reduction assay after the indicated time point. 12 individual samples per condition and timepoint were measured. One representative experiment of three independent biological repeats is shown. *p*-values: Two way ANOVA with Tukey's multiple comparisons test. * $p < 0.0001$ between Mock and +Dox condition, ns: not significant. **(e, f)** As (c) but VSV-Luc (MOI: 1) was used for infection. **(e)** Mean luciferase activity ±s.d. of quadruplicate measurements 6h after infection. **(f)** Cell viability as measured by resazurine conversion assay 6h after infection. *p*-values: as (c), four independent samples of one representative experiment of three independent biological repeats is shown. (**g**) Confocal microscopy images of ANXAR2 and IFIT3 in HeLa FlpIn TREX cells. Doxycycline-treated ANXAR2 or control (IFIT3)-expressing HeLa-FlpIn TREX cells were fixed 24h after induction and immunostained for CNOT1 and HA-tagged proteins. Scale bars, 10 µm. n = 2 independent experiments. **(h-j)** Proteomic analysis of cells depleted for CNOT1 or overexpressing ANXA2R. **(h)** HeLa-FlpIn TREX cells were treated with siRNAs against CNOT1 or control (siScr) and the total proteome was analyzed by LC-MS/MS 48h later. Volcano plot shows all identified proteins. In blue: significantly up or downregulated proteins (student's t-test, FDR ≤ 0.05, S0 = 0.05, n = four independent measurements). Proteins that are also significantly regulated in the same direction upon ANXA2R induction are highlighted in red, yellow or green. **(i, j)** HeLa-FlpIn TREX ANXA2R or control (IFIT3) cells were left unstimulated or stimulated with doxycycline and total proteome was analysed by LC-MS/MS 12h, 18h and 24h later. **(i)** Volcano plot showing proteome changes in doxycycline treated vs untreated HeLa-FlpIn TREX ANXA2R cells 24 hours post induction. Significantly changing (both in comparison to the no Dox control and to IFIT3 induction) proteins are highlighted in red (general linear model hypothesis test, Benjamini-Yekutieli adjusted *p*-value ≤ 0.001), and proteins significantly changing in (h) are further highlighted in blue. **(j)** Density plots showing changes of protein abundance distribution upon ANXA2R or control (IFIT3) induction. Proteins were grouped according to their change in CNOT1-depleted conditions shown in (h): unchanged upon CNOT1 depletion: grey, downregulated: blue, upregulated: pink. Numbers on top of each panel show *p*-values of two-sided K-S test for similarities between proteins co-regulated in CNOT1-depleted and ANXA2R- or control- (IFIT3) expressing conditions. ns: not significant.

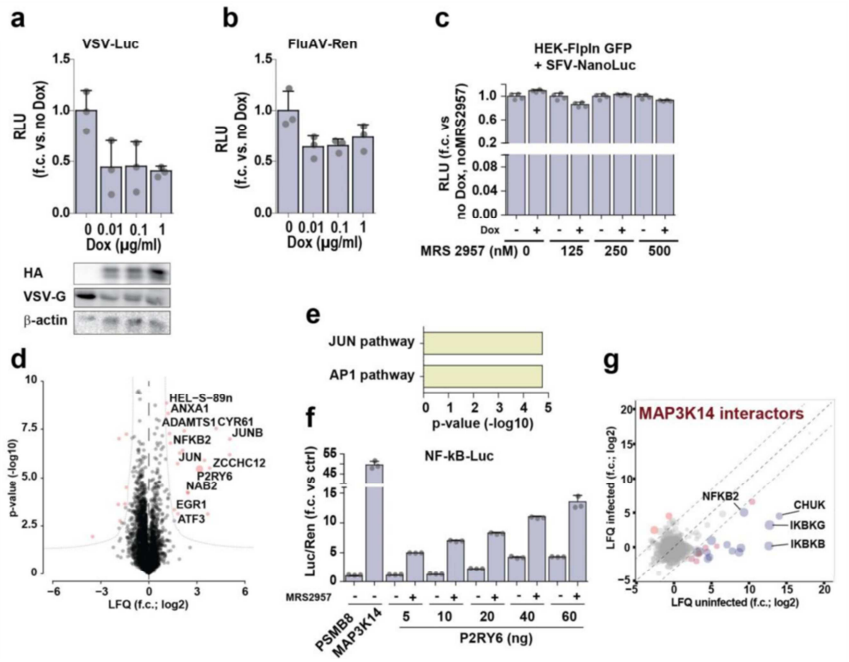

Supplementary Figure 6

Activity of P2RY6.

(a, b) HEK-FlpIn TREX P2RY6 cells were stimulated with the indicated concentration of doxycycline (Dox) and infected with the indicated viruses. Bar plots show mean luciferase expression ±s.d. of doxycycline treated cells infected with VSV (MOI = 0.01) for 20h (a) and FluAV (MOI = 0.05) for 24h (b). Values were normalised to the non-doxycycline treated condition. Lysates in (a) were used for immunoblotting against HA-P2RY6, VSV-G and β-tubulin. Graphs show mean ±s.d. of three technical replicates, one representative experiment of three independent biological repeats is shown. **(c)** HEK-FlpIn TREX GFP cells were treated or not with doxycycline (Dox) for 20h and an additional 8h with the P2RY6 ligand MRS2957, as indicated. Cells were infected with SFV-NanoLuc (MOI: 0.01) for 24h and luciferase activity was measured. Histogram shows mean relative luciferase activity of quadruplicate measurements ±s.d. normalized to the uninduced control. **(d, e)** Proteome analysis of HEK-FlipIn TREX cells after doxycycline (Dox; 1µg/ml) induced P2RY6 expression for 24h. **(d)** Volcano plot shows average protein expression in doxycycline induced compared to uninduced HEK-FlipIn TREX cells (x-axis) and the transformed *p*-value for each protein (y-axis; two tailed *t*-test). Red dots: significant enriched proteins, curved dotted line separates significant enriched proteins from background population (black dots) (two-tailed *t*-test permutation based FDR < 0.01, S0 = 0.5, n = 6 independent measurements). *p*-values: One-way ANOVA with Dunnett's multiple comparisons test. One representative experiment of three is shown. **(e)** Functional enrichment annotation analysis of significantly changed proteins compared to protein background population (Fisher's exact test, Benjamini-Hochberg FDR < 0.05, enrichment factor > 2). Pathways derived from Panther database (http://www.pantherdb.org): AP1 pathway = Inflammation mediated by chemokine and cytokine signaling pathway → activator protein-1; JUN pathway = Gonadotropin-releasing hormone receptor pathway → JUN). **(f)** HEK 293 cells were co-transfected with a NF-KB-firefly luciferase reporter construct, an EIF1a-renilla control and increasing amounts of P2RY6 for 20h. GFP plasmid was used to adjust amounts of DNA for transfection. Cells were either treated or not with the P2RY6 specific ligand (MRS 2957, 250 nM) for additional 8h. Graph shows relative mean luciferase/renilla values ±s.d. of three replicates in relation to GFP control transfection. One representative experiment of three independent biological repeats is shown. **(g)** Control HEK-FlpIn TREX cells and HEK-FlpIn TREX MAP3K14 cells were infected with RVFV (Clone 13) for 18h, MOI 0.1 or not infected and used for AE-LC-MS/MS experiments. Analysis was performed as described in Fig. 6d and material and methods.

Habjan M*, **Hubel P***, Lacerda L, Benda C, Holze C, Eberl CH, Mann A, Kindler E, Gil-Cruz C, Ziebuhr J, Thiel V, Pichlmair A. PLoS Pathog. 2013;9(10):e1003663. doi: 10.1371/journal.ppat.1003663. Epub 2013 Oct 3. PMID: 24098121, *contributed equally

2.2 PUBLICATION 2: SEQUESTRATION BY IFIT1 IMPAIRS TRANSLATION OF 2' O-UNMETHYLATED CAPPED RNA

A key step in cellular antiviral defense response is the recognition of foreign pathogen-derived structures. From central importance are cellular factors which distinguish foreign- from their own molecular-structures. IFIT proteins were shown to form a tight complex which binds to 5′triphosporylated-RNA (PPP-RNA) and inhibits virus replication subsequently.

In this project I collaborated with Dr. Matthias Habjan, a post-doc in our lab at this time, who identified IFIT proteins (consisting of IFIT1, 2 and 3) as specific 2' O-unmethylated capped RNA binders by AE-LC-MS/MS experiments. In validation experiments we could show that the IFIT1 protein binds directly to such cap-RNAs with high affinity.

I studied the consequences of this interaction on the proteome of the cell. Therefore, I established a SILAC pulse label workflow capable to depict transcription and translation rates of both, virus and cellular derived proteins during infection of a murine coronavirus (MCV) model. We used a wild type strain and a mutated clone that lacks the ability to methylate its virus derived RNA at 2' O position of the RNA-cap structure. In combination with RNA based experiments, the observed results clearly showed that IFIT1 potently inhibits transcription and subsequent translation of viral 2' O-unmethylated capped RNA without altering cellular protein expression. This strategy allows the cell to efficiently block replication of viruses by maintaining normal proteome homeostasis in the cell at the same time.

OPEN ACCESS Freely available online

PLOS | PATHOGENS

Sequestration by IFIT1 Impairs Translation of 2′O-unmethylated Capped RNA

Matthias Habjan[1☯], Philipp Hubel[1☯], Livia Lacerda[1], Christian Benda[2], Cathleen Holze[1], Christian H. Eberl[3], Angelika Mann[1], Eveline Kindler[4], Cristina Gil-Cruz[4], John Ziebuhr[5], Volker Thiel[4,6], Andreas Pichlmair[1]*

1 Innate Immunity Laboratory, Max-Planck Institute of Biochemistry, Martinsried/Munich, Germany, **2** Department of Structural Cell Biology, Max-Planck Institute of Biochemistry, Martinsried/Munich, Germany, **3** Department of Proteomics and Signal Transduction, Max-Planck Institute of Biochemistry, Martinsried/Munich, Germany, **4** Institute of Immunobiology, Kantonspital St. Gallen, St. Gallen, Switzerland, **5** Institute of Medical Virology, Justus Liebig University, Giessen, Germany, **6** Vetsuisse Faculty, University of Zürich, Zürich, Switzerland

Abstract

Viruses that generate capped RNA lacking 2′O methylation on the first ribose are severely affected by the antiviral activity of Type I interferons. We used proteome-wide affinity purification coupled to mass spectrometry to identify human and mouse proteins specifically binding to capped RNA with different methylation states. This analysis, complemented with functional validation experiments, revealed that IFIT1 is the sole interferon-induced protein displaying higher affinity for unmethylated than for methylated capped RNA. IFIT1 tethers a species-specific protein complex consisting of other IFITs to RNA. Pulsed stable isotope labelling with amino acids in cell culture coupled to mass spectrometry as well as *in vitro* competition assays indicate that IFIT1 sequesters 2′O-unmethylated capped RNA and thereby impairs binding of eukaryotic translation initiation factors to 2′O-unmethylated RNA template, which results in inhibition of translation. The specificity of IFIT1 for 2′O-unmethylated RNA serves as potent antiviral mechanism against viruses lacking 2′O-methyltransferase activity and at the same time allows unperturbed progression of the antiviral program in infected cells.

Citation: Habjan M, Hubel P, Lacerda L, Benda C, Holze C, et al. (2013) Sequestration by IFIT1 Impairs Translation of 2′O-unmethylated Capped RNA. PLoS Pathog 9(10): e1003663. doi:10.1371/journal.ppat.1003663

Editor: Michael S. Diamond, Washington University School of Medicine, United States of America

Received April 4, 2013; **Accepted** August 12, 2013; **Published** October 3, 2013

Copyright: © 2013 Habjan et al. This is an open-access article distributed under the terms of the Creative Commons Attribution License, which permits unrestricted use, distribution, and reproduction in any medium, provided the original author and source are credited.

Funding: This work was supported by the Max Planck Society Free-Floater program to AP, the European Research Council (iViP)to AP, the Humboldt Research Fellowship to MH, and the German Research Society (DFG; SFB1022) to JZ. The funders had no role in study design, data collection and analysis, decision to publish, or preparation of the manuscript.

Competing Interests: The authors have declared that no competing interests exist.

* E-mail: apichl@biochem.mpg.de

☯ These authors contributed equally to this work.

Introduction

Effective control of viral infection by host organisms requires sensing of pathogens and activation of appropriate defence mechanisms [1–3]. One component commonly sensed by the host is viral genetic material, whether DNA delivered to the cytoplasm through viral infection or viral RNA bearing motifs not commonly found on eukaryotic RNAs [4,5]. Most cellular cytoplasmic RNAs are single-stranded, and bear a 5′monophosphate (rRNAs and tRNAs), or an N7 methylated guanosine cap (mRNAs) linked via a 5′-to-5′ triphosphate bridge to the first base. In higher eukaryotes, mRNA is further methylated at the 2′O position of the first ribose [6,7]. Viruses, in contrast, can form long double-stranded RNA (dsRNA) and generate RNAs bearing 5′triphosphosphates (PPP-RNA) or RNAs lacking methylation [8–10]. All these distinct features of viral as opposed to cellular RNAs have been shown to activate the innate immune system and elicit synthesis of antiviral cytokines including Type I interferons (IFN-α/β), which ultimately restrict virus growth [11–14]. Among the proteins that sense viral RNA and are linked to IFN-α/β synthesis are retinoic acid-inducible gene I (RIG-I) and melanoma differentiation-associated gene 5 (Mda-5), which form the family of RIG-like receptors (RLRs) [5]. A further set of host proteins appears to bind virus-derived RNAs to directly inhibit virus production [8]. Several of these proteins are highly expressed upon stimulation of cells with cytokines like IFN-α/β and their antiviral effects become apparent only after binding to virus-derived nucleic acid. Prominent examples for such proteins are dsRNA binding proteins such as dsRNA-activated protein kinase R and 2′-5′ oligoadenylate synthetase, and proteins that bind PPP-RNA, like interferon-induced proteins with tetratricopeptide repeats (IFIT) 1 and -5 [3,15,16]. Little is known about the repertoire of cellular proteins that recognise unmethylated cap structures, although replication of viruses with inactive RNA 2′O methyltransferase is strongly inhibited by IFN-α/β *in vitro* and *in vivo* [11,15]. Some of this antiviral activity has been genetically linked to Ifit1 and -2 in mice [17–19]. Here, we used an unbiased mass-spectrometry-based approach to identify cellular proteins that bind to 5′ unmethylated and methylated capped RNA, and explored their contribution to antiviral host responses.

Results

Identification of human and mouse proteins that bind capped RNA

To identify proteins that interact with 5′ capped RNA we used a proteomics approach based on affinity purification and mass

Author Summary

Cellular messenger RNAs of higher eukaryotes are capped with a methylated guanine and, in addition, methylated at the 2′O position of the first ribose. Viruses unable to methylate their RNA at the 2′O position of the cap and viruses generating uncapped RNA with 5′ triphosphate groups are inhibited by an antiviral complex of different IFIT proteins. How IFIT proteins restrict viruses lacking 2′O methylation at the RNA cap remained unclear. We used a mass spectrometry-based approach to identify proteins binding to capped RNA with different methylation states. We found that IFIT1 directly binds to capped RNA and that this binding was dependent on the methylation state of the cap. Having identified IFIT1 as being central for recognition of 2′O-unmethylated viral RNA we further examined the mode of action of IFITs *in vitro* and *in vivo*. Our experiments clearly show that the antiviral mechanism of IFIT1 is based on sequestration of viral RNA lacking cap 2′O methylation, thereby selectively preventing translation of viral RNA. Our data establish IFIT1 as a general sensor for RNA 5′ end structures and provide an important missing link in our understanding of the antiviral activity of IFIT proteins.

spectrometry (AP-MS) [16]. RNA bearing terminal 5′ hydroxyl (OH-RNA), 5′ triphosphate (PPP-RNA), an unmethylated cap (CAP-RNA), a guanosine-N7 methylated cap (CAP0-RNA), or a guanosine-N7 methylated cap and a ribose-2′O methylated first nucleotide (CAP1-RNA) was coupled to agarose beads. The beads were then incubated with lysates of naïve HeLa cells or HeLa cells treated with IFN-α to increase the abundance of antiviral proteins (Fig. 1a, Fig. S1). By employing liquid-chromatography coupled to tandem mass spectrometry (LC-MS/MS) followed by quantitative interaction proteomics analysis, we identified 528 proteins that interacted with unmodified or RNA-coated beads (Fig. S2a, Table S1). While a large number of proteins were equally well represented in the bound fractions obtained with all RNAs (Fig. S2a), 68 proteins were found to be significantly enriched in samples recovered with 5′modified RNA compared to OH-RNA (Fig. S2b). As expected, the PPP-RNA binding proteins RIG-I (DDX-58), the IFIT1, -2, -3 complex and IFIT5 were enriched in PPP-RNA affinity purifications of IFN-α-treated HeLa cell lysate (Fig. 1b), validating the approach and confirming previous data [16]. Using unmethylated CAP-RNA as bait, we significantly enriched for proteins known to associate with cellular capped RNA (12 of 16 proteins) (Fig. 1c, Fig. S2b, Table S1). However, an important feature of cellular mRNAs is methylation on the N7 position of the guanosine cap and the ribose-2′O position of the first nucleotide (CAP1). N7 methylation is known to increase the affinity of the cap structure for proteins such as EIF4E and other cap-binding proteins [6,7]. A methylation-dependent increase in protein binding was also evident in our AP-MS analysis when unmethylated CAP-RNA and methylated CAP1-RNA were used as baits (16 vs. 27 identified proteins), as the latter captured a higher number of significantly enriched proteins and, overall, these were enriched to a greater degree, as measured by label-free quantification (Fig. 1c–d, Table S1). Notably, we identified IFIT1, -2 and -3 among the uncharacterised CAP-RNA binding proteins, suggesting that the IFIT complex binds to RNA in a cap-dependent manner (Fig. 1c). IFIT5, which shows 57.2% aminoacid sequence identity and 75.6% similarity to IFIT1 and has recently been shown to form a tight binding pocket that specifically accommodates PPP-RNA [20], was not detected in fractions that bound capped RNA. When we compared our AP-MS dataset with transcriptome data of interferon-stimulated cells [21], IFITs were the only interferon-induced proteins found to be specifically enriched in CAP-RNA purifications, suggesting a predominant role of IFITs in innate immune responses directed against CAP-RNA (Fig. 1c, Fig. S2b). To analyse whether the set of proteins that binds to 5′modified RNA is conserved in other species, we performed the same AP-MS analysis on lysates of naïve and IFN-α-treated mouse embryonic fibroblasts (MEFs) (Fig. S3a, b, Table S2). Surprisingly, although PPP-RNA specifically enriched for Ifit1, the abundance of Ifit2 and Ifit3 was not increased (Fig. 1e). Instead we found enrichment of Ifit1c (also known as Gm14446), an uncharacterised IFIT protein that is strongly induced by IFN-α/β or virus infection (Fig. S4), suggesting that the architecture of the murine IFIT complex differs from that of its human counterpart. Significant enrichment for Ifit1 and Ifit1c could also be achieved with unmethylated CAP-RNA, but not with methylated CAP1-RNA, despite the fact that the latter bait captured more proteins with higher enrichment scores (Fig. 1f, g). We concluded from these analyses that, in both human and mouse, the IFIT complex is the only IFN-induced component that shows significant affinity for capped RNA.

IFIT1 is the only IFIT that binds capped RNA

Since human IFIT1, -2 and -3 associate with each other to form a multiprotein complex, we wished to determine which of them was responsible for tethering the IFIT complex to unmethylated CAP-RNA. We overexpressed each of the IFIT proteins, tagged with *Renilla* luciferase, in 293T cells and performed affinity purifications using OH-RNA, PPP-RNA and CAP-RNA. Remarkably, only human and murine IFIT1 were detected when CAP-RNA was used as bait (Fig. 2a, b), suggesting that IFIT1 mediates binding of the IFIT complex to CAP-RNA. Consistent with the MS analysis, IFIT5 exclusively bound to PPP-RNA but not to CAP-RNA. To exclude contribution of cellular factors to the interaction between IFIT1 and CAP-RNA we used recombinant human IFIT proteins for RNA precipitations which confirmed a direct interaction of IFIT1 with capped RNA (Fig. 2c). A structure-based modelling approach using IFIT5 [20] as template suggested that the RNA-binding cavity of IFIT1 is ~700 $Å^3$ larger than that of IFIT5 (Fig. S5) – implying that IFIT1 has slightly different RNA-binding properties. However, a lysine at position 151 and an arginine at position 255 of IFIT1, two residues involved in binding the terminal 5′ triphosphate group on PPP-RNA by IFIT5 and IFIT1 [20], were also required for binding of IFIT1 to capped RNA (Fig. 2d), indicating an overall similar mode of binding.

To provide additional evidence that binding of IFIT1 is indeed responsible for associating the IFIT complex to CAP-RNA, we performed AP-MS experiments on wild-type ($Ifit1^{+/+}$) and mutant, Ifit1-deficient ($Ifit1^{-/-}$) MEFs. The overall precipitation efficiency was comparable in both cell types, as evidenced by equal enrichment of the RNA-binding protein Syncrip and the cap-binding protein Ncbp1 (Fig. 2e and Fig. S4b). Ifit1c was not enriched in precipitates from $Ifit1^{-/-}$ MEFs, which is consistent with the notion that the murine Ifit complex binds to CAP-RNA through Ifit1. These results show that the specific binding properties of IFIT1 are essential for recruitment of the human and murine IFIT complexes to their RNA targets.

IFIT1 binding depends on the methylation status of the RNA cap

To identify proteins that bind capped RNA in a methylation-dependent manner we used unmethylated CAP-RNA and fully

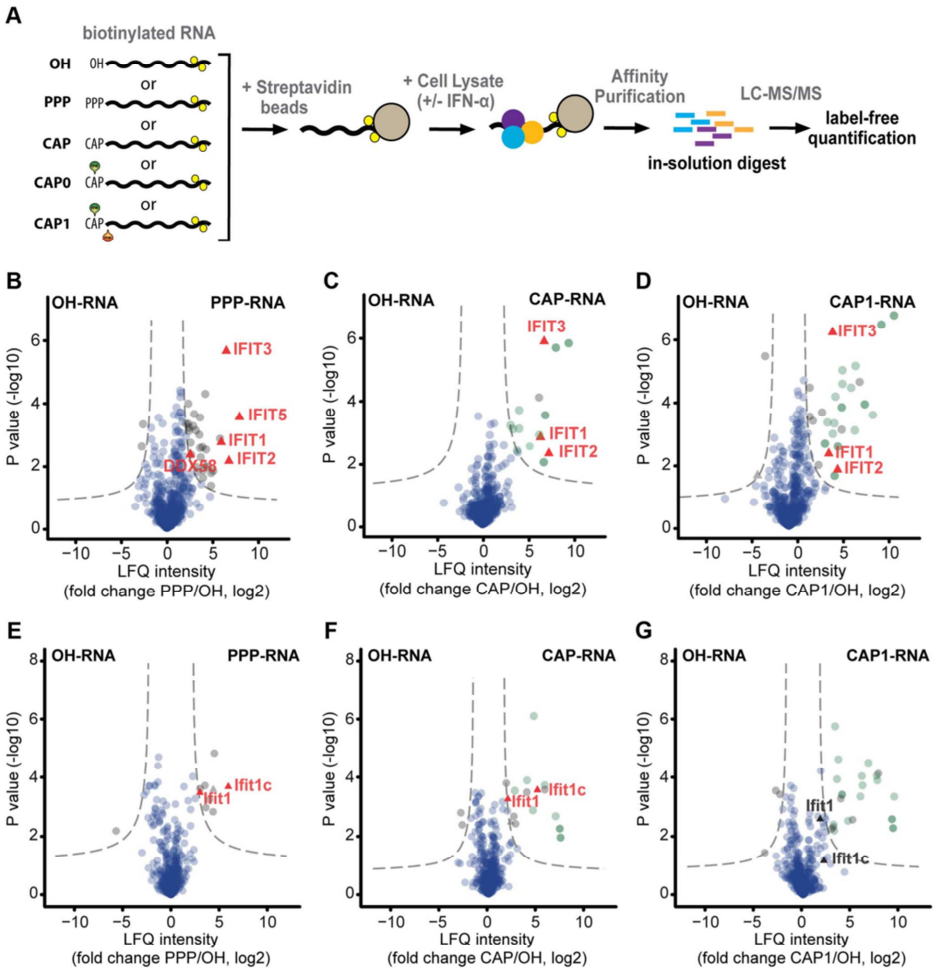

Figure 1. Mass spectrometry-based identification of human and murine interactors of capped RNA. (**a**) Schematic depiction of the experimental approach used for mass spectrometry (MS)-based identification of cellular RNA binding proteins. Biotinylated RNA with different 5′ end structures (OH, PPP, CAP, CAP0, CAP1) was coupled to streptavidin beads, and incubated with lysates obtained from cells that had been left untreated or treated with 1000 U/ml IFN-α for 16 h. Bound proteins were denatured, alkylated and directly digested with trypsin. The resulting peptides were subjected to shotgun liquid chromatography-tandem MS (LC-MS/MS). Three independent experiments were performed for each RNA bait, and the data were analysed with the MaxQuant software [37] using the label-free quantification algorithm [38]. (**b–d**) Proteins obtained from lysates of IFN-α-treated HeLa cells using the indicated biotinylated RNA baits were analysed by LC-MS/MS. Volcano plots show the degrees of enrichment (ratio of label-free quantitation (LFQ) protein intensities; x-axis) and p-values (t-test; y-axis) by PPP-RNA (**b**), CAP-RNA (**c**), and CAP1-RNA (**d**) baits as compared to OH-RNA. Significantly enriched interactors (see Materials and Methods) are separated by a hyperbolic curve (dotted line) from background proteins (blue dots), known cap-binding proteins (dark-green), and proteins known to associate with capped RNA (light green). Interferon-induced proteins [21] detected in the significantly enriched fractions (IFIT1-3 and 5, DDX58) are highlighted (red triangles). (**e–g**) As in (**b–d**) but for lysates of IFN-α-treated mouse embryo fibroblasts (MEFs). The interferon-induced proteins Ifit1 and Ifit1c [42] in significantly enriched and non-enriched fractions are highlighted.
doi:10.1371/journal.ppat.1003663.g001

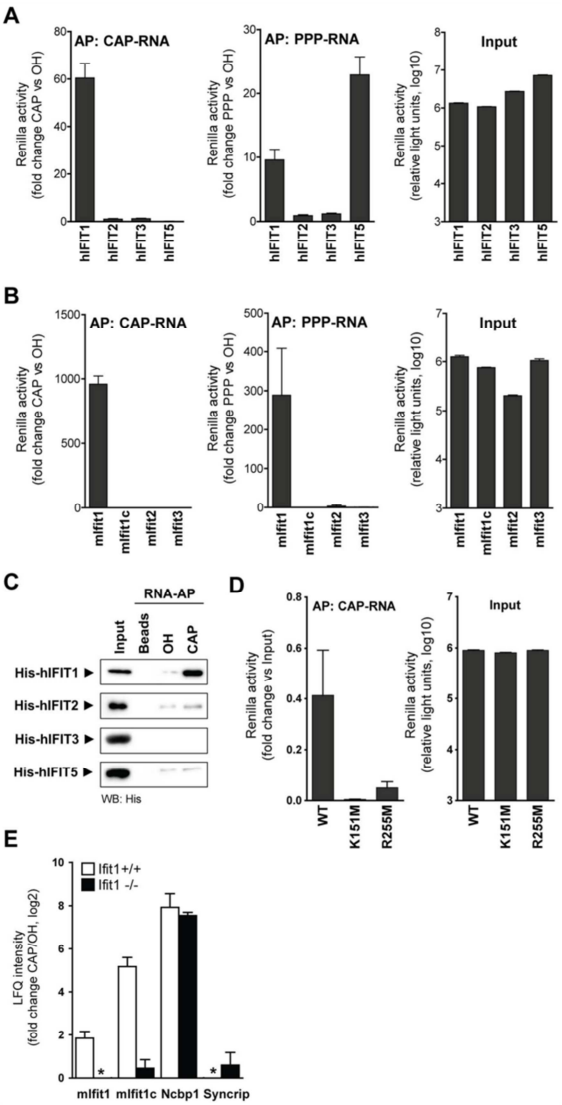

Figure 2. Human and mouse IFIT1 bind directly to unmethylated capped RNA. (**a**) Isolation of luciferase-tagged human IFIT (hIFIT) proteins from transfected 293T cells with beads coated with 250 ng RNA bearing 5′ OH, PPP or CAP. The graphs show luciferase activity after affinity purification (AP) with PPP-RNA and CAP-RNA (normalized to OH-RNA) and the activity of 10% of the input lysates. (**b**) Data obtained (as in **a**) for luciferase-tagged murine Ifit (mIfit) proteins affinity purified with PPP-RNA and CAP-RNA. (**c**) Recombinant His-tagged hIFIT1, -2, -3, and -5 were incubated with beads only or beads coated with OH-RNA or CAP-RNA. Bound proteins were detected by western blotting. Input shows 1/10th of the amount incubated with beads. (**d**) Purification of luciferase-tagged wild-type (WT) and hIFIT1 mutants with CAP-RNA-coated beads. The graphs show luciferase activity after affinity purification and the activity of 10% of the input lysates. (**e**) Ratios of LFQ intensities of proteins identified by mass spectrometry in precipitates of CAP-RNA vs. OH-RNA in IFN-α-treated MEFs from wild-type (Ifit1$^{+/+}$, grey bars) and Ifit1-deficient (Ifit1$^{-/-}$, black bars) C57BL/6 mice. Error bars indicate means (±SD) from three independent affinity purifications. Asterisks indicate ratios with negative values.
doi:10.1371/journal.ppat.1003663.g002

methylated CAP1-RNA as baits with IFN-treated HeLa cell lysates and quantified the captured proteins by LC-MS/MS. As expected [6,7], most cellular proteins were significantly enriched in the CAP1-RNA bound fraction (Fig. 3a, Fig. S2c). The most notable exceptions were IFITs and the cellular 2′O-methyltransferase FTSJD2, both of which clearly favoured CAP-RNA (Fig. 3a, Fig. S2c and Fig. 1 c, d and f, g). We confirmed the MS data by a series of RNA precipitations followed by western blotting for endogenous proteins. Proteins associating to RNA in a 5′ independent manner, such as ILF3, precipitated similarly well regardless of the RNA used (Fig. 3b). Cap N7 methylation increased the association of EIF4E to RNA and methylation of the 2′O position did not impair precipitation efficiency. In accordance with the MS results, IFIT1 bound well to unmethylated CAP-RNA and CAP0-RNA (N7 methylated cap) but revealed reduced binding to CAP1-RNA (N7 methylated cap and 2′O methylated first ribos).

We next tested the contributions of individual cap methylation sites to IFIT1 binding. To this end, we measured binding of luciferase-tagged human and murine IFIT1 with either CAP-, CAP0- or CAP1-RNA. The unmethylated CAP-RNA bait captured more human or murine IFIT1 than either of the methylated RNAs (Fig. 3c). Furthermore, the analysis suggested that N7 methylation on the cap and 2′O methylation of the first ribose both contributed to the reduced binding of IFIT1 to RNA. Similarly, the precipitation efficiency of recombinant human and murine IFIT1 was reduced when capped *in vitro* transcribed RNAs were enzymatically methylated at the N7 and 2′O position (Fig. 3d) or when chemically synthesised RNAs with the same modifications were used (Fig. 3e). This was in contrast to EIF4E that showed prominent binding when CAP0- or CAP1-RNA was used (Fig. 3d, e). Collectively, these data suggest that human and murine IFIT1 have the capability to directly sense the methylation state of capped RNA.

Antiviral activity of IFIT1 against 2′O methyltransferase-deficient viruses

Having established that IFIT1 binds directly to capped RNA and that methylation on the 2′O position of the first ribose markedly reduces binding, we tested the impact of IFIT1 on virus replication. Probably as a result of evolutionary pressure, most viruses that infect higher eukaryotes have evolved mechanisms to generate RNA that is methylated on both the N7 position of the guanosine cap and the 2′O position of the first ribose [9]. We therefore used wild-type human coronavirus (HCoV) 229E (229E-WT), which generates CAP1-RNA, and a mutant variant that has a single amino acid substitution (D129A) in the viral 2′O methyltransferase that is part of non-structural protein 16 (229E-DA), and consequently only produces CAP0-RNA [11]. IFN-α-treated HeLa cells infected with the 229E-DA mutant expressed significantly reduced levels of viral RNA and protein relative to those exposed to 229E-WT (Fig. 4a, b). Moreover, this effect was strictly dependent on IFIT1, since the two viruses replicated equally well in HeLa cells treated with siRNA against IFIT1 (Fig. 4a, b). Similar effects were observed in an analogous mouse model. Thus, when IFN-α treated macrophages (MΦs) from C57BL/6 (Ifit $^{+/+}$) mice were infected with a wild-type murine coronavirus (mouse hepatitis virus strain A59; MHV-WT) and a mutant strain carrying the equivalent amino acid substitution (D130A) in its 2′O methyltransferase [11,17] (MHV-DA), the latter produced 100-fold less viral RNA and comparably reduced levels of viral protein (Fig. 4c, d). In contrast, when Ifit1-deficient MΦs were infected, no significant virus-dependent differences were observed, again pointing to a critical role for Ifit1 in restricting replication of MHV-DA. Note that the presence of Ifit1 itself did not increase IFN-α/β production (Fig. S6), suggesting a direct antiviral effect of Ifit1. We next assessed the impact of Ifit1 on virus growth *in vivo*. MHV-WT grew to high titres in the spleens of infected Ifit1$^{+/+}$ mice, whereas no viral replication could be detected upon infection with MHV-DA (Fig. 4e). In agreement with the *in vitro* data, growth of MHV-DA was partially restored in Ifit1-deficient animals. These data suggest that IFIT1 has a central role in restraining the growth of 2′O methyltransferase-deficient coronaviruses *in vitro* and *in vivo*, which is compatible with the greater affinity of IFIT1 for non-2′O-methylated RNA cap structures. The data further imply that this role is conserved in mouse and human.

IFIT1 specifically regulates the translation of 2′O unmethylated capped viral RNA

RNA capping is essential for a variety of cellular functions. The presence of a 5′ cap regulates mRNA export from the nucleus, protects RNAs from degradation and is necessary for efficient translation [7,22]. An involvement of IFIT1 in nuclear-cytoplasmic transport is unlikely, given the exclusively cytoplasmic localisation of IFIT proteins and their negative effect on coronaviruses, which replicate in the cytoplasm. We therefore measured the stability of the RNAs generated by MHV-WT or MHV-DA in MΦs that had been stimulated with IFN-α. Since MHV-WT replicates significantly better than the mutant virus, we blocked virus replication by adding cycloheximide (CHX) shortly after infecting MΦs with the two viruses (Fig. 5a). CHX inhibits de novo synthesis of the viral polymerase, a prerequisite for transcription of viral RNA and thereby allows to normalise for viral transcripts in coronavirus infected cells. The abundance of viral transcripts 4 h and 8 h after infection was indistinguishable in CHX treated cells infected with MHV-WT and MHV-DA (Fig. 5b), suggesting that 2′O methylation of the first ribose does not affect the stability of the viral RNA within the timeframe of this experiment.

Many cellular antiviral defence mechanisms generally block translation of mRNA, thereby also severely inhibiting virus growth. To assess the global impact of Ifit1 on the translation machinery, we used pulsed stable isotope labelling in cell culture (SILAC) [23]. In pulsed SILAC, unlabelled cells are transferred to SILAC growth medium containing ^{13}C- and ^{15}N-labelled arginine (Arg10) and lysine (Lys8). Newly synthesized proteins incorporate the heavy label and pre-existing proteins remain in the light form, which allows to measure relative changes in the translation of individual proteins, regardless of the absolute amount of RNA present. We pulsed Ifit1$^{+/+}$ and Ifit1$^{-/-}$ MΦs infected for 5½ h with either MHV-WT or MHV-DA for 2 h with SILAC medium (Fig. 5c) and analysed infected cells by whole-proteome shotgun LC-MS/MS. We could reliably quantify 721 proteins in terms of heavy/light ratios in all three biological replicates tested. Heavy/light ratios of cellular proteins were comparable in Ifit1$^{+/+}$ and Ifit1$^{-/-}$ MΦs, irrespective of the virus used for infection (Fig. 5d, boxes), suggesting that neither the presence of Ifit1 nor infection with MHV-DA affected the overall rate of translation in the cells. The expression profiles of individual proteins known to be important in innate immune responses against viruses, such as the pattern recognition receptor RIG-I (DDX58), signalling molecules (STAT1, -2, -3), interferon-induced proteins (Ifi205b, Ifi35, Gvin1) and components of the major histocompatibility complex (H2-K1, H2-D1, Cd74), were similar in both cell types infected with either virus (Fig. S7). However, translation of viral nucleocapsid and membrane proteins was selectively reduced in Ifit1$^{+/+}$ MΦs infected with MHV-DA (Fig. 5d and Fig. S7).

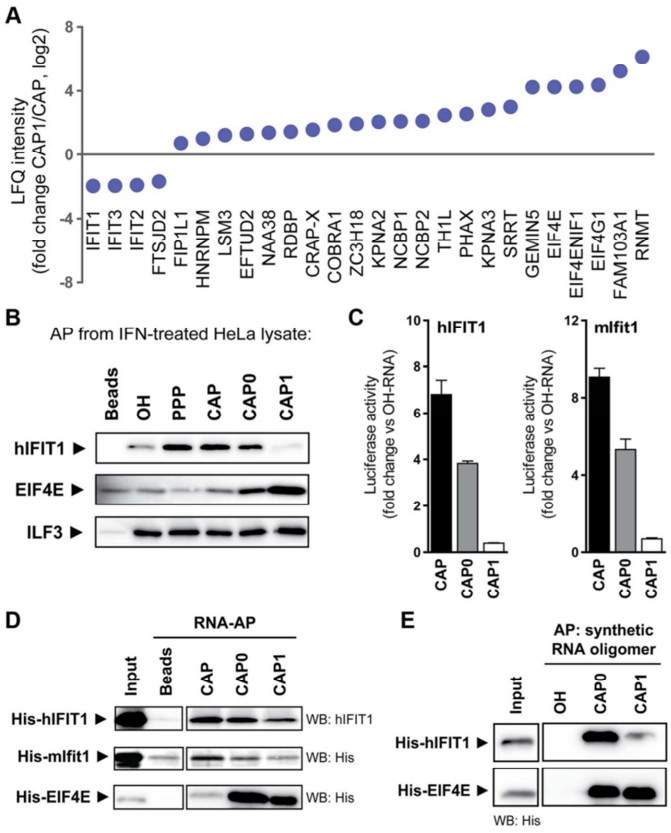

Figure 3. IFIT1 binds capped RNA in a methylation state-dependent manner. (**a**) Ratio of LFQ intensities of proteins identified by LC-MS/MS as significantly enriched in CAP1-RNA relative to CAP-RNA affinity purifications from IFN-treated HeLa cells, after filtering against the set of proteins that showed enrichment relative to 5′ OH-RNA(see Fig. S2b). Error bars indicate means (±SD) from three independent affinity purifications. (**b**) Precipitation of endogenous proteins from lysates of IFN-α treated HeLa cells with biotinylated RNA bearing 5′ OH, PPP, CAP, CAP0 or CAP1 structures. Human IFIT1 (hIFIT1), EIF4E and ILF3 in precipitates were detected by western blotting. Input shows 1/10th (mIFIT1, EIF4E) and 1/30th (hIFIT1) of the amount incubated with beads. (**c**) Affinity purification of luciferase-tagged human (hIFIT1) and murine (mIfit1) IFIT1 expressed in 293T cells on beads bearing 5′ OH, CAP, CAP0, or CAP1 RNA. (**d**) Binding of recombinant IFIT1 to capped RNAs. As in (**c**), but RNA-coated beads were incubated with recombinant His-tagged mouse Ifit1 (His-mIfit1), human His-hIFIT1 or human His-EIF4E and bound protein was quantified by western blotting. (**e**) Binding of recombinant His-tagged hIFIT1 and EIF4E to chemically synthesized, biotinylated RNA oligomers. Synthetic triphosphorylated RNAs with (CAP1) or without (CAP0) 2′O-methyl group on the first ribose were capped in vitro using recombinant vaccinia virus capping enzyme (see Materials and Methods). As control we used a synthetic RNA harbouring a 5′ hydroxyl group (OH). Synthetic RNAs were coupled to beads, incubated with recombinant proteins and bound proteins detected by western blotting. Input shows 1/10th of the amount incubated with beads.
doi:10.1371/journal.ppat.1003663.g003

Variation in large datasets can be best evaluated by principal-component analysis, which computes the variable with the greatest effect in a given dataset. This analysis revealed that Ifit1$^{+/+}$ MΦs infected with MHV-DA showed the highest variation (Component 1 accounting for 55.9% of variation) as compared to all other conditions tested (Fig. 5e), and among all identified proteins, MHV proteins were mainly responsible for this variation (Fig. 5f). Taken together, these data indicate that synthesis of proteins encoded by viral RNAs lacking 2′O methylation on the first ribose is specifically inhibited by IFIT1. Expression of proteins encoded by fully methylated RNA, such as cellular mRNA or 2′O methylated viral RNA, is not affected by the activity of IFIT1.

IFIT1 and translation factors compete for mRNA templates

Translation of cellular capped mRNA requires binding of the cap-binding protein EIF4E, which has a high affinity for

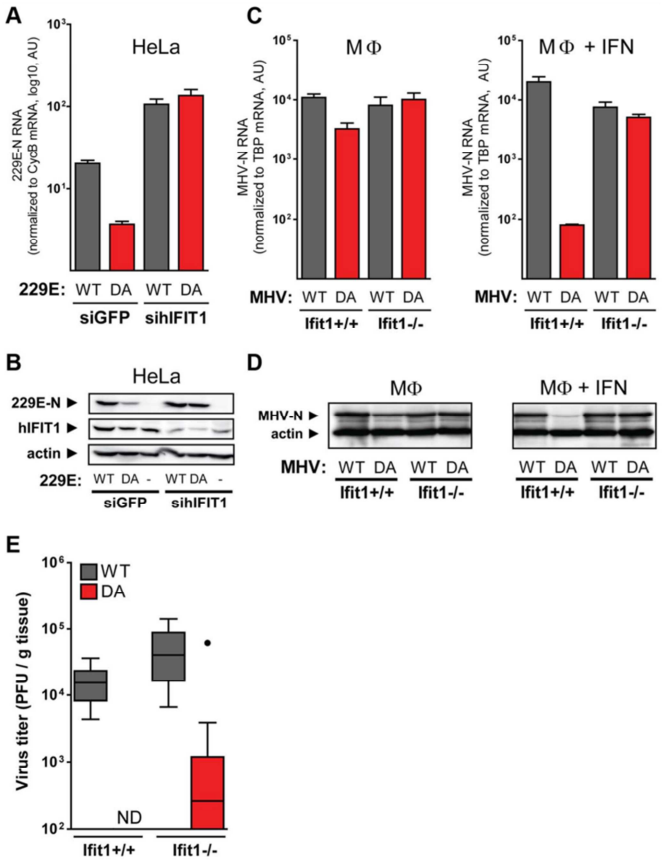

Figure 4. IFIT1 inhibits viral RNA and protein synthesis in cells infected with 2′O methyltransferase-deficient coronavirus. (**a–b**) HeLa cells were cotransfected for 48 h with an expression construct for the HCoV-229E receptor, human aminopeptidase N, and siRNAs targeting IFIT1 or the green fluorescent protein (GFP). Cells were then treated with 20 U IFN-α and infected with wild-type HCoV-229E (229E-WT; grey bars) or the 2′O methyltransferase-deficient HCoV-229E (D129A) mutant (229E-DA; red bars). Total RNA and protein were harvested 24 h post infection and analysed by quantitative RT-PCR (**a**) and western blotting (**b**), respectively. Quantitative RT-PCR data are from one of three representative experiments showing means ±SD for HCoV-229E nucleoprotein (229E-N) RNA after normalization to cyclin B (CycB) mRNA. (**c–d**) Bone marrow-derived macrophages (Mϕ) derived from C57BL/6 (Ifit1$^{+/+}$) and Ifit1-deficient (Ifit1$^{-/-}$) mice were treated or not with 50 U of IFN-α for 2 h and infected with wild-type MHV (WT; grey bars) or 2′O methyltransferase-deficient MHV (DA; red bars). RNA and protein were harvested 8 h post infection and analysed by quantitative RT-PCR (**c**) and western blotting (**d**). Quantitative RT-PCR results are from one of three representative experiments, showing means ±SD for MHV nucleoprotein (MHV-N) RNA after normalization to the TATA-binding protein (TBP) mRNA. (**e**) Ifit1$^{+/+}$ and Ifit1$^{-/-}$ mice were infected intraperitoneally with 5,000 plaque-forming units of MHV WT (grey bars) or DA (red bars). Viral titers in the spleens of 12 mice per condition were measured 48 h after infection. Data are shown as Tukey box-whisker plots (ND, not detectable; outlier indicated as black dot).
doi:10.1371/journal.ppat.1003663.g004

methylated cap structures [7,22]. Therefore, we tested whether IFIT1 could compete with EIF4E for binding to RNA template. We coupled limiting amounts of unmethylated CAP-RNA, N7-methylated CAP0-RNA and fully methylated CAP1-RNA to beads and tested whether the binding ability of recombinant EIF4E is altered by the presence of recombinant IFIT1. When we used CAP-RNA or CAP0-RNA, EIF4E binding to the beads was reduced by addition of IFIT1, suggesting that the two proteins compete for the RNA target (Fig. 6a). In contrast, when methylated CAP1-RNA was used the amount of EIF4E recovered was not affected by the presence of IFIT1. Competition between Eif4e and Ifit1 for capped RNA was also seen when total lysates of IFN-α-stimulated MEFs were used as inputs for experiments. Unmethylated CAP-RNA captured considerably more Eif4e from

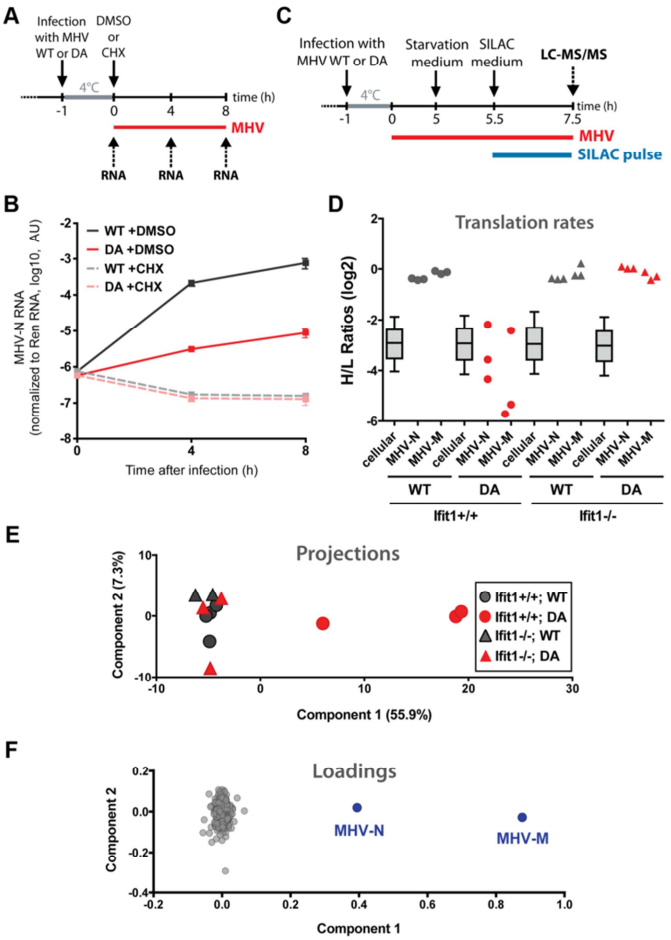

Figure 5. IFIT1 specifically blocks translation of 2′-O-unmethylated capped viral RNA. (**a**) Experimental design used to assess the stability of MHV RNA in infected cells. Bone marrow-derived macrophages (Mϕ) from C57/BL6 mice were treated with 50 U of IFN-α for 2 h prior to infection with wild-type MHV (WT) or 2′O methyltransferase-deficient MHV (DA) at 4°C for 1 h. Directly after infection, cells were treated with 100 μg/ml cycloheximide (CHX) or DMSO. Total RNA was harvested at 0, 4, and 8 h post infection and analysed by quantitative RT-PCR. (**b**) MHV nucleoprotein (MHV-N) RNA in cells infected with MHV WT (grey) or DA mutant (red), treated with DMSO (solid lines) or CHX (dashed lines). Data from one representative experiment of three are depicted, showing means ±SD after normalization to a known amount of in vitro transcribed *Renilla* luciferase RNA (Ren) added to cell lysates. (**c**) Experimental design for pulsed SILAC coupled to mass spectrometry to determine relative changes in protein translation during infection. Macrophages from C75/BL6 (Ifit1$^{+/+}$) and Ifit1-deficient (Ifit1$^{-/-}$) mice grown in normal growth medium containing light (L) amino acids were infected at 4°C for 1 h with wild-type MHV (WT) or 2′O methyltransferase-deficient MHV (DA). Five hours post infection cells were incubated with starvation medium (lacking Lys and Arg) for 30 min, then SILAC medium containing heavy (H) labelled amino acids (Lys8, Arg10) was added, and 2 h later total protein lysate was prepared and subjected to LC-MS/MS analysis. (**d**) Translation rates for 721 cellular proteins, as determined by heavy (H) to light (L) ratios from LC-MS/MS, were plotted as box-whisker plots (whiskers from 10th to 90th percentile). Individual ratios for the MHV nucleoprotein (MHV-N) and membrane protein (MHV-M) in WT- (grey) and DA-infected (red) Ifit1$^{+/+}$ (circles) and Ifit1$^{-/-}$ (triangles) macrophages are plotted separately. Data are from three independent experiments. (**e,f**) Principal Component Analysis based on valid H/L ratios of all measurements from (**d**) showing clustering of the individual samples of the entire dataset (**e**). Panel (**f**) shows all proteins plotted for their contribution to the variation in components 1 and 2. MHV proteins are indicated in blue.
doi:10.1371/journal.ppat.1003663.g005

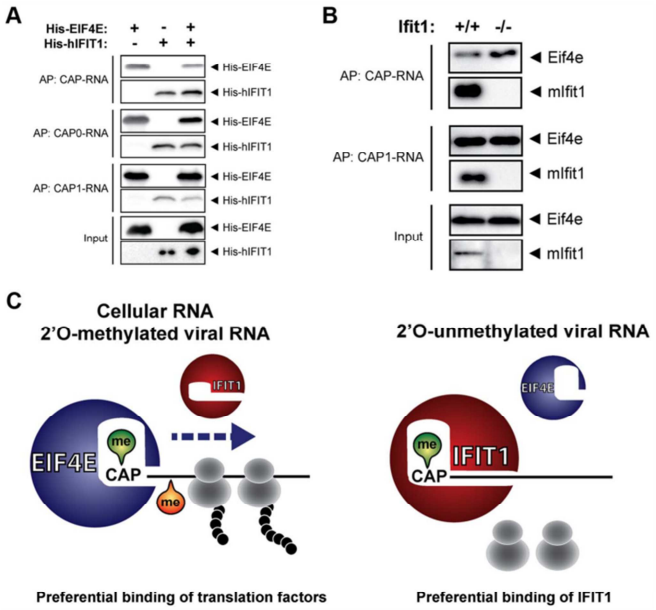

Figure 6. Competition between IFIT1 and translation factor EIF4E for mRNA templates. (**a**) Recovery of recombinant human EIF4E based on RNA affinity binding in the presence or absence of IFIT1. Streptavidin beads were coupled to 250 ng of the indicated RNA and mixed with 5 µg of recombinant His-tagged hIFIT1 and/or His-tagged EIF4E, as indicated. Bound proteins were analysed by western blotting with antibodies directed against the His-tag. (**b**) As in (**a**), except that RNA-coated beads were incubated with lysates of interferon-treated Ifit1$^{+/+}$ and Ifit1$^{-/-}$ mouse embryo fibroblasts. Bound proteins were analysed by western blotting with antibodies directed against murine Eif4e and mIfit1. (**c**) Proposed model for IFIT1-mediated translational inhibition of 2′O-unmethylated viral RNA. Capped and 2′O-methylated cellular and viral RNA is bound by EIF4E to initiate translation. Viral mRNA lacking 2′O methylation at the first ribose is recognized by IFIT1 which prevents binding of cellular factors required for efficient translation. The model is based on data presented here and elsewhere [16,17,19,20].
doi:10.1371/journal.ppat.1003663.g006

lysates of IFN-α treated Ifit1$^{-/-}$ MEFs than from lysates of Ifit1$^{+/+}$ MEFs (Fig. 6b). This difference disappeared when methylated CAP1-RNA was used as bait (Fig. 6b). We therefore conclude that IFIT1 competes with cellular translation initiation factors for mRNA, thereby selectively regulating translation based on the 5′ methylation status of the RNA templates present (Fig. 6c).

Discussion

We previously identified IFIT1 as a nucleic acid-binding protein that recognises the 5′triphosphosphate present on genomes and transcripts of most negative-strand RNA viruses [16]. Here we show that, in addition, IFIT1 binds mRNAs that lack 2′O methylation on the first ribose, such as those produced by RNA viruses that replicate in the cytoplasm and are deficient in RNA cap-specific ribose-2′-O methyltransferase activity. This suggests that IFIT1 has a unique ability to recognize 5′ RNA modifications that are present on viral nucleic acids. Co-purification experiments with human IFIT proteins clearly show formation of a multi-protein complex comprising IFIT1, -2 and -3. Overexpression of single IFIT proteins, including IFIT1, only marginally affects viral growth [16,17], suggesting that the cooperative action of IFIT proteins is required for full antiviral action. This is supported by loss-of-function experiments in cell culture and *in vivo* that show a requirement for Ifit2, which by itself does not bind CAP-RNA, to restrict viruses lacking 2′O methyltransferase activity [17,18]. IFIT2 is known to bind to components of the cytoskeleton [24], which could allow intracellular trafficking of the IFIT complex to its sites of action. While some IFITs possess conserved biological activities in different species, e.g. human and murine IFIT1 which bind to PPP-RNA and unmethylated CAP-RNA, others appear to have evolved in a species-specific manner. We showed here that the yet uncharacterised murine interferon-induced Ifit1c binds to RNA-coated beads in an Ifit1-dependent manner, and we therefore propose that a corresponding Ifit complex with a different protein composition exists in mice.

Residues previously identified to be important for binding of the triphosphate moiety are also required for binding of unmethylated CAP-RNA by IFIT1, suggesting a conserved mechanism of RNA binding. In this context it is of interest to note that crystallographic analysis indicates that PPP-RNA binding to IFIT5, which shows high similarity to IFIT1, occurs in a fashion that is reminiscent of CAP-RNA binding by cap-binding proteins, in that the first two nucleotides are stacked by an aromatic phenylalanine [20]. However, the higher affinity of IFIT1 for unmethylated relative to fully methylated capped RNA is unusual among cellular

proteins since 5′ methylation has so far been reported to increase the affinity of cellular proteins for RNA [7], a notion clearly supported by our RNA AP-MS data. Like its specific antiviral activity, this property of IFIT1 may only become apparent during infections with viruses that produce non-methylated RNA 5′ ends [25,26]. We propose that IFIT1 acts as a molecular switch that allows selective translation based on the 5′ methylation state of the mRNA. The phenomenon of translational control by IFIT1 based on its differential affinity for the capped RNA is reminiscent of the 4E homologous protein (4EHP) in Drosophila and mice, which has been found to control translation by competing with EIF4E for the RNA cap structure, thereby regulating development-specific gene expression [27,28]. Similarly, in our hands, IFIT1 does not associate directly with the translation machinery ([16] and data not shown), which again suggests that it perturbs translation through sequestration of viral RNA. Such a model is consistent with the high expression levels of IFIT proteins resulting from infections with viruses or treatment with IFN-α/β.

Rather than mediating general inhibition of translation, IFIT1 shows high selectivity for mRNAs that lack 5′ methylation. This is supported by pulsed SILAC experiments showing specific, IFIT1-dependent inhibition of translation of capped RNAs lacking 2′O methylation at the first ribose, such as those generated by MHV and HCoV mutants expressing inactive 2′O methyltransferase. Lower eukaryotes and viruses that infect them lack 2′O methylated CAP RNA [29–31], and the latter should be susceptible to the antiviral activity of IFITs. Consequently, the IFIT defence system is likely to contribute to a species barrier that puts selective pressure on viruses to generate 5′ methylated RNA. Our data provide a mechanistic rationale for why most viruses make considerable effort and dedicate part of their coding capacity to produce genomic and subgenomic RNAs with 5′-terminal ends that perfectly mimic those of cellular mRNAs, including fully methylated 5′-cap structures [9,31–33]. Other viruses have evolved specific mechanisms to hide their uncapped/unmethylated 5′ ends, for example, by covalent binding of viral proteins to the 5′ end of viral RNAs and use of alternative strategies for translation initiation, thereby escaping IFIT1-based surveillance, which is centred on RNA 5′ end structures. Despite these viral strategies to generate host-like mRNAs, IFIT1 remains active against viruses that generate 5′ triphosphate RNA, most likely through translation-independent mechanisms. The ability of IFIT1 to target viral RNAs selectively allows the cell to specifically fight virus infections while pursuing an antiviral program aimed at destroying the intruding pathogen.

Materials and Methods

Ethics statement

All animal experiments were performed in accordance with Swiss federal legislation on animal protection and with the approval of the Animal Studies Committee of the Cantonal Veterinary Office (St. Gallen, Switzerland), license nr. SG 11/03.

Reagents, cells and viruses

Interferon-α (IFN-α A/D) was a kind gift from Peter Stäheli. Expression constructs for human and murine IFIT proteins [16,20] and the human aminopeptidase N (APN) were described previously. Products tagged with *Renilla* luciferase were expressed from constructs obtained by Gateway cloning into pCDNA-REN-NT-GW (a kind gift from Albrecht v. Brunn). For expression in bacteria, human EIF4E cDNA was cloned into pETG10A-GW [16]. Recombinant IFIT proteins and human EIF4E were expressed in *E. coli* and purified using HisPur Ni-NTA resin (Thermo Scientific). Streptavidin-agarose beads were obtained from Novagen. Polyclonal antibodies directed against human and mouse IFIT1 were described previously [16]. The antibody against MHV nucleoprotein (MHV-N556) was kindly donated by Stuart Siddell. Primary antibodies against ILF-3 (Sigma; HPA001897), the nucleoprotein of HCoV-229E (Ingenasa; mAb 1H11) and EIF4E (Cell Signaling; C46H6) were obtained from commercial sources. For western blot analysis we used horseradish peroxidase (HRP)-coupled antibodies specific for actin (Santa Cruz; sc-47778), the His-tag (Santa Cruz; sc-8036) or the c-Myc-tag (Roche; 1667149), and HRP-coupled secondary antibodies (Jackson ImmunoResearch). All cell lines used (293T, HeLa, Vero-E6, Huh7, L929, 17Clone1, and $Ifit1^{+/+}$ and $Ifit1^{-/-}$ mouse embryonic fibroblasts) were described previously [11,16], and were maintained in DMEM (PAA Laboratories) containing 10% fetal calf serum (PAA Laboratories) and antibiotics (100 U/ml penicillin, 100 µg/ml streptomycin). DMEM medium containing antibiotics, 10 mM L-glutamine, 10% dialyzed fetal calf serum (PAA Laboratories) and 84 mg/L $^{13}C_6$ $^{15}N_4$ L-arginine and 146 mg/L $^{13}C_6$ $^{15}N_2$ lysine (Cambridge Isotope Laboratories) was used for SILAC experiments. Murine bone marrow-derived macrophages were generated *in vitro* by cultivating bone marrow from mouse femur and tibia in DMEM supplemented with 10% (v/v) fetal calf serum, 5% (v/v) horse serum, 10 mM HEPES pH 7.4, 1 mM sodium pyruvate, 10 mM L-glutamine and 20% (v/v) L929 cell-conditioned medium (containing macrophage colony-stimulating factor) for 6 days. Reagents for transfection with plasmid DNA (Nanofectin) or siRNA duplexes (siRNA Prime) were obtained from PAA Laboratories. Wild-type and 2′-O-methyltransferase-deficient recombinant coronaviruses [mouse hepatitis virus strain A59 (MHV) and human coronavirus 229E (HCoV-229E) [11]], Sendai virus, RVFV Clone13 [34] and VSV-M2 (mutant VSV with the M51R substitution in the matrix protein) [35] have been described previously. Duplex siRNAs targeting human IFIT1 [sense#1: r(CAUGGGAGUUAUC-CAUUGA)dTdT; antisense#1: r(UCAAUGGAUAACUCC-CAUG)dTdA; sense#2: r(CCUUGGGUUCGUCUA-CAAA)dTdT, antisense#2: r(UUUGUAGACGAACCCAA-GG)dAdG] and the green fluorescent protein [sense: 5′ r(AAG-CAGCACGACUUCUUCAAGU)dT 3′; antisense 5′ r(CUU-GAAGAAGUCGUGCUGCUUU)dT 3′] were synthesized by the Core Facility at the MPI of Biochemistry.

Capping and methylation of in vitro transcribed RNA

Triphosphorylated PPP-RNA was synthesized by in vitro transcription with SP6 or T7 polymerase (RiboMAX Large Scale RNA Production Systems; Promega), in the presence or absence of biotin-16-UTP (Enzo), from plasmids encoding antisense 7SK RNA (7SK-as) [13] or *Renilla* luciferase (pRL-SV40; Promega), and purified by ammonium-acetate isopropanol precipitation. Aliquots of PPP-RNA were then mock-treated, dephosphorylated with alkaline phosphatase (FastAP; Fermentas), or modified with different 5′ cap structures using the ScriptCap 2′-O-Methyltransferase and m7G Capping System (CellScript) according to the manufacturer's instructions. Briefly, 20-µg samples of RNA were heat-denatured at 65°C for 5 min, cooled on ice, then incubated with ScriptCap Buffer in the presence of 500 µM GTP, 100 µM SAM, 100 U 2′-O-methyltransferase (VP39), 10 U Vaccinia Capping Enzyme (VCE) and 40 U RNase inhibitor for 1 h at 37°C. Capped RNAs were further treated with FastAP to dephosphorylate any residual PPP-RNA, and then column-purified using the NucleoSpin RNA II kit (Macherey-Nagel). To add radioactively labelled methyl groups to in vitro transcribed RNA, 500 ng of each RNA was incubated with 100 U 2′-O-

methyltransferase or 10 U of VCE in 0.5 µM S-adenosylmethionine and 1.4 µM S-[^{3}H-methyl]-adenosylmethionine (78 Ci/mmol; Perkin-Elmer) for 1 h at 37°C. Reactions were purified on SigmaSpin Post-Reaction Clean-Up columns (Sigma) and eluates were mixed with 2 ml Ultima Gold scintillation fluid for measurement of ^{3}H incorporation with a Packard Tri-Carb liquid scintillation counter (Perkin Elmer).

Generation and capping of chemically synthesized RNA oligomers

Capped m7Gppp-oligoribonucleotides matching the first 22 nucleotides of the 5′ untranslated region of Severe Acute Respiratory Syndrome Coronavirus HKU-39849 were prepared by adding N7-methylated cap structures to chemically synthesized RNA oligomers with a 3′-terminal C6 amino linker. A triphosphorylated RNA oligomer [PPP-r(AUAUUAGGUUUUUACCUACCC)-NH_2) and a corresponding 2′O-ribose methylated RNA-oligomer [PPP-r(AmUAUUAGGUUUUUACCUACCC)-NH_2] were ordered from ChemGenes Corporation (Wilmington, MA, USA) and capped as described above using the m7G Capping System (CellScript). Capped RNA oligomers were then HPLC-purified, biotinylated with biotin-N-hydroxysuccinimide ester (Epicentre) according to the manufacturer's instructions and again HPLC-purified. As control we used a corresponding 3′-terminal biotinylated and HPLC-purified oligoribonucleotide harbouring a 5′ hydroxyl group [OH-r(AUAUUAGGUUUUUACCUACCCU)-biotin].

Identification and quantitation of RNA-binding proteins

For quantitative purification of RNA-binding proteins, streptavidin affinity resin was first incubated with 1-µg aliquots of biotin-labelled OH-RNA, PPP-RNA, CAP-RNA, CAP0-RNA or CAP1-RNA (all 7SK-antisense) in TAP buffer [50 mM Tris pH 7.5, 100 mM NaCl, 5% (v/v) glycerol, 0.2% (v/v) Nonidet-P40, 1.5 mM $MgCl_2$ and protease inhibitor cocktail (EDTA-free, cOmplete; Roche)] in the presence of 40 U RNase inhibitor (Fermentas) for 60 min at 4°C on a rotary wheel. Control or RNA-coated beads were then incubated with 2-mg samples of HeLa cell lysate for 60 min, washed three times with TAP buffer, and twice with TAP buffer lacking Nonidet-P40 to remove residual detergent. Three independent affinity purifications were performed for each RNA. Bound proteins were dentatured by incubation in 6 M urea-2 M thiourea with 1 mM DTT (Sigma) for 30 min and alkylated with 5.5 mM iodoacetamide (Sigma) for 20 min. After digestion with 1 µg LysC (WAKO Chemicals USA) at room temperature for 3 h, the suspension was diluted in 50 mM ammonium bicarbonate buffer (pH 8). The beads were removed by filtration through 96-well multiscreen filter plates (Millipore, MSBVN1210), and the protein solution was digested with trypsin (Promega) overnight at room temperature. Peptides were purified on stage tips with three C18 Empore filter discs (3M) and analyzed by mass spectrometry as described previously [36]. Briefly, peptides were eluted from stage tips and separated on a C18 reversed-phase column (Reprosil-Pur 120 C18-AQ, 3 µM, 150×0.075 mm; Dr. Maisch) by applying a 5% to 30% acetonitrile gradient in 0.5% acetic acid at a flow rate of 250 nl/min over a period of 95 min, using an EASY-nanoLC system (Proxeon Biosystems). The nanoLC system was directly coupled to the electrospray ion source of an LTQ-Orbitrap XL mass spectrometer (Thermo Fisher Scientific) operated in a data dependent mode with a full scan in the Orbitrap cell at a resolution of 60,000 with concomitant isolation and fragmentation of the ten most abundant ions in the linear ion trap.

Affinity purification of luciferase-tagged and recombinant proteins

N-terminally *Renilla* luciferase-tagged proteins were transiently expressed in 293T cells. Three micrograms of each construct were transfected into 6×10^6 cells using 9.6 µl nanofectin (PAA Laboratories) in 10-cm dishes according to the manufacturer's instructions. After 24 h, the medium was removed, and cells were lysed in ice-cold TAP lysis buffer. An aliquot (10%) of the lysate was removed to determine input luciferase activity. The rest was added to streptavidin-agarose beads coated with 250 ng of RNA as described above, and incubated on a rotary wheel at 4°C for 60 min. Beads were washed three times and resuspended in 50 µl TAP buffer. Luciferase activities present in the suspension and in the input lysate were assayed in Renilla reaction buffer (100 mM K_3PO_4, 500 mM NaCl, 1 mM EDTA, 25 mM thiourea) containing 10 µM coelenterazine as substrate. The reactions were performed in triplicate and results were quantified using an Infinite 200 PRO series microplate reader (Tecan). For affinity purification of recombinant proteins with different RNAs, 50 to 250 ng of biotinylated RNA were coupled to streptavidin-agarose beads for 60 min at 4°C. Beads were washed three times with TAP buffer and incubated with recombinant His-tagged proteins for 60 min at 4°C. After three washes beads were boiled in Laemmli buffer for 10 min at 95°C and subjected to SDS-PAGE and Western Blot analysis.

Real-time RT-PCR

Total RNA was isolated using the NucleoSpin RNA II kit (Macherey-Nagel), including on-column DNase digestion, and 200 to 500 ng of RNA was reverse transcribed with the RevertAid H Minus First Strand cDNA Synthesis Kit (Fermentas). RNA levels were then quantified by real-time RT-PCR using the QuantiTect SYBR Green RT-PCR kit (Qiagen) and a CFX96 Touch Real-Time PCR Detection System (BioRad). Each cycle consisted of 15 sec at 95°C, 30 sec at 50°C and 30 sec at 72°C, followed by melting curve analysis. Primer sequences were as follows: *Renilla* luciferase (5′-CGAAAGTTTATGATCCAGAAC-3′ and 5′-AATCATAATAATTAATAAATG-3′), hCycB (5′-CAGCAAGTTCCATCGTGTCATCAAGG-3′ and 5′-GGAAGCGCTCACCATAGATGCTC-3′), mTBP (5′-CCTTCACCAATGACTCCTATGAC-3′ and 5′- CAAGTTTACAGCCAAGATTCA-3′), mIFN-β (5′-ATGGTGGTCCGAGCAGAGAT-3′ and 5′-CCACCACTCATTCTGAGGCA-3′), MHV-N (5′-GCCTCGCCAAAAGAGGACT-3′ and 5′- GGGCCTCTCTTTCCAAAACAC-3′), 229E-N (5′-CAGTCAAATGGGCTGATGCA-3′ and 5′- AAAGGGCTATAAAGAGAATAAGGTATTCT-3′), mIfit1 (5′- CCATAGCGGAGGTGAATATC-3′ and 5′- GGCAGGACAATGTGCAAGAA-3′), mIfit1c (5′-AATCAGAAGAGGCAGCCATC-3′ and 5′-CATGGCTTCACTTGTGTTCC-3′), mIfit2 (5′-TCAGCACCTGCTTCATCCAA-3′ and 5′-CACCTTCGGTATGGCAACTT-3′), and mIfit3 (5′-GCTGCGAGGTCTTCAGACTT-3′ and 5′-TGGTCATGTGCCGTTACAGG-3′).

Virus infection experiments in cell culture and in vivo

C57BL/6 mice were obtained from Charles River Laboratories (Sulzfeld, Germany), and *Ifit1*$^{-/-}$ mice have been described [16,17]. Mice were maintained in individually ventilated cages and used at 6 to 9 weeks of age. All animal experiments were performed in accordance with Swiss federal legislation on animal protection and with the approval of the Animal Studies Committee of the Cantonal Veterinary Office (St. Gallen, Switzerland). Wild-type and *Ifit1*$^{-/-}$ mice (kindly provided by

Michael Diamond) were injected intraperitoneally with 5,000 plaque-forming units of MHV. Virus titers in samples of spleens removed and frozen 48 h post infection were assessed by standard plaque assay on L929 cells. Bone marrow-derived macrophages or mouse embryo fibroblasts (1 to 5×10^5 cells) were treated or not with IFN-α and infected with the indicated viruses at a multiplicity of infection (MOI) of 5. For synchronised infection, cells were infected with virus on ice and pre-warmed DMEM growth medium was added 1 h later. To quantify the effects of siRNA-mediated knockdown of IFIT1, aliquots of 10^5 HeLa cells that had been transfected for 48 h with 15 pmol siRNA and 500 ng expression plasmid for human APN using the siRNA Prime reagent (PAA Laboratories) according to the manufacturer's instructions, were pretreated with IFN-α as indicated and infected with HCoV-229E at an MOI of 1 for 24 h.

Pulsed SILAC and mass spectrometry

For pulsed SILAC, mouse macrophages labelled with heavy isotopes (see above) were lysed in SDS lysis buffer (50 mM Tris pH 7.5, 4% sodium dodecyl sulfate). The lysate was then heated for 5 min at 95°C, sonicated for 15 min with a Bioruptor (Diagenode) and centrifuged for 5 min at 16,000× *g* at room temperature. Protein concentration was determined by Lowry assay (DC Protein Assay, BioRAD), and 50-µg aliquots were reduced with 10 mM DTT for 30 min, alkylated with 55 mM IAA for 20 min at room temperature, and precipitated with 80% acetone for 3 h at −20°C. After centrifugation for 15 min at 16,000× *g* at 4°C, pellets were washed with 80% acetone, dried for 30 min at room temperature and dissolved in 6 M urea-2 M thiourea. Proteins were digested with LysC and trypsin at room temperature and peptides were purified on stage tips and analysed by LC-MS/MS using a Easy nano LC system coupled to a Q Exactive mass spectrometer (Thermo Fisher Scientific). Peptide separation was achieved on a C18-reversed phase column (Reprosil-Pur 120 C18-AQ, 1.9 µM, 200×0.075 mm; Dr. Maisch) using a 95-min linear gradient of 2 to 30% acetonitrile in 0.1% formic acid. The mass spectrometer was set up to run a Top10 method, with a full scan followed by isolation, HCD fragmentation and detection of the ten most abundant ions per scan in the Orbitrap cell.

Bioinformatic analysis

Raw mass-spectrometry data were processed with MaxQuant software versions 1.2.7.4 and version 1.3.0.5 [37] using the built-in Andromeda search engine to search against human and mouse proteomes (UniprotKB, release 2012_01) containing forward and reverse sequences, and the label-free quantitation algorithm as described previously [36,38]. In MaxQuant, carbamidomethylation was set as fixed and methionine oxidation and N-acetylation as variable modifications, using an initial mass tolerance of 6 ppm for the precursor ion and 0.5 Da for the fragment ions. For SILAC samples, multiplicity was set to 2 and Arg10 and Lys8 were set as heavy label parameters. Search results were filtered with a false discovery rate (FDR) of 0.01 for peptide and protein identifications. Protein tables were filtered to eliminate the identifications from the reverse database and common contaminants.

In analyzing mass spectrometry data from RNA affinity purifications, only proteins identified on the basis of at least two peptides and a minimum of three quantitation events in at least one experimental group were considered. Label-free quantitation (LFQ) protein intensity values were log-transformed and missing values filled by imputation with random numbers drawn from a normal distribution, whose mean and standard deviation were chosen to best simulate low abundance values. Significant interactors of RNAs with different 5′ end structures were determined by multiple equal variance t-tests with permutation-based false discovery rate statistics [39]. We performed 250 permutations and the FDR threshold was set between 0.02 and 0.1. The parameter S_0 was empirically set between 0.2 and 1, to separate background from specifically enriched interactors.

For data analysis from pulsed SILAC experiments, we used log-transformed heavy to light protein ratios. Only proteins with valid values were considered for analysis, and normalized by dividing by the row median. Profile plots were generated using LFQ intensities of log-transformed heavy-labelled protein intensities. We excluded proteins containing less than 10 valid values in all 12 measurements, and missing values were filled by imputation. LFQ intensities were then normalized by dividing by the row median.

Results were plotted using R (www.R-project.org) and GraphPad Prism version 5.02. Multiple sequence alignments were generated with ClustalW (http://www.ebi.ac.uk/Tools/msa/clustalw2/).

Structural modelling

A homology model of human IFIT1 was obtained with MODELLER [40] using the X-ray structure of human IFIT5 (4HOQ) as a structural template [20]. A pairwise sequence alignment was generated with ClustalW (http://www.ebi.ac.uk/Tools/msa/clustalw2/) and further refined with MODELLERs align2d. Human IFIT1 and IFIT5 share approximately 75.6% sequence similarity, with 57.2% of all residues being identical. Cavity volumes in both structures were calculated in a two-step process with the rolling probe method using 3V [41]. First, a solvent-excluded volume was calculated for each structure using a probe radius of 1.5 Å (corresponding to water). A larger probe size of 5 Å was used to calculate so-called "shell volumes". The solvent-accessible cavity volumes were obtained by subtraction of each solvent-excluded volume from the corresponding shell volume.

Supporting Information

Figure S1 Generation of 5′end modified in-vitro transcribed RNA. (**a**) Schematic overview of synthesis of the biotinylated RNA used in this study. 5′ triphosphorylated (PPP-) 7SK-antisense RNA obtained by in vitro transcription with SP6 polymerase was modified enzymatically at the 5′ end by incubating with alkaline phosphatase (AP) to remove 5′ phosphates (OH-RNA), with recombinant Vaccinia virus capping enzyme (VCE) to produce unmethylated capped RNA (CAP-RNA), with VCE in the presence of S-adenosyl methionine (SAM) to generate N7-methylated capped RNA (CAP0-RNA), or with VCE and recombinant Vaccinia virus 2′O methyltransferase (VP39) in the presence of SAM to generate N7-methylated capped RNA methylated at the 2′O position of the first ribose (CAP1-RNA) [43],[44]. (**b**) Agarose gel image showing 200 ng of in vitro transcribed, biotinylated RNA following the enzymatic treatments depicted in (**a**). (**c**) Evaluation of the N7- and 2′O-methylation efficiency of recombinant Vaccinia virus enzymes. Capped RNAs produced as in (**a**) were incubated either with VCE or VP39 in the presence of ^{3}H-labeled SAM, and the incorporation efficiency was measured by scintillation counting. ^{3}H-labeled methyl groups were transferred from SAM only if the RNA had not previously been methylated (N7-methylation of CAP-RNA, and 2′O methylation of CAP0-RNA), showing that methylation of RNA by both VCE and VP39 was maximally efficient.
(TIF)

Figure S2 RNA affinity purifications from HeLa cell lysates. (**a**) Heatmap of all proteins identified in RNA affinity purifications from HeLa cell lysates. Hierarchical clustering of proteins was performed on logarithmic LFQ protein intensities using Euclidean distances. The colour code represents LFQ intensities in rainbow colours (see colour scale). (**b**) Heatmap showing hierarchical clustering (Euclidean distances) of interactors that were significantly enriched (see Materials and Methods) in fractions bound by at least one RNA with a modified 5′ end structure (compared to OH-RNA). The plot shows means of Z-score transformed logarithmic LFQ intensities. Blue colours indicate Z-score <0, red colours indicate Z-score >0, white indicates Z-score = 0. The saturation threshold is set at -2.25 and +2.25. Asterisks indicate the IFIT complex. (**c**) Volcano plots showing enrichment (ratio of LFQ protein intensities; x-axis) and p-values (t-test; y-axis) of CAP1-RNA to CAP-RNA. Data are from three independent affinity purifications. Significantly enriched interactors (see Materials and Methods) are separated from background proteins (blue dots) by a hyperbolic curve (dotted line). Among the significant interactors, IFIT proteins and FTSJD2 (red) are highlighted.
(TIF)

Figure S3 RNA affinity purifications from lysates of mouse embryo fibroblasts. (**a–b**) As in Fig. S2, but showing proteins identified in RNA affinity purifications from mouse embryo fibroblasts. In (**b**) the saturation threshold is set at −1. 5 and +1. 5. The asterisk indicates the Ifit complex.
(TIF)

Figure S4 Characterisation of the murine IFIT complex. (**a**) Expression of Ifit genes in wild-type ($Ifit1^{+/+}$) and Ifit1-deficient ($Ifit1^{-/-}$) mouse embryonic fibroblasts (MEFs). MEFs were left untreated, treated with 1000 U/ml IFN-α, or infected with Rift Valley fever virus Clone13 or a mutant version of vesicular stomatitis virus (VSV-M2) at a multiplicity of infection of 1 or 0.01, respectively. Sixteen hours later RNA was analysed by quantitative RT-PCR for mIfit1, mIfit1c, mIfit2 and mIfit3. In each case, one representative experiment of three is shown, with means ±SD after normalization to the TATA-binding protein (TBP) mRNA. (**b**) Heatmap of selected proteins identified in RNA affinity purifications from cell lysates of $Ifit1^{+/+}$ and $Ifit1^{-/-}$ MEFs. The plot shows the means of log-transformed label-free quantitation protein intensities in rainbow colours (see colour scale). (**c**) Alignment of murine and human IFIT proteins using ClustalW. (**d**) Matrix showing amino acid similarity (based on ClustalW alignment) of all murine and human IFIT proteins. Percent similarity is indicated as color coded from white to red, and the exact similarity is shown within each element of the matrix.
(TIF)

Figure S5 Comparison of the RNA binding cavities of IFIT5 and IFIT1. Sections of surface representations of the solvent-accessible surfaces of IFIT5 (top) and IFIT1 (bottom) are shown, with PPP-RNA bound as in IFIT5 (stick representation, superimposed on IFIT1), and the corresponding cavity volumes V calculated as described in Materials and Methods. In our calcuations, the main RNA-binding cavity in IFIT5 has volume of 11881 $Å^3$. The calculated volume of the corresponding cavity of the modelled IFIT1, at 12627 $Å^3$, is about 700 $Å^3$ larger.
(TIF)

Figure S6 Induction of interferon-β in wild-type and Ifit1-deficient mouse cells. Interferon-stimulated bone marrow-derived macrophages (MΦs) from C57/BL6 ($Ifit1^{+/+}$) or Ifit1-deficient ($Ifit1^{-/-}$) mice were left untreated, or infected with wild-type MHV (WT), 2′O-methyltransferase-deficient MHV (DA), or Sendai virus (SeV). Twelve hours later total RNA was harvested and analysed by quantitative RT-PCR for interferon β (IFN-β) mRNA. Data from three independent experiments showing fold change relative to untreated cells (mean ±SD) after normalization to the TATA-binding protein (TBP) mRNA.
(TIF)

Figure S7 Translation profiles of individual proteins in MHV-infected macrophages. Translation profiles based on pulsed SILAC of macrophages from C75/BL6 ($Ifit1^{+/+}$) and Ifit1-deficient ($Ifit1^{-/-}$) mice infected with wild-type MHV (WT) or 2′O methyltransferase-deficient MHV (DA) as shown in Fig. 5. The profile plot shows normalized LFQ intensities of heavy proteins, representing a total number of 451 proteins labelled during the 2 h pulse period. Data show average LFQ intensities from three independent replicates. Selected profiles are coloured and represent MHV proteins and cellular proteins involved in immune responses.
(TIF)

Table S1 Quantitative MS data from RNA affinity purifications with HeLa cell lysates. Proteins identified by LC-MS/MS from lysates of HeLa cells upon affinity purification with different RNA baits. Table contains log-transformed and imputed label-free quantification (LFQ) intensities of all identified proteins. Significantly enriched proteins, p values and mean differences from t-test based analyses are indicated.
(XLSX)

Table S2 Quantitative MS data from RNA affinity purifications with MEF lysates. Proteins identified by LC-MS/MS from lysates of mouse embryo fibroblasts (MEF) upon affinity purification with different RNA baits. Table contains log-transformed and imputed label-free quantification (LFQ) intensities of all identified proteins. Significantly enriched proteins, p values and mean differences from t-test based analyses are indicated.
(XLSX)

Acknowledgments

We thank Matthias Mann, Felix Meissner, Korbinian Mayer, Igor Paron, Gabi Sowa, Falk Butter, Jürgen Cox, and Bernd Haas and Stephan Übel (MPI of Biochemistry Core Facility) for technical support, Albrecht von Brunn for the Lumier plasmids, and Elena Conti for scientific input and critical reading of the manuscript. We further want to thank Giulio Superti-Furga for providing reagents.

Author Contributions

Conceived and designed the experiments: MH PH VT AP. Performed the experiments: MH PH LL CH AM EK CGC AP. Analyzed the data: MH PH CB CHE VT AP. Contributed reagents/materials/analysis tools: JZ VT. Wrote the paper: MH PH AP.

References

1. Versteeg GA, Garcia-Sastre A (2010) Viral tricks to grid-lock the type I interferon system. Curr Opin Microbiol 13: 508–516.
2. Iwasaki A, Medzhitov R (2010) Regulation of adaptive immunity by the innate immune system. Science 327: 291–295.

3. Sadler AJ, Williams BR (2008) Interferon-inducible antiviral effectors. Nat Rev Immunol 8: 559–568.
4. Hornung V, Latz E (2010) Intracellular DNA recognition. Nat Rev Immunol 10: 123–130.
5. Kato H, Takahasi K, Fujita T (2011) RIG-I-like receptors: cytoplasmic sensors for non-self RNA. Immunol Rev 243: 91–98.
6. Gebauer F, Hentze MW (2004) Molecular mechanisms of translational control. Nat Rev Mol Cell Biol 5: 827–835.
7. Topisirovic I, Svitkin YV, Sonenberg N, Shatkin AJ (2011) Cap and cap-binding proteins in the control of gene expression. Wiley Interdiscip Rev RNA 2: 277–298.
8. Pichlmair A, Reis e Sousa C (2007) Innate Recognition of Viruses. Immunity 27: 370–383.
9. Decroly E, Ferron F, Lescar J, Canard B (2012) Conventional and unconventional mechanisms for capping viral mRNA. Nat Rev Microbiol 10: 51–65.
10. Colonno RJ, Stone HO (1976) Newcastle disease virus mRNA lacks 2′-O-methylated nucleotides. Nature 261: 611–614.
11. Zust R, Cervantes-Barragan L, Habjan M, Maier R, Neuman BW, et al. (2011) Ribose 2′-O-methylation provides a molecular signature for the distinction of self and non-self mRNA dependent on the RNA sensor Mda5. Nat Immunol 12: 137–143.
12. Hornung V, Ellegast J, Kim S, Brzozka K, Jung A, et al. (2006) 5′-Triphosphate RNA is the ligand for RIG-I. Science 314: 994–997.
13. Pichlmair A, Schulz O, Tan CP, Naslund TI, Liljestrom P, et al. (2006) RIG-I-mediated antiviral responses to single-stranded RNA bearing 5′-phosphates. Science 314: 997–1001.
14. Kato H, Takeuchi O, Mikamo-Satoh E, Hirai R, Kawai T, et al. (2008) Length-dependent recognition of double-stranded ribonucleic acids by retinoic acid-inducible gene-I and melanoma differentiation-associated gene 5. J Exp Med 205: 1601–1610.
15. Diamond MS, Farzan M (2013) The broad-spectrum antiviral functions of IFIT and IFITM proteins. Nat Rev Immunol 13: 46–57.
16. Pichlmair A, Lassnig C, Eberle CA, Gorna MW, Baumann CL, et al. (2011) IFIT1 is an antiviral protein that recognizes 5′-triphosphate RNA. Nat Immunol 12:624–630.
17. Daffis S, Szretter KJ, Schriewer J, Li J, Youn S, et al. (2010) 2′-O methylation of the viral mRNA cap evades host restriction by IFIT family members. Nature 468: 452–456.
18. Fensterl V, Wetzel JL, Ramachandran S, Ogino T, Stohlman SA, et al. (2012) Interferon-induced Ifit2/ISG54 protects mice from lethal VSV neuropathogenesis. PLoS Pathog 8: e1002712.
19. Szretter KJ, Daniels BP, Cho H, Gainey MD, Yokoyama WM, et al. (2012) 2′-O methylation of the viral mRNA cap by West Nile virus evades ifit1-dependent and -independent mechanisms of host restriction in vivo. PLoS Pathog 8: e1002698.
20. Abbas YM, Pichlmair A, Gorna MW, Superti-Furga G, Nagar B (2013) Structural basis for viral 5′-PPP-RNA recognition by human IFIT proteins. Nature 494: 60–64.
21. Shapira SD, Gat-Viks I, Shum BO, Dricot A, de Grace MM, et al. (2009) A physical and regulatory map of host-influenza interactions reveals pathways in H1N1 infection. Cell 139: 1255–1267.
22. Furuichi Y, Shatkin AJ (2001) Caps on Eukaryotic mRNAs. eLS. doi: 10.1038/npg.els.0000891
23. Schwanhausser B, Busse D, Li N, Dittmar G, Schuchhardt J, et al. (2011) Global quantification of mammalian gene expression control. Nature 473: 337–342.
24. Saha S, Sugumar P, Bhandari P, Rangarajan PN (2006) Identification of Japanese encephalitis virus-inducible genes in mouse brain and characterization of GARG39/IFIT2 as a microtubule-associated protein. J Gen Virol 87: 3285–3289.
25. Li J, Fontaine-Rodriguez EC, Whelan SP (2005) Amino acid residues within conserved domain VI of the vesicular stomatitis virus large polymerase protein essential for mRNA cap methyltransferase activity. J Virol 79: 13373–13384.
26. Li J, Wang JT, Whelan SP (2006) A unique strategy for mRNA cap methylation used by vesicular stomatitis virus. Proc Natl Acad Sci U S A 103: 8493–8498.
27. Morita M, Ler LW, Fabian MR, Siddiqui N, Mullin M, et al. (2012) A novel 4EHP-GIGYF2 translational repressor complex is essential for mammalian development. Mol Cell Biol 32: 3585–3593.
28. Cho PF, Poulin F, Cho-Park YA, Cho-Park IB, Chicoine JD, et al. (2005) A new paradigm for translational control: inhibition via 5′-3′ mRNA tethering by Bicoid and the eIF4E cognate 4EHP. Cell 121: 411–423.
29. Sripati CE, Groner Y, Warner JR (1976) Methylated, blocked 5′ termini of yeast mRNA. J Biol Chem 251: 2898–2904.
30. Zimmern D (1975) The 5′ end group of tobacco mosaic virus RNA is m7G5′ppp5′ Gp. Nucleic Acids Res 2: 1189–1201.
31. Bouloy M, Plotch SJ, Krug RM (1980) Both the 7-methyl and the 2′-O-methyl groups in the cap of mRNA strongly influence its ability to act as primer for influenza virus RNA transcription. Proc Natl Acad Sci U S A 77: 3952–3956.
32. Fechter P, Brownlee GG (2005) Recognition of mRNA cap structures by viral and cellular proteins. J Gen Virol 86: 1239–1249.
33. Ruigrok RW, Crepin T, Hart DJ, Cusack S (2010) Towards an atomic resolution understanding of the influenza virus replication machinery. Curr Opin Struct Biol 20: 104–113.
34. Muller R, Saluzzo JF, Lopez N, Dreier T, Turell M, et al. (1995) Characterization of clone 13, a naturally attenuated avirulent isolate of Rift Valley fever virus, which is altered in the small segment. Am J Trop Med Hyg 53: 405–411.
35. Stojdl DF, Lichty BD, tenOever BR, Paterson JM, Power AT, et al. (2003) VSV strains with defects in their ability to shutdown innate immunity are potent systemic anti-cancer agents. Cancer Cell 4: 263–275.
36. Hubner NC, Bird AW, Cox J, Splettstoesser B, Bandilla P, et al. (2010) Quantitative proteomics combined with BAC TransgeneOmics reveals in vivo protein interactions. J Cell Biol 189: 739–754.
37. Cox J, Mann M (2008) MaxQuant enables high peptide identification rates, individualized p.p.b.-range mass accuracies and proteome-wide protein quantification. Nat Biotechnol 26: 1367–1372.
38. Luber CA, Cox J, Lauterbach H, Fancke B, Selbach M, et al. (2010) Quantitative proteomics reveals subset-specific viral recognition in dendritic cells. Immunity 32: 279–289.
39. Tusher VG, Tibshirani R, Chu G (2001) Significance analysis of microarrays applied to the ionizing radiation response. Proc Natl Acad Sci U S A 98: 5116–5121.
40. Eswar N, Webb B, Marti-Renom MA, Madhusudhan MS, Eramian D, et al. (2006) Comparative protein structure modeling using Modeller. Curr Protoc Bioinformatics Chapter 5: Unit 5 6.
41. Voss NR, Gerstein M (2010) 3V: cavity, channel and cleft volume calculator and extractor. Nucleic Acids Res 38: W555–562.
42. Liu SY, Sanchez DJ, Aliyari R, Lu S, Cheng G (2012) Systematic identification of type I and type II interferon-induced antiviral factors. Proc Natl Acad Sci U S A 109: 4239–4244.
43. Martin SA, Moss B (1975) Modification of RNA by mRNA guanylyltransferase and mRNA (guanine-7-)methyltransferase from vaccinia virions. J Biol Chem 250: 9330–9335.
44. Barbosa E, Moss B (1978) mRNA(nucleoside-2′-)-methyltransferase from vaccinia virus. Characteristics and substrate specificity. J Biol Chem 253: 7698–7702.

Holze C, Michaudel C, Mackowiak C, Haas DA, Benda C, **Hubel P**, Pennemann FL, Schnepf D, Wettmarshausen J, Braun M, Leung DW, Amarasinghe GK, Perocchi F, Staeheli P, Ryffel B, Pichlmair A. Nat Immunol. 2018 Feb;19(2):130-140. doi: 10.1038/s41590-017-0013-y. Epub 2017 Dec 18. PMID: 29255269

2.3 PUBLICATION 3: OXEIPTOSIS, A ROS-INDUCED CASPASE-INDEPENDENT APOPTOSIS-LIKE CELL-DEATH PATHWAY

Accumulation of reactive oxygen species (ROS) is known to occur during virus replication. Resulting elevated cellular ROS levels trigger cell-death pathways and consequence into the suicide of cells. However, cells function as the feeding ground for virus replication. Therefore, viruses evolved strategies to counteract cell death and to keep the host cell vital until the viral replication cycle is completed.

I joined this project, which was spearheaded by Cathleen Holze, a PhD student in our lab at this time. She studied the function of the cellular proteins KEAP1, PGAM5 and AIFM1 in a novel caspase independent ROS-mediated cell-death pathway named oxeiptosis. This cell-death pathway proofed to be of central importance for inflammation response *in vivo*. Through comprehensive *in vivo* and *in vitro* studies using specific chemical inhibitors and gene knock out experiments, we could show the independence of oxeiptosis from other already described inflammation-associated cell-death pathways. Additionally, we could confirm the central importance of PGAM5, KEAP1 and AIFM1 for this novel ROS-induced cell-death pathway. By integrating and mining available virus-host protein interactions we could additionally show, that these central factors are targeted by several virus species.

I mainly contributed to this project by generating, integrating and analyzing AE- and AP-LC-MS/MS experiments and by identifying protein-protein interactions between oxeiptosis-relevant cellular factors and virus-derived proteins.

ARTICLES
https://doi.org/10.1038/s41590-017-0013-y

nature immunology

Oxeiptosis, a ROS-induced caspase-independent apoptosis-like cell-death pathway

Cathleen Holze[1], Chloé Michaudel[2], Claire Mackowiak[2], Darya A. Haas[1], Christian Benda[3], Philipp Hubel[1], Friederike L. Pennemann[1], Daniel Schnepf[4,5], Jennifer Wettmarshausen[6,7], Marianne Braun[8], Daisy W. Leung[9], Gaya K. Amarasinghe[9], Fabiana Perocchi[6,7], Peter Staeheli[4,10], Bernhard Ryffel[2,11] and Andreas Pichlmair[1,12,13]*

Reactive oxygen species (ROS) are generated by virus-infected cells; however, the physiological importance of ROS generated under these conditions is unclear. Here we found that the inflammation and cell death induced by exposure of mice or cells to sources of ROS were not altered in the absence of canonical ROS-sensing pathways or known cell-death pathways. ROS-induced cell-death signaling involved interactions among the cellular ROS sensor and antioxidant factor KEAP1, the phosphatase PGAM5 and the proapoptotic factor AIFM1. *Pgam5*$^{-/-}$ mice showed exacerbated lung inflammation and proinflammatory cytokines in an ozone-exposure model. Similarly, challenge with influenza A virus led to increased infiltration of the virus, lymphocytic bronchiolitis and reduced survival of *Pgam5*$^{-/-}$ mice. This pathway, which we have called 'oxeiptosis', was a ROS-sensitive, caspase independent, non-inflammatory cell-death pathway and was important for protection against inflammation induced by ROS or ROS-generating agents such as viral pathogens.

Reactive nitrogen species and reactive oxygen species (ROS) such as $\cdot O_2$ and ·OH are generated as natural byproducts of normal oxygen metabolism. ROS serve an important role in cell signaling by regulating the proliferation and survival of cells[1,2]. However, exposure to pollutants, an increased protein-folding load, elevated fatty-acid oxidation and energy metabolism can result in pathological accumulation of ROS in the endoplasmic reticulum, peroxisomes and mitochondria[3,4]. Since oxidation by ROS can cause irreversible conformational changes to proteins and lipids, as well as DNA mutations[5], several enzymatic and non-enzymatic mechanisms have evolved to protect cells from the detrimental accumulation of ROS.

The main intracellular sensor that monitors ROS is KEAP1[6]. Under physiological conditions, KEAP1 ubiquitinates and degrades the transcription factor NRF2, a positive regulator of the expression of genes encoding cytoprotective molecules. Increased intracellular ROS oxidizes KEAP1, which results in its inability to degrade NRF2; the latter then accumulates, translocates to the nucleus and induces the expression of antioxidant factors such as NQO1, HOX1 and TXN[7–10]. Prolonged or considerable oxidative stress, however, does not induce sufficient expression of cytoprotective proteins and can result in cell damage and/or cell death[11].

Exogenous stimuli such as ultraviolet light, heat or inflammatory cytokines increase intracellular ROS that contribute to the severity of pathological disorders[12,13]. Furthermore, viral infection can increase intracellular ROS levels due to the perturbation of cellular metabolism[14,15]. It has been proposed that in cases of persistent viral infection, ROS contribute to organ damage and exacerbate disease progression[16]. Some viruses have evolved mechanisms to avoid detrimental ROS generation to facilitate viral proliferation. For example, dengue virus[17], human herpes virus 8 (Kaposi's sarcoma-associated herpesvirus (KSHV))[18] and encephalomyocarditis virus[14] have evolved distinct mechanisms to modulate ROS-mediated cell-death pathways. Conversely, other viruses, such as Marburg virus, specifically perturb stress responses by promoting cytoprotective programs[19,20].

ROS-induced cell death can induce caspase-dependent apoptosis and inflammasome-driven pyroptosis, as well as caspase-independent cell-death pathways, including necroptosis, ferroptosis and autophagic cell death[21–25]. Despite the apparent importance of ROS in physiological and pathological processes, relatively little is known about their sensors and downstream signaling pathways that lead to cell death in response to oxidative stress. We demonstrate here a ROS-induced form of apoptosis-like cell death that we have called 'oxeiptosis'. This previously unknown form of cell death was independent of all previously characterized cell-death pathways and had an important role in limiting harmful ROS-associated inflammation.

Results

Ozone exposure induces inflammasome-independent inflammation in vivo. To investigate the involvement of known pathways in ROS-induced cell death, we used an in vivo ozone-exposure model (Fig. 1a). A single exposure to ozone induced the accumulation of

[1]Innate Immunity Laboratory, Max-Planck Institute of Biochemistry, Martinsried, Munich, Germany. [2]INEM, Experimental Molecular Immunology, UMR7355 CNRS and University, Orleans, France. [3]Department of Structural Cell Biology, Max-Planck Institute of Biochemistry, Martinsried, Munich, Germany. [4]Institute of Virology, University of Freiburg, Freiburg, Germany. [5]Spemann Graduate School of Biology and Medicine, Albert Ludwigs University Freiburg, Freiburg, Germany. [6]Department of Biochemistry, Gene Center Munich, Munich, Germany. [7]Institute for Diabetes and Obesity, Helmholtz Zentrum Munchen, Neuherberg, Germany. [8]EM-Histo Lab, Max-Planck Institute of Neurobiology, Martinsried, Munich, Germany. [9]Department of Pathology and Immunology, Washington University School of Medicine, St Louis, MO, USA. [10]Faculty of Medicine, University of Freiburg, Freiburg, Germany. [11]Institute of Infectious Diseases and Molecular Medicine, University of Cape Town, Cape Town, South Africa. [12]School of Medicine, Institute of Virology, Technical University of Munich, Munich, Germany. [13]German Center for Infection Research (DZIF), Munich partner site, Munich, Germany. *e-mail: andreas.pichlmair@tum.de

© 2018 Nature America Inc., part of Springer Nature. All rights reserved.

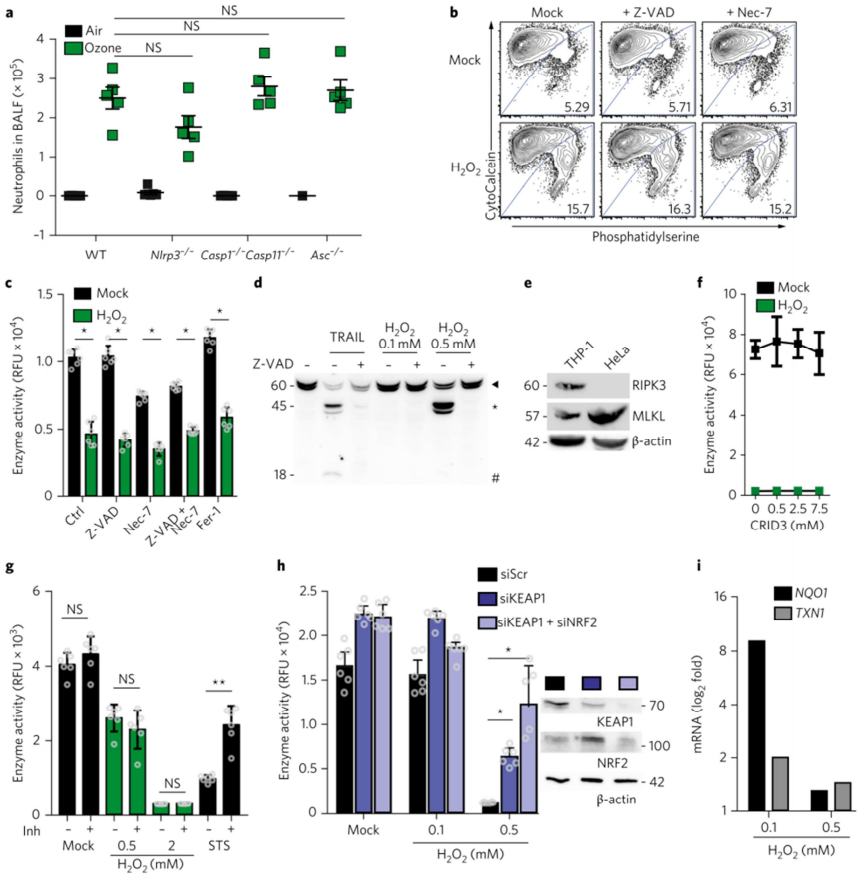

Fig. 1 | Inflammasome-, caspase- and necroptosis-independent but KEAP1-dependent cell death after stimulation with ROS. a, Cytospin quantification of neutrophils in the BALF of C57BL/6 mice (WT), *Nlrp3*$^{-/-}$ mice, *Casp1*$^{-/-}$*Casp11*$^{-/-}$ mice and *Asc*$^{-/-}$ mice ($n = 5$ per genotype) 24 h after 1 h of exposure to air or to ozone at a dose of 1 ppm (key). **b**, Flow cytometry of MEFs given no pretreatment (Mock) or pretreated for 1 h with Z-VAD (20 μM) or Nec-7 (10 μM) (above plots), followed by 20 h of mock treatment or treatment with H_2O_2 (left margin), assessed with the fluorogenic dye CytoCalcein, which is retained by living cells (a measure of viability), and phosphatidylserine (a measure of apoptosis). Numbers in outlined areas indicate percent cells with decreased CytoCalcein and/or increased phosphatidylserine. **c**, Resazurin-conversion assay of the viability of HeLa cells left untreated (control (Ctrl)) or treated for 1 h with Z-VAD or Nec-7 or both, or with 1 μM ferrostatin-1 (Fer-1) (horizontal axis), followed by 21 h of mock treatment or exposure to 0.5 mM H_2O_2 (key); results presented as relative fluorescence units (RFU). **d**, Immunoblot analysis of full-length caspase-8 (arrowhead), cleaved caspase-8 (*) or the p18 fragment of caspase-8 (#) (right margin) in cells left untreated (–) or treated for 1 h with 20 μM Z-VAD (+) (above lanes), followed by 10 h of no further treatment (far left lane) or treatment with TRAIL (300 ng/ml) or H_2O_2 (0.1 mM or 0.5 mM) (above blot). Left margin, size markers, in kilodaltons. **e**, Immunoblot analysis of RIPK3, the pseudo-kinase MLKL and β-actin (loading control) in lysates of THP-1 human monocytic cells and HeLa cells (above lanes). **f**, Resazurin-conversion assay (as in **c**) of HeLa cells pretreated with various concentrations (horizontal axis) of CRID3, followed by mock treatment or exposure to 0.5 mM H_2O_2 (key). **g**, Resazurin-conversion assay (as in **c**) of HeLa cells pretreated with a combination of the inhibitors Z-VAD, 5 μM necrosulfonamide and ferrostatin-1 (+) or not (–) (horizontal axis), followed by mock treatment or stimulation with H_2O_2 (0.5 mM or 2 mM) or staurosporine (STS) (below plot). **h**, Resazurin-conversion assay (left; as in **c**) of HeLa cells transfected for 48 h with control (non-targeting) siRNA with a scrambled sequence (siScr) or siRNA targeting KEAP1 (siKEAP1) or both KEAP1 and NRF2 (siKEAP1 + siNRF2) (key), followed by mock treatment or exposure to 0.5 mM H_2O_2 (below plot); right, immunoblot analysis of KEAP1, NRF2 and β-actin (below blots) in cells as at left (colors above lanes match colors in key). **i**, Expression of the NRF2-regulated target genes *NQO1* and *TXN1* (key) in cells after 21 h of treatment with 0.5 mM or 1 mM H_2O_2 (horizontal axis); results are presented relative to those of cells not treated with H_2O_2. Each symbol (**a**,**c**,**g**–**i**) represents an individual mouse (**a**) or measurement (**c**,**g**–**i**); small horizontal lines (**a**) indicate the mean (±s.e.m.). NS, not significant ($P > 0.05$); *$P < 0.001$ and **$P < 0.0001$ (two-tailed Mann Whitney test (**a**) or two-way analysis of variance (ANOVA) (**c**,**g**,**h**)). Data are from one experiment representative of at least three experiments (**a**–**e**,**g**,**h**) or two experiments (**f**,**h**) with similar results (mean ± s.d. of six technical replicates in **c**,**f**–**h**).

© 2018 Nature America Inc., part of Springer Nature. All rights reserved.

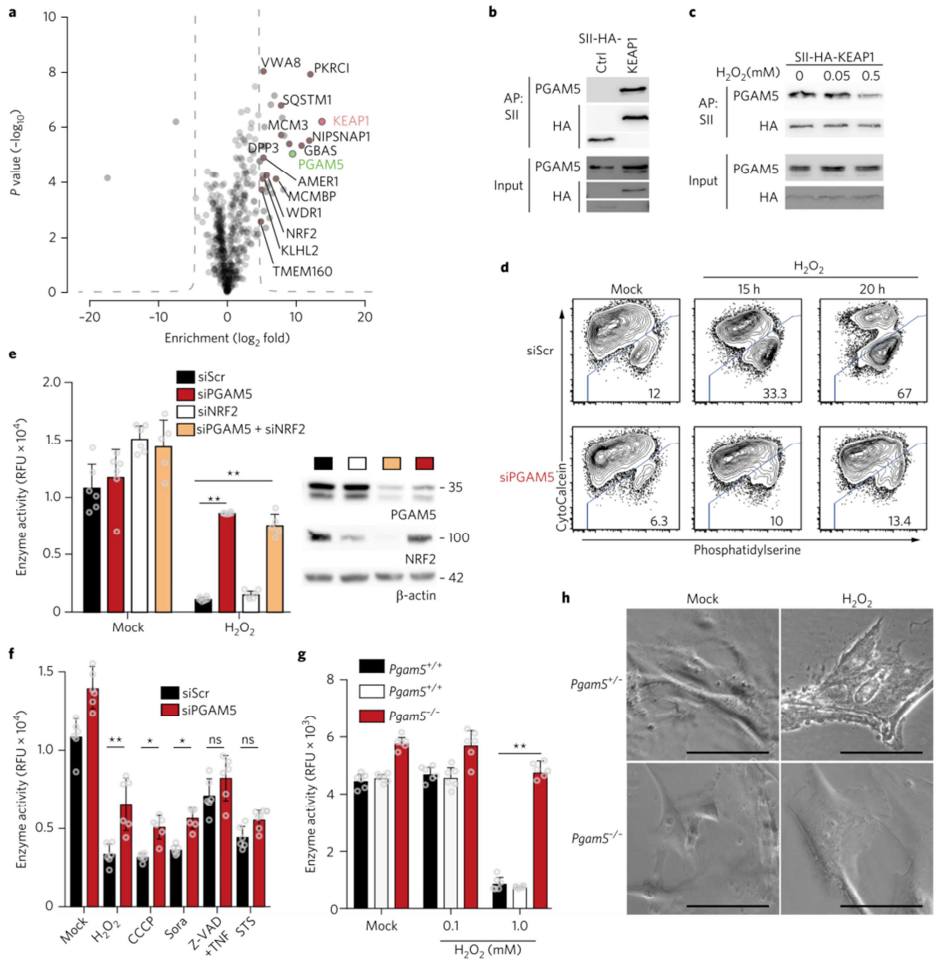

Fig. 2 | KEAP1 binds PGAM5, which is required for the induction of ROS-dependent cell death. a, Identification of KEAP1's binding partners by SII affinity purification of SII-HA-tagged KEAP1 and THYN1 (control (ctrl)), followed by LC-MS/MS analysis, presented as the degree of enrichment (average values) of label-free quantitation by KEAP1 relative to that by THYN1 (horizontal axis) plotted against the transformed *P* value (two-tailed *t*-test) for each protein identified (vertical axis), including KEAP1 (red), proteins known to interact with KEAP1 (on the basis of the BioGRID database of interaction data sets) (brown) and proteins associated with cell death (green); hyperbolic curves separate proteins showing significant enrichment (false-discovery rate (FDR) < 0.00001; S0 = 100) versus background. **b**, Immunoblot analysis of precipitates before (Input; bottom) and after (top) affinity purification with SII-HA-KEAP1 (KEAP1) or SII-HA-THYN1 (Ctrl) (above lanes). **c**, Immunoblot analysis of HeLa Flp-In cells expressing SII-HA-KEAP1, treated for 8 h with various concentrations (above lanes) of H_2O_2, assessed before (Input; bottom) and after (top) affinity purification of SII. **d**, Flow cytometry (as in Fig. 1b) of HeLa cells transfected for 48 h with control siRNA (siScr) or siRNA targeting PGAM5 (siPGAM5) (left margin), followed by mock treatment or treatment for 15 or 20 h (above plots) with 0.5 mM H_2O_2. **e**, Resazurin-conversion assay (as in Fig. 1c) of HeLa cells treated for 48 h with control siRNA or siRNA targeting PGAM5 or NRF2 or both (key) and mock treated or stimulated for 20 h with H_2O_2 (horizonal axis) (left), and immunoblot analysis of PGAM5, NRF2 and β-actin (below blots) in cells as at left at 48 h after transfection of siRNA (colors above lanes match colors in key), assessing knockdown efficiency (right). **f**, Resazurin-conversion assay (as in **e**) of HeLa cells transfected for 48 h with control siRNA or siRNA targeting PGAM5 (key) and mock treated or stimulated with H_2O_2, 20 μM CCCP, 20 μM sorafenib (Sora), 20 μM Z-VAD plus 20 μM TNF (Z-VAD + TNF) or 1 μM staurosporine (horizontal axis). **g**, Resazurin-conversion assay (as in **e**) of *Pgam5*$^{+/+}$, *Pgam5*$^{+/-}$ and *Pgam5*$^{-/-}$ MEFs (key) mock treated or stimulated with 0.1 mM or 1 mM H_2O_2 (horizontal axis). **h**, Light microscopy of *Pgam5*$^{+/+}$ *and Pgam5*$^{-/-}$ MEFs (left margin) after 20 h of mock treatment or treatment with 1 mM H_2O_2 (above images). Scale bars, 100 μM. Each symbol (**e**–**g**) represents an individual sample. $^*P < 0.05$ and $^{**}P < 0.001$ (two-way ANOVA). Data are representative of four independent affinity purifications per bait (**a**) or are from one experiment representative of three (**b**–**f**,**h**), six (**e**) or four (**g**) experiments (mean ± s.d. of six measurements in **e**,**f**,**g**).

© 2018 Nature America Inc., part of Springer Nature. All rights reserved.

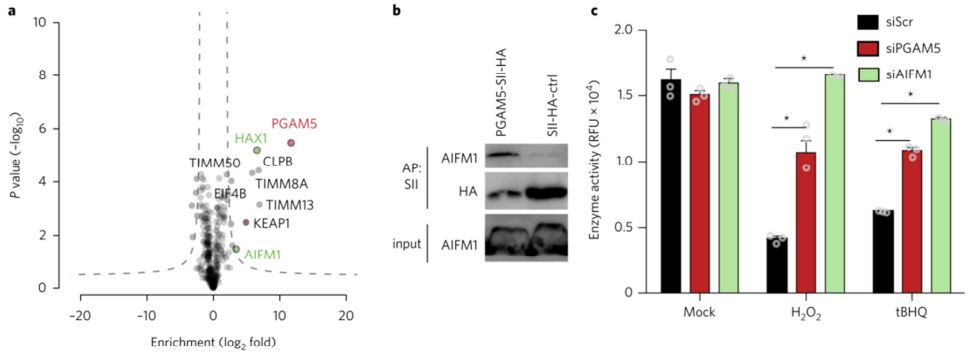

Fig. 3 | PGAM5 interacts with AIFM1. a, LC-MS/MS analysis of proteins showing enrichment with SII-HA-PGAM5 and THYN1 (control) from HeLa FlpIn cells (presented as in Fig. 2a, except values for hyperbolic curves: FDR = 0.001 and S0 = 0.2): red, PGAM5; green, proteins known to be involved in cell death. **b**, Immunoblot analysis of SII-HA-PGAM5 or SII-HA-control (ctrl) precipitates (top) and input lysates (bottom). **c**, Resazurin-conversion assay (as in Fig. 1c) of HeLa cells transfected with control siRNA (siScr) or siRNA targeting PGAM5 or AIFM1 (key), followed by 21 h of mock treatment or treatment with H_2O_2 or tert-butylhydroquinone (tBHQ) (horizontal axis). Each symbol (**c**) represents an individual sample. *$P < 0.001$ (two-way ANOVA). Data are representative of four independent affinity purifications per bait (**a**) or are from one experiment representative of eight experiments (**b**) or one experiment representative of four experiments (**c**; mean ± s.d. of three technical replicates).

ROS in mouse airway cells in vivo and led to severe inflammation, as indicated by an increased abundance of proteins, lymphocytes and cytokines in bronchoalveolar lavage fluid (BALF) of ozone-treated mice[26] (Fig. 1a and Supplementary Fig. 1a,b). In this in vivo model, the ozone-driven inflammation in mice that lacked key components of the inflammasome pathway such as NLRP3 (*Nlrp3*$^{-/-}$), caspase-1 and caspase-11 (*Casp1*$^{-/-}$*Casp11*$^{-/-}$) or the adaptor ASC (*Asc*$^{-/-}$) was not significantly different from that of wild-type mice (Fig. 1a). Furthermore, caspase-3 and caspase-7, which are required for apoptosis, are not activated after a single exposure to ozone[27,28]. Thus, in this experimental model, it was not clear which pathways were involved in ozone-mediated injury, inflammation or cell death.

Caspase-independent and kinase RIPK3–independent ROS-induced cell death. To investigate the pathways involved in ROS-mediated cell death in greater detail, we studied cell survival in response to the ROS inducer hydrogen peroxide (H_2O_2). Mouse embryonic fibroblasts (MEFs) exposed to H_2O_2 showed lower viability than that of untreated MEFs (Fig. 1b). Induction of cell death was not changed by pre-treatment with the caspase inhibitor Z-VAD or the necroptosis inhibitor Nec-7 (Fig. 1b). Furthermore, we assessed the morphology of MEFs by electron microscopy after exposure of the cells to H_2O_2. After treatment with H_2O_2, cells showed apoptotic membrane blebbing, which was also present in Z-VAD-treated cells exposed to H_2O_2 (Supplementary Fig. 1c). To confirm those data in different cell lines, we assessed the sensitivity of HeLa human cervical cancer cells and Jurkat human T lymphocytes to H_2O_2. As expected, treatment with H_2O_2 induced cell death, as measured by a resazurin-reduction assay, an ATP-abundance assay, a tetrazolium dye (MTT) assay and a lactate dehydrogenase–release assay (Fig. 1c and Supplementary Fig. 1d–f). Z-VAD was not able to restore cell viability (Fig. 1c and Supplementary Fig. 1f), despite successful inhibition of the cleavage of caspase-8 (Fig. 1d); this suggested a caspase-independent process. HeLa cells are naturally deficient in the kinase RIPK3 (Fig. 1e), a central component of the necroptosis pathway. Moreover, in line with published data[29], pretreatment of cells with Nec-7 or a combination of Nec-7 plus Z-VAD did not rescue the cells from H_2O_2-induced death (Fig. 1c). The ferroptosis inhibitor ferrostatin-1 also did not rescue cells from H_2O_2-triggered death (Fig. 1c and Supplementary Fig. 1h,i). Furthermore, the concentrations of H_2O_2 used did not lead to the accumulation of LC3-A, an indicator of autophagic cell death (Supplementary Fig. 1g), nor did the chemical inhibition of inflammasomes by CRID3 produce an effect (Fig. 1f). Combining inhibitors of apoptosis, necroptosis and ferroptosis did not influence H_2O_2-induced toxicity (Fig. 1g). Collectively, our data suggested that H_2O_2-induced cell death could be mediated by a pathway independent of caspases, ferroptosis, pyroptosis, autophagy or necroptosis.

KEAP1 is required for H_2O_2-induced cell death. A protein that directly links sensing of ROS to cell death has not been identified thus far. However, a well-studied sensor of ROS is KEAP1. KEAP1 contains carboxy-terminal cysteine residues that are oxidized by ROS and mediate a conformational change in the protein that results in the release of NRF2 for regulation of the expression of genes encoding cytoprotective molecules, to counterbalance oxidative stress[30]. We aimed to establish cellular systems with differential sensitivity to ROS; therefore, we depleted HeLa cells of KEAP1 and NRF2 and assessed their survival after treatment with H_2O_2. As expected, cellular depletion of KEAP1 led to upregulation of genes encoding cytoprotective molecules relative to their expression in control cells without such depletion (Supplementary Fig. 1j), and it significantly decreased cell death after treatment with H_2O_2 (Fig. 1h). Depleting cells of both KEAP1 and NRF2, which we expected would increase sensitivity to H_2O_2, also rescued cells from H_2O_2-induced death (Fig. 1h), despite no detectable upregulation of genes encoding cytoprotective molecules (Supplementary Fig. 1j). Moreover, expression of NRF2-dependent genes was increased by low concentrations of H_2O_2, while toxic concentrations of H_2O_2 did not increase gene expression (Fig. 1i). Collectively, we concluded that the transcriptional activity NRF2 was dispensable for cytoprotection after depletion of KEAP1, which suggested that KEAP1 is a concentration-dependent ROS sensor with an active role in a ROS-dependent cell-death pathway.

© 2018 Nature America Inc., part of Springer Nature. All rights reserved.

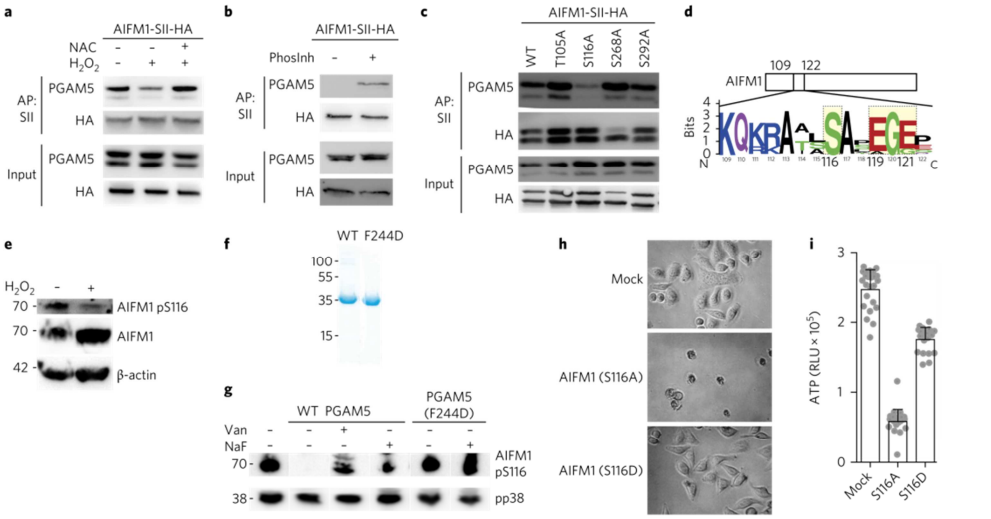

Fig. 4 | PGAM5 dephosphorylates AIFM1 Ser116. a, Immunoblot analysis of precipitates of AIFM1-SII-HA Hela FlpIn cells treated for 1 h with 2 mM *N*-acetylcysteine (NAC) (+) or not (–), followed by 10 h of treatment with 0.5 mM H_2O_2 (+) or not (–) (above lanes), assessed before (Input; bottom) and after (top) SII affinity purification. **b**, Immunoblot analysis of PGAM5 precipitated with SII-HA-AIFM1 in the presence (+) or absence (–) of phosphatase inhibitors (PhosInh). **c**, Immunoblot analysis of HEK293R1 (parental) cells transfected to express AIFM1-SII-HA wild-type or mutant proteins (above lanes), assessing the co-precipitation of those proteins with PGAM5 before (Input; bottom) and after (top) affinity purification with SII-beads. **d**, Sequence 'logo' of AIFM1 Ser116 and surrounding amino acids in 13 mammalian species. **e**, Immunoblot analysis of AIFM1 phosphorylated at Ser116 (AIFM1 pS116) or total AIFM1, and β-actin (right margin), in Jurkat cells left untreated (–) or treated (+) for 2 h with 0.5 mM H_2O_2 (above lanes). **f**, Coomassie blue–stained gel of purified recombinant wild-type PGAM5 (WT) or PGAM5(F244D) (above lanes). **g**, Immunoblot analysis of AIFM1 phosphorylated at Ser116 and phosphorylated p38 (pp38) (right margin) on nitrocellulose membranes onto which lysates of HeLa cells were blotted and then incubated for 30 min at 30 °C with 11 μg of recombinant wild-type PGAM5 or PGAM5(F244D) (above blots) or not (far left lane) in the presence (+) or absence (–) of sodium orthovanadate (Van) or sodium fluoride (NaF) (above lanes). **h**,**i**, Microscopy (**h**) and luminescent cell-viability assay (**i**) of HEK293 cells in which AIFM1 was knocked out, assessed 12 h after mock infection or infection with lentivirus encoding AIFM1(S116A) or AIFM1(S116D); results (**i**) are presented as relative light units (RLU). Each symbol (**i**) represents an individual sample. Data are representative of eight experiments (**a**) or four independent experiments (**i**; mean ± s.d. of six technical replicates in each) or are from one experiment representative of three (**b**,**e**,**f**), four (**c**) or five (**h**) experiments with similar results or one experiment representative of three experiments (**g**).

KEAP1 utilizes PGAM5 to mediate ROS-induced cell death. We next sought to identify potential interaction partners of KEAP1 that could convey signals that lead to cell death. Using affinity purification followed by tandem mass spectrometry (AP-LC-MS/MS), we identified 32 proteins for which KEAP1 purifications showed significant enrichment, relative to the abundance of an unrelated control protein (Fig. 2a and Supplementary Table 1). These 32 proteins included 14 known binding partners of KEAP1, including NRF2 (Fig. 2a). Only one protein identified had been previously associated with cell-death pathways: the phosphatase PGAM5 (Fig. 2a). PGAM5 is a convergence point of multiple cell-death pathways and has been shown to be involved in ROS-induced cell death[29]. PGAM5 bears an amino-terminal mitochondrial localization signal and transmembrane domain. Furthermore, PGAM5 interacts with KEAP1 and tethers it to the mitochondrial membrane[31]. We confirmed the association of KEAP1 with PGAM5 by co-immunoprecipitation of KEAP1 (tagged with streptavidin II and hemagglutinin (SII-HA)) with endogenous PGAM5 (Fig. 2b), as well as by co-immunoprecipitation of SII-HA-tagged PGAM5 with endogenous KEAP1 (Fig. 2c), and confirmed that amino acids 69–89 of PGAM5 were critical for its interaction with KEAP1[31] (Supplementary Fig. 2a). KEAP1 releases NRF2 after exposure to ROS and thereby allows accumulation of NRF2. This prompted us to investigate whether the interaction between KEAP1 and PGAM5 was similarly regulated by ROS. Indeed, binding of PGAM5 to KEAP1 was reduced in the presence of 0.5 mM H_2O_2, while non-toxic amounts of H_2O_2, which regulated NRF2-dependent gene expression (Fig. 1h,i), did not affect the interaction between KEAP1 and PGAM5 (Fig. 2c). KEAP1 and PGAM5 localized together with the mitochondrial marker COX IV under steady-state conditions[32] (Supplementary Fig. 2b). In the presence of 0.5 mM H_2O_2, only KEAP1, not PGAM5, lost its localization together with COX IV (Supplementary Fig. 2b), which further supported the proposal of a ROS-sensitive interaction between KEAP1 and PGAM5.

To determine functionally whether PGAM5 is involved in ROS-mediated cell death, we used small interfering RNA (siRNA)-mediated knockdown of PGAM5 and assessed the cells by a flow cytometry–based cell-survival assay after treatment with H_2O_2. In HeLa cells transfected with control (non-targeting) siRNA, treatment with H_2O_2 led to the death of 33% and 67% cells after 15 h and 20 h, respectively (Fig. 2d). Depleting cells of PGAM5 rescued the majority of cells from death; only 10% and 13% of the cells showed signs death at 15 h and 20 h, respectively, after treatment with H_2O_2 (Fig. 2d). Similarly, reduction enzyme activity was substantially decreased (< 10%) in cells transfected with control siRNA and treated with H_2O_2, while cells lacking PGAM5 showed more

© 2018 Nature America Inc., part of Springer Nature. All rights reserved.

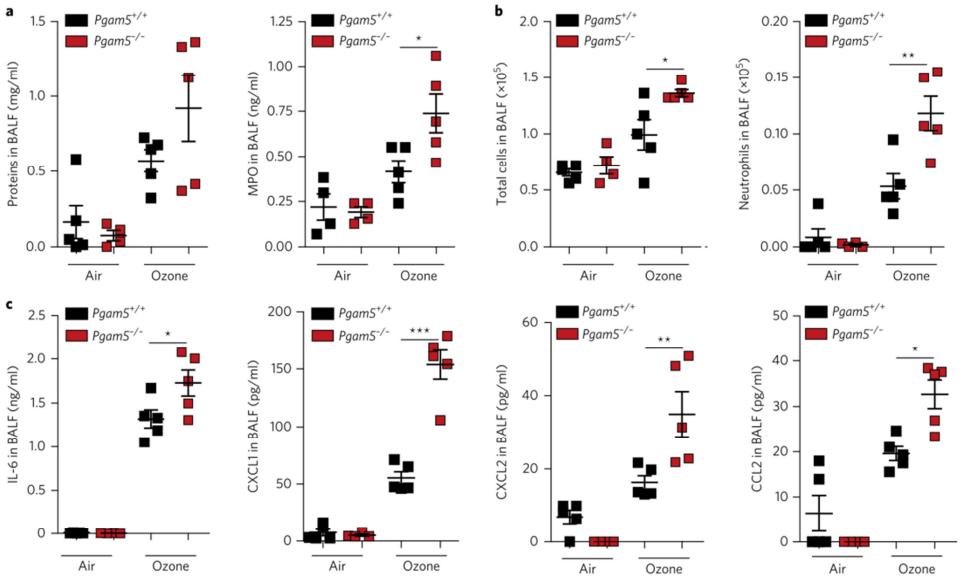

Fig. 5 | *Pgam5*$^{-/-}$ mice show severe inflammation in response to ozone exposure. a, Quantification of proteins (left) and myeloperoxidase (MPO) (right) in BALF of *Pgam5*$^{-/-}$ and wild-type (WT) mice ($n = 5$ per genotype) treated for 1 h with air or ozone (1 ppm) (horizontal axis), assessed after 4 h of recovery. **b**, Total cells (left) and neutrophils (right) in BALF of mice as in **a**. **c**, Luminex analysis of cytokines in BALF of mice as in **a**. Each symbol represents an individual mouse; small horizontal lines indicate the mean (±s.e.m.). $^{*}P < 0.05$, $^{**}P < 0.05$ and $^{***}P < 0.0001$ (one-way ANOVA and Bonferroni post *t*-test). Data are from one experiment representative of two experiments with similar results.

than 73% activity (Fig. 2e and Supplementary Fig. 2c,d). Depleting cells of both PGAM5 and NRF2 also rescued them from H_2O_2-induced death (Fig. 2e). While depleting cells of PGAM5 rescued them from H_2O_2-induced death, it did not affect the induction of apoptosis by staurosporin or the induction of necroptosis by Z-VAD plus TNF and mildly affected ferroptosis induced by the tyrosine kinase inhibitor sorafenib and autophagic cell death triggered by the electron-transport-chain accelerator CCCP (Fig. 2f). Inhibition of caspases in cells depleted of PGAM5 did not further increase cell viability (Supplementary Fig. 2e), which further excluded the possibility of apoptosis in this experimental setting. These data collectively suggested that depleting HeLa cells of PGAM5 did not produce a general effect but was specific for H_2O_2-induced cell death. We reproduced these data in a genetically 'clean' system; *Pgam5*$^{+/+}$ and *Pgam5*$^{+/-}$ MEFs (Supplementary Fig. 2f) treated with H_2O_2 showed severe signs of cytotoxicity (Fig. 2g). Morphologically, these cells showed membrane blebbing (Fig. 2h), a classic indicator of apoptotic cell death. However, *Pgam5*$^{-/-}$ MEFs tolerated treatment with a high dose of H_2O_2 (Fig. 2g) and were morphologically similar to untreated MEFs (Fig. 2h). Sorafenib decreased the viability of *Pgam5*$^{+/-}$ MEFs and *Pgam5*$^{-/-}$ MEFs similarly (Supplementary Fig. 2g). We concluded that PGAM5 was specifically involved in an H_2O_2-induced signaling cascade unrelated to other known cell-death pathways.

PGAM5-dependent cell-death induction utilizes AIFM1. PGAM5 has been proposed to be of central importance to the transmission of cell-death signals[29], but its molecular partners are not known. AP-LC-MS/MS with PGAM5 as bait identified eight interacting proteins with high confidence (Fig. 3a and Supplementary Table 2). As expected, PGAM5 associated with KEAP1 (Fig. 3a). Furthermore, PGAM5 precipitated together with proteins of the TIM complex (TIMM50, TIMM8A and TIMM13), which facilitates the transport of proteins to the inner mitochondrial membrane[33]. Among the proteins identified as interacting with PGAM5, only HAX1 ('HCLS1-associated protein X-1') and AIFM1 have been previously associated with cell-death pathways (Fig. 3a). Notably, AIFM1 has previously been linked to caspase-independent cell death[34]. We confirmed the PGAM5–AIFM1 interaction by co-precipitation followed by immunoblot analysis (Fig. 3b). Studies of AIFM1 mutants lacking various domains indicated that AIFM1 bound to PGAM5 through its amino-terminal domains (amino acids 2–103), which include the mitochondrial localization signal and the transmembrane domain, while carboxy-terminal sequences (amino acids 480–613) were not involved in its binding to PGAM5 (Supplementary Fig. 3a).To investigate whether AIFM1 serves as a downstream target of PGAM5, we depleted HeLa cells of AIFM1 or PGAM5 and monitored their survival after stimulation with H_2O_2 or the mitochondrial ROS inducer tBHQ. As expected, cells treated with the control siRNA were highly sensitive to treatment with H_2O_2 and tBHQ (Fig. 3c and Supplementary Fig. 3b). Notably, HeLa cells and SKN-BE2 human neuroblastoma cells depleted of AIFM1 or PGAM5 exhibited survival rates superior to those of control cells after treatment with H_2O_2 and tBHQ (Fig. 3c and Supplementary Fig. 3b, c). Combined depletion of KEAP1, PGAM5 and AIFM1 did not significantly increase viability in response to treatment with H_2O_2, relative to the viability of cells depleted of only one of these molecules (Supplementary Fig. 3d), which suggested that all three proteins were operating in

© 2018 Nature America Inc., part of Springer Nature. All rights reserved.

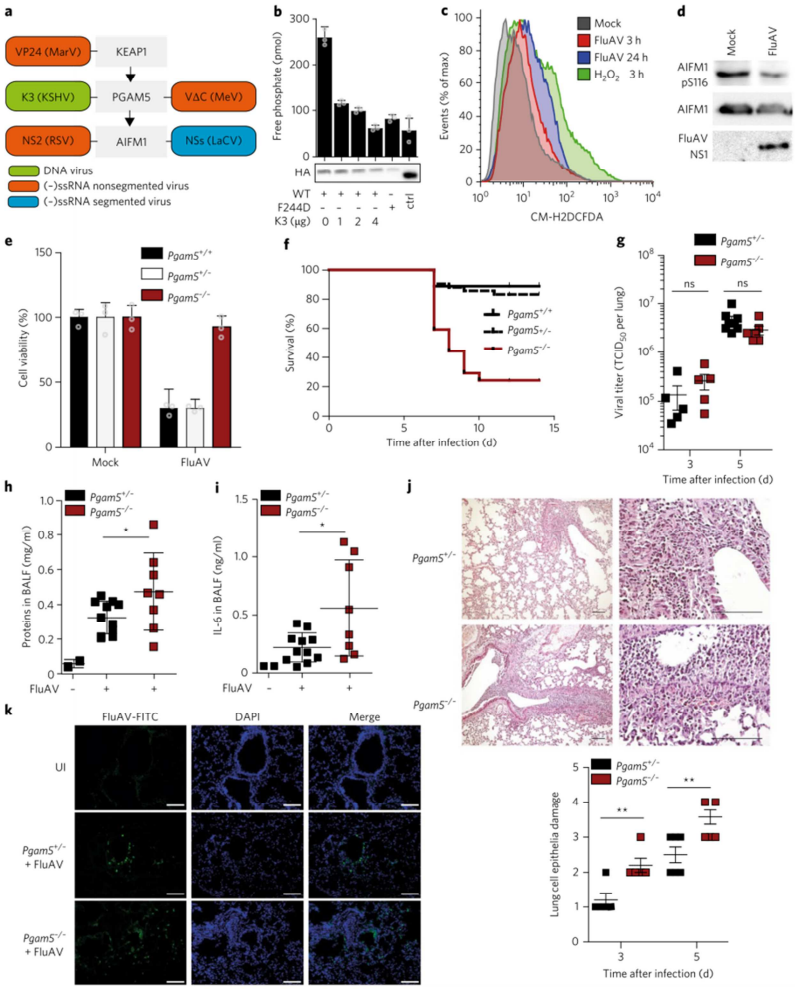

Fig. 6 | Oxeiptosis is activated by viral infection and targeted by viral proteins. a, Viral proteins identified (as published[48] and in Supplementary Fig. 6) as binding to KEAP1, PGAM5 or AIFM1. **b**, Phosphatase activity (top) of SII-tagged proteins precipitated from HEK293 cells transfected to express wild-type SII-HA-PGAM5 (WT) or SII-HA-PGAM5(F244D), together with various concentrations of the K3 protein of KSHV (grid below plot), evaluated with a peptide containing phosphorylated serine as a pseudo-substrate; middle, immunoblot analysis of SII-HA-tagged proteins in cell lysates. **c**, Flow cytometry of HeLa cells mock treated, infected for 3 h or 24 h with FluAV (multiplicity of infection, 3) or treated for 3 h with 0.5 mM H_2O_2 (key), assessed with CM-H2DCFDA (chloromethyl derivative of the fluorogenic reagent H2DCFDA), an indicator of ROS. **d**, Immunoblot analysis of AIFM1 phosphorylated at Ser116 (AIFM1 pS116), total AIFM1 and the FluAV protein NS1 (left margin) in Jurkat cells mock infected or infected for 24 h with FluAV (above lanes). **e**, Viability of *Pgam5*$^{+/+}$, *Pgam5*$^{+/-}$ and *Pgam5*$^{-/-}$ MEFs (key) after mock infection or infection for 21 h with FluAV (multiplicity of infection, 3), assessed by a resazurin viability assay. **f**, Survival of *Pgam5*$^{+/+}$ mice ($n = 9$), *Pgam5*$^{+/-}$ mice ($n = 42$) and *Pgam5*$^{-/-}$ mice ($n = 20$) (all littermates) monitored for 14 d after infection with FluAV and euthanized when they lost > 25% of their initial body weight. **g**, Viral titers in the lungs of mice as in **f** at 3 or 5 d after infection, presented as the half-maximal tissue culture infectious dose ($TCID_{50}$). **h**,**i**, Total protein (**h**) and IL-6 (**i**) in BALF of mice as in **f** left uninfected (−) or at 5 d after infection (+). **j**, Microscopy (H&E staining) of lungs from mice as in **f** at 5 d after infection (top), and lung damage in mice as in **f** at 3 and 5 d after infection (bottom). **k**, Immunofluorescence analysis of lung tissue from mice as in **f** left uninfected (UI) or at 5 d after infection (left margin). FITC, fluorescein isothiocyanate; DAPI, DNA-binding dye. Scale bars (**j**,**k**), 100 μm; original magnification, ×10 (**j**, left) or ×40 (**j**, right). Each symbol (**b**,**e**,**g**–**j**) represents an individual mouse; small horizontal lines (**g**–**j**) indicate the mean (±s.e.m.).*$P < 0.05$ and **$P < 0.02$ (two sided *t*-test). Data are representative of three (**b**,**c**,**k**), five (**d**), eight (**e**), two (**f**–**i**) or four (**j**) experiments (mean ± s.d. of three technical replicates in **b**; three replicates in **c**; mean ± s.d. of three individual treatments in **e**).

© 2018 Nature America Inc., part of Springer Nature. All rights reserved.

the same pathway. AIFM1 has been described to be central for the oxidoreductase pathway[35]. However, the mitochondrial respiration of HeLa cells left untreated or treated with various doses of H_2O_2 was indistinguishable (Supplementary Fig. 3e), which suggested that death-inducing amounts of intracellular ROS were independent of the oxidoreductase function of AIFM1.

PGAM5 dephosphorylates AIFM1 Ser116. We next investigated the functional interaction between PGAM5 and AIFM1. Notably, the binding of AIFM1 to PGAM5 was reduced when cells were treated with H_2O_2 (Fig. 4a). The binding was restored by the ROS scavenger N-acetylcysteine (Fig. 4a), which suggested that ROS can modulate the interaction between PGAM5 and AIFM1. PGAM5 is reported to have serine-threonine–phosphatase activity[29], and several studies have shown that processed substrates often lose interaction with their modifying enzymes[31]. Notably, binding of PGAM5 to AIFM1 was also diminished in the absence of phosphatase inhibitors (Fig. 4b). We replaced residues known to be phosphorylated in the amino-terminal region of AIFM1 (as identified online at https://www.phosphosite.org) with alanine and assessed their ability to precipitate together with endogenous PGAM5. Replacement of the serine at position 116 of AIFM1 with alanine (S116A) impaired the binding of AIFM1 to PGAM5, whereas replacement of other residues did not affect the association with PGAM5 (Fig. 4c). Sequence-alignment analysis revealed notable conservation of AIFM1 Ser116 and surrounding amino acid residues among mammals (Fig. 4d and Supplementary Fig. 4a). Of particular interest in this region were two glutamic acid residues (which contribute negative charges) located three and five amino acids carboxy-terminally of Ser116 (Fig. 4d and Supplementary Fig. 4a). Such contribution of negative charges has been reported to support the binding of substrates to the positively charged phosphatase active site of PGAM5[36] (Supplementary Fig. 4c). A 'custom-raised' antibody to AIFM1 phosphorylated at Ser116 indicated that Ser116 was phosphorylated under steady-state conditions (Fig. 4e and Supplementary Fig. 4b). Strikingly, treatment of cells with H_2O_2 led to dephosphorylation of phosphorylated Ser116 (Fig. 4e).

We generated recombinant PGAM5 and a phosphatase-inactive PGAM5 mutant unable to form dimers (PGAM5(F244D)) (Fig. 4f and Supplementary Fig. 4d–f,h) in order to assess the phosphatase activity of PGAM5. PGAM5 lacking amino acids 2–28 (PGAM5Δ2–28) was able to release phosphates from phosphorylated serine residues but not from pseudo-substrate peptides with phosphorylated threonine residues, while PGAM5Δ2–28(F244D) was inactive in this context (Supplementary Fig. 4i). Dephosphorylation of the pseudo-substrates was inhibited by the phosphatase inhibitor sodium orthovanadate (Supplementary Fig. 4i). We proceeded using membrane-bound lysates of HeLa cells as a substrate for recombinant PGAM5. Treatment of the membranes with recombinant proteins, followed by staining for phosphorylated AIFM1, showed that incubation with PGAM5Δ2–28 led to dephosphorylation of AIFM1 phosphorylated at Ser116 (Fig. 4g). This process was inhibited by sodium orthovanadate and sodium fluoride (Fig. 4g). The mutant protein PGAM5Δ2–28(F244D) did not dephosphorylate AIFM1 phosphorylated at Ser116 (Fig. 4g). The effect of recombinant PGAM5 was specific for AIFM1 phosphorylated at Ser116, since the kinase p38 was not dephosphorylated in this assay.

To assess the consequences of the dephosphorylation of AIFM1 Ser116 on cell survival, we reconstituted HEK293 human embryonic kidney cells in which AIFM1 was knocked out via CRISPR-Cas9 with expression plasmids for AIFM1, the mutant AIFM1(S116A) that cannot be phosphorylated or the mutant AIFM1(S116D) that mimics phosphorylation and monitored their survival. Expression of AIFM1(S116A) was sufficient to induce cell death, as indicated by rounding up of the cells and reduced levels of intracellular ATP, but expression of AIFM1(S116D) was not (Fig. 4h,i).

The data reported above showed that AIFM1 phosphorylated at Ser116 was dephosphorylated during oxidative stress and that PGAM5 was able to mediate this dephosphorylation. Furthermore, they highlighted the dephosphorylation of AIFM1 Ser116 as a hallmark of this cell-death pathway. We call this 'oxeiptosis', as it involves a cell-death pathway ('-ptosis') that can be triggered by oxidative stress.

***Pgam5*$^{-/-}$ mice show severe inflammation in response to ozone treatment.** In order to gain information about the role of PGAM5 in vivo, we assessed the response of *Pgam5*$^{+/+}$ mice (as a control) and *Pgam5*$^{-/-}$ mice to the ROS inducer ozone. We exposed *Pgam5*$^{+/+}$ and *Pgam5*$^{-/-}$ mice to ozone and assessed inflammation parameters 4 h and 24 h later. Treatment with ozone led to a greater abundance of protein in the BALF of *Pgam5*$^{-/-}$ mice than in that of *Pgam5*$^{+/+}$ mice (Fig. 5a and Supplementary Fig. 5a). Specifically, we noted significantly more myeloperoxidase, an inflammation-specific marker generated by myeloid cells, in the BALF of *Pgam5*$^{-/-}$ mice than in that of *Pgam5*$^{+/+}$ mice (Fig. 5a). Ant increase in inflammation was confirmed by the greater total number of cells in the BALF of ozone-treated *Pgam5*$^{-/-}$ mice than in that of their *Pgam5*$^{+/+}$ counterparts, most strikingly a significantly greater number of neutrophils in *Pgam5*$^{-/-}$ mice than in *Pgam5*$^{+/+}$ mice (Fig. 5b and Supplementary Fig. 5b). The BALF of ozone-treated *Pgam5*$^{-/-}$ mice had significantly higher concentrations of the cytokine IL-6 and the chemokines CXCL1, CXCL2 and CCL2 than did that of their *Pgam5*$^{+/+}$ counterparts (Fig. 5c). Collectively, these data indicated that PGAM5 deficiency in mice led to increased inflammation after exposure to an inducer of ROS. This suggested that PGAM5 is needed to dampen inflammatory responses and that the absence of PGAM5 in vivo leads to compensatory inflammatory responses.

Oxeiptosis is targeted by viral open reading frames. Viral infection commonly triggers the generation of intracellular ROS[18], which can lead to cell death. As a countermeasure, many viruses regulate cell-death pathways in order to optimize their own replication and spread. Mining an AP-MS data set that identified cellular binding partners of regulators in the innate immune system[37] for molecules that interact with KEAP1, PGAM5 or AIFM1 revealed four proteins from distantly related viruses that interacted with any of these three proteins (Fig. 6a). VP24 of Marburg virus bound KEAP1[19,38]; VΔC of measles virus and K3 of KSHV associated with PGAM5 (Supplementary Fig. 6a–d and Supplementary Table 3); and the non-structural protein NSs of La Crosse virus bound AIFM1 (Supplementary Fig. 6e,f). In additional interaction studies of the non-structural protein NS2 of respiratory syncytial virus, we identified the PGAM5-interaction site (amino acids 2–55) of AIFM1 as a cellular target (Supplementary Fig. 6g–i and Supplementary Table 4). We proceeded to functionally assess the interaction of K3 (KSHV) and PGAM5. The binding of PGAM5 to K3 required amino acids 29–69 of PGAM5 (Supplementary Fig. 6d), a region that has previously been identified as being important for full PGAM5 functionality[36]. Precipitates of SII-HA-PGAM5 from cells co-expressing K3 showed diminished phosphatase activity (Fig. 6b), which confirmed the functional interaction between PGAM5 and K3. Collectively, these data indicated that distantly related viruses shared an ability to bind KEAP1, PGAM5 or AIFM1, suggestive of evolutionary pressure to target this pathway.

PGAM5 regulates virus-induced inflammation in vivo. We used infection with influenza A virus (FluAV) as model to assess the involvement of oxeiptosis in viral infection. HeLa cells infected with FluAV strain SC35M showed accumulation of intracellular ROS (Fig. 6c) and expression of genes encoding cytoprotective molecules (Supplementary Fig. 6j). Furthermore, infection with FluAV led to less phosphorylation of AIFM1 at Ser116 than that of unin-

© 2018 Nature America Inc., part of Springer Nature. All rights reserved.

fected control cells (Fig. 6d), indicative of the activation of oxeiptosis. In line with that, HeLa cells depleted of PGAM5 (via siRNA) showed significantly less FluAV-induced cytotoxicity than that of cells treated with control siRNA (Supplementary Fig. 6k). Similarly, infection of *Pgam5*$^{-/-}$ MEFs with FluAV resulted in survival rates superior to those of FluAV-infected *Pgam5*$^{+/+}$ or *Pgam5*$^{+/-}$ (control) cells (Fig. 6e), indicative of a role for PGAM5 in virus-induced cell death in vitro. To assess the function of PGAM5 in vivo, we infected *Pgam5*$^{+/+}$, *Pgam5*$^{+/-}$ and *Pgam5*$^{-/-}$ mice with 1,500 plaque-forming units of FluAV. This infection regime caused only 10% mortality in *Pgam5*$^{+/+}$ and *Pgam5*$^{+/-}$ mice (Fig. 6f). In contrast, *Pgam5*$^{-/-}$ mice showed a markedly greater mortality rate, since 78% of these mice succumbed to infection with FluAV (Fig. 6f). Surprisingly, viral titers and levels of viral mRNA in the lungs of *Pgam5*$^{+/-}$ mice on days 3 and 5 after infection were indistinguishable from those in *Pgam5*$^{-/-}$ mice (Fig. 6g and Supplementary Fig. 6l), which suggested that PGAM5 did not directly affect viral replication and that the increased susceptibility to infection to FluAV was not due to an exacerbated viral load. However, in line with the results of the ozone-exposure experiments (Fig. 5c), mouse lungs showed significantly more *Il6* mRNA in the absence of PGAM5 than in its presence (Supplementary Fig. 6m). Similarly, the BALF of FluAV-infected *Pgam5*$^{-/-}$ mice contained more protein (Fig. 6h) and significantly more inflammatory cytokines such as IL-6, CXCL1 and CCL2 (Fig. 6i and Supplementary Fig. 6n) than that of FluAV-infected *Pgam5*$^{+/-}$ mice. These experiments suggested exacerbated inflammatory processes during infection with FluAV in the absence of PGAM5. Indeed, histological analysis of the lungs of FluAV-infected mice showed more-severe lung pathology, with significantly more destruction of the epithelial layer in the bronchioles and more infiltration of lymphocytes in *Pgam5*$^{-/-}$ mice than in *Pgam5*$^{+/-}$ mice (Fig. 6j). However, immunohistochemistry analyzing the distribution of FluAV proteins in the lungs of infected mice showed much deeper infiltration of FluAV in *Pgam5*$^{-/-}$ mice than in *Pgam5*$^{+/-}$ mice (Fig. 6k). From these experiments, we concluded that PGAM5 was needed to modulate inflammatory responses in vivo and that lack of PGAM5 in the context of infection with FluAV resulted in acute necrotic intrabronchial and peribronchial inflammation, which allowed deeper infiltration of the virus.

DISCUSSION

Cells have to make critical 'decisions' about how to respond to physiological and pathological insults. Infections, inflammatory cytokines and other environmental cues can raise ROS levels to detrimental concentrations that contribute to pathological disease manifestations[16,39,40]. However, a dedicated sensor of ROS that is linked to cell death or mediates inflammatory responses has not been described thus far. Here we found that the well-described ROS sensor KEAP1 induced a cell-death pathway that signaled through PGAM5 and AIFM1.

Interestingly, KEAP1 bears 27 cysteine residues in its carboxyl terminus, which can be modified in a stimulus-dependent manner[6]. These cysteine residues not only might allow sensing of the presence or absence of ROS but also might be able to quantify ROS and induce concentration-specific responses. Such a system might allow a single protein to integrate quantitative information in order to regulate diverse cellular signaling pathways and to respond to environmental needs in an appropriate manner. That model is supported by the finding of dissociation of KEAP1 and PGAM5 that was observed only in the presence of a high concentration of H_2O_2, while concentrations that activated KEAP1-dependent activation of NRF2 did not perturb this interaction. This would probably explain the dual characteristics of KEAP1 in regulating NRF2-dependent protection at low levels of ROS while mediating the induction of cell death through the release of PGAM5 at high levels of oxidative stress.

PGAM5 has been proposed to function at a convergence point of multiple caspase-independent cell death pathways[29]. Notably, cell-death stimuli reported to signal through PGAM5, such as TNF, H_2O_2, *t*-butyl hydroxide and A23187, have all been shown to generate intracellular ROS[41,42], which might explain the ability of PGAM5 to integrate many diverse cell-death signals.

The signaling downstream of PGAM5 that results in cell death remains unknown. By AP-LC-MS/MS analysis, we identified AIFM1 as a binding partner of PGAM5. AIFM1 resides inside mitochondria and thus should be spatially dissociated from PGAM5. However, KEAP1 is reported to be tethered to the outer membrane of mitochondria through engagement of PGAM5[32]. Conversely, the same mechanism could mediate retention of PGAM5 at the outer mitochondrial membrane in order to spatially dissociate it from its phosphatase target, AIFM1. Interestingly, PGAM5 bears a CX9C motif (two cysteine residues separated by nine irrelevant amino acids (X9), in the region from Cys229 to Cys239) that can be used by the Mia40 complex to import proteins into mitochondria[43]. In line with the possibility of an activity in mitochondria, PGAM5 physically interacts with members of the TIMM complex (TIMM8 and TIMM13), which is known to be involved in regulating protein import into mitochondria[33]. Release of PGAM5 by KEAP1 during oxidative stress might be part of an activation process that allows internalization of PGAM5 into the mitochondria so it can interact with its target AIFM1. We identified the highly conserved residue Ser116 in AIFM1 as a target of the phosphatase activity of PGAM5. PGAM5 dephosphorylated AIFM1 at Ser116 during treatment with large amounts of H_2O_2 and during the course of viral infection. Functionally, expression of AIFM1(S116A) was sufficient to induce death of AIFM1-deficient cells.

On the basis of those data, we propose the existence of a caspase-independent cell-death pathway, which we have called 'oxeiptosis'. This pathway encompasses KEAP1–PGAM5–AIFM1 and is activated by detrimental levels of ROS. Dephosphorylated AIFM1 Ser116 serves as a marker and is at the same time a key regulator of the activity of the oxeiptosis pathway.

An increase in oxidative stress has been linked to necroptosis, apoptosis, ferroptosis, autophagy and pyroptosis[44,45]. These pathways operate in parallel and integrate additional signals. The engagement of these pathways is also cell type dependent, since some of the individual pathways are limited to certain cell types. We propose that oxeiptosis operates in parallel with other cell-death pathways and leads to a non-inflammatory, caspase-independent, apoptosis-like cell-death phenotype. It is operational in a wide range of cells, with the possible exception of macrophages, since PGAM5 deficiency has been reported to be dispensable for ROS-dependent death in these cells[46]. In line with the possibility of an apoptosis-like anti-inflammatory activity for PGAM5 in vitro, *Pgam5*$^{-/-}$ mice showed increased inflammatory parameters in their BALF after exposure to ozone or infection with FluAV.

ROS are produced during many disorders, including allergy, autoimmunity, allograft rejection, cancer and infection with pathogens, which suggests that oxeiptosis might be activated in many different pathological situations[47]. Notably, it has been shown that treatment of tumors with ROS-inducing agents such as BZL101 induces cell death in an AIFM1-dependent manner[48]. *Keap1* is often mutated in lung, gallbladder and head-and-neck cancers, and *Keap1* expression is silenced by hypermethylation of its promoter in various cell lines derived from lung and prostate cancers[49]; this could lead to dysfunction of the oxeiptosis pathway and could thereby promote the survival of transformed cells. Similarly, evolutionary distinct viruses interfered with KEAP1, PGAM5 and AIFM1. This indicated that modulation of oxeiptosis is involved in antiviral immunity. Indeed, we identified an important role for PGAM5 during infection with FluAV, and PGAM5 deficiency in mice led to increased inflammatory responses.

© 2018 Nature America Inc., part of Springer Nature. All rights reserved.

Published reports suggest activation of RIPK3-dependent necroptosis by FluAV, and FluAV-infected *Ripk3*$^{-/-}$ mice show decreased inflammatory parameters in their lungs[50]. It is likely that the pro-inflammatory phenotype of FluAV-infected *Pgam5*$^{-/-}$ mice was mediated by compensatory activation of Ripk3-dependent necroptosis.

An important complication of treating virus-derived tumors might be the activity of viral proteins, such as the K3 protein of KSHV, which directly affected the functionality of PGAM5.

Our study has identified oxeiptosis, a ROS-induced cell-death pathway that leads to a caspase-independent non-inflammatory cell death and encompasses KEAP1, PGAM5 and AIFM1. Similar to viral interference with KEAP1, PGAM5 or AIFM1, we propose that targeting oxeiptosis through therapeutic intervention might constitute a means with which to modulate the progression of diseases that involve oxidative stress.

Methods

Methods, including statements of data availability and any associated accession codes and references, are available at https://doi.org/10.1038/s41590-017-0013-y.

Received: 10 January 2017; Accepted: 17 November 2017;
Published online: 18 December 2017

References

1. Sauer, H., Wartenberg, M. & Hescheler, J. Reactive oxygen species as intracellular messengers during cell growth and differentiation. *Cell. Physiol. Biochem.* **11**, 173–186 (2001).
2. Nakamura, H., Nakamura, K. & Yodoi, J. Redox regulation of cellular activation. *Annu. Rev. Immunol.* **15**, 351–369 (1997).
3. Sandalio, L. M., Rodríguez-Serrano, M., Romero-Puertas, M. C. & del Río, L. A. Role of peroxisomes as a source of reactive oxygen species (ROS) signaling molecules. *Subcell. Biochem.* **69**, 231–255 (2013).
4. Rosca, M. G. et al. Oxidation of fatty acids is the source of increased mitochondrial reactive oxygen species production in kidney cortical tubules in early diabetes. *Diabetes* **61**, 2074–2083 (2012).
5. Lü, J.-M., Lin, P. H., Yao, Q. & Chen, C. Chemical and molecular mechanisms of antioxidants: experimental approaches and model systems. *J. Cell. Mol. Med.* **14**, 840–860 (2010).
6. Taguchi, K., Motohashi, H. & Yamamoto, M. Molecular mechanisms of the Keap1-Nrf2 pathway in stress response and cancer evolution. *Genes to Cells* **16**, 123–140 (2011).
7. Song, J. J. et al. Role of glutaredoxin in metabolic oxidative stress. Glutaredoxin as a sensor of oxidative stress mediated by H2O2. *J. Biol. Chem.* **277**, 46566–46575 (2002).
8. Zhang, D. D. & Hannink, M. Distinct cysteine residues in Keap1 are required for Keap1-dependent ubiquitination of Nrf2 and for stabilization of Nrf2 by chemopreventive agents and oxidative stress. *Mol. Cell. Biol.* **23**, 8137–8151 (2003).
9. Bryan, H. K., Olayanju, A., Goldring, C. E. & Park, B. K. The Nrf2 cell defence pathway: Keap1-dependent and -independent mechanisms of regulation. *Biochem. Pharmacol.* **85**, 705–717 (2013).
10. Kaspar, J. W., Niture, S. K. & Jaiswal, A. K. Nrf2:INrf2 (Keap1) signaling in oxidative stress. *Free Radic. Biol. Med.* **47**, 1304–1309 (2009).
11. Circu, M. L. & Aw, T. Y. Reactive oxygen species, cellular redox systems, and apoptosis. *Free Radic. Biol. Med.* **48**, 749–762 (2010).
12. Yang, D. et al. Pro-inflammatory cytokines increase reactive oxygen species through mitochondria and NADPH oxidase in cultured RPE cells. *Exp. Eye Res.* **85**, 462–472 (2007).
13. Hroudová, J., Singh, N. & Fišar, Z. Mitochondrial dysfunctions in neurodegenerative diseases: relevance to Alzheimer's disease. *BioMed. Res. Int.* **2014**, 175062 (2014).
14. Ano, Y. et al. Oxidative damage to neurons caused by the induction of microglial NADPH oxidase in encephalomyocarditis virus infection. *Neurosci. Lett.* **469**, 39–43 (2010).
15. Li, Y., Boehning, D. F., Qian, T., Popov, V. L. & Weinman, S. A. Hepatitis C virus core protein increases mitochondrial ROS production by stimulation of Ca^{2+} uniporter activity. *FASEB J.* **21**, 2474–2485 (2007).
16. Bhattacharya, A. et al. Superoxide dismutase 1 protects hepatocytes from type I interferon-driven oxidative damage. *Immunity* **43**, 974–986 (2015).
17. Olagnier, D. et al. Cellular oxidative stress response controls the antiviral and apoptotic programs in dengue virus-infected dendritic cells. *PLoS Pathog.* **10**, e1004566 (2014).
18. Bottero, V., Chakraborty, S. & Chandran, B. Reactive oxygen species are induced by Kaposi's sarcoma-associated herpesvirus early during primary infection of endothelial cells to promote virus entry. *J. Virol.* **87**, 1733–1749 (2013).
19. Edwards, M. R. et al. The Marburg virus VP24 protein interacts with Keap1 to activate the cytoprotective antioxidant response pathway. *Cell Reports* **6**, 1017–1025 (2014).
20. Johnson, B. et al. Dimerization controls Marburg virus VP24-dependent modulation of host antioxidative stress responses. *J. Mol. Biol.* **428**, 3483–3494 (2016).
21. Amri, F., Ghouili, I., Amri, M., Carrier, A. & Masmoudi-Kouki, O. Neuroglobin protects astroglial cells from hydrogen peroxide-induced oxidative stress and apoptotic cell death. *J. Neurochem.* **140**, 151–169 (2017).
22. Kim, J.-Y. & Park, J.-H. ROS-dependent caspase-9 activation in hypoxic cell death. *FEBS Lett.* **549**, 94–98 (2003).
23. Radogna, F. et al. Cell type-dependent ROS and mitophagy response leads to apoptosis or necroptosis in neuroblastoma. *Oncogene* **35**, 3839–3853 (2016).
24. Ravindran, J., Gupta, N., Agrawal, M., Bala Bhaskar, A. S. & Lakshmana Rao, P. Modulation of ROS/MAPK signaling pathways by okadaic acid leads to cell death via, mitochondrial mediated caspase-dependent mechanism. *Apoptosis* **16**, 145–161 (2011).
25. Shen, C. et al. Aldehyde dehydrogenase 2 deficiency negates chronic low-to-moderate alcohol consumption-induced cardioprotecion possibly via ROS-dependent apoptosis and RIP1/RIP3/MLKL-mediated necroptosis. *Biochim. Biophys. Acta* **1863**, 1912–1918 (2017).
26. Wiegman, C. H. et al. Oxidative stress-induced mitochondrial dysfunction drives inflammation and airway smooth muscle remodeling in patients with chronic obstructive pulmonary disease. *J. Allergy Clin. Immunol.* **136**, 769–780 (2015).
27. Triantaphyllopoulos, K. et al. A model of chronic inflammation and pulmonary emphysema after multiple ozone exposures in mice. *Am. J. Physiol. Lung Cell. Mol. Physiol.* **300**, L691–L700 (2011).
28. Kosmider, B., Loader, J. E., Murphy, R. C. & Mason, R. J. Apoptosis induced by ozone and oxysterols in human alveolar epithelial cells. *Free Radic. Biol. Med.* **48**, 1513–1524 (2010).
29. Wang, Z., Jiang, H., Chen, S., Du, F. & Wang, X. The mitochondrial phosphatase PGAM5 functions at the convergence point of multiple necrotic death pathways. *Cell* **148**, 228–243 (2012).
30. Kobayashi, A. et al. Oxidative stress sensor Keap1 functions as an adaptor for Cul3-based E3 ligase to regulate proteasomal degradation of Nrf2. *Mol. Cell. Biol.* **24**, 7130–7139 (2004).
31. Lo, S.-C. & Hannink, M. PGAM5, a Bcl-XL-interacting protein, is a novel substrate for the redox-regulated Keap1-dependent ubiquitin ligase complex. *J. Biol. Chem.* **281**, 37893–37903 (2006).
32. Lo, S.-C. & Hannink, M. PGAM5 tethers a ternary complex containing Keap1 and Nrf2 to mitochondria. *Exp. Cell Res.* **314**, 1789–1803 (2008).
33. Ceh-Pavia, E., Spiller, M. P. & Lu, H. Folding and biogenesis of mitochondrial small Tim proteins. *Int. J. Mol. Sci.* **14**, 16685–16705 (2013).
34. Susin, S. A. et al. Molecular characterization of mitochondrial apoptosis-inducing factor. *Nature* **397**, 441–446 (1999).
35. Joza, N. et al. AIF: not just an apoptosis-inducing factor. *Ann. NY Acad. Sci.* **1171**, 2–11 (2009).
36. Wilkins, J. M., McConnell, C., Tipton, P. A. & Hannink, M. A conserved motif mediates both multimer formation and allosteric activation of phosphoglycerate mutase 5. *J. Biol. Chem.* **289**, 25137–25148 (2014).
37. Pichlmair, A. et al. Viral immune modulators perturb the human molecular network by common and unique strategies. *Nature* **487**, 486–490 (2012).
38. Page, A. et al. Marburgvirus hijacks nrf2-dependent pathway by targeting nrf2-negative regulatorkeap1. *Cell Rep.* **6**, 1026–1036 (2014).
39. Medvedev, R., Ploen, D. & Hildt, E. HCV and oxidative stress: implications for HCV life cycle and HCV-associated pathogenesis. *Oxid. Med. Cell. Longev.* **2016**, 9012580 (2016).
40. Ren, J.-H. et al. Protective Role of Sirtuin3 (SIRT3) in oxidative stress mediated by hepatitis B virus X protein expression. *PLoS One* **11**, e0150961 (2016).
41. Kajitani, N. et al. Mechanism of A23187-induced apoptosis in HL-60 cells: dependency on mitochondrial permeability transition but not on NADPH oxidase. *Biosci. Biotechnol. Biochem.* **71**, 2701–2711 (2007).
42. Blaser, H., Dostert, C., Mak, T. W. & Brenner, D. TNF and ROS crosstalk in inflammation. *Trends Cell Biol.* **26**, 249–261 (2016).
43. Chacinska, A. et al. Essential role of Mia40 in import and assembly of mitochondrial intermembrane space proteins. *EMBO J.* **23**, 3735–3746 (2004).
44. Shindo, R., Kakehashi, H., Okumura, K., Kumagai, Y. & Nakano, H. Critical contribution of oxidative stress to TNFα-induced necroptosis downstream of RIPK1 activation. *Biochem. Biophys. Res. Commun.* **436**, 212–216 (2013).
45. Dixon, S. J. et al. Ferroptosis: an iron-dependent form of nonapoptotic cell death. *Cell* **149**, 1060–1072 (2012).
46. Moriwaki, K. et al. The mitochondrial phosphatase PGAM5 is dispensable for necroptosis but promotes inflammasome activation in macrophages. *J. Immunol.* **196**, 407–415 (2016).

© 2018 Nature America Inc., part of Springer Nature. All rights reserved.

47. Szatrowski, T. P. & Nathan, C. F. Production of large amounts of hydrogen peroxide by human tumor cells. *Cancer Res.* **51**, 794–798 (1991).
48. Marconett, C. N. et al. BZL101, a phytochemical extract from the Scutellaria barbata plant, disrupts proliferation of human breast and prostate cancer cells through distinct mechanisms dependent on the cancer cell phenotype. *Cancer Biol. Ther.* **10**, 397–405 (2010).
49. Wang, R. et al. Hypermethylation of the Keap1 gene in human lung cancer cell lines and lung cancer tissues. *Biochem. Biophys. Res. Commun.* **373**, 151–154 (2008).
50. Nogusa, S. et al. RIPK3 activates parallel pathways of MLKL-driven necroptosis and fadd-mediated apoptosis to protect against influenza A virus. *Cell Host Microbe* **20**, 13–24 (2016).

Acknowledgements

We thank F. Weber (Veterinary University Giessen) for pI.18_3xFlag_NSs and pI.18_3xFlag_DMx_1xFlag; F. Meissner (Max-Planck Institute of Biochemistry, Munich) for Jurkat cells; R. Klein (Max-Planck Institute of Neurobiology, Munich) for SKN-BE2 cells; A. Bowie (Trinity College Dublin) for HEK293 cells; A. Musacchio (Max-Planck Institute of Cell Biology, Dresden) for HeLa FlpIn cells; G. Kochs (University of Freiburg) for antibody to FluAV NS1; A. Chaikuad and S. Knapp (University of Oxford) for amino-terminal His-tagged PGAM5 (pNIC28-Bsa4-PGAM5(Δ2–28); the innate immunity laboratory for critical discussions and suggestions; A. Mann for technical assistance; the MPI-B core facility for technical assistance with protein purification, analysis and imaging; M. Wilson and ECM Biosciences for raising the antibody to AIFM1 phosphorylated at Ser116; K. Mayr, I. Paron and G. Sowa for maintaining mass spectrometers; and S. Kaphengst and the MPI-B animal facility for breeding mice. Supported by the Max-Planck Free Floater program (A.P.), the German research foundation (PI 1084/2 and TRR179 to A.P. and SFB 1160, project 13) to P.S.), the European Research Council (starting grant ERC-StG iVIP, 311339 to A.P.), Infect-Era and the German Federal Ministry of Education and Research (ERASE) (A.P.), the US National Institutes of Health (R01 AI107056 and 1R41AI127009 (Moir) to D.W.L and G.K.A.), the Centre National de la Recherche Scientifique (B.R.) and the European Regional Development Fund (BIO-TARGET 2016-00110366 to Region Centre Val de Loire and la Région Centre (Respir_Ozone, 2014-00091905) (Valerie Quesniaux), to B.R.).

Author contributions

C.H., Ch.M., Cl.M., D.A.H., F.L.P., D.S., J.W., M.B. and P.S. conducted the experiments; C.B. performed structural modelling; C.H., D.A.H. and P.H. analyzed data; D.W.L and G.K.A. contributed reagents; and C.H., D.W.L, G.K.A., F.P., P.S., B.R. and A.P. designed the experiments and wrote the paper.

Competing interests

The authors declare no competing financial interests.

Additional information

Supplementary information is available for this paper at https://doi.org/10.1038/s41590-017-0013-y.

Reprints and permissions information is available at www.nature.com/reprints.

Correspondence and requests for materials should be addressed to A.P.

Publisher's note: Springer Nature remains neutral with regard to jurisdictional claims in published maps and institutional affiliations.

© 2018 Nature America Inc., part of Springer Nature. All rights reserved.

Methods

Plasmids. Expression constructs were generated by PCR amplification of plasmids from ImaGenes cDNA Library (MPI core Facility) and a cDNA library obtained from HeLa cells followed by Gateway cloning (Invitrogen) into the plasmids pcDNA3-Ren-GW, pTO-SII-HA-GW and pLenti6-V5-GW[37,51]. Mutations and truncations were introduced by PCR. pI.18_3xFlag_NSs (La Crosse virus) and pI.18_3xFlag_DMx_1xFlag were provided by F. Weber (Giessen). Sequences were verified by Sanger sequencing.

Cells, reagents and viruses. HeLa S3 cells (CCL-2.2) and Vero E6 cells (CRL-1586) were purchased from ATCC. THP-1 cells (300356) were purchased from CLS. Jurkat cells were a gift from Felix Meissner (MPI of Biochemistry, Munich). SKN-BE2 cells were provided by R. Klein (MPI of Neurobiology, Munich). HEK293 cells were a gift from A. Bowie. HeLa FlpIn cells (a gift from A. Musacchio, MPI of Cell Biology, Dresden) stably expressing SII-HA-tagged human PGAM5, AIFM1, KEAP1, K3, K5, NS2 and THYN1 under control of the CMV promoter were generated by hygromycin selection. Mouse embryonic fibroblasts (MEFs) were isolated from 13.5-day-old embryos from heterozygous breeding pairs.

Cell lines were maintained in DMEM (PAA Laboratories) or RPMI (PAA Laboratories) (for THP-1 and Jurkat cells) containing 10% FCS (GE Healthcare) and antibiotics (100 U/ml penicillin and 100 µg/ml streptomycin). Streptavidin-agarose beads were obtained from Novagen. Hydrogen peroxide, M2-Flag beads, Malachite green, *N*-acetylcysteine, necrostatin-7, resazurin, sodium fluoride, tert-butylhydroquinone (tBHQ) and thiazolyl blue tetrazolium bromide (MTT) were from Sigma, Necrosulfomamide was from Merck, Polyethylenimine linear MW 25.000 was from Polysciences, and orthovanadate was from Alfa Aesar. The pan-caspase inhibitor Z-VAD-FMK was from R&D Systems. Primary antibodies used in this study were directed against the following molecules: PGAM5 (HPA036978) (Sigma); renilla-tag (MAB4410) (Millipore); AIFM1 (5318), caspase-8 (9746), KEAP1 (8047), MLKL (14993), NRF2 (12721), phosphorylated p38 (4511), RIPK3 (13526) and COX IV (11967) (all from Cell Signaling); and AIFM1 phosphorylated at Ser116 (AP5501) (ECM Bioscience). Antibody to FluAV NS1 was a gift from G. Kochs (Freiburg). Antibodies to actin (sc-47778) (Santa Cruz), His-tag (sc-8036) (Santa Cruz), Flag-M2-tag (A8592) (Sigma) and HA-tag (H6533) (Sigma), and secondary antibodies detecting mouse IgG (Dako P0447) or rabbit IgG (Dako P0448) (Jackson ImmunoResearch, Dako) were horseradish peroxidase (HRP) coupled. CM-H_2DCFDA and 4′,6-diamidino-2-phenylindole (DAPI) were purchased from Invitrogen. Secondary antibodies for immunofluorescense analyses were FITC-coupled goat anti-rabbit (BD 554020), Alexa488-coupled goat anti-mouse (Invitrogen A32723) and Alexa594-coupled goat anti-rabbit (Invitrogen A-11012). The Apoptosis/Necrosis assay Detection Kit was purchased from Abcam. The CellTiter-Glo assay kit and CytoTox 96 Non-Radioactive Cytotoxicity Assay (lactate dehydrogenase assay) were purchased from Promega. Recombinant influenza virus (strain SC35M wild-type) was described previously[52]. Reagents for electron microscopy were the following: sodium cacodylate 0.2 M (Electron Microscopy Sciences, cat.#11653), 2% osmium tetroxide (Electron Microscopy Sciences, cat.#19152) and Low Viscosity Embedding Media Spurr's Kit (Electron Microscopy Sciences, cat.# E14300).

Cloning and expression of recombinant proteins and phosphatase assay. Amino-terminal His-tagged PGAM5 (pNIC28-Bsa4-PGAM5(Δ2–28)) (PDB accession code 3MXO) was provided by A. Chaikuad and S. Knapp (University of Oxford). For solubility reasons, the recombinant protein carried a deletion of amino acids 2–28. The substitution F244D was introduced into PGAM5 by site-directed mutagenesis. Sequences of all cloning primers are available on request. Expression of recombinant proteins was induced overnight at 18 °C in *Escherichia coli* strain Rosetta(DE3) using 0.5 mM IPTG (Thermo). Cells were lysed in lysis buffer (50 mM Tris-HCl, pH 8.5, 500 mM NaCl, 10% glycerol, 40 mM imidazole, 1 mM DTT and protease inhibitor cocktail (EDTA-free, cOmplete; Roche)) using an Emulsiflex-C3 homogenizer, and cleared lysate was used for protein purification using a HisTrap HP column (GE Healthcare: 17-5247-01) and was further purified by gel filtration (mobile phase: 30 mM Tris-HCl, pH 8.5, 300 mM NaCl, 10% glycerol and 1 mM DTT). Identity of recombinant PGAM5Δ2–28 wild-type and PGAM5Δ2–28(F244D) was confirmed by mass spectrometry. Far ultraviolet (UV) circular dichroism (CD) spectra of wild type and a mutant version of PGAM5 were recorded on a Jasco J-810 CD-Photometer at room temperature in 20 mM sodium phosphate buffer, pH 7.4,and 50 mM NaF. For each sample and the buffer (baseline), four scans were recorded and averaged. The averaged baseline spectrum was subtracted from the averaged sample spectra and the resulting spectra were smoothed using an FFT filter (as part of the software package). Measurements were made only down to wavelengths where the instrument dynode voltage indicated the detector was still in its linear range (190 nm). Spectra are shown as the mean residue ellipticity. Secondary structure compositions were estimated using the CONTINLL program[53].

To determine phosphatase activity in vitro of affinity purified proteins, beads with bound proteins were resuspended in ddH_2O and were incubated in phosphatase buffer (50 mM imidazole, pH 7.2, 0.2 mM EGTA, 0.02% β-mercaptoethanol and 0.1 mg/ml BSA) and 50 µM phosphorylated peptide (peptide sequences: RRA(pT)VA and AAL(pS)ASE) for 20 min at 30 °C. The reaction was stopped by addition of Malachite Green Reagent as described before[42]. After 15 min of incubation at room temperature, absorbance at 630 nm was measured using an Infinite 200 PRO series micro plate reader (Tecan). To determine phosphatase activity *in silico*, recombinant proteins were used incubated in phosphatase buffer as described above. To detect dephosphorylation of AIFM1, HeLa cell lysate was separated by SDS–PAGE and transferred onto a nitrocellulose membrane. The membranes were incubated with recombinant PGAM5Δ2–28 wild-type and PGAM5Δ2–28(F244D) in phosphatase buffer for 60 min at 30 °C, washed, blocked and stained with primary antibodies.

Cell-viability assays, flow cytometry and immunofluorescence. To test cell viability, we used three different assays. We measured ATP levels by CellTiter-Glo assay according to the manufacturer's protocol. We measured the activity of released lactate dehydrogenase by a lactate dehydrogenase assay according to the manufacturer's protocol. We measured succinate dehydrogenase mitochondrial activity by an MTT assay. In brief, 0.5 mg/ml MTT was added to the cells and incubated for 3 h at 37 °C; the reaction was stopped by aspiration of the medium and solving the crystals in 1:1 mix of DMSO/ethanol for 15 min shaking at room temperature, followed by measurement of absorbance (570 nm) using an Infinite 200 PRO series micro plate reader (Tecan). We measured general enzyme-reduction activity by a resazurin-based cell-viability assay. 50 µg/ml resazurin was added to each well of a 96-well plate and incubated for 30 min at 37 °C, followed by measurement of fluorescence (535/590 nm) using an Infinite 200 PRO series micro plate reader (Tecan). Flow-cytometry-based cell-death assays were performed using the apoptosis-necrosis assay according to the manufacturer's instructions. To measure intracellular ROS, cells were incubated for 30 min with 1 µM CM-H_2DCFDA in the dark and were fixed using 4% paraformaldehyde. Flow cytometry analyses were done using a FACSCalibur (BD) or MACSQuant analyzer (Miltenyi). For immunofluorescence, HeLa cells were grown on coverslips and fixed with 4% (w/v) paraformaldehyde for 15 min, permeabilized with 0.1% (v/v) Triton X-100 for 5 min and washed three times with blocking buffer (1 × PBS containing 0.1% FCS (w/v)). Immunofluorescence analysis was performed as described previously[2]. Confocal imaging was performed using a LSM780 confocal laser scanning microscope (ZEISS, Jena, Germany) equipped with a Plan-APO 63x/NA1.46 oil-immersion objective (ZEISS).

Real-time RT-PCR. RNA was reverse-transcribed with PrimeScript RT Master Mix (TAKARA) and quantified by real-time RT-PCR using the QuantiFast SYBR Green RT-PCR Kit (Qiagen) and a CFX96 Touch Real-Time PCR Detection System (BioRad). Each cycle consisted of 10 s at 95 °C and 30 s at 60 °C, followed by melting-curve analysis. Primer sequences were as follows: huGAPDH (5′-GATTCCACCCATGGCAAATTC-3′ and 5′-AGCATCGCCCCACTTGATT-3′), hTBP (5′-GTTCTGAATAGGCTGTGGGG-3′ and 5′-ACAACAGCCTGCCACCTTAC-3′), KEAP1 (5′-GCTGATGAGGGTCACCAGTT-3′ and 5′-CCAACTTCGCTGAGCAGATT-3′), NRF2 (5′-GCTCATACTCTTTCCGTCGC-3′ and 5′- ATCATGATGGACTTGGAGCTG-3′), NQO1 (5′-GCATAGAGGTCCGACTCCAC-3′ and 5′-GGACTGCACCAGAGCCAT-3′), TXN (5′-AATGTTGGCATGCATTTGAC-3′ and 5′-CCTTGCAAAATGATCAAGCC-3′), mIL6 (5′-TAGTCCTTCCTACCCCAATTTCC-3′ and 5′-TTGGTCCTTAGCCACTCCTTC-3′) and NS1 (5′-GACCAGGCGATCATGGATAA-3′ and 5′-TGCTTCTCCAAGCGAATCTC-3′).

Affinity purification and quantitative LC-MS/MS, bioinformatics analysis. For affinity purification, cell lysates were prepared by lysing cells for 5 min on ice in TAP lysis buffer (50 mM Tris, pH 7.5, 100 mM NaCl, 5% (v/v) glycerol, 0.2% (v/v) Nonidet-P40, 1.5 mM $MgCl_2$ and protease inhibitor cocktail (EDTA-free, cOmplete; Roche)) or Cell Signaling IP buffer (20 mM TrisHCl, pH 7.5, 150 mM NaCl, 1 mM Na_2EDTA, 1 mM EGTA, 1% Triton and protease inhibitor cocktail (EDTA-free, cOmplete; Roche)). Where indicated, phosphatase inhibitor cocktail (PhosSTOP; Roche) or sodium fluoride (NaF) and sodium orthovanatade were added. For affinity purification with HA-SII-tagged proteins, streptavidin affinity resin was incubated with cell lysate in either TAP lysis buffer or Cell Signaling IP buffer for 60 min at 4 °C on a rotary wheel. For affinity purification with Flag-M2-tagged proteins, Flag-M2 affinity resin was incubated with cell lysate and processed as above. Beads were washed four times with TAP lysis buffer, followed by two times with TAP wash buffer (lacking 0.2% (v/v) Nonidet-P40) or five times with Cell Signaling IP buffer, boiled in 2x Cell Signaling SDS buffer for 5 min at 95 °C and subjected to SDS–PAGE and immunoblot analysis. For LUMIER experiments, cell lysates (1:10 diluted in TAP wash buffer) or beads were resuspended in TAP wash buffer and transferred in 4 × 20 µl aliquots to white well plate (Nunc) and mixed with 2x Renilla reagent (100 mM K_3PO_4, 500 mM NaCl, 1 mM EDTA, 25 mM thiourea and 30 µM coelenterazine), and luminescence was measured using an Infinite 200 PRO series micro plate reader (Tecan).

To detect and quantify proteins bound to HA-SII-tagged bait proteins by affinity purification and mass spectrometry, samples were prepared as described

© 2018 Nature America Inc., part of Springer Nature. All rights reserved.

above. After the final four washes in TAP lysis buffer, samples were in addition washed four times with TAP wash buffer to remove residual detergent. Four independent affinity purifications were performed for each bait. Sample preparations and LC-MS/MS analysis was performed as described previously[53]. In brief, samples were sequentially digested with LysC (Wako Chemicals USA) and Trypsin (Promega), acidified with 0.1% TFA, desalted with C18 stage tips and analyzed by liquid chromatography coupled to mass spectrometry on an Orbitrap XL platform (Thermo Fisher Scientific).

For analysis of interaction proteomics data, mass spectrometry raw files were processed with MaxQuant version 1.3.0.5 or 1.4.0.6[54] using the built-in Andromeda engine to search against human proteome (UniprotKB, release 2012_06) containing forward and reverse sequences. In MaxQuant, the label-free quantitation (LFQ) algorithm[55] and Match Between Runs option were used as described previously[53]. Only proteins identified on the basis of at least two peptides and a minimum of three quantitation events in at least one experimental group were considered. LFQ protein intensity values were log-transformed, and missing values were filled by imputation. Specific enrichment was determined by multiple equal variance *t*-tests with permutation-based false-discovery rate (FDR) statistics, performing 250 permutations. FDR thresholds and S_0 parameters were empirically set to separate background from specifically enriched proteins. Data was analyzed using Perseus version 1.5.2.11. Results were plotted using R (www.R-project.org). Sequence logo was generated using WebLogo[56].

Mitochondrial respiration. HeLa cells were mock treated or treated with 0.1 mM or 0.5 mM H_2O_2 for 5 h. After 5 h, medium was changed to SeaHorse Assay medium (DMEM D5030 with 10 mM pyruvate and 2 mM glutamine) without H_2O_2 treatment. After 1 h, read out in a SeaHorse Analyzer was performed with injections of 1.5 µM OliogA (ATP coupler) after 24 min, 1 µM CCCP (carbonyl cyanide m-chlorophenyl hydrazone; electron-transport-chain accelerator) after 45 min and 4 µM antimycin A and 2 µM rotenone (mitochondrial inhibitors) after 69 min. Results were normalized by total DNA using CyQuant.

Electron microscopy. MEFs were treated as indicated, than were washed once and fixed with glutaraldehyde. Fixed cells were washed with 0.2 M sodium cacodylate, osmicated with 1% OSO_4 for 40 min, washed twice and subsequently dehydrated in ethanol and infiltrated with Low Viscosity Embedding Media Spurr's Kit (Electron Microscopy Sciences, cat.# E14300) according to the manual. After polymerization (overnight at 70–80 °C), ultrathin serial sections (thickness, 60 nm) were counterstained with 0.5% uranyl acetate and 3% lead citrate. Images were acquired with JEOL JEM-1230 transmission electron microscope (magnification 5000-30000x), with 80 kV, Gatan Orius SC1000 digital Camera and software Gatan DigitalMicrograph™.

In vivo experiments. Heterozygous *Pgam5*-deficient mice (*Pgam5*$^{+/-}$) on the C57BL/6 N background were obtained from the European Mouse Mutant Archive (EMMA). Mice were bred at the MPI of Biochemistry animal facility under license number 55.2-54-2532.116.2015. Primer sequences for genotyping were as follows: L3f_6764 5′-AGGCTGGATCACTATAAGGC-3′ and L3r_6765 5′-CTGGAGACATTGTGACCATC-3′. *Asc*$^{-/-}$ mice (C57BL/6 J), *Nlrp3*$^{-/-}$ mice (C57BL/6 J), *Casp1*$^{-/-}$*Casp11*$^{-/-}$ mice (SV129 background) or wild-type mice (C57BL/6 J) were housed and bred in the animal facility at Transgenose Institute (TAAM-CNRS, Orléans, France, UPS 44 under agreement D-45-234-6, 2014) under SPF conditions in a temperature-controlled environment with free access to food and water. All animal experiments have been performed according to animal welfare regulations and have been approved by the responsible authorities (University Freiburg, Germany, G-12/46, CNRS Orleans, France, CLE CCO 2012-047). For ozone-treatment experiments, mice were exposed to ozone (1 ppm) for 1 h in a Plexiglas chamber (EMB 104, EMMS). An ozonisator (Ozoniser S 500 mg, Sander) was used to generate ozone, and ozone levels were controlled by an ozone sensor (ATI 2-wire transmitter, Analytical Technology). Mice were euthanized 4 h or 24 h after ozone exposure by progressive CO_2 inhalation. BALF was collected, and cardiac perfusion was performed with ISOTON II (Acid free balanced electrolyte solution Beckman Coulter, Krefeld, Germany) before removal of lungs for further analysis. BALF was isolated by four consecutive saline lavages (500 µl per lavage; 0.9% NaCl) via a cannula introduced into the trachea. After centrifugation (2,000 rpm for 10 min at 4 °C), the supernatants were removed and stored at −20 °C for ELISA, and cell pellets were analyzed by Cytopsin (Thermo Scientific, Waltham, USA) followed by Diff-Quick coloration (Merz & Dade A.G., Dudingen, Switzerland). Differential cell counts were performed with at least 400 cells. For FluAV-infection experiments, mice were anesthetized with ketamine (100 µg per gram body weight) and xylazine (5 µg per gram body weight) before infection by the intranasal route with 1.5×10^3 plaque-forming units of SC35M per animal in a 40 µl volume. Mice were monitored for weight for 14 d and were euthanized when they lost > 25% of their initial body weight.

Measurement of infection, cell death and inflammatory parameters in vivo. Mouse myeloperoxidase was assessed by ELISA (R&D Systems, Abingdon, UK), cytokines were measured by Multiplex Immunoassay (ProcartaPlex, eBioscience) and total protein levels in BALF were analyzed using the Bio-Rad DC Protein Assay according to the manufacturer's instructions.

For histological analyses, the left lobes of the lungs were fixed in 4% buffered formaldehyde and embedded in paraffin. After tissue sections (3 µm), cuts were stained with hematoxylin and eosin. Epithelial damage and inflammatory cell infiltration were assigned scores for severity of epithelial injury and inflammation (0–5)[57]. Lungs were stained with anti-FluAV antiserum, ApopTag Fluorescein *In situ* Apoptosis Detection Kit (Merck) and DAPI.

RNA-mediated knockdown. Duplex siRNAs (1nmol of siRNA per 1×10^6 cells) were transfected using the Neon Transfection System (Invitrogen) according to the manufacturer´s instructions for HeLa and SKN-BE2 cells. siRNAs were purchased from Qiagen or Dharmacon or were synthesized by the Core Facility at the MPI of Biochemistry. siRNA target sequences were as follows: human PGAM5 (#1: 5′-CCCGCCCGTGTCTCATTGGAA-3′; #2: 5′-TCCAAGCTGGACCACTACAAA-3′; #3: 5′-CTCGGCCGTGGCGGTAGGGAA-3′; #4: 5′-CGCTAGTGACAGCCCAATAT-3′; #5: 5′-GGAGAAACCAATATAGAATT-3′), human AIFM1 (#1: 5′-GAACATCTTTAACCGAATG-3′; #2: 5′-GCATGAAGATCTCAATGAA-3′; #3: 5′-CAAGGAAGATCATTAAGGA-3′; #4: 5′-GGTAGAAACTGACCACATA-3"; #5: 5′-GATCAAGTCCTTTGTG-3"; #6: 5′-CCTGAGAGGAGGTCGA-3"; #7: 5′-GGAATTGGCAAACCCAC-3"; #8: 5′-GGAGGTCGAATGGGTA-3′), human KEAP1 (#1: 5′-GGACAAACCGCCTTAATTC-3′; #2: 5′-CAGCAGAACTGTACCTGTT-3′; #3: 5′-GGGCGTGGCTGTCCTCAAT-3′; #4: 5′-CGAATGATCACAGCAATGA-3′), human NFE2L2 (#1: 5′-TAAAGTGGCTGCTGAGAAT-3′; #2: 5′-GAGTTACAGTGTCTTAATA-3′; #3: 5′-TGGAGTAAGTCGAGAAGTA-3′; #4: 5′-CACCTTATATCTCGAAGTT-3′) and scrambled (5′- AAGGTAATTGCGCGTGCAACT-3).

Life Sciences Reporting Summary. Further information on experimental design and reagents is available in the Life Sciences Reporting Summary.

Data availability. The data that support the findings of this study are available from the corresponding author upon request.

References

51. Habjan, M. et al. Sequestration by IFIT1 impairs translation of 2'O-unmethylated capped RNA. *PLoS Pathog.* **9**, e1003663 (2013).
52. Gabriel, G. et al. The viral polymerase mediates adaptation of an avian influenza virus to a mammalian host. *Proc. Natl. Acad. Sci. USA* **102**, 18590–18595 (2005).
53 Provencher, S. W. & Glöckner, J. Estimation of globular protein secondary structure from circular dichroism. *Biochemistry* **20**, 33–37 (1981).
54 Cox, J. & Mann, M. MaxQuant enables high peptide identification rates, individualized p.p.b.-range mass accuracies and proteome-wide protein quantification. *Nat. Biotechnol.* **26**, 1367–1372 (2008).
55 Cox, J. et al. Accurate proteome-wide label-free quantification by delayed normalization and maximal peptide ratio extraction, termed MaxLFQ. *Mol. Cell. Proteomics* **13**, 2513–2526 (2014).
56 Crooks, G. E., Hon, G., Chandonia, J.-M. & Brenner, S. E. WebLogo: a sequence logo generator. *Genome Res.* **14**, 1188–1190 (2004).
57 Besnard, A.-G. et al. Dual Role of IL-22 in allergic airway inflammation and its cross-talk with IL-17A. *Am. J. Respir. Crit. Care Med.* **183**, 1153–1163 (2011).

© 2018 Nature America Inc., part of Springer Nature. All rights reserved.

nature immunology

SUPPLEMENTARY INFORMATION

https://doi.org/10.1038/s41590-017-0013-y

In the format provided by the authors and unedited.

Oxeiptosis, a ROS-induced caspase-independent apoptosis-like cell-death pathway

Cathleen Holze[1], Chloé Michaudel[2], Claire Mackowiak[2], Darya A. Haas[1], Christian Benda[3], Philipp Hubel[1], Friederike L. Pennemann[1], Daniel Schnepf[4,5], Jennifer Wettmarshausen[6,7], Marianne Braun[8], Daisy W. Leung[9], Gaya K. Amarasinghe[9], Fabiana Perocchi[6,7], Peter Staeheli[4,10], Bernhard Ryffel[2,11] and Andreas Pichlmair[1,12,13]*

[1]Innate Immunity Laboratory, Max-Planck Institute of Biochemistry, Martinsried, Munich, Germany. [2]INEM, Experimental Molecular Immunology, UMR7355 CNRS and University, Orleans, France. [3]Department of Structural Cell Biology, Max-Planck Institute of Biochemistry, Martinsried, Munich, Germany. [4]Institute of Virology, University of Freiburg, Freiburg, Germany. [5]Spemann Graduate School of Biology and Medicine, Albert Ludwigs University Freiburg, Freiburg, Germany. [6]Department of Biochemistry, Gene Center Munich, Munich, Germany. [7]Institute for Diabetes and Obesity, Helmholtz Zentrum Munchen, Neuherberg, Germany. [8]EM-Histo Lab, Max-Planck Institute of Neurobiology, Martinsried, Munich, Germany. [9]Department of Pathology and Immunology, Washington University School of Medicine, St Louis, MO, USA. [10]Faculty of Medicine, University of Freiburg, Freiburg, Germany. [11]Institute of Infectious Diseases and Molecular Medicine, University of Cape Town, Cape Town, South Africa. [12]School of Medicine, Institute of Virology, Technical University of Munich, Munich, Germany. [13]German Center for Infection Research (DZIF), Munich partner site, Munich, Germany.
*e-mail: andreas.pichlmair@tum.de

© 2017 Nature America Inc., part of Springer Nature. All rights reserved.

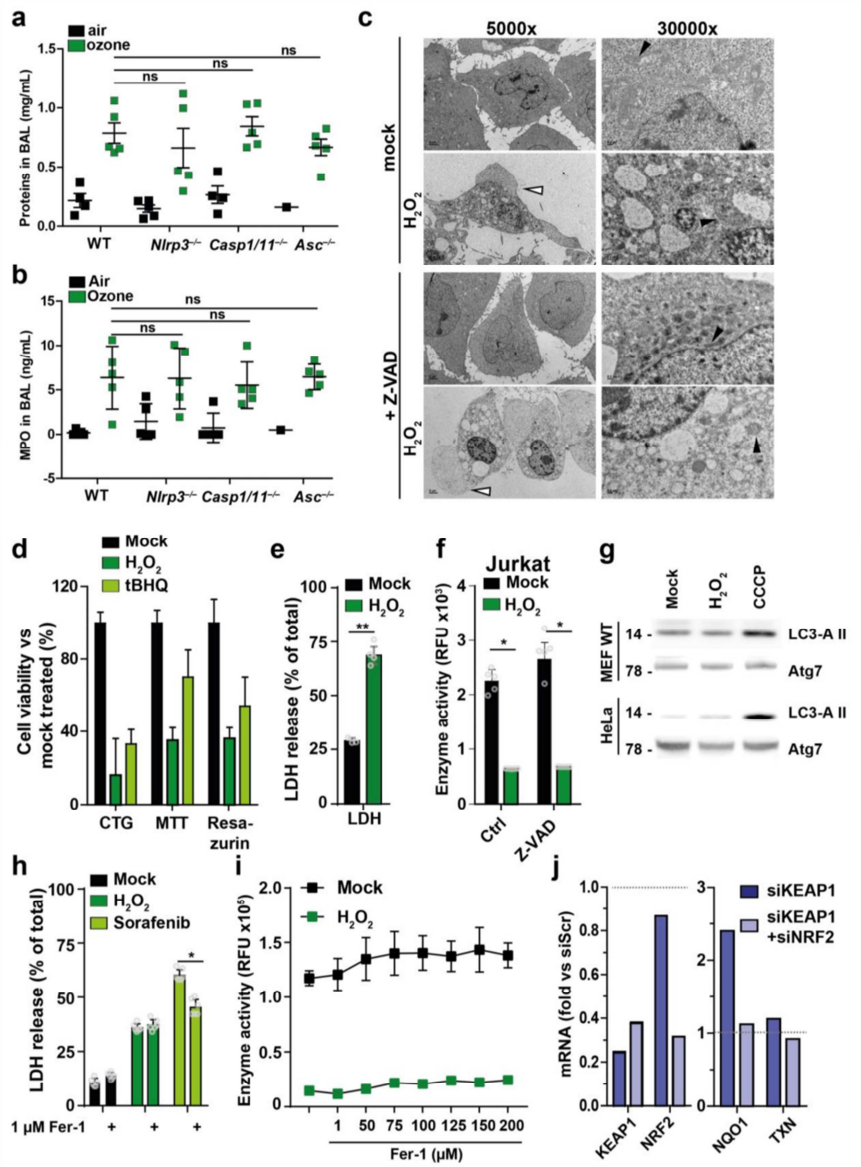

Supplementary Figure 1

Ozone- and H_2O_2-exposure model: testing of cell-death pathways.

(a-b) C57BL/6 mice (wt) or *Nlrp3*$^{-/-}$, *Casp1/11*$^{-/-}$ and *Asc*$^{-/-}$ mice were exposed to 1 ppm of ozone for 1h and BAL analyzed for protein content and for myeloperoxidase (MPO) 24h later. Dots indicate individual mice. Graph shows average +/- SD, two-sided t-test, ns: non-significant. **(c)** Electron microscopy analysis of H_2O_2 treated MEFs. Representative micrographs show MEFs wt treated for 6h with 1 mM H_2O_2 with or without pre-treatment with Z-VAD. Left panel shows 5000x magnification, right panel shows 30000x magnifications. One representative experiment of three is shown. **(d)** Comparison of cell viability assays of HeLa cells after hydrogen peroxide (H_2O_2) treatment. Cells were treated for 21h with 0.5 mM H_2O_2. Cell titers were determined by CellTiter-Glo, MTT and resazurin-based cell viability assay. The plot shows the mean ± S.D. of six individual treatments. **(e)** LDH-assay to determine cell viability of HeLa cells after hydrogen peroxide (H_2O_2) treatment. Cells were treated 21h with 0.5 mM H_2O_2. Release of active LDH was determined by LDH-assay. The plot shows the mean ± S.D. of six individual treatments. One representative experiment of four is shown. ** p-value < 0.0001, two-sided t-test. **(f)** Viability of Jurkat cells after hydrogen peroxide (H_2O_2) treatment. Cells were left untreated or treated with 20 µM Z-VAD-FMK (Z-VAD) for 1h, followed by 21h treatment with 0.5 mM H_2O_2. Cell titers were determined by resazurin-based cell viability assay. The plot shows the mean ± S.D. of six individual treatments. One representative experiment of three is shown. * p-value < 0.001, two-sided t-test. **(g)** Immunoblot analysis of HeLa cells and MEFs treated with autophagy inducer Carbonyl cyanide m-chlorophenylhydrazone (CCCP) and H_2O_2 as comparison for expression levels of LC3-A II and Atg7. One experiment of three is shown. **(h)** HeLa cells were left untreated or treated with 1 µM Ferrostatin-1 (Fer-1) for 1h, followed by 21h treatment with 0.5 mM H_2O_2 or 20 µM ferroptosis-inducer Sorafenib. The plot shows the mean release of active LDH ± S.D. of six individual treatments. One representative experiment of three is shown. * p-value < 0.001, 2way ANOVA. **(i)** Cells were left untreated or treated with indicated concentrations of Ferrostatin-1 for 1h, followed by 21h treatment with 0.5 mM H_2O_2. Cell titers were determined by resazurin-based cell viability assay. The plot shows the mean ± S.D. of six individual treatments. One representative experiment of two is shown. **(j)** Expression of NRF2 regulated target genes after siRNA mediated knockdown of KEAP1, KEAP1 and NRF or siScr in HeLa cells 48h after siRNA treatment.

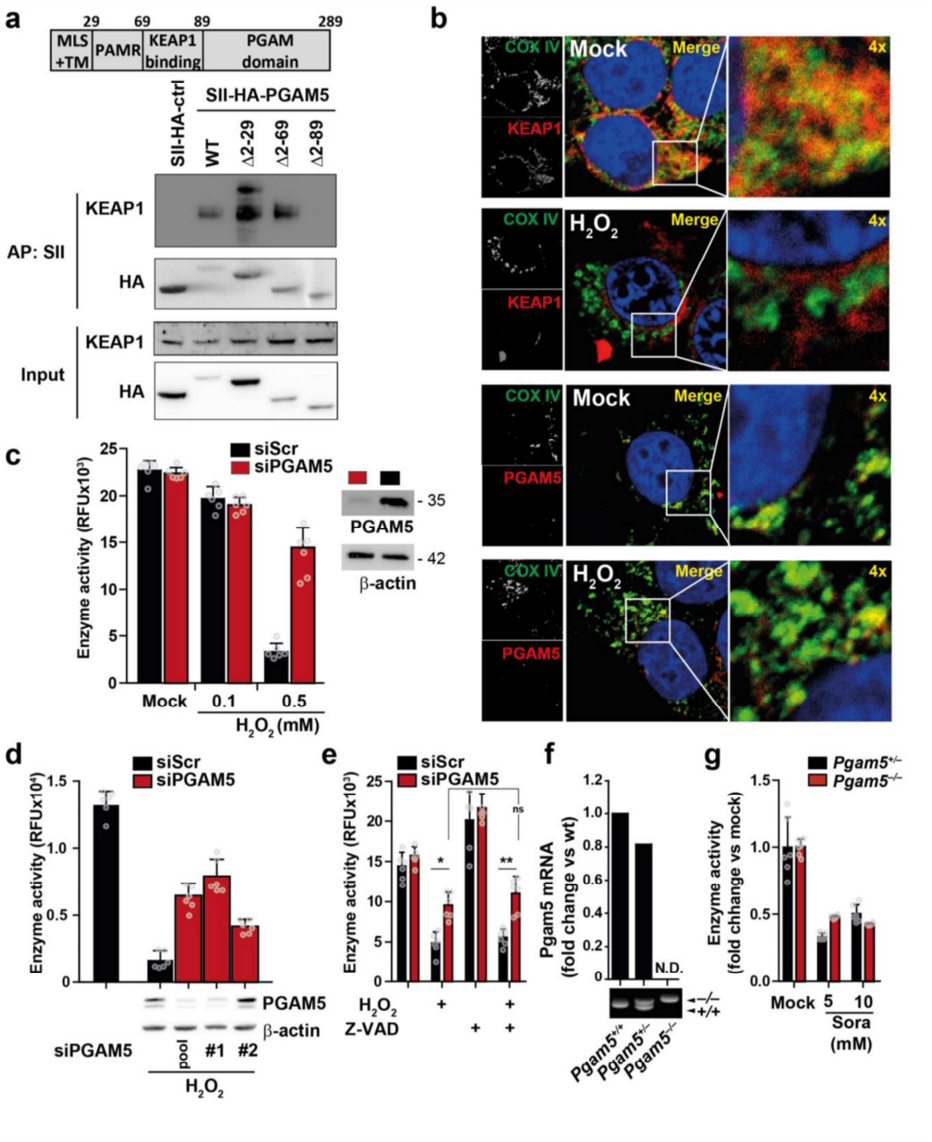

Supplementary Figure 2

KEAP1 interacts with PGAM5, which is required for H_2O_2-mediated cell death.

(a) Binding of endogenous KEAP1 to PGAM5 deletion mutants. Expression of SII-HA-tagged PGAM5 wild-type (wt) and deletion mutants lacking MLS and TM domain (Δ 2-29), lacking MLS, TM domain and phosphatase activity modulating region (PAMR) (Δ 2-69) and lacking MLS, TM domain, PAMR and KEAP1 binding site (Δ2-89) in HEK293T cells. Immunoblot analysis of input lysates and SII-AP. One of two experiments with similar results are shown. **(b)** Representative confocal images of HeLa cells left untreated or treated with 0.5 mM H_2O_2 for 12h and stained for DAPI (blue), the mitochondrial marker COX IV (green) and PGAM5 or KEAP1 (red), respectively. Overlays are shown in yellow. One representative experiment of six is shown. **(c)** Viability of HeLa cells treated with siRNA against PGAM5 and siScr after 21h H_2O_2 treatment. Cell viability was determined by resazurin-conversion assay. The plot shows the mean ± S.D. of four individual treatments. One representative experiment of two is shown. **(d)** as **(c)** but different siRNAs targeting PGAM5 were used. **(e)** as **(c)** but cells were pre-treated with 20 μM Z-VAD-FMK (Z-VAD) for 1h before 21h treatment with 0.5 mM H_2O_2. * $p < 0.01$, ** $p < 0.001$, ns: non-significant, 2way ANOVA with Bonferroni post t-test. **(f)** Characterization of *Pgam5* knockout MEFs by genotyping (PCR) (bottom) and quantification of Pgam5 mRNA levels by RT-qPCR (top) normalized to hydroxymethylbilane synthase mRNA (Hmbs). Histogram shows mean fold change of analyses done in triplicates. N.D.: not detectable, one representative experiment of three is shown **(g)** MEFs of the indicated genotype were treated with the indicated concentrations of Sorafenib (Sora) for 20h and viability was tested by resazurin-conversion assay. The graph shows mean activity ± S.D. of six measurements. One representative experiment of two is shown.

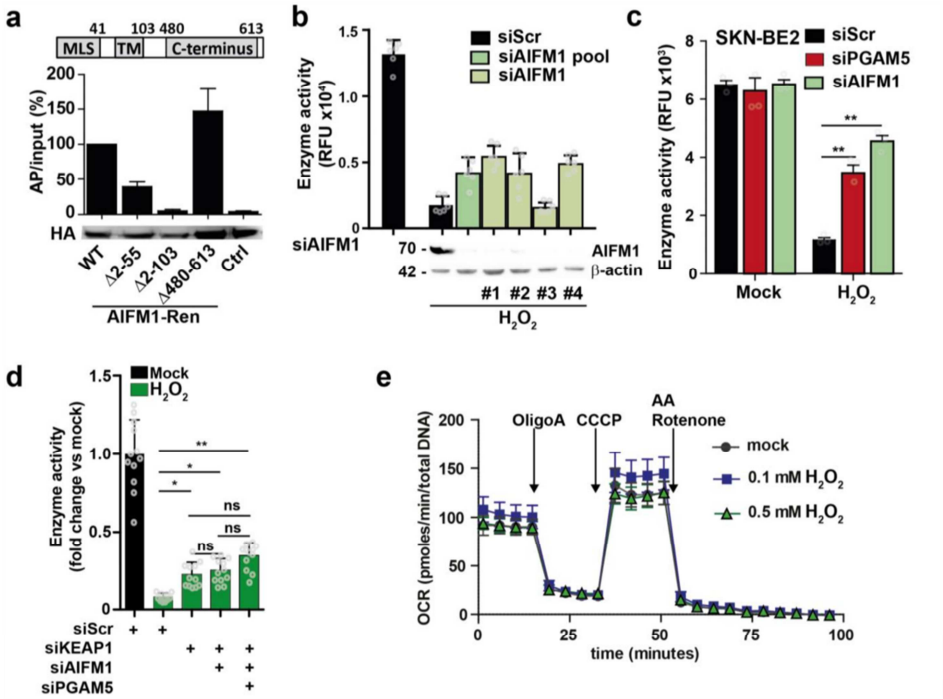

Supplementary Figure 3

PGAM5 interacts with AIFM1, which is involved in H_2O_2.mediated cell death.

(a) AP of Renilla tagged (-Ren) AIFM1 mutant proteins with SII-HA-PGAM5. HEK293T cells were co-transfected with SII-HA-tagged PGAM5 and Renilla-tagged AIFM1 mutants or Renilla-tagged-control (THYN1; ctrl). After 24h Renilla activity was measured in cell lysate and SII precipitates. Immunoblot shows expression of bait proteins in cell lysates. One representative experiment of five with similar results is shown. **(b)** HeLa cells were treated with siRNAs against AIFM1 and siScr exposed 0.5 mM H_2O_2 for 21h. Cell viability was determined by resazurin assay. The plot shows the mean ± S.D. of four individual treatments. One representative experiment of two is shown. **(c)** As **(b)** but siRNA against AIFM1 and PGAM5 was transfected in SKN-BE2 cells. **(d)** Viability of HeLa cells treated with indicated siRNA combinations against KEAP1, AIFM1 and PGAM5 or siScr after 21h H_2O_2 treatment. Cell titers were determined by resazurin-based viability assay. **(c), (d)** The plot shows the mean ± S.D. of six individual treatments. One representative experiment of two is shown. * p-value < 0.01, ** p-value < 0.001, ns: non-significant, 1way ANOVA with Bonferroni post t-test. **(e)** HeLa cells were treated for 5h with the indicated amounts of H_2O_2 followed by measuring mitochondrial respiration. Addition of 1.5 µM Oligomycin (OligoA), 1 µM Carbonyl cyanide m-chlorophenyl hydrazone (CCCP), 4 µM Antimycin A (AA) and 2 µM Rotenone is indicated. The graph shows average oxygen consumption rate (OCR) ± S.D. of three measurements.

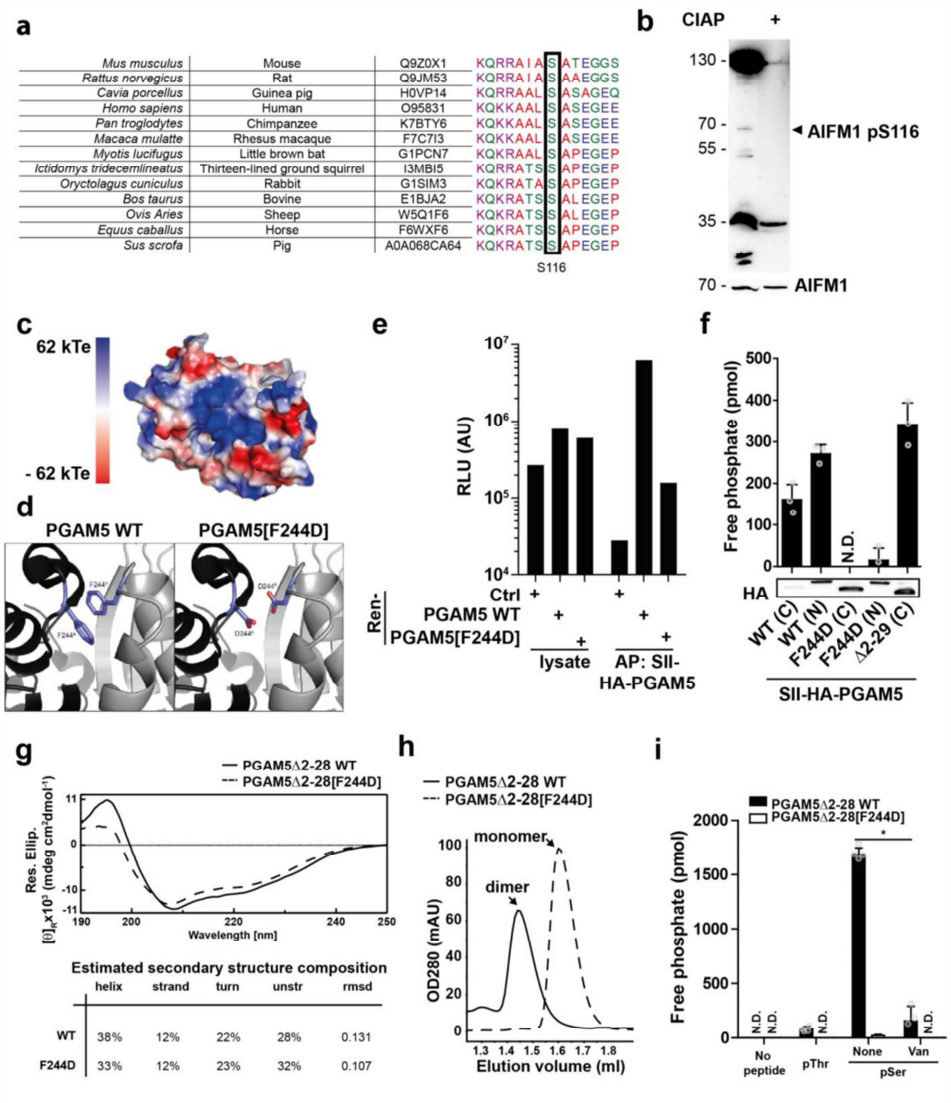

Supplementary Figure 4

PGAM5–AIFM1 interaction and PGAM5's phosphatase activity.

(a) Sequence alignment of AIFM1 amino acids 109-122 of the indicated species. **(b)** Selectivity of AIFM1 pS116 antibody. HeLa cell lysates were treated for 15 min with or without calf intestine alkaline phosphatase (CIAP) and subjected to Immunoblot stained for AIFM1 pS116 and AIFM1. One representative experiment of three with similar results is shown. **(c)** Surface charge potential of PGAM5 dimer crystal structure (PDB 3MXO). **(d)** Zoom in on dimer interphase interface of PGAM5. One monomer is highlighted in black, the other in grey. Left panel shows the wild-type (wt) protein, right panel shows the modeled mutant PGAM5[F244D]. Side chains of phenylalanine (F) 244 and, after mutation, aspartic acid (D) 244 are highlighted in purple (carbon) and red (oxygen). **(e)** Binding of Ren-PGAM5, Ren-PGAM5[F244D] or Ren-ctrl (THYN1) to SII-HA-PGAM5 in HEK293T cells. Renilla assay of cell lysates or SII precipitates. **(f)** Phosphatase activity of PGAM5 and PGAM5 mutants carrying an N-terminal (N) or C-terminal (C) tag precipitated from cell lysates. The plot shows the mean ± S.D. of one AP with three independent measurements. One representative experiment of three is shown. **(g)** Circular dichroism (CD) spectroscopy of PGAM5Δ2-28 and PGAM5Δ2-28[F244D] to test comparability of secondary structures and overall integrity of both recombinant proteins. **(h)** Size exclusion chromatography analysis of PGAM5Δ2-28 wt and [F244D] mutant for dimer and monomer formation. **(i)** Phosphatase activity of 0.1 µg recombinant PGAM5Δ2-28 wt and [F244D] mutant. Where indicated phosphatase inhibitor 1 mM orthovanatade (Van) has been added to the reaction mix. The plot shows the mean ± S.D. of three independent measurements. One representative experiment of three is shown. * p-value < 0.001 2way ANOVA.

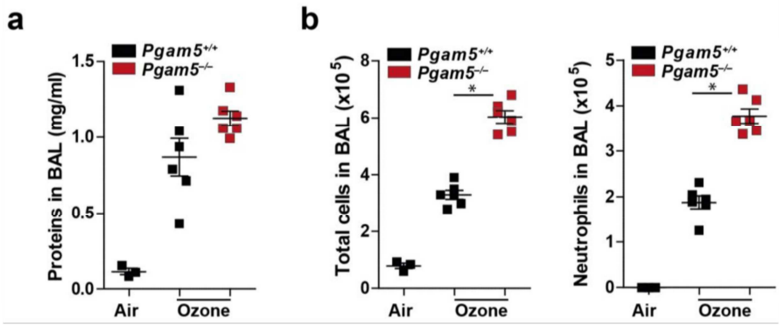

Supplementary Figure 5

Exposure of *Pgam5*$^{-/-}$ mice to ozone.

Pgam5$^{+/+}$ and *Pgam5*$^{-/-}$ mice (n = 3-6 per condition) were treated 1 ppm ozone for 1h and sacrificed after 24h recovery time. **(a)** Determination of total proteins in BAL. **(b)** Total cells and neutrophils in BAL. **(a), (b)** * p-value < 0.001 by 1way Anova and Bonferroni post t-test. Graphs show individual mice (dots), mean +/- SEM. One representative experiment of two is shown.

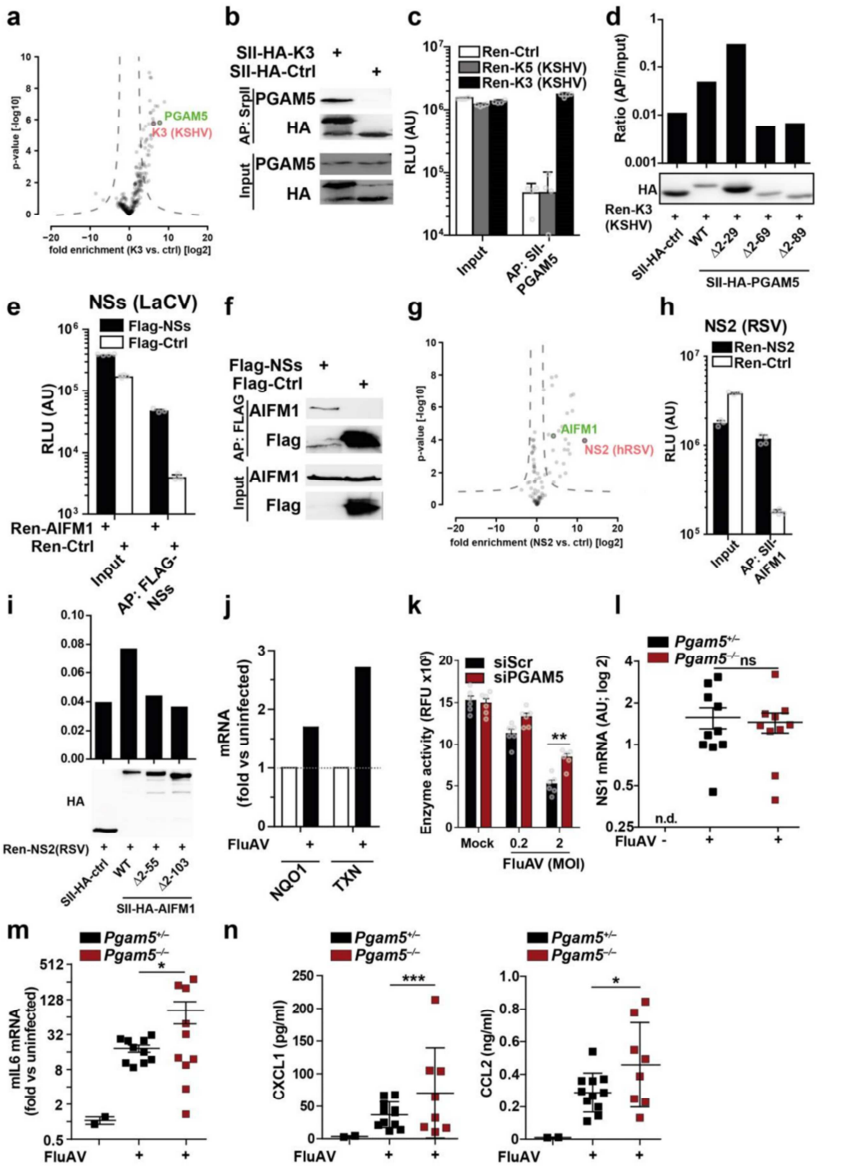

Supplementary Figure 6

Targeting and activation of oxeiptosis during viral infection.

(a) AP-LC-MS/MS experiments using SII-HA-tagged K3 of Karposi Sarcoma Herpes virus (KSHV) and SII-HA-THYN1 (ctrl) as baits. Volcano plots show the average degrees of enrichment (ratio of label-free quantitation (LFQ) protein intensities; x-axis) and p-value (two-tailed t-test; y-axis) for each identified protein. Significantly enriched proteins (FDR: 0.01, S0=1) are separated from background proteins by a hyperbolic curve (dotted line). Bait is marked in red, PGAM5 is highlighted in green. Four independent APs were performed for all baits. **(b)** As in (a) but Immunoblot for endogenous PGAM5 and HA tagged bait proteins was performed. **(c)** Ren-K3, Ren-K5 or Ren-ctrl were co-transfected with SII-HA-PGAM5 into HEK293T cells and used for Immunoblot analysis or Renilla activity measurement in input lysate or after SII precipitation. Graphs show mean +/- SD of triplicate measurements. **(d)** HEK293T cells were co-transfected with SII-HA-tagged PGAM5mutant construct and Renilla-tagged K3 or Renilla-tagged-ctrl (THYN1). After 24h Renilla activity was measured in lysate and SII precipitates. Immunoblot shows expression of bait proteins in cell lysates. **(e)** AP of Ren-AIFM1 using Flag tagged non-structural protein S (NSs) of LaCV or Flag-(ctrl) (ΔMx) as baits followed by Renilla assay. **(f)** AP of endogenous AIFM1 in HEK cells using transfected Flag-NSs or Flag-ctrl (ΔMx) as baits followed by Immunoblot analysis. **(g)** As in (a) but with non-structural protein 2 (NS2) of RSV or non-expressing controls, AIFM1 is highlighted in green. **(h)** AP of Ren-NS2 (RSV) and Ren-ctrl (THYN1) using SII-HA-AIFM1 as bait followed by Renilla assay. Graph shows mean +/- SD of triplicate (input) or quadruplicate (AP) measurements. **(i)** Interaction of SII-HA-AIFM1 and AIFM1 mutant proteins and SII-HA-ctrl (THYN1) with co-expressed Ren-NS2 in HEK293T cells. Renilla activity was tested in cell lysates and after SII precipitation. **(j)** Influence of FluAV infection on NRF2 regulated gene transcription in HeLa cells tested by RT-qPCR normalized to mRNA of TATA-binding protein (TBP). **(k)** Viability of HeLa cells treated with siRNAs against PGAM5 or control (siSCR) and infected with the indicated MOI of FluAV for 40h. Histograms show average resazurin activity of six measurements +/- SD. One representative experiment of three is shown, ** p-value < 0.01, 2way ANOVA with Bonferroni post t-test. **(l)** Flu NS1 and **(m)** IL-6 mRNA levels in lung tissue of *Pgam5*$^{+/-}$ and *Pgam5*$^{-/-}$ mice that were infected with FluAV for five days (n = 10) and uninfected wt mice (n = 2). * p-value < 0.05, two-sided t-test. **(n)** CXCL1 and CCL2 accumulation in BAL of *Pgam5*$^{+/-}$ and *Pgam5*$^{-/-}$ mice that were infected with FluAV for five days and uninfected wt mice. **(d-g), (i)** Histograms show mean +/-SD of triplicate measurements. * p-value < 0.05, *** p-value < 0.001, t-test. One representative experiment of two **(i)**, three **(d), (e), (f), (h)** or four **(b), (c)** is shown.

2.4 PUBLICATION 4: VIPERIN TARGETS FLAVIVIRUS VIRULENCE BY INDUCING ASSEMBLY OF NONINFECTIOUS CAPSID PARTICLES

The Interferon stimulated gene (ISG) viperin is antiviral active against a broad range of different viruses including herpes-, orthomyxo- and flaviviruses. Viperin interferes with budding processes by changing the cellular membrane composition and by inhibiting the release of newly synthesized virus particles.

In this project I collaborated with the Laboratory of Prof. Överby (Department of Clinical Microbiology, Umea University, Sweden). We studied the antiviral activity of viperin against tick-borne encephalitis virus, a member of the Flavivirus family. We identified a novel viperin-mediated antiviral mechanism that inhibits flavivirus replication. In collaborative efforts with Arunkumar Upadhyay, a PhD student in the Överby Laboratory at that time, I identified the Golgi Brefeldin A resistant guanine nucleotide exchange factor 1 (GBF1) as a novel interactor of viperin by AE-LC-MS/MS analysis. In subsequent experiments we could show, that viperin targets and inhibits the function of GBF1. This in turn affects cellular secretion and finally impairs the assembly of tick-borne encephalitis virus particles which results in the release of premature non-infectious viruses.

I contributed to the identification of GBF1 as cellular viperin target by designing and performing a comparative AE-LC-MS/MS analysis between viperin and an antiviral inactive viperin deletion mutant that lacks the first 50 N-terminal amino acids. GBF1 showed high specificity to the antiviral active wild type protein but not to the mutated variant. This interaction was subsequently validated and mapped by co-immunoprecipitation analysis and was further characterized by my collaborators in Umea.

AMERICAN SOCIETY FOR MICROBIOLOGY | Journal of Virology®

CELLULAR RESPONSE TO INFECTION

Viperin Targets Flavivirus Virulence by Inducing Assembly of Noninfectious Capsid Particles

Kirstin Vonderstein,[a,b]* Emma Nilsson,[a,b] Philipp Hubel,[c] Larsård Nygård Skalman,[d,e] Arunkumar Upadhyay,[a,b] Jenny Pasto,[a,b] Andreas Pichlmair,[c] Richard Lundmark,[b,d,e] Anna K. Överby[a,b]

[a]Department of Clinical Microbiology, Virology, Umeå University, Umeå, Sweden
[b]Laboratory for Molecular Infection Medicine Sweden, Umeå University, Umeå, Sweden
[c]Max Planck Institute for Biochemistry, Martinsried, Munich, Germany
[d]Department of Medical Biochemistry and Biophysics, Umeå University, Umeå, Sweden
[e]Integrative Medical Biology, Umeå University, Umeå, Sweden

ABSTRACT Efficient antiviral immunity requires interference with virus replication at multiple layers targeting diverse steps in the viral life cycle. We describe here a novel flavivirus inhibition mechanism that results in interferon-mediated obstruction of tick-borne encephalitis virus particle assembly and involves release of malfunctioning membrane-associated capsid (C) particles. This mechanism is controlled by the activity of the interferon-induced protein viperin, a broad-spectrum antiviral interferon-stimulated gene. Through analysis of the viperin-interactome, we identified the Golgi brefeldin A-resistant guanine nucleotide exchange factor 1 (GBF1) as the cellular protein targeted by viperin. Viperin-induced antiviral activity, as well as C-particle release, was stimulated by GBF1 inhibition and knockdown and reduced by elevated levels of GBF1. Our results suggest that viperin targets flavivirus virulence by inducing the secretion of unproductive noninfectious virus particles via a GBF1-dependent mechanism. This as-yet-undescribed antiviral mechanism allows potential therapeutic intervention.

IMPORTANCE The interferon response can target viral infection on almost every level; however, very little is known about the interference of flavivirus assembly. We show here that interferon, through the action of viperin, can disturb the assembly of tick-borne encephalitis virus. The viperin protein is highly induced after viral infection and exhibit broad-spectrum antiviral activity. However, the mechanism of action is still elusive and appears to vary between the different viruses, indicating that cellular targets utilized by several viruses might be involved. In this study, we show that viperin induces capsid particle release by interacting and inhibiting the function of the cellular protein Golgi brefeldin A-resistant guanine nucleotide exchange factor 1 (GBF1). GBF1 is a key protein in the cellular secretory pathway and is essential in the life cycle of many viruses, also targeted by viperin, implicating GBF1 as a novel putative drug target.

KEYWORDS COPI, COPII, GBF1, assembly, capsid, flavivirus, interferon, tick-borne encephalitis virus, viperin

The type I interferon (IFN) system is the first line of antiviral defense and an important part of the intrinsic innate immune response that controls virus dissemination and protects against serious disease. Binding of IFN to the IFN receptor activates a signaling cascade that leads to the transcriptional activation of hundreds of IFN-stimulated genes (ISGs), which encode proteins with diverse biological function where some are potent antiviral proteins and part of the response against mammalian viruses (1). The antiviral function of ISGs is only partially understood. However, it is well

Received 11 October 2017 **Accepted** 12 October 2017

Accepted manuscript posted online 18 October 2017

Citation Vonderstein K, Nilsson E, Hubel P, Nygård Skalman L, Upadhyay A, Pasto J, Pichlmair A, Lundmark R, Överby AK. 2018. Viperin targets flavivirus virulence by inducing assembly of noninfectious capsid particles. J Virol 92:e01751-17. https://doi.org/10.1128/JVI.01751-17.

Editor Julie K. Pfeiffer, University of Texas Southwestern Medical Center

Copyright © 2017 Vonderstein et al. This is an open-access article distributed under the terms of the Creative Commons Attribution 4.0 International license.

Address correspondence to Anna K. Överby, anna.overby@umu.se.

* Present address: Kirstin Vonderstein, Biomedicum Imaging Unit, Faculty of Medicine and HiLIFE, University of Helsinki, Helsinki, Finland.

K.V. and E.N. contributed equally to this article.

accepted that ISGs target different steps in the virus life cycle ranging from cell entry, virus protein translation, genome replication, and exit of virus particles (reviewed in reference 2).

The genus *Flavivirus*, within the family of *Flaviviridae*, comprises important human pathogens transmitted by mosquitos and ticks, such as yellow fever virus, dengue virus (DENV), West Nile virus, Zika virus, and tick-borne encephalitis virus (TBEV). These are small (~50-nm), spherical, enveloped, positive-stranded RNA viruses. It is well known that the type I IFN response is crucial for restricting different flaviviruses, and several ISGs have been identified to restrict flavivirus growth. However, very little is known about how specific ISGs target the assembly and release of virions. Prior to the assembly of virions, a single polyprotein is translated from the viral RNA genome. The polyprotein is cleaved into seven nonstructural proteins and three structural proteins. Although the nonstructural proteins promote genomic replication and assembly, the three structural proteins—capsid (C), prM/M (membrane and its precursor), and envelope (E)—form the viral particles (3). The C proteins of all flaviviruses are highly basic, which gives them the ability to bind the viral genomic RNA to form a nucleocapsid, which buds into the endoplasmic reticulum (ER), acquiring a host-derived lipid bilayer coated by the membrane-bound glycoproteins prM and E (4–6). From the ER, the virion is transported along the secretory pathway toward the Golgi compartment, where the maturation of carbohydrate groups on prM and E, as well as the cleavage of prM to M, occurs (7). Finally, the mature virion is released by exocytosis (reviewed in reference 3).

Two major ISGs, tetherin and viperin (virus inhibitory protein, ER associated, IFN inducible), have been shown to affect assembly and release of viruses (reviewed in reference 2). Tetherin is encoded by the ISG *BST2* and is localized within lipid rafts on the cell surface, in the *trans*-Golgi compartment, and/or within recycling endosomes (8, 9). It inhibits release of human immunodeficiency virus type 1 (HIV-1) viral particles by anchoring the virion to the plasma membrane (10), leading to internalization and degradation (11, 12). Viperin, encoded by the ISG *RSAD2*, is highly induced in an IFN-dependent or -independent manner (as reviewed previously [13]). Viperin is located to the cytoplasmic side of the ER (14) and has a broad-spectrum antiviral activity against many different enveloped viruses, e.g., DENV, West Nile virus, TBEV, hepatitis C virus (HCV), HIV-1, influenza A virus, Sindbis virus, Chikungunya virus, and human cytomegalovirus (13, 15–24). Viperin interferes with HIV-1 and influenza A virus budding from the plasma membrane. It binds and inhibits farnesyl diphosphate synthase (FPPS), an enzyme involved in isoprenoid biosynthesis, leading to altered fluidity of lipid rafts, thereby interfering with virus budding (21, 22). Viperin also inhibits genome replication of DENV and HCV by interacting with viral nonstructural proteins (15, 16, 23). The antiviral mechanism(s) of action are poorly understood for most viruses and seem to be dependent on the virus. However, viral or cellular proteins important in the viral life cycle are often sequestered by viperin (21, 23, 25).

In this study, we show that type I IFN treatment interferes with the assembly of TBEV virions. We identified that the viperin protein is responsible for this effect and demonstrate that viperin interacts with and inhibits the function of the GBF1 (Golgi brefeldin A-resistant guanine exchange factor 1) protein, a key factor for the secretory pathway. This interaction affects the assembly of progeny virions by strongly increasing the release of enveloped malfunctioning particles, thereby reducing the production of infectious particles.

RESULTS

IFN treatment induces secretion of capsid protein. IFN and the expression of ISGs can target almost any step of the viral life cycle. However, very little is known about the effect of IFN on particle assembly and egress of flaviviruses. To study viral particle release, we established an expression system that allows the generation of virus-like particles (VLPs) composed of the structural proteins C, prM, and E (Fig. 1A) (26). This system enabled us to study the secretion of VLPs into the supernatant of transfected A549 cells (Fig. 1B). To test the influence of IFN-α, we compared intracellular and

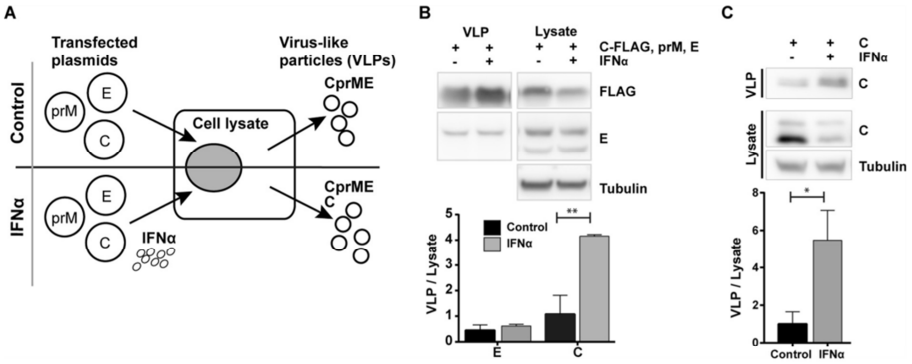

FIG 1 IFN-α induces the release of C protein from cells. (A) Schematic drawing of the experimental setup. (B) Release of CprME-VLPs in the presence or absence of IFN-αB/D. A549 cells were transfected with plasmids expressing TBEV Hypr C-FLAG, prM, and E. At 8 h posttransfection, 10,000 U/ml IFN-αB/D was added, and the supernatant and cell lysate were harvested 48 h later. Supernatants were concentrated by ultracentrifugation, and proteins were separated and detected using immunoblotting with the indicated antibodies. (C) Release of C protein in the presence of IFN-αB/D. A549 cells were transfected with only C protein expression plasmid and treated as described in panel B, except that C proteins were detected with rabbit anti-C antibody. Representative blots are shown; graphs show quantification (means and standard deviations [$n = 3$]) of the Western blots, where C and E proteins in the supernatant were normalized to proteins C and E in the lysate. **, $P < 0.01$; *, $P < 0.05$ (Student t test).

extracellular abundance of flavivirus protein and particles in presence or absence of recombinant IFN-αB/D (Fig. 1B). The effect of IFN treatment on particle assembly was measured by quantifying the ratio between secreted E and C proteins (VLP) and E and C proteins in the cell lysate (Lysate). Surprisingly, compared to control treatment, IFN-αB/D treatment led to a strong increase in C protein release, while the secretion of E protein remained unaltered (Fig. 1B). Flavivirus C protein has not previously been described to be secreted separately from the other structural proteins. To test this, only TBEV C protein was expressed in A549 cells and found to be sufficient for protein release (Fig. 1C). Again, treatment of transfected cells with IFN-αB/D led to an increase of C protein secreted to the supernatant (Fig. 1C). Collectively, this suggested that type I IFN affect the viral structural proteins differently, indicating that C and E proteins are secreted by different mechanisms.

Capsid particles are membrane associated and exit the ER via a COPII dependent mechanism bypassing the Golgi compartment. Since flavivirus C protein secretion has not been described before, we set out to characterize the phenomenon in detail. The C protein detected in the supernatant could be released from cells as soluble proteins, protein aggregates, or membrane-associated proteins. To characterize the nature of the secreted C protein, a flotation assay was performed. C protein floated up and behaved (Fig. 2A, first row) in the same manner as Langat virus (LGTV; a low-virulence member of the TBEV serogroup, which has been used extensively as a nonpathogenic models for TBEV) and VLPs containing prM and E (Fig. 2A). This showed that the C protein released from cells was membrane associated. After the addition of detergent, the C protein was mainly found in the pellet (Fig. 2A, second row, fraction 6), confirming the membrane association. Analysis of the enriched C-particle fraction using electron microscopy revealed particles with a round morphology similar to LGTV and VLPs containing C, prM, and E (Fig. 2B).

It is generally assumed that flavivirus virions assemble in the ER and exit via the conventional secretory pathway (7, 27), and lipid droplets have been suggested to play a role in DENV encapsidation (28). However, to gain further information on the exact localization of TBEV C protein, we performed confocal analysis of cells transfected with plasmid encoding C-FLAG. The C protein was found in the nucleus and colocalized with E and the ER marker calnexin (ER) but not with GM130 (Golgi matrix protein) and was

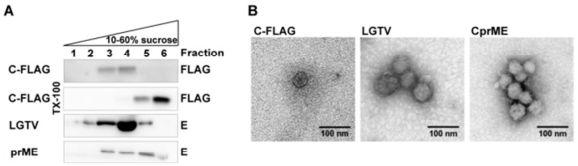

FIG 2 C protein is released as membrane-associated particles. (A) A flotation assay was used to determine the membrane association of C protein, prME VLPs, or LGTV. Supernatant from HeLa cells, which were transiently transfected with plasmids expressing C-FLAG or prM and E, and VeroB4 cells infected with LGTV were concentrated by ultracentrifugation, followed by a flotation assay. The gradient was fractionated from top to bottom and analyzed by immunoblot analysis. Representative blots from two independent experiments are shown. (B) Morphology of VLPs and LGTV as determined by transmission electron microscopy. Supernatant from cells transfected with C-FLAG or the structural proteins C, prM, and E or infected with LGTV were harvested, concentrated by using a flotation assay, and analyzed by negative staining after glutaraldehyde fixation. Representative images are shown.

only in some cells associated with lipid droplets (Fig. 3A and B). To specifically block COPII-mediated transport from the ER toward the ERGIC (ER-Golgi intermediate compartment) and Golgi compartment, a dominant-active mutant of the small GTPase Sar1 (Sar1-H79G) was overexpressed, together with prME or C, and progeny particles were monitored. The Sar1 mutant binds to the ER and initiate the COPII coat protein recruitment but is not able to detach from the ER, thereby blocking ER-to-Golgi-compartment transport (29). The overexpression of Sar1-H79G blocked both prME-particle and C-particle release (Fig. 3C and D), suggesting that COPII-mediated antero-

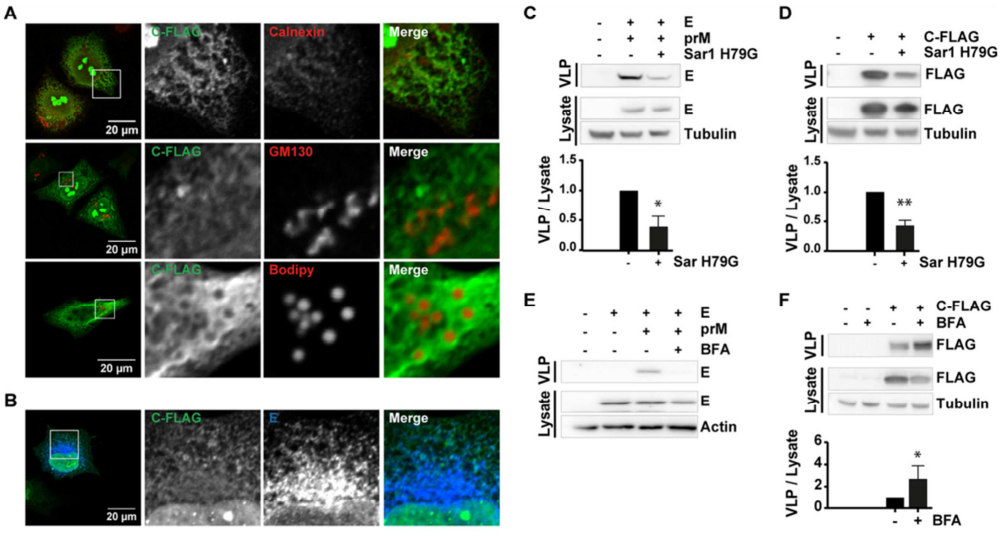

FIG 3 E and C localize to the ER and prME VLP release is COPII and COPI dependent, whereas C-particle release is only COPII dependent. Intracellular localization of C-FLAG with different cellular markers (A). HeLa cells were transfected with C-FLAG, fixed, and stained using antibodies against FLAG, calnexin (ER), and GM130 (Golgi). Lipid droplets were stained with Bodipy 493/503 at 1 μg/ml. For a clear arrangement, the lipid droplets are colored red in the overlay. (B) HeLa cells transfected with C-FLAG, prM, and E protein were stained with antibodies against FLAG and TBEV E. (C) Secretion of prME protein was analyzed in HeLa cells transfected with or without Sar1 H79G (dominant-active mutant) by immunoblot analysis. (D) Immunoblot analysis showing the intracellular expression of C and the secreted C in the presence or absence of Sar1 H79G. (E and F) Involvement of COPI during prME- or C-particle release. Immunoblot analysis showing the intracellular expression of E and C, and also E and C secreted from transfected HeLa cells treated with 0.5 μg/ml BFA (E and F, respectively). Representative blots are shown; the graphs show the quantification (means and standard deviations from $n = 3$ [C, D, and E] and $n = 4$ [F] Western blot experiments), where protein in the supernatant (VLP) was normalized to protein in the lysate. Significance was calculated using a Student t test (*, $P < 0.05$; **, $P < 0.01$).

grade transport is involved in the release of C particles. Next, the cells were treated with brefeldin A (BFA), which blocks both retrograde transport via COPI vesicles and the secretion from the *trans*-Golgi compartment via clathrin-coated vesicles and subsequently causes disruption of the Golgi apparatus (30). This leads to a collapse of the Golgi compartment into the ER and thereby blocks the release of proteins via this pathway (31). BFA efficiently inhibited the secretion of prME particles (Fig. 3E). However, BFA increased the secretion of C particles similar to the IFN treatment (Fig. 3F and Fig. 1C).

Our data suggest that C protein is released as membrane-associated particles and transported from the ER via a COPII-dependent mechanism. However, whereas virus particles and prME VLPs use the classical COPI-dependent secretory pathway, the C particles are released from the cell via a different mechanism, which is induced by both BFA and IFN treatment.

Viperin enhances the release of TBEV capsid particles. To our knowledge, an ISG that positively regulates and induce budding of particles has not been reported. TBEV is budding into the ER and a prominent ISG that localizes to this compartment is viperin. Viperin has previously been reported to inhibit assembly and egress of influenza A and HIV-1 (21, 22) and inhibits TBEV replication (19). Interestingly, the effect on TBEV particle release is greater than the effect on RNA replication (19), suggesting a viperin activity on posttranscriptional level. Viperin colocalized with calnexin (Fig. 4A), confirming it is localization to the ER. Moreover, we could colocalize viperin with C and E protein (Fig. 4A), suggesting an involvement of viperin in particle formation.

To assay the effect of viperin on virus protein secretion, we cotransfected FLAG-tagged C and viperin into 293 FLP-IN T Rex cells expressing prME upon addition of tetracycline (tet). The accumulation of secreted proteins in the supernatant was analyzed by immunoblotting for E protein and C-FLAG, respectively. Expression of viperin did not have an effect on TBEV prME-particle secretion (Fig. 4B) or NS1 protein secretion (data not shown). However, the amount of released C protein increased drastically in the presence of viperin (Fig. 4B). The positive effect on C protein release depended on the dose of transfected viperin (Fig. 4C). In agreement with this, C particles were detected in the supernatant by electron microscopy when C-FLAG and viperin were coexpressed (Fig. 4D).

Next, we analyzed which domains in viperin were involved in the enhanced release of C, using transient transfection of different mutated versions of viperin (Fig. 4E). Truncation in the C terminus (Δ342-361) and the mutant in the radical SAM motif (M1) did not impair the ability of viperin to induce secretion of C protein (Fig. 4F). However, deletion of the N-terminal amphipathic alpha-helix (Δ1-50, also known as TN50 [19]), which directs the protein to the ER (14) significantly reduced the potency of viperin to promote C protein release (Fig. 4F and G).

To verify the antiviral effect of viperin on particle release during viral infection, 293 FLP-IN T Rex cells inducibly expressing viperin upon addition of tet were infected with a high multiplicity of LGTV. Viperin showed a clear antiviral activity against LGTV (Fig. 5), and the antiviral effect was stronger on released viral particles (Fig. 5B) and infectivity (Fig. 5E) than on the viral RNA (Fig. 5D) and viral proteins in the cell lysate (Fig. 5A). The total amount of C protein in the supernatant compared to the E protein (Fig. 5B and C) was greatly enhanced in the presence of viperin (Fig. 5C).

Collectively, our data show that viperin induces C protein release both during viral infection and in transient transfected cells expressing C protein. This function requires localization to the ER and does not impair other cellular secretion systems.

Viperin interacts with GBF1 and induce C-particle secretion. Next, we aimed to reveal the mechanism behind viperin-induced secretion of C particles. As no direct interaction between viperin and C protein could be detected (data not shown), host factors might be involved. We therefore used an affinity proteomics approach to study cellular interaction partners of viperin. We precipitated wild-type (wt) viperin, the Δ1-50

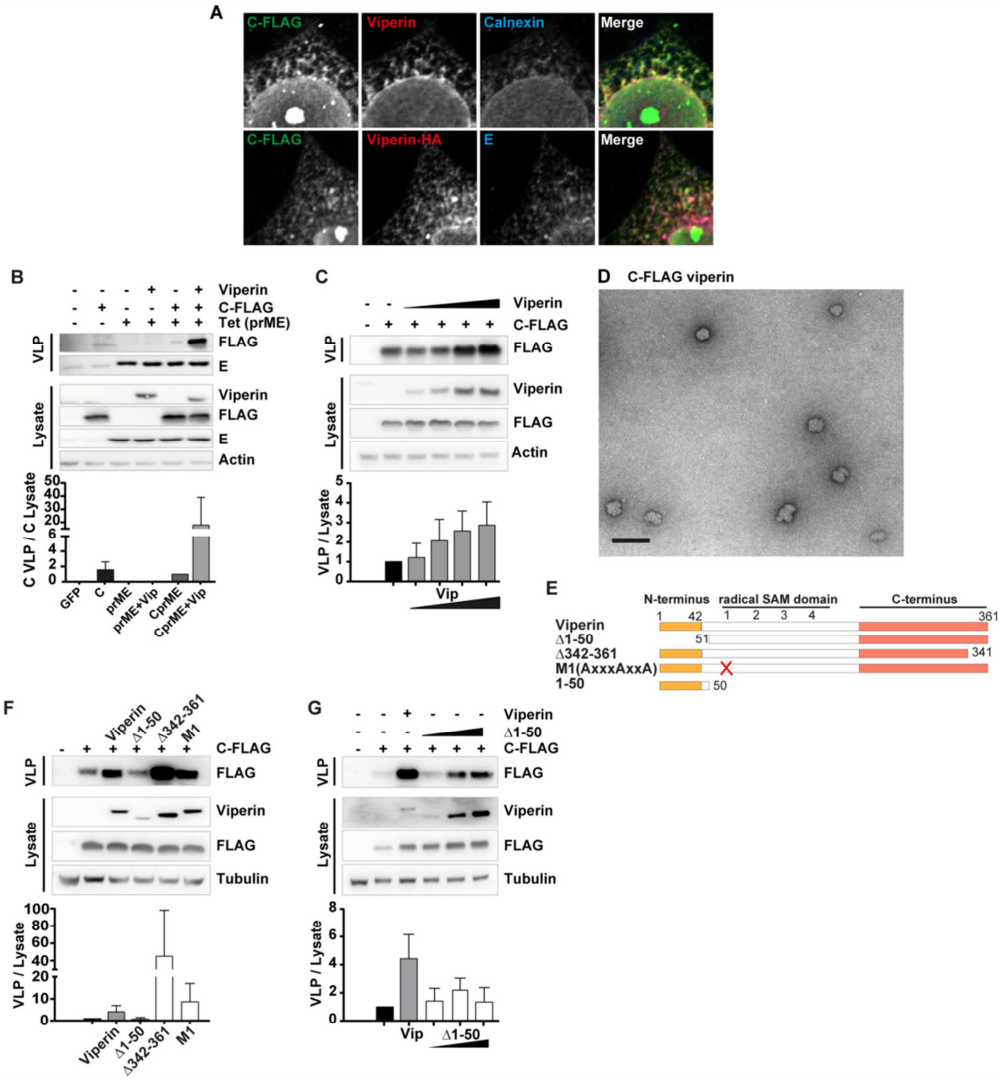

FIG 4 Viperin colocalizes with C and E and induces C-particle release via its N-terminal domain. (A) HeLa cells transfected with C-FLAG and viperin or with C-FLAG, viperin-HA, prM, and E protein stained with antibodies against FLAG, HA, viperin, calnexin, and TBEV E. Representative confocal images are shown. (B) Release of CprME-VLPs in the presence or absence of viperin. A 293 FLP-IN T Rex cell line inducibly expressing TBEV Hypr prME was treated with 1 μg/ml tet and transiently transfected with wt viperin and TBE Hypr C 3× FLAG (C-FLAG). Western blot analysis showing the intracellular and secreted proteins. (C) Dose-dependent release of C protein in the presence of viperin. HeLa cells were transfected with C-FLAG and increasing amounts of viperin (0.75, 1.5, 3, and 6 μg). (D) Morphology of C-FLAG particles by transmission electron microscopy. Supernatants from cells transfected with C-FLAG and viperin were harvested, concentrated using a flotation assay, and analyzed by negative staining after glutaraldehyde fixation. Scale bar, 100 nm. A representative picture is shown. (E) Schematic drawing of viperin mutants. (F) Secretion of C protein in the presence of wt and viperin mutants. HeLa cells were transfected with wt, Δ1-50, Δ341-361, and mutant M1, together with plasmid encoding C–FLAG. (G) Dose-independent release of C protein in the presence of mutant Δ1-50. Increasing amounts of plasmid expressing Δ1-50 were transfected into HeLa cells, together with C-FLAG. C protein release was measured with or without wt viperin expression. Representative blots are shown; graphs show the quantification (means and standard deviations from $n = 3$ [B and C] and $n = 2$ [F and G] Western blot experiments), where C in the supernatant is normalized to C in the lysate.

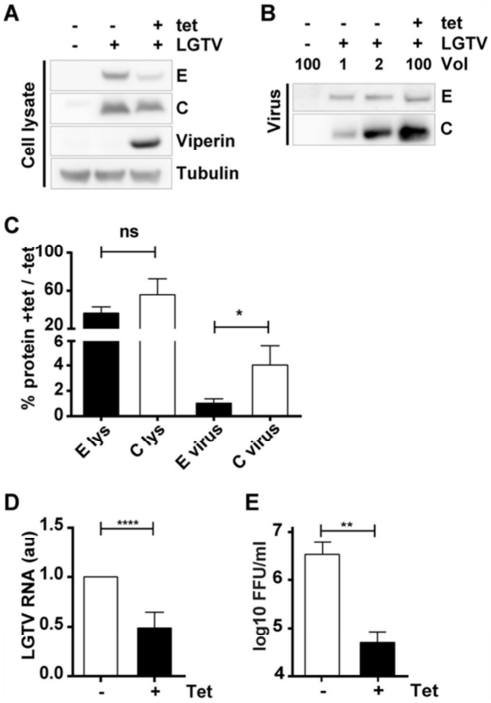

FIG 5 Viperin induces LGTV C protein secretion during infection. 293 FLP-IN T Rex cells inducibly expressing viperin were infected with LGTV and either treated with 1 μg/ml tet at the time point of infection or left untreated. Cells and virus in the supernatant were harvested 48 h postinfection. (A) Amounts of viral proteins E and C detected in cell lysate by Western blotting. (B) Supernatants were concentrated by ultracentrifugation, and comparable levels of viral E proteins with or without viperin were loaded and detected by Western blotting. The lower panel shows the corresponding C protein in the supernatant. Representative blots are shown from three independent experiments. (C) Percentages of E and C protein in the presence of tet-induced viperin compared to uninduced quantification (means and standard deviations) in Western blots of E and C from the lysate (A) and released particles (B) from three independent experiments. (D) LGTV RNA levels in the cell lysate measured by real-time RT-PCR. (E) Plaque assay detecting the infectivity of progeny virions. Mean values and standard deviations ($n = 6$ [D and E]). Significance was calculated with a Student t test (*, $P = 0.0275$; **, $P < 0.01$; ****, $P < 0.0001$).

viperin mutant, or GFP as a control and analyzed associated proteins by liquid chromatography coupled to tandem mass spectrometry (LC-MS/MS) (Fig. 6A).

We identified 115 proteins specifically binding to viperin or the Δ1-50 mutant (Fig. 6B and C; see also Table S1 in the supplemental material). Direct comparison of viperin to the Δ1-50 mutant identified 34 proteins that were significantly more enriched in the wt protein precipitates compared to precipitations with the mutant protein (Fig. 6D, red and green dots). Ciao1 identified previously (19) is comparably well enriched by wt viperin and Δ1-50 mutant, suggesting that the immunoprecipitation (IP) conditions were similar overall. As additional filter method we considered the subcellular localization of these proteins using annotations based on the Human Protein Atlas. This analysis showed that the majority proportion of candidates localized to the nucleus. However, three proteins ARL1 (ADP-ribosylation factor-like protein 1), RCN2 (ERC-55; ER $Ca2^{+}$ binding protein, 55 kDa), and GBF1 (Fig. 6D, green dots) were annotated to localize to the ER or the Golgi compartment. Of these proteins, ARL1 has been reported to regulate intracellular trafficking between the plasma membrane, endosomes, and

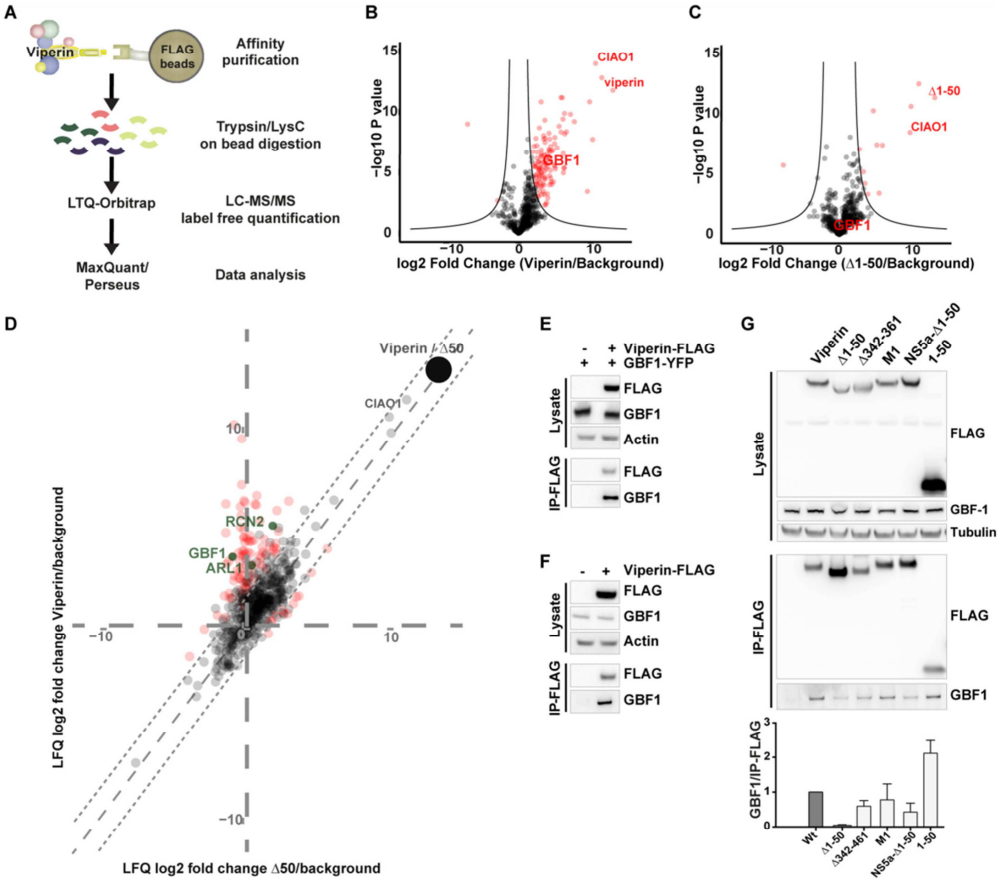

FIG 6 Identification of the protein interactome of viperin by mass spectrometry analysis and verification of GBF1. (A) Schematic representation of an affinity purification/MS strategy. N-terminal FLAG-tagged viperin, Δ1-50 mutant, and GFP (as control) were expressed by tet treatment of 293 FLP-IN T-Rex cells that contained a stably integrated transgene or not expressed when tet was omitted. Cells were lysed under mild lysis conditions, and proteins were precipitated using FLAG beads. After precipitation and extensive washing, the proteins were digested with trypsin and LysC, and the peptides were purified and analyzed by LC-MS/MS. (B and C) Volcano blots of proteins enriched in viperin wt (B) or Δ1-50 (C) precipitates compared to the GFP background control. The hyperbolic line delineates nonsignificantly to significantly enriched proteins. (D) Two-dimensional scatter plot comparing proteins enriched in viperin or the Δ1-50 mutant. Colors: red, significant changes versus the background (two-tailed Welch's *t* test [cutoff: FDR = 0.001 with S0 = 1]); green, significant candidates with association with ER or the Golgi compartment. (E and F) Coimmunoprecipitation analysis shows the interaction between viperin and GBF1. FLAG-tagged viperin was immunoprecipitated with anti-FLAG antibody either from extracts of HEK293T cells transfected with FLAG-tagged viperin and YFP-tagged GBF1 (E) or only FLAG-tagged viperin (F). (G) Coimmunoprecipitation analysis of endogenous GBF1 and viperin mutants. HEK293T cells were transfected with plasmids expressing FLAG-tagged wt viperin, Δ1-50, Δ341-361, M1, HCV NS5a-Δ1-50, or 1-50 mutant and immunoprecipitated with FLAG antibody. HCV NS5a-Δ1-50 is a chimera with the HCV-NS5a amphipathic alpha helix fused to the viperin Δ1-50 mutant (19). Immunoblots show protein input, and immunoprecipitation (IP) graphs show the quantification of IP GBF1 (means and standard deviations from three independent experiments).

the *trans*-Golgi compartment (32). RCN2 has been shown to be a chaperone in the ER and involved in signal transduction (33). GBF1 is a GTP-exchange factor (GEF), which is involved in COPI trafficking. BFA treatment is known to inhibit COPI-coated vesicle formation by binding to and stabilizing the GBF1-ARF1-GDP complex (34). Since BFA induces C-particle secretion (Fig. 3F), the positive effect of viperin on C-particle release could be explained by GBF1 targeting. We therefore set out to further study the

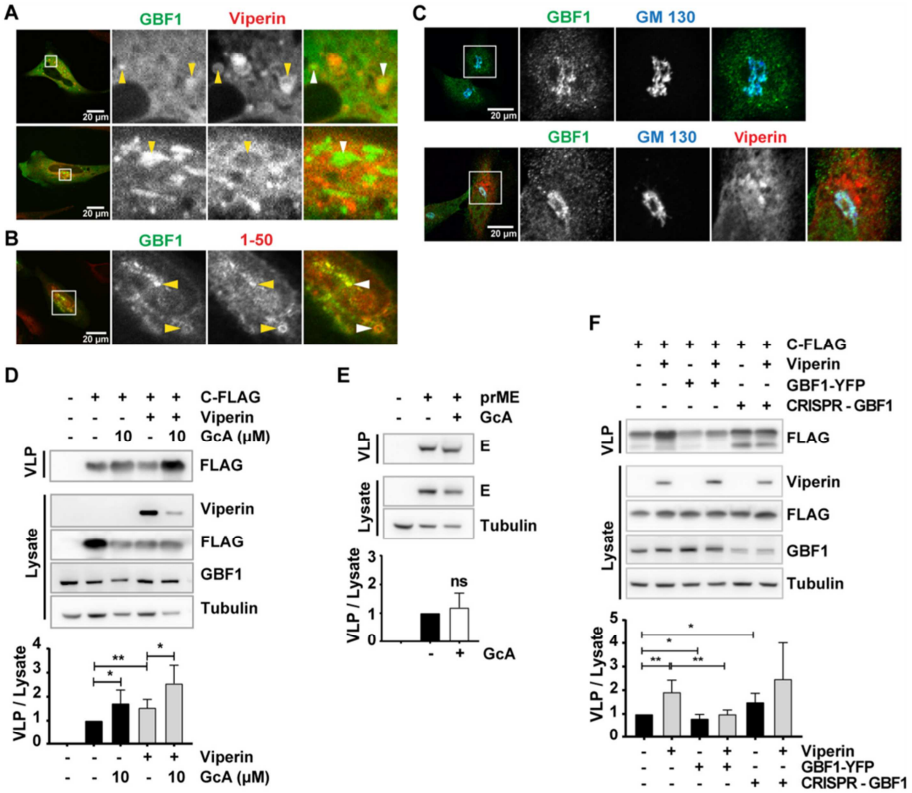

FIG 7 Viperin sequester GBF1 to induce C-particle release. (A) HeLa cells transiently expressing eGFP-GBF1 and mCherry-viperin analyzed in Live-cell confocal spinning disc microscopy show the colocalization of GBF1 and viperin. Arrowheads indicate vesicular structures. (B) Colocalization of the overexpression of viperin 1-50 and eGFP-GBF1 in HeLa cells. (C) Overexpression of mCherry-viperin in HeLa cells and localization of endogenous GBF1 relative to the Golgi marker GM130. Representative confocal images of nontransfected control cells (upper row) and cells transfected with mCherry-viperin (lower row) are shown. The involvement of GBF1 during C (D)- or prME (E)-particle release was assessed. Immunoblot analysis shows the intracellular expression of C (in the presence or absence of viperin) and E, as well as the secreted C and E in transfected HeLa cells treated with 10 μM Golgicide (GcA), a specific GBF1 inhibitor. (F) Effect of availability of wt GBF1 on the release of C protein. HeLa cells were transfected with GBF1-YFP to increase cellular amounts or with CRISPR Cas9 GBF1 plasmid to knock down the cellular GBF1 level. The amounts of protein in the supernatant and cell lysate were measured by immunoblotting at 48 h after the second transfection. Representative blots are shown; graph show the quantification (means and standard deviations from a minimum of $n = 4$ Western blot experiments [D to F]), where C or E in the supernatant is normalized to C and E in the lysate. Significance was calculated using a Student t test (*, $P < 0.05$; **, $P < 0.01$).

interaction between viperin and GBF1. The interaction between viperin and GBF1 could be confirmed by coimmunoprecipitation of both transiently transfected and of endogenous GBF1 (Fig. 6E and F). Mapping of the interaction domain revealed that the 50 first amino acids of viperin containing the amphipathic alpha-helix were important for the binding GBF1 (Fig. 6G), further confirming the mass spectrometry data.

To gain additional knowledge on the subcellular localization of viperin and GBF1, we assessed the subcellular localization of both proteins. Live cell imaging analysis of mCherry-viperin and eGFP-GBF1 showed that eGFP-GBF1 localized to vesicular structures surrounded by viperin (Fig. 7A). The colocalization between GBF1 and the N-terminal 1 to 50 amino acids of viperin in such structures was even more pronounced (Fig. 7B), confirming the coimmunoprecipitation results and suggesting a critical role of the viperin N terminus in these assays. The steady-state distribution of GBF1, together

with the Golgi marker GM130, was not altered in the presence of viperin (Fig. 7C). To clarify whether the function of GBF1 is involved in C-particle secretion, we used a specific GBF1 inhibitor, Golgicide. Cells transfected with plasmids expressing C-FLAG and/or viperin were treated with Golgicide, and the effect on C protein release was evaluated by immunoblotting as described before. Notably, the inhibition of GBF1 by Golgicide strongly induced secretion of C particles, especially in the presence of viperin (Fig. 7D). Importantly, no effect of Golgicide was detected on prME secretion (Fig. 7E), confirming a selective function of GBF1 in flavivirus protein release. To test the functional relationship between viperin and GBF1, the production of C particles was analyzed during modulated cellular levels of GBF1 and in the presence of viperin (Fig. 7F). Viperin-induced increase of C-particle release could be inhibited by overexpression of YFP-GBF1, and transient knockdown of GBF1 with CRISPR Cas9 induced the C-particle release (Fig. 7F), confirming a functional interaction between viperin and GBF1 and, in addition, the importance of GBF1 in the assembly of TBEV.

Taken together, our data demonstrate that viperin inhibits the function of GBF1, leading to the selective release of C particles. This decreases the total number of infectious TBEV particles and thereby reduces the overall infectivity.

DISCUSSION

Very few studies have focused on the antiviral action of ISGs targeting the assembly of virions. Here, we show that type I IFN interferes with flavivirus assembly by inducing unproductive capsid particle release. We found that the IFN-stimulated protein viperin mediates this host cell response by interacting and interfering with the cellular protein GBF1, which is a central molecule in vesicle budding and remodeling of membranes. GBF1 has previously been shown to play a central role in the life cycle of many RNA viruses, which utilize vesicular trafficking for targeting of viral proteins, and cellular membranes in their replication cycle and assembly process (35–39). We found that interfering with GBF1 induce egress of membrane associated C particles, while leaving secretion of prME particles unaffected.

Particle assembly of flavivirus virions occurs by nucleocapsid budding into the ER acquiring the E and prM envelope near the replication complex (6, 40, 41). Secretion of both C particles and prME VLPs were found to be dependent on the conventional COPII secretory pathway, whereas only prME VLPs appeared be released via the Golgi compartment through conventional secretion, in a way similar to that described for other flaviviruses (7). C particles, however, are released from the cell via a different mechanism, which is induced by BFA, Golgicide treatment, and viperin expression.

Both viperin and GBF1 are able to peripherally attach to membranes of the ER, and viperin seems to affect protein secretion when membrane associated. Viperin has been shown to target the ER membrane via its N-terminal amphipathic helical domain (14, 19). This domain has also been found to induce crystalloid ER and thereby rearranging the smooth ER membranes into a lattice-like pattern (14). We demonstrate here that the enhanced secretion of C protein by viperin was dependent on its N terminus and binding to GBF1. Interestingly, the N-terminal domain of viperin seems to be very important for viperin function since the numbers of cellular proteins interacting with the mutant lacking the amphipathic helix were very low (see Table S1 in the supplemental material). This indicates that the intracellular localization of viperin to the ER membrane or the N-terminal itself is important for protein-protein interaction. This domain in viperin is also important for the inhibition of Chikungunya virus (18), TBEV (19), and HCV (16) and directly mediates the binding to GBF1. GBF1 normally regulates membrane dynamics in the secretory pathway, and most RNA viruses rely on cellular vesicular trafficking for proper intracellular localization of viral proteins. GBF1 is important in the life cycles of several different viruses: GBF1 is necessary for RNA replication of DENV, HCV, and SARS coronavirus (35–37), for particle assembly of Ebola virus and influenza A virus (38, 39), and for targeting of DENV C protein to lipid droplets, which is important for DENV infection (36, 42). An interaction between DENV C protein and the N-terminal of viperin has been shown (15). This interaction occurred at the interface

of lipid droplets (15), a hub for DENV assembly (28). Interestingly, a physical interaction between viperin and TBEV C protein could not be detected and thus might not be necessary for the induced secretion of C particles. Immunofluorescence analysis revealed that the N-terminal region of viperin localized to vesicular structures, together with GBF1 in agreement that this region is sufficient to target GBF1. It can be envisaged that modulation of GBF1 by viperin would potentially modulate all of the above-mentioned functions both in the presence and in the absence of interaction between viperin and viral proteins and therefore constitute a widely used mechanism to impair virus spread.

Viperin increases the secretion of membrane-associated C protein but does not affect the transport and release of transmembrane protein prME or vesicular stomatitis virus glycoprotein (14). Similarly, inhibiting GBF1 with BFA completely blocks secretion of prME VLPs and soluble proteins (43) but induces the secretion of TBEV C particles, indicating that proteins are selectively loaded in transport vesicles and viperin affects protein secretion differently, depending on whether they are soluble, membrane-associated, or transmembrane proteins. This selectivity also suggests that cells expressing viperin can reduce viral assembly specifically while leaving the cytokine release untouched.

The membrane association of C protein observed in this study is probably mediated via a hydrophobic domain within the C protein. A similar type of hydrophobic membrane association of the C protein has been suggested for DENV, yellow fever virus, and West Nile virus (44, 45) and even tick-borne flaviviruses (LGTV, Powassan, and TBEV). Notably, the C protein appears to have an intrinsic ability *in vitro* to assemble into particles even in the absence of membranes (46, 47). However, assembly and release of capsid particle in cell culture have not been previously reported for flaviviruses. Interestingly, naked capsid-like HCV particles have been reported *in vivo* (48–50), raising the possibility that viperin might be involved in inducing secretion of such capsid-like HCV particles. We found that the membrane association of the TBEV capsid particles was quite sensitive to mechanical stress; therefore, it could be that the HCV C particles are also secreted with a membrane that is lost shortly after cellular release. HCV C particles are taken up by clathrin-mediated endocytosis in human hepatoma cells (48, 51) and can induce an immune response by modifying specific phenotypic and functional markers in T cells (52). TBEV C particles may have a similar immune modular capacity. A potential antiviral purpose of C-particle secretion could be multifarious ranging from being a side product of disturbed viral assembly, thereby reducing the overall infectivity, to having paracrine or endocrine functions, as reported for HCV (48, 52).

Taken together, we show that IFN selectively induces TBEV C-particle release from cells and that the ISG viperin expression increases C-particle release after infection. We identified GBF1 as a novel interaction partner to viperin. The mechanism behind the induced release of C particles seems to depend on the ability of viperin to interact with GBF1. Viperin is known to have an antiviral effect against a broad range of viruses such as DENV, HCV, influenza A virus, and Chikungunya virus (15, 18, 21, 25). Most of these viruses use GBF1 for their life cycles (35, 39, 53), suggesting that the viperin-GBF1 interaction might be relevant for the antiviral defense against many different viruses and identifying GFB1 as a novel putative drug target for antivirals.

MATERIALS AND METHODS

Cells, viruses, and reagents. Simian Vero B4 cells were grown in M199 (Invitrogen), and human lung carcinoma cells (A549), HeLa cells, and HEK293T cells were grown in Dulbecco modified Eagle medium (DMEM), both supplemented with 5% fetal calf serum (FCS) and penicillin-streptomycin. Human 293 FLP-IN T Rex cells inducibly expressing wt viperin were kindly provided by Ju-Tao Guo. Human 293 FLP-IN T Rex cells (Invitrogen) inducibly expressing TBEV Hypr E and prM protein were generated according to protocol (Invitrogen). Human 293 FLP-IN T Rex cells were propagated in DMEM supplemented with 5% tetracycline-negative FCS (PAA) and penicillin-streptomycin. For induction, 1 μg/ml tetracycline (Sigma) was used. Langat strain TP21 (kindly provided by Gerhard Dobler, Bundeswehr Institute of Microbiology, Munich, Germany) was propagated in Vero B4 cells under biosafety laboratory 2 conditions. BFA stock solution was 5 mg/ml in ethanol (Sigma). Golgicide (Sigma) stock solution was 17 mM in dimethyl

sulfoxide. The recombinant human IFN-αB/D hybrid (54) (kindly provided by Peter Stäheli, Institute of Virology, Medical Center University of Freiburg, Freiburg, Germany).

Plasmids. Expression plasmids encoding TBE Hypr C, C 3× FLAG, prM, and E (41)—as well as human wt viperin, Δ1-50 (TN50), Δ342-461 (TC20), and M1 mutant viperin—and N-terminally FLAG-tagged wt and mutated viperin in the eukaryotic expression vector pI.18 or pcDNA 3.1 have all been described previously (19). The YFP-GBF1-wt plasmid (34) was kindly provided by Catherine L. Jackson, Institut Jacques Monod, University Paris Diderot, Paris, France. The eGFP-GBF1-wt plasmid was generated from the YFP-GBF-wt plasmid by site-directed mutagenesis. The pIRES DsRed2 Sar1 H79G (active mutant) plasmid (55) was kindly provided by Hirofumi Kai, Kumamoto University, Kumamoto, Japan. The mCherry-viperin was constructed by lifting viperin from pI.18 into a mCherry backbone. Transfection was performed with Nanofectin (PAA) or GeneJuice (Novagen) according to the manufacturer's protocol; the transfection efficiency ranged between 40 and 80%.

Antibodies. Primary antibodies were directed against TBEV E (mouse monoclonal antibodies 1493.1 and 1786.3 [56]). TBEV C protein polyclonal antibody was generated in rabbits by immunization with peptide CMVKKAILKGKGGGPPRRVSK according to a standard protocol (Agrisera). Additional primary antibodies included the following: actin (rabbit polyclonal; Sigma), FLAG epitope (mouse monoclonal M2 [Stratagene]; chicken polyclonal [Abcam]; and rabbit polyclonal [Sigma]), HA epitope (rabbit polyclonal; Abcam), viperin (rabbit polyclonal and mouse monoclonal; Abcam), calnexin (rabbit polyclonal and mouse monoclonal; Abcam), GM130 (mouse monoclonal; BD Biosciences), beta-tubulin (rabbit polyclonal; Abcam), eGFP (rabbit polyclonal; Invitrogen), and GBF1 (rabbit polyclonal [Abcam], rabbit polyclonal [Invitrogen]). Secondary antibodies included goat anti-chicken Alexa Fluor 488 (Invitrogen), goat anti-chicken Alexa Fluor 555 (Abcam), donkey anti-mouse Alexa Fluor 488/555 and donkey anti-rabbit Alexa Fluor 488/555 (Invitrogen), goat anti-mouse Alexa Fluor 647 (Life Technologies), goat anti-rabbit Alexa Fluor 488 (Life Technologies), and horseradish peroxidase (HRP)-conjugated goat anti-rabbit IgG and goat anti-mouse IgG secondary antibody (Thermo Fisher).

Immunoblotting. The cells were lysed, and proteins were separated by SDS-PAGE and Western blotting was performed as previously described (19). The membrane was incubated with primary and HRP-conjugated secondary antibodies (Pierce). Detection was performed by using a SuperSignal West Pico or Femto kit (Pierce). For semiquantitative analysis, the Gel Analyzer program in Fiji/Image J was used.

Immunofluorescence. Cells were grown on coverslips to 20 to 40% confluence, transfected, and incubated for 24 h. Cells were washed, fixed, and stained with antibodies. Confocal images were acquired using a Nikon A1R laser scanning confocal microscope (Nikon) with a 60× oil immersion lens (Plan-Apochromat VC) under the control of NIS-Elements microscope imaging software (Nikon). For live-cell microscopy, 140,000 HeLa cells were seeded in a 35-mm MatTek glass-bottom dish. Cells were transiently transfected with eGFP-GBF1 and mCherry-viperin using Lipofectamine 2000 (Invitrogen) according to the manufacturer's recommendations. After 8 h, the transfection medium was replaced with fresh medium, followed by incubation for another 16 h. Spinning-disc confocal live-cell microscopy was performed at 5% CO_2 using a 63× objective lens (Plan-Apochromat 1.40 Oil DIC M27) in a Cell Observer spinning disc confocal microscope system (Andor iXon Ultra; Zeiss) controlled by ZEN software. Image analysis and preparation were completed using ImageJ and Adobe Photoshop CS5.

Viral infection, quantification, and titration. LGTV infection and viral titers were determined by a focus-forming assay as previously described (41). Total RNA was isolated at 48 h postinfection using NucleoSpin RNA II kit (Macherey-Nagel) as previously described (41), and cDNA was synthesized from 500 ng of RNA using a QuantiTect reverse transcription kit (Qiagen) according to the manufacturer's instructions. mRNA expression of actin was detected by a QuantiTect primer assay (Qiagen) and the Kapa SYBR FAST qPCR kit (Kapa Biosystems) using a StepOnePlus fast-real-time PCR system (Applied Biosystems). TBEV RNA was quantified using previously described primers (57) and a Kapa Probe Fast qPCR kit (Kapa Biosystems).

Concentration, purification, and flotation of VLPs and virus particles. Supernatants of transfected or infected cells were collected, concentrated by ultracentrifugation as previously described (58), and resuspended in reducing Laemmli SDS-PAGE sample buffer before Western blot analysis. In the case of further analysis steps, particles were concentrated by ultracentrifugation through a 20/60% sucrose (sucrose in TN buffer [0.1 M NaCl, 0.05 M Tris-HCl; pH 7.4]) cushion at 100,000 × *g* for 1.5 h at 4°C (SW32; Beckman Coulter), and the interface between 20 and 60% sucrose was harvested. A flotation assay was performed as previously described (59). Briefly, the sucrose concentration was adjusted to a final concentration of ~60% sucrose, incubated with or without 1% Triton X-100 for 1 h at 4°C, overlaid with a 30 and 10% sucrose solution, and centrifuged at 200,000 × *g* for 5 h at 4°C (SW60; Beckman Coulter). Fractions were collected and further concentrated by ultracentrifugation (100,000 × *g*, 45 min, 4°C, SW41; Beckman Coulter).

Electron microscopy. Supernatants from cells transfected with C-FLAG or the structural proteins prM and E or infected with LGTV were harvested and concentrated using a flotation assay. Glow-discharged Formvar carbon-coated nickel grids were floated on drops of the virus or VLP suspensions washed with water, fixed with glutaraldehyde 2.5% for 2 min, washed again with water, and stained with 1.5% aqueous uranyl acetate.

Affinity purification/LC-MS/MS experiments. 293 FLP-IN T-Rex cells expressing FLAG-tagged viperin, Δ1-50 mutant, or green fluorescent protein (GFP) were lysed, and α-FLAG antibody coupled beads were used to immunoprecipitate proteins of interest. Four independent affinity purifications were performed for each bait. Sample preparations and LC-MS/MS analysis were conducted as described previously (60). Briefly, FLP-IN cells expressing the FLAG-tagged protein of interest were lysed by

snap-freezing cells in liquid nitrogen, incubation in TAP buffer (50 mM Tris [pH 7.5], 100 mM NaCl, 5% [vol/vol] glycerol, 0.2% [vol/vol] Nonidet P-40, 1.5 mM $MgCl_2$, and protease inhibitor cocktail [EDTA-free, cOmplete; Roche]) for 30 min on ice, and clarification of the lysate by centrifugation at 16,000 × *g*. α-FLAG antibody-coupled beads were incubated with 6-mg portions of cleared lysates for 60 min on a rotating wheel, and the proteins were precipitated and washed with TAP buffer. After the final three washes in TAP buffer, the samples were in also washed twice with TAP buffer lacking Nonidet P-40 to remove residual detergent. Samples were sequentially digested with LysC (Wako Chemicals USA) and trypsin (Promega), acidified with 0.1% TFA, desalted with C18-stage tips, and analyzed by LC-MS on an Orbitrap XL instrument (Thermo Fisher Scientific).

Mass spectrometry raw files were processed with MaxQuant software versions 1.5.1.1 (61, 62) using the built-in Andromeda engine to search against human and mouse proteomes (UniprotKB, release 2012_06) containing forward and reverse sequences. In MaxQuant, the label-free quantitation (LFQ) (63) algorithm and the Match Between Runs option were used as described previously (60). The MaxQuant output tables were transferred to the Perseus computational platform (64) for statistical enrichment analysis. Only proteins identified on the basis of at least two peptides and a minimum of three quantitation events in at least one experimental group were considered. LFQ protein intensity values were log transformed, and missing values were supplied by imputation. Specific enrichment was determined by multiple equal variance *t* tests with permutation-based false discovery rate (FDR) statistics ($n = 250$ permutations). FDR thresholds and S0 parameters were empirically set to separate background from specifically enriched proteins.

Coimmunoprecipitation. HEK293T cells were transfected 24 h before cell lysis (1 mM $MgCl_2$, 1 M Tris-HCl, 5 M NaCl, 5% glycerol, 0.2% NP-40, and protease inhibitor). The FLAG-viperin/GBF1 complex was immunoprecipitated with monoclonal antibodies directed against FLAG (Stratagene), as previously described (19, 65).

CRISPR Cas9 knockdown of GBF1. Three different targets for human GBF1 were selected and cloned into pSpCas9(BB)-2A-GFP (PX458) (Addgene number 48138) using the protocol established by F. Zhang (66). The primer sequences were as follows: TBE 434F, CRISPR Cas9 GBF1.1 (CACCGATGGATTAC GTCAATCCCCG); TBE 435R, CRISPR Cas9 GBF1.1 (AAACCGGGGATTGACGTAATCCATC); TBE 436F, CRISPR Cas9 GBF1.2 (CACCGACACGACCGCCATAACTCAG); TBE 437R, CRISPR Cas9 GBF1.2 (AAACCTGAGTTATGG CGGTCGTGTC); TBE 438F, CRISPR Cas9 GBF1.3 (CACCGACAGTGATTGACAGCACCG); and TBE 439R, CRISPR Cas9 GBF1.3 (AAACCGGTGCTGTCAATCACTGTC). All three target plasmids were cotransfected at a ratio of 1:1:1; at 48 h posttransfection, the cells were reseeded and used for experiments.

SUPPLEMENTAL MATERIAL

Supplemental material for this article may be found at https://doi.org/10.1128/JVI.01751-17.

SUPPLEMENTAL FILE 1, XLSX file, 0.1 MB.

ACKNOWLEDGMENTS

We thank Gerhard Dobler from the Bundeswehr Institute of Microbiology (Munich, Germany) for providing the virus strains Langat virus TP21. The YFP-GBF-wt plasmid (34) was kindly provided by Catherine L. Jackson, Institut Jacques Monod, University Paris Diderot, Paris, France. The pIRES DsRed2 Sar1 H79G (active mutant) plasmid (67) was kindly provided by Hirofumi Kai, Kumamoto University, Kumamoto, Japan. We also thank Karin Edlund for the excellent technical assistance and the Biochemical Imaging Centre Umeå within the National Microscopy Infrastructure for outstanding imaging support.

This study was supported by the Kempe Foundations, the Laboratory for Molecular Medicine Sweden, the Umeå Center for Microbial Research and Linneus Support (A.K.Ö. and R.L.), the Swedish Research Council (VR) (2011-2795), and the Swedish Foundation for Strategic Research (SSF) (ICA10-0059 and FFL12-0089 [A.K.Ö.] and FFL09-0181 [R.L.]). The funders had no role in study design, data collection and interpretation, or the decision to submit the work for publication.

REFERENCES

1. Weber F, Kochs G, Haller O. 2004. Inverse interference: how viruses fight the interferon system. Viral Immunol 17:498–515. https://doi.org/10.1089/vim.2004.17.498.
2. Schneider WM, Chevillotte MD, Rice CM. 2014. Interferon-stimulated genes: a complex web of host defenses. Annu Rev Immunol 32:513–545. https://doi.org/10.1146/annurev-immunol-032713-120231.
3. Roby JA, Funk A, Khromykh AA. 2012. Flavivirus replication and assembly, p 21–50. *In* Shi P-Y (ed), Molecular virology and control of flaviviruses. Caister Academic Press, Norfolk, United Kingdom.
4. Chambers TJ, Hahn CS, Galler R, Rice CM. 1990. Flavivirus genome organization, expression, and replication. Annu Rev Microbiol 44:649–688. https://doi.org/10.1146/annurev.mi.44.100190.003245.
5. Ivanyi-Nagy R, Darlix JL. 2010. Intrinsic disorder in the core proteins of flaviviruses. Protein Pept Lett 17:1019–1025. https://doi.org/10.2174/092986610791498911.
6. Welsch S, Miller S, Romero-Brey I, Merz A, Bleck CK, Walther P, Fuller SD, Antony C, Krijnse-Locker J, Bartenschlager R. 2009. Composition and three-dimensional architecture of the dengue virus replication and assembly sites. Cell Host Microbe 5:365–375. https://doi.org/10.1016/j.chom.2009.03.007.

7. Mackenzie JM, Westaway EG. 2001. Assembly and maturation of the flavivirus Kunjin virus appear to occur in the rough endoplasmic reticulum and along the secretory pathway, respectively. J Virol 75:10787–10799. https://doi.org/10.1128/JVI.75.22.10787-10799.2001.
8. Kupzig S, Korolchuk V, Rollason R, Sugden A, Wilde A, Banting G. 2003. Bst-2/HM1.24 is a raft-associated apical membrane protein with an unusual topology. Traffic 4:694–709. https://doi.org/10.1034/j.1600-0854.2003.00129.x.
9. Masuyama N, Kuronita T, Tanaka R, Muto T, Hirota Y, Takigawa A, Fujita H, Aso Y, Amano J, Tanaka Y. 2009. HM1.24 is internalized from lipid rafts by clathrin-mediated endocytosis through interaction with alpha-adaptin. J Biol Chem 284:15927–15941. https://doi.org/10.1074/jbc.M109.005124.
10. Perez-Caballero D, Zang T, Ebrahimi A, McNatt MW, Gregory DA, Johnson MC, Bieniasz PD. 2009. Tetherin inhibits HIV-1 release by directly tethering virions to cells. Cell 139:499–511. https://doi.org/10.1016/j.cell.2009.08.039.
11. Evans DT, Serra-Moreno R, Singh RK, Guatelli JC. 2010. BST-2/tetherin: a new component of the innate immune response to enveloped viruses. Trends Microbiol 18:388–396. https://doi.org/10.1016/j.tim.2010.06.010.
12. Sauter D, Specht A, Kirchhoff F. 2010. Tetherin: holding on and letting go. Cell 141:392–398. https://doi.org/10.1016/j.cell.2010.04.022.
13. Helbig KJ, Beard MR. 2014. The role of viperin in the innate antiviral response. J Mol Biol 426:1210–1219. https://doi.org/10.1016/j.jmb.2013.10.019.
14. Hinson ER, Cresswell P. 2009. The N-terminal amphipathic α-helix of viperin mediates localization to the cytosolic face of the endoplasmic reticulum and inhibits protein secretion. J Biol Chem 284:4705–4712. https://doi.org/10.1074/jbc.M807261200.
15. Helbig KJ, Carr JM, Calvert JK, Wati S, Clarke JN, Eyre NS, Narayana SK, Fiches GN, McCartney EM, Beard MR. 2013. Viperin is induced following dengue virus type-2 (DENV-2) infection and has antiviral actions requiring the C-terminal end of viperin. PLoS Negl Trop Dis 7:e2178. https://doi.org/10.1371/journal.pntd.0002178.
16. Helbig KJ, Eyre NS, Yip E, Narayana S, Li K, Fiches G, McCartney EM, Jangra RK, Lemon SM, Beard MR. 2011. The antiviral protein viperin inhibits hepatitis C virus replication via interaction with nonstructural protein 5A. Hepatology 54:1506–1517. https://doi.org/10.1002/hep.24542.
17. Szretter KJ, Brien JD, Thackray LB, Virgin HW, Cresswell P, Diamond MS. 2011. The interferon-inducible gene viperin restricts West Nile virus pathogenesis. J Virol 85:11557–11566. https://doi.org/10.1128/JVI.05519-11.
18. Teng TS, Foo SS, Simamarta D, Lum FM, Teo TH, Lulla A, Yeo NK, Koh EG, Chow A, Leo YS, Merits A, Chin KC, Ng LF. 2012. Viperin restricts Chikungunya virus replication and pathology. J Clin Invest 122:4447–4460. https://doi.org/10.1172/JCI63120.
19. Upadhyay AS, Vonderstein K, Pichlmair A, Stehling O, Bennett KL, Dobler G, Guo JT, Superti-Furga G, Lill R, Overby AK, Weber F. 2014. Viperin is an iron-sulfur protein that inhibits genome synthesis of tick-borne encephalitis virus via radical SAM domain activity. Cell Microbiol 16:834–848. https://doi.org/10.1111/cmi.12241.
20. Wang S, Wu X, Pan T, Song W, Wang Y, Zhang F, Yuan Z. 2011. Viperin inhibits hepatitis C virus replication by interfering with the binding of NS5A to host protein hVAP-33. J Gen Virol 93(Pt 1):83–92. https://doi.org/10.1099/vir.0.033860-0.
21. Wang X, Hinson ER, Cresswell P. 2007. The interferon-inducible protein viperin inhibits influenza virus release by perturbing lipid rafts. Cell Host Microbe 2:96–105. https://doi.org/10.1016/j.chom.2007.06.009.
22. Nasr N, Maddocks S, Turville SG, Harman AN, Woolger N, Helbig KJ, Wilkinson J, Bye CR, Wright TK, Rambukwelle D, Donaghy H, Beard MR, Cunningham AL. 2012. HIV-1 infection of human macrophages directly induces viperin which inhibits viral production. Blood 120:778–788. https://doi.org/10.1182/blood-2012-01-407395.
23. Wang S, Wu X, Pan T, Song W, Wang Y, Zhang F, Yuan Z. 2012. Viperin inhibits hepatitis C virus replication by interfering with binding of NS5A to host protein hVAP-33. J Gen Virol 93:83–92. https://doi.org/10.1099/vir.0.033860-0.
24. Chin KC, Cresswell P. 2001. Viperin (cig5), an IFN-inducible antiviral protein directly induced by human cytomegalovirus. Proc Natl Acad Sci U S A 98:15125–15130. https://doi.org/10.1073/pnas.011593298.
25. Helbig KJ, Lau DT, Semendric L, Harley HA, Beard MR. 2005. Analysis of ISG expression in chronic hepatitis C identifies viperin as a potential antiviral effector. Hepatology 42:702–710. https://doi.org/10.1002/hep.20844.
26. Lorenz IC, Kartenbeck J, Mezzacasa A, Allison SL, Heinz FX, Helenius A. 2003. Intracellular assembly and secretion of recombinant subviral particles from tick-borne encephalitis virus. J Virol 77:4370–4382. https://doi.org/10.1128/JVI.77.7.4370-4382.2003.
27. Lindenbach BD, Rice CM. 2003. Molecular biology of flaviviruses. Adv Virus Res 59:23–61. https://doi.org/10.1016/S0065-3527(03)59002-9.
28. Samsa MM, Mondotte JA, Iglesias NG, Assuncao-Miranda I, Barbosa-Lima G, Da Poian AT, Bozza PT, Gamarnik AV. 2009. Dengue virus capsid protein usurps lipid droplets for viral particle formation. PLoS Pathog 5:e1000632. https://doi.org/10.1371/journal.ppat.1000632.
29. Bielli A, Haney CJ, Gabreski G, Watkins SC, Bannykh SI, Aridor M. 2005. Regulation of Sar1 NH2 terminus by GTP binding and hydrolysis promotes membrane deformation to control COPII vesicle fission. J Cell Biol 171:919–924. https://doi.org/10.1083/jcb.200509095.
30. Grieve AG, Rabouille C. 2011. Golgi bypass: skirting around the heart of classical secretion. Cold Spring Harb Perspect Biol 3:a005298. https://doi.org/10.1101/cshperspect.a005298.
31. Fujiwara T, Oda K, Yokota S, Takatsuki A, Ikehara Y. 1988. Brefeldin A causes disassembly of the Golgi complex and accumulation of secretory proteins in the endoplasmic reticulum. J Biol Chem 263:18545–18552.
32. Huang LH, Lee WC, You ST, Cheng CC, Yu CJ. 2015. Arfaptin-1 negatively regulates Arl1-mediated retrograde transport. PLoS One 10:e0118743. https://doi.org/10.1371/journal.pone.0118743.
33. Honore B. 2009. The rapidly expanding CREC protein family: members, localization, function, and role in disease. Bioessays 31:262–277. https://doi.org/10.1002/bies.200800186.
34. Niu TK, Pfeifer AC, Lippincott-Schwartz J, Jackson CL. 2005. Dynamics of GBF1, a brefeldin A-sensitive Arf1 exchange factor at the Golgi. Mol Biol Cell 16:1213–1222. https://doi.org/10.1091/mbc.E04-07-0599.
35. Carpp LN, Rogers RS, Moritz RL, Aitchison JD. 2014. Quantitative proteomic analysis of host-virus interactions reveals a role for Golgi brefeldin A resistance factor 1 (GBF1) in dengue infection. Mol Cell Proteomics 13:2836–2854. https://doi.org/10.1074/mcp.M114.038984.
36. Farhat R, Seron K, Ferlin J, Feneant L, Belouzard S, Goueslain L, Jackson CL, Dubuisson J, Rouille Y. 2016. Identification of class II ADP-ribosylation factors as cellular factors required for hepatitis C virus replication. Cell Microbiol 18:1121–1133. https://doi.org/10.1111/cmi.12572.
37. de Wilde AH, Wannee KF, Scholte FE, Goeman JJ, Ten Dijke P, Snijder EJ, Kikkert M, van Hemert MJ. 2015. A kinome-wide small interfering RNA screen identifies proviral and antiviral host factors in severe acute respiratory syndrome coronavirus replication, including double-stranded RNA-activated protein kinase and early secretory pathway proteins. J Virol 89:8318–8333. https://doi.org/10.1128/JVI.01029-15.
38. Yamayoshi S, Neumann G, Kawaoka Y. 2010. Role of the GTPase Rab1b in ebolavirus particle formation. J Virol 84:4816–4820. https://doi.org/10.1128/JVI.00010-10.
39. Watanabe T, Kawakami E, Shoemaker JE, Lopes TJ, Matsuoka Y, Tomita Y, Kozuka-Hata H, Gorai T, Kuwahara T, Takeda E, Nagata A, Takano R, Kiso M, Yamashita M, Sakai-Tagawa Y, Katsura H, Nonaka N, Fujii H, Fujii K, Sugita Y, Noda T, Goto H, Fukuyama S, Watanabe S, Neumann G, Oyama M, Kitano H, Kawaoka Y. 2014. Influenza virus-host interactome screen as a platform for antiviral drug development. Cell Host Microbe 16:795–805. https://doi.org/10.1016/j.chom.2014.11.002.
40. Miorin L, Romero-Brey I, Maiuri P, Hoppe S, Krijnse-Locker J, Bartenschlager R, Marcello A. 2013. Three-dimensional architecture of tick-borne encephalitis virus replication sites and trafficking of the replicated RNA. J Virol 87:6469–6481. https://doi.org/10.1128/JVI.03456-12.
41. Overby AK, Popov VL, Niedrig M, Weber F. 2010. Tick-borne encephalitis virus delays interferon induction and hides its double-stranded RNA in intracellular membrane vesicles. J Virol 84:8470–8483. https://doi.org/10.1128/JVI.00176-10.
42. Iglesias NG, Mondotte JA, Byk LA, De Maio FA, Samsa MM, Alvarez C, Gamarnik AV. 2015. Dengue virus uses a noncanonical function of the host GBF1-Arf-COPI system for capsid protein accumulation on lipid droplets. Traffic 16:962–977. https://doi.org/10.1111/tra.12305.
43. Klausner RD, Donaldson JG, Lippincott-Schwartz J. 1992. Brefeldin A: insights into the control of membrane traffic and organelle structure. J Cell Biol 116:1071–1080. https://doi.org/10.1083/jcb.116.5.1071.
44. Markoff L, Falgout B, Chang A. 1997. A conserved internal hydrophobic domain mediates the stable membrane integration of the dengue virus capsid protein. Virology 233:105–117. https://doi.org/10.1006/viro.1997.8608.
45. Yamshchikov VF, Compans RW. 1994. Processing of the intracellular form

of the west Nile virus capsid protein by the viral NS2B-NS3 protease: an in vitro study. J Virol 68:5765–5771.
46. Kiermayr S, Kofler RM, Mandl CW, Messner P, Heinz FX. 2004. Isolation of capsid protein dimers from the tick-borne encephalitis flavivirus and in vitro assembly of capsid-like particles. J Virol 78:8078–8084. https://doi.org/10.1128/JVI.78.15.8078-8084.2004.
47. Lopez C, Gil L, Lazo L, Menendez I, Marcos E, Sanchez J, Valdes I, Falcon V, de la Rosa MC, Marquez G, Guillen G, Hermida L. 2009. In vitro assembly of nucleocapsid-like particles from purified recombinant capsid protein of dengue-2 virus. Arch Virol 154:695–698. https://doi.org/10.1007/s00705-009-0350-8.
48. Tsitoura P, Georgopoulou U, Petres S, Varaklioti A, Karafoulidou A, Vagena D, Politis C, Mavromara P. 2007. Evidence for cellular uptake of recombinant hepatitis C virus nonenveloped capsid-like particles. FEBS Lett 581:4049–4057. https://doi.org/10.1016/j.febslet.2007.07.032.
49. Hijikata M, Shimizu YK, Kato H, Iwamoto A, Shih JW, Alter HJ, Purcell RH, Yoshikura H. 1993. Equilibrium centrifugation studies of hepatitis C virus: evidence for circulating immune complexes. J Virol 67:1953–1958.
50. Maillard P, Krawczynski K, Nitkiewicz J, Bronnert C, Sidorkiewicz M, Gounon P, Dubuisson J, Faure G, Crainic R, Budkowska A. 2001. Nonenveloped nucleocapsids of hepatitis C virus in the serum of infected patients. J Virol 75:8240–8250. https://doi.org/10.1128/JVI.75.17.8240-8250.2001.
51. Katsarou K, Lavdas AA, Tsitoura P, Serti E, Markoulatos P, Mavromara P, Georgopoulou U. 2010. Endocytosis of hepatitis C virus nonenveloped capsid-like particles induces MAPK-ERK1/2 signaling events. Cell Mol Life Sci 67:2491–2506. https://doi.org/10.1007/s00018-010-0351-5.
52. Doumba PP, Serti E, Boutsikou M, Konstadoulakis MM, Georgopoulou U, Koskinas J. 2013. Phenotypic and functional alterations of primary human PBMCs induced by HCV nonenveloped capsid-like particles uptake. Cell Mol Life Sci 70:3463–3474. https://doi.org/10.1007/s00018-013-1344-y.
53. Goueslain L, Alsaleh K, Horellou P, Roingeard P, Descamps V, Duverlie G, Ciczora Y, Wychowski C, Dubuisson J, Rouille Y. 2010. Identification of GBF1 as a cellular factor required for hepatitis C virus RNA replication. J Virol 84:773–787. https://doi.org/10.1128/JVI.01190-09.
54. Horisberger MA, de Staritzky K. 1987. A recombinant human interferon-alpha B/D hybrid with a broad host-range. J Gen Virol 68(Pt 3):945–948. https://doi.org/10.1099/0022-1317-68-3-945.
55. Susuki S, Sato T, Miyata M, Momohara M, Suico MA, Shuto T, Ando Y, Kai H. 2009. The endoplasmic reticulum-associated degradation of transthyretin variants is negatively regulated by BiP in mammalian cells. J Biol Chem 284:8312–8321. https://doi.org/10.1074/jbc.M809354200.
56. Niedrig M, Klockmann U, Lang W, Roeder J, Burk S, Modrow S, Pauli G. 1994. Monoclonal antibodies directed against tick-borne encephalitis virus with neutralizing activity in vivo. Acta Virol 38:141–149.
57. Schwaiger M, Cassinotti P. 2003. Development of a quantitative real-time RT-PCR assay with internal control for the laboratory detection of tick borne encephalitis virus (TBEV) RNA. J Clin Virol 27:136–145. https://doi.org/10.1016/S1386-6532(02)00168-3.
58. Overby AK, Popov V, Neve EP, Pettersson RF. 2006. Generation and analysis of infectious virus-like particles of Uukuniemi virus (*Bunyaviridae*): a useful system for studying bunyaviral packaging and budding. J Of Virology 80:10428–10435. https://doi.org/10.1128/JVI.01362-06.
59. Kiernan RE, Ono A, Freed EO. 1999. Reversion of a human immunodeficiency virus type 1 matrix mutation affecting Gag membrane binding, endogenous reverse transcriptase activity, and virus infectivity. J Virol 73:4728–4737.
60. Habjan M, Hubel P, Lacerda L, Benda C, Holze C, Eberl CH, Mann A, Kindler E, Gil-Cruz C, Ziebuhr J, Thiel V, Pichlmair A. 2013. Sequestration by IFIT1 impairs translation of 2′O-unmethylated capped RNA. PLoS Pathog 9:e1003663. https://doi.org/10.1371/journal.ppat.1003663.
61. Cox J, Mann M. 2008. MaxQuant enables high peptide identification rates, individualized p.p.b.-range mass accuracies and proteome-wide protein quantification. Nat Biotechnol 26:1367–1372. https://doi.org/10.1038/nbt.1511.
62. Tyanova S, Temu T, Cox J. 2016. The MaxQuant computational platform for mass spectrometry-based shotgun proteomics. Nat Protoc 11:2301–2319. https://doi.org/10.1038/nprot.2016.136.
63. Cox J, Hein MY, Luber CA, Paron I, Nagaraj N, Mann M. 2014. Accurate proteome-wide label-free quantification by delayed normalization and maximal peptide ratio extraction, termed MaxLFQ. Mol Cell Proteomics 13:2513–2526. https://doi.org/10.1074/mcp.M113.031591.
64. Tyanova S, Temu T, Sinitcyn P, Carlson A, Hein MY, Geiger T, Mann M, Cox J. 2016. The Perseus computational platform for comprehensive analysis of (prote)omics data. Nat Methods 13:731–740. https://doi.org/10.1038/nmeth.3901.
65. Upadhyay AS, Stehling O, Panayiotou C, Rosser R, Lill R, Overby AK. 2017. Cellular requirements for iron-sulfur cluster insertion into the antiviral radical SAM protein viperin. J Biol Chem 292:13879–13889. https://doi.org/10.1074/jbc.M117.780122.
66. Ran FA, Hsu PD, Wright J, Agarwala V, Scott DA, Zhang F. 2013. Genome engineering using the CRISPR-Cas9 system. Nat Protoc 8:2281–2308. https://doi.org/10.1038/nprot.2013.143.
67. Okiyoneda T, Harada K, Yamahira K, Wada I, Hashimoto Y, Ueno K, Suico MA, Shuto T, Kai H. 2004. Characterization of the trafficking pathway of cystic fibrosis transmembrane conductance regulator in baby hamster kidney cells. J Pharmacol Sci 95:471–475. https://doi.org/10.1254/jphs.SC0040081.

2.5 PUBLICATION 5: VIRULENCE FACTOR NSS OF RIFT VALLEY FEVER VIRUS RECRUITS THE F-BOX PROTEIN FBXO3 TO DEGRADE SUBUNIT P62 OF GENERAL TRANSCRIPTION FACTOR TFIIH

Viruses rely on a diverse range of strategies to counteract and inhibit cellular defense responses. A common strategy of viruses is the inhibition of the transcription of antiviral acting genes by interfering with the transcription machinery of the host.

The Rift Valley fever virus (RVFV) encodes for the NSs protein which is known to facilitate immune modulation. Expression of the RVFV encoded NSs protein during infection mediates the degradation of the p62 subunit, a member of the general transcription factor TFIIH. In collaboration with the Laboratory of Prof. Weber (at that time: Institute for Virology, Philipps-University Marburg. Now: Institute for Virology, FB10-Veterinary Medicine, Justus-Liebig University, Giessen) we identified the F-box protein FBXO3 as the cellular E3 ubiquitin ligase responsible for the ubiquitination and subsequent degradation of p62 during RVFV infection. AP-LC-MS/MS analysis of RVFV NSs revealed physical interaction to FBXO3 and suggested the contribution of the SCF ubiquitin ligase complex in the NSs mediated p62 depletion process. Subsequent rescue siRNA mediated knock down experiments of the SCF ubiquitin ligase complex members revealed that Skp1 but not cullin-proteins or Rbx1 are required for NSs induced p62 degradation.

I contributed to this project by analyzing AP-LC-MS/MS data. Thereby I was able to support the characterization of RVFV NSs interactors and to identify further FBXO3 associated proteins such as SCF ubiquitin ligase factors.

JVI
Journals.ASM.org

Virulence Factor NSs of Rift Valley Fever Virus Recruits the F-Box Protein FBXO3 To Degrade Subunit p62 of General Transcription Factor TFIIH

Markus Kainulainen,[a] Matthias Habjan,[b,c] Philipp Hubel,[b] Laura Busch,[a] Simone Lau,[a] Jacques Colinge,[d] Giulio Superti-Furga,[d] Andreas Pichlmair,[b,d] Friedemann Weber[a,c]

Institute for Virology, Philipps-University Marburg, Marburg, Germany[a]; Innate Immunity Laboratory, Max-Planck Institute of Biochemistry, Martinsried/Munich, Germany[b]; Department of Virology, University Freiburg, Freiburg, Germany[c]; CeMM Research Center for Molecular Medicine of the Austrian Academy of Sciences, Vienna, Austria[d]

ABSTRACT

The nonstructural protein NSs is the main virulence factor of Rift Valley fever virus (RVFV; family *Bunyaviridae*, genus *Phlebovirus*), a serious pathogen of livestock and humans in Africa. RVFV NSs blocks transcriptional upregulation of antiviral type I interferons (IFN) and destroys the general transcription factor TFIIH subunit p62 via the ubiquitin/proteasome pathway. Here, we identified a subunit of E3 ubiquitin ligases, F-box protein FBXO3, as a host cell interactor of NSs. Small interfering RNA (siRNA)-mediated depletion of FBXO3 rescued p62 protein levels in RVFV-infected cells and elevated IFN transcription by 1 order of magnitude. NSs interacts with the full-length FBXO3 protein as well as with a truncated isoform that lacks the C-terminal acidic and poly(R)-rich domains. These isoforms are present in both the nucleus and the cytoplasm. NSs exclusively removes the nuclear pool of full-length FBXO3, likely due to consumption during the degradation process. F-box proteins form the variable substrate recognition subunit of the so-called SCF ubiquitin ligases, which also contain the constant components Skp1, cullin 1 (or cullin 7), and Rbx1. siRNA knockdown of Skp1 also protected p62 from degradation, suggesting involvement in NSs action. However, knockdown of cullin 1, cullin 7, or Rbx1 could not rescue p62 degradation by NSs. Our data show that the enzymatic removal of p62 via the host cell factor FBXO3 is a major mechanism of IFN suppression by RVFV.

IMPORTANCE

Rift Valley fever virus is a serious emerging pathogen of animals and humans. Its main virulence factor, NSs, enables unhindered virus replication by suppressing the antiviral innate immune system. We identified the E3 ubiquitin ligase FBXO3 as a novel host cell interactor of NSs. NSs recruits FBXO3 to destroy the general host cell transcription factor TFIIH-p62, resulting in suppression of the transcriptional upregulation of innate immunity.

Rift Valley fever virus (RVFV; family *Bunyaviridae*, genus *Phlebovirus*) is a serious, arthropod-borne pathogen affecting wild animals, livestock, and humans (1, 2). The RVFV outbreaks that regularly occur in Africa result in devastating losses of lives and wealth. In ruminants like cattle and sheep, the typical onset of an RVFV epidemic is characterized by so-called abortion storms and the deaths of about 100% of the newborns. In adult animals, the infection causes hepatitis and hemorrhage with a mortality rate of 10 to 20%. Human infections are mostly restricted to a self-limiting febrile illness, but in 1% to 2% of cases the symptoms can aggravate to fulminant hepatitis, encephalitis, retinitis, blindness, or a hemorrhagic syndrome (3). In hospitalized patients, the typical case fatality rate is 10% to 20%, but higher rates have been reported (4).

RVFV is transmitted by a multitude of mosquito and sandfly species (5, 6) but also through aerosols or contact with aborted fetuses (1, 2). It is capable of infecting a wide range of animals and has repeatedly proven its potential to spread into new areas and cause large epidemics (7). These features, together with the fact that preventive and therapeutic possibilities are limited, have led to the classification of RVF as a notifiable disease and a potential biological weapon (8).

The particles of RVFV consist of a lipid envelope with two integral glycoproteins, Gn and Gc, surrounding a core of three ribonucleoproteins (RNPs) (9). These RNPs are complexes of nucleoprotein (N), RNA-dependent RNA polymerase (L), and a viral genomic RNA (vRNA). RVFV has three different vRNA segments, of which two (designated L and M) are in negative sense and one (S) is in ambisense. The L segment encodes the L protein, the M segment encodes a polyprotein that is processed to the glycoproteins Gn and Gc along with the nonstructural proteins NSm1 and NSm2, and the S segment encodes the N protein and the nonstructural protein NSs.

NSs plays a central role in the pathogenesis of RVFV by downregulating the antiviral type I interferon (IFN-α/β) system (10, 11). IFNs are cytokines that are produced by infected cells to establish an antiviral state in the surrounding cells, mediated by products of the so-called IFN-stimulated genes (ISGs) (12). The induction of the IFN response occurs on the transcriptional level. RVFV NSs was shown to block both the specific upregulation of IFN genes and the general transcription of host cell mRNAs (reviewed in references 13 and 14). The molecular basis of the specific

Received 4 October 2013 **Accepted** 29 December 2013
Published ahead of print 8 January 2014
Editor: A. García-Sastre
Address correspondence to Friedemann Weber, friedemann.weber@staff.uni-marburg.de.
Copyright © 2014, American Society for Microbiology. All Rights Reserved.
doi:10.1128/JVI.02914-13

IFN inhibition by NSs was proposed to be the recruitment of the transcriptional repressor SAP30 to the IFN promoter (15), whereas the general effect was attributed to depletion of the general transcription factor TFIIH from its subunit p44 (16). These mechanisms are reliant on stoichiometric sequestration of target proteins, which is a relatively slow process requiring NSs to be present at least at a 1:1 ratio with the target protein. IFN gene transcription, however, is triggered by just a few viral signature structures detected by the host cell (17, 18) and occurs shortly after infection (19, 20). It remains therefore questionable whether the rapid and potent shutdown of IFN induction imposed by NSs (10) could be completely explained by a stoichiometric mechanism involving binding and sequestration of host cell targets, which at least in the initial phase of infection outnumber the viral proteins. In fact, a recent report shows that RVFV can act on host transcription through a different mechanism, namely, the proteasomal degradation of p62, a subunit of the general transcription factor TFIIH (21). It remained unclear, however, how this destructive activity is achieved and how it contributes to IFN antagonism. Therefore, in the present study, we investigated the connection between the RVFV NSs IFN antagonism, TFIIH-p62, and the proteasomal system. We demonstrate that p62 is degraded by NSs almost immediately after virus entry. Based on results from a large-scale proteomic screen (22), we identified the F-box protein FBXO3 as an interactor of RVFV NSs. FBXO3 and its cofactor Skp1 seem to form part of an E3 ubiquitin ligase responsible for the NSs-driven p62 degradation and IFN suppression. To our knowledge, this is the first report on a host cell interactor of RVFV NSs that is involved in IFN suppression via rapid degradation of host cell targets.

MATERIALS AND METHODS

Cells, viruses, and reagents. HeLa, A549, Vero E6, 293T, and BHK-21 cells were cultivated in Dulbecco's modified Eagle's medium (DMEM) supplemented with 5% (HeLa cells) or 10% (all other cells) fetal calf serum (FCS). RVFV strains rZH548 and Clone 13 and the newly generated recombinant RVFV strains (see below) were propagated on Vero E6 cells under biosafety level 3 (BSL-3) conditions. MG132 was purchased from Biomol.

Plasmid constructs. The RVFV plasmids for rescuing recombinant RVFV, pI.18_RVFV_L, pI.18_RVFV_N (helper plasmids), pHH21_RVFV_vL, and pHH21_RVFV_vM (rescue plasmids) were described previously (23). The rescue plasmids used to express tandem affinity purification (TAP)-tagged fusion proteins via RVFV are based on an ambisense S segment rescue construct (termed pHH21_RVFV_vN_MCS-CTAP) containing a tandem AarI cloning site followed by a C-terminal TAP tag sequence instead of the NSs gene. The 5′ and 3′ AarI restriction sites are compatible with NcoI and HinDIII sites, respectively, and the C-terminal TAP sequence is in frame with the ATG start codon created by the NcoI-compatible 5′ AarI site (23). To express NSs fused with a C-terminal TAP tag via recombinant RVFV, the NSs gene of strain ZH548 was cloned into pHH21_RVFV_vN_MCS-CTAP, giving rise to the S segment rescue plasmid pHH21_RVFV_vN_NSsZH-CTAP. In a similar manner, the negative-control plasmid pHH21_RVFV_vN_GFP-CTAP was generated, expressing the enhanced green fluorescent protein (EGFP) gene fused with a C-terminal TAP tag, as well as the S segment rescue plasmids expressing a C-terminal Flag epitope-tagged RVFV NSs (pHH21_RVFV_vN_NSsZH_CFlag) or a 3×Flag-tagged ΔMx control protein (pHH21_RVFV_vN_3×Flag_ΔMx).

To express epitope tag-equipped FBXO3 isoforms, total RNA isolated from 293T cells was used for reverse transcription (RT) followed by amplification of the respective cDNAs with specific primers. The amplicons were subcloned, and the resulting constructs were used as the templates for generating amplicons with N-terminal 3× hemagglutinin (HA) tags. These amplicons were cloned to pcDNA3.1 by T/A cloning (Invitrogen). The constructs pcDNA3.1-3×HA-FBXO3/1 and pcDNA3.1-3×HA-FBXO3/2 were sequenced to verify that the inserts corresponded to GenBank entries NM_012175.3 and NM_033406.2, respectively. FBXO3 cDNAs were PCR amplified from these constructs and ligated to pDONR221 vector using the Gateway technology (Invitrogen). These constructs were used for cloning plasmids expressing tandem affinity tagged (StrepII-HA) proteins and transfected into 293 FLP-IN TREX cells in order to generate stable, doxycycline (DOX)-inducible cell lines. Detailed cloning strategies and primers are available upon request.

Western blot analyses. Samples for Western blot analysis were separated by SDS-PAGE, blotted to polyvinylidene difluoride (PVDF) membranes, and blocked using 5% (wt/vol) milk powder in Tris-buffered saline with 0.1% Tween 20. The membranes were probed with antibodies against the following targets: HA tag, GTF2H1 (p62), Skp1 (monoclonal antibody [MAb] EPR3304), cullin 1 (MAb EPR3102Y), ROC1 (Rbx1) (all by Abcam), Flag tag (Sigma), cullin 7 (Thermo Scientific), cdk7 (MAb MO1) and β-actin (MAb 8H10D10) (both by Cell Signaling), PKR (MAb 71/10) (24), and RVFV N (25). Peroxidase-conjugated anti-mouse and anti-rabbit IgG polyclonals (Thermo Fisher) were used as secondary antibodies.

Generation of recombinant RVF viruses. Recombinant Rift Valley fever virus strain ZH548 expressing TAP-tagged NSs (rZHΔNSs::NSs_{ZH548}-CTAP or TAP-tagged GFP (rZHΔNSs::GFP-CTAP), Flag-NSs (rZHΔNSs::CF-NSs_{ZH548}; rZH-CF-NSs in short), and 3×Flag-ΔMx (rZHΔNSs::F-ΔMx; rZH-NF-ΔMx in short) were rescued from cloned cDNA using the pol I/pol II system (23). Briefly, cocultures of 293T and BHK-21 cells grown in 6-well dishes were transfected with the helper constructs pI.18_RVFV_L and pI.18_RVFV_N (0.5 μg each) and the rescue constructs pHH21_RVFV_vL (L segment) and pHH21_RVFV_vM (M segment) combined with an S segment plasmid (1 μg each). After 5 days of incubation, cell supernatants were harvested and transferred onto Vero E6 cells to grow virus stocks. The genetic and biological properties of the recombinant viruses were confirmed by RT-PCR, sequencing of the NSs locus, and functional assays (data not shown).

Preparation of lysates for proteomics. 293T cells seeded in 15-cm dishes were infected with RVFVΔNSs::NSs_{ZH548}-CTAP or RVFVΔNSs::GFP-CTAP at a multiplicity of infection (MOI) of 5 for 16 h. Then, cells were washed once with cold phosphate-buffered saline (PBS), scraped off in 5 ml cold PBS, and centrifuged at 1,000 × *g* for 5 min at 4°C, and the pellet was snap-frozen in liquid nitrogen. After addition of 5 ml of TAP buffer (50 mM Tris-HCl [pH 7.5], 5% glycerol, 0.2% NP-40, 1.5 mM $MgCl_2$, 100 mM NaCl, and protease and phosphatase inhibitors), pellets were again snap-frozen in liquid nitrogen and stored at −80°C.

Real-time RT-PCR. Total cellular RNA was isolated with the RNeasy Minikit (Qiagen) and eluted in 40 μl of double-distilled water (ddH_2O). An aliquot of 100 ng RNA was then used as a template for cDNA synthesis and PCR using the QuantiTect Reverse Transcription and QuantiTect SYBR green PCR kits (Qiagen) and a StepOne Real-Time PCR system (Applied Biosystems). mRNA levels of human IFN-β, IP-10, FBXO3, and GAPDH (glyceraldehyde-3-phosphate dehydrogenase) were determined with QuantiTect primers (Qiagen) QT00203763, QT01003065, QT00061285, and QT01192646, respectively. All values obtained were normalized against the GAPDH mRNA signal using the $\Delta\Delta C_T$ method (26). For the cytokine assays, mock samples that showed no PCR amplification were arbitrarily set to a threshold cycle (C_T) value of 40. RVFV L RNA was measured by TaqMan quantitative RT-PCR (RT-qPCR) as described by Bird et al. (27).

Immunofluorescence assays. HeLa cells were grown on coverslips to 30 to 50% confluence and infected and incubated for the indicated time. Then, cells were fixed with 4% paraformaldehyde, permeabilized with 0.5% Triton X-100 in PBS, and washed with PBS containing 1% FCS. The following primary antibodies were used, diluted in PBS containing 1% FCS: Anti-Flag (Sigma), Anti HA.11 (Covance), and Anti-GTF2H1 (Abcam). After incubation at room temperature for 1 h, the coverslips were

washed three times with 1% FCS in PBS and treated at room temperature for 45 min with anti-mouse and anti-rabbit IgG polyclonals coupled with Alexa Fluor 488 or Alexa Fluor 555 dyes. DAPI (4′,6-diamidino-2-phenylindole) was used at 0.1 μg/ml to counterstain nuclei. After washing three times with PBS and once with ddH_2O, coverslips were mounted using Fluorsave solution (Calbiochem). Stained cell samples were examined using a Leica SP5 confocal microscope.

siRNA knockdown. Knockdown of gene expression was achieved by 2-fold reverse transfection of small interfering RNAs (siRNAs). AllStar Negative Control siRNA as well as validated pools of four siRNAs (Qiagen) against mRNAs for FBXO3 (GeneSolution GS26273), Rbx1 (GeneSolution GS9978), Skp1 (GeneSolution GS6500), cullin 1 (GeneSolution GS8454), and cullin 7 (GeneSolution GS9820) were used. For reverse transfections, siRNAs were transfected with 50 nM total concentrations using Lipofectamine RNAiMAX (Invitrogen) according to the manufacturer's instructions. Four hours after transfection, the medium was changed. Three days after the first transfection, the cells were harvested and counted, and equal amounts of cells were again reverse transfected as described above. Experiments were performed 1 day after the second transfections.

Coimmunoprecipitation assays. 293 FLP-IN TREX cells stably expressing SII-HA-tagged FBXO3 isoforms 1 or 2 were used for coimmunoprecipitation experiments. Expression was induced by treating the cells with 2 μg/ml doxycycline hyclate for 2 days. The cells were then infected with rZH-CF-NSs or rZH-NF-ΔMx (MOI of 3). Doxycycline was included in the medium added after removing the inoculum. Three hours later, 20 μM MG132 was added, and the incubation was continued for 1 h. Cells were scraped into cold PBS and pelleted by centrifugation. The cells were lysed in cold TAP buffer. After centrifugation, lysis supernatant was incubated with Dynabeads (Invitrogen) coupled with either Anti HA.11 antibody (Covance) or Anti-Flag M2 antibody (Stratagene) for 1 h at +4°C. After three washes with TAP buffer, the complexes were eluted by boiling the beads in SDS-loading buffer and analyzed by Western blotting.

RESULTS

Rapid degradation of NSs targets. So far, two main host cell targets have been described to be degraded by RVFV NSs: p62, the TFIIH subunit mentioned above, and double-stranded RNA (dsRNA)-dependent protein kinase R (PKR), one of the main ISGs inhibiting RVFV replication (25, 28). We performed a time course experiment to obtain kinetics for p62 and PKR degradation after virus infection. In agreement with previous studies (16, 21, 25, 28), we observed rapid degradation of both PKR and p62 after infection with the recombinant wild-type (wt) strain ZH548, whereas the NSs-truncated strain Clone 13 had no such effect (Fig. 1A). A much weaker susceptibility to NSs-mediated degradation was observed for CDK7, a regulatory kinase of TFIIH (Fig. 1B). Similar results were obtained using human A549 cells (see below). Thus, we were able to confirm in our system that p62 and PKR are efficiently removed by RVFV NSs.

To investigate the onset of p62 and PKR degradation in more detail, we added the proteasomal inhibitor MG132 at different time points of infection. As seen in Fig. 1C, addition of MG132 at 1 h after infection is required to preserve PKR levels, whereas later addition had no protective effect. To preserve p62 levels, the inhibitor had to be present even earlier. MG132 had to be added either from the first moment the virus contacted the cell (i.e., already in the inoculum) or directly after the virus inoculum was replaced by cell culture medium (Fig. 1C). Later addition of MG132 did not prevent p62 degradation, although the inhibitor largely slows down virus infection. Interestingly, immediate early addition of MG132 revealed the presence of a high-molecular-weight ladder of p62 as well as a short form of it, suggesting ubiquitin attachment and a degradation intermediate. Nonetheless, we were unable to directly demonstrate ubiquitination, possibly due to the fact that only a fraction of p62 is affected at any given time (data not shown). The data indicate that RVFV NSs induces the rapid proteasomal destruction of both PKR and p62, with the latter being even more quickly or more efficiently degraded than the former.

NSs interacts with the E3 ubiquitin ligase component FBXO3. We have recently performed a proteomic screen for host cell interactors of 70 viral IFN antagonists, including the NSs of the virulent RVFV strain ZH548 (22). Since RVFV NSs inhibits RNA polymerase II-driven mRNA synthesis, it is difficult to express from eukaryotic plasmids. We had to construct a recombinant RVFV encoding an NSs with a C-terminal TAP tag. Approximately 2×10^8 293T cells were infected with the TAP-NSs virus at an MOI of 5 and lysed after overnight incubation. A recombinant RVFV encoding the EGFP gene fused with a C-terminal TAP tag served as a negative control. TAP tag-purified protein complexes were analyzed by one-dimensional (1D) gel liquid chromatography-mass spectrometry. The purified TAP-NSs complexes contained several significant NSs interactors, among them a poorly characterized F-box protein termed FBXO3 (Fig. 2). F-box proteins are components of the so-called SCF ubiquitin ligases, multisubunit complexes that are named after their main components, Skp1, cullin, and an F-box protein. Mammals have around 70 different F-box proteins (29). The F-box protein component constitutes the variable part of the SCF ubiquitin ligase and directs the complex to specific substrates. The signature F-box motif connects to the Skp1 subunit, and the ubiquitination substrate is recruited through another protein-protein interaction domain, which is situated at the C terminus. According to their type of C-terminal interaction domain, F-box proteins are classified as either FBXW (containing WD40 repeats), FBXL (containing leucine-rich repeats), and FBXO (for "other"). Since FBXO3 was the only host cell interactor with a connection to the ubiquitin-proteasome system (UPS), we decided to further investigate its potential link to the action of RVFV NSs.

Human FBXO3 is 471 amino acids (aa) long, with several domains (Fig. 3A). Besides the full-length protein (NCBI sequence NM_012175), a shorter splice variant is predicted (NCBI sequence NM_033406), lacking the C-terminal acidic domain and poly(R) region. Due to a paucity of appropriate antisera to detect endogenous FBXO3, we cloned both the full-length protein (termed isoform 1; FBXO3/1) and the shorter isoform (isoform 2; FBXO3/2) and equipped them with an N-terminal HA epitope tag. In a first set of experiments, we confirmed the interaction with NSs. Stable 293 FLP-IN TREX cell lines were generated, containing an expression cassette for the HA-tagged FBXO3 isoforms under the control of a doxycycline-inducible promoter. The 293 FLP-IN TREX cells were treated with DOX to induce FBXO3 expression and then infected with a recombinant RVFV encoding the NSs of wt strain ZH548 equipped with a C-terminal Flag tag (Flag-NSs). As a control, we employed a recombinant RVFV encoding a Flag-tagged, biologically inactive fragment of the human MxA protein (Flag-ΔMx). Three hours after infection, cells were treated with MG132 and incubated for another hour. Cells were lysed and subjected to immunoprecipitations using antibodies against the epitope tags. Both the cell lysates and the immunoprecipitates were analyzed by immunoblotting, using epitope tag-specific antibodies. The Western blot of the cell lysates shows that all investigated proteins

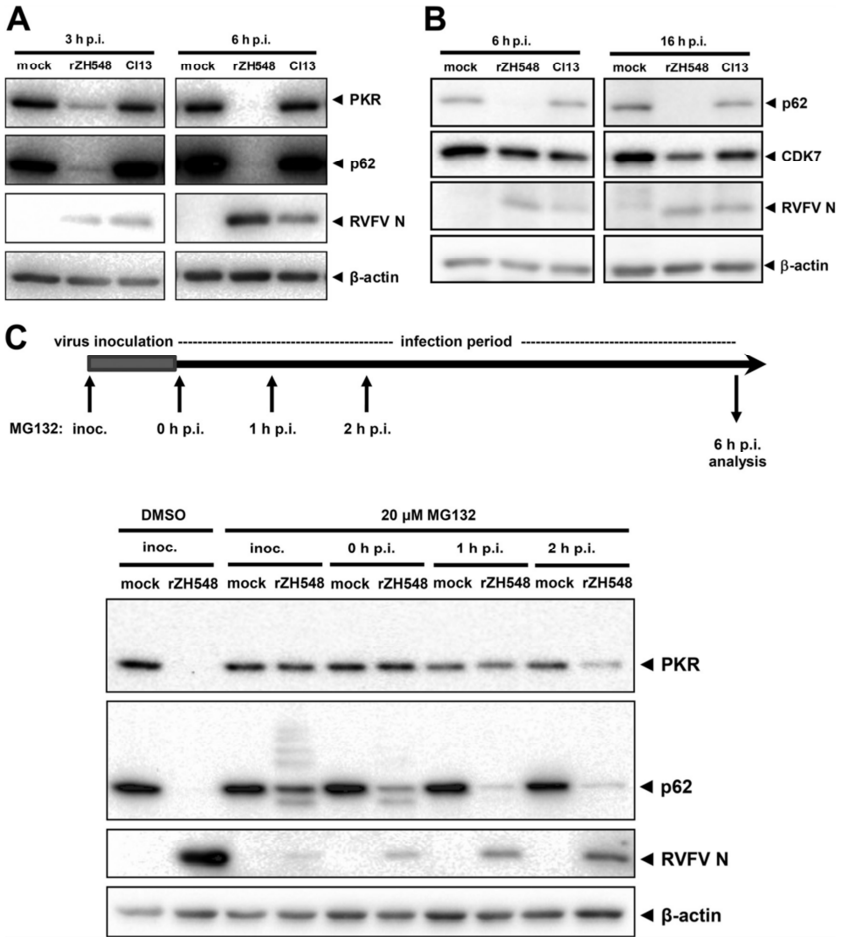

FIG 1 Rapid proteasomal degradation of p62 by RVFV NSs. (A and B) Time course of target degradation. HeLa cells were infected with recombinant wt RVFV strain ZH548 (rZH548) or the NSs-truncated mutant Clone 13 (Cl13) at an MOI of 5 (A) or 10 (B) or were left uninfected (mock). Cells were lysed after the indicated time periods and subjected to Western blot analyses against PKR and p62 (A) or p62 and CDK7 (B). RVFV N and β-actin were detected as infection and loading control, respectively. (C) Time course of MG132 addition. HeLa cells were mock infected or infected with rZH548 at an MOI of 10 for 1 h in infection medium (inoculum). Then, cells were incubated either in 0.2% dimethyl sulfoxide (DMSO) alone or in 20 μM MG132 and 0.2% DMSO at different time points of infection. Inoc., DMSO or MG132 was present in the virus inoculum and later in the cell culture medium; 0 h p.i., virus inoculum was replaced by cell culture medium containing MG132; 1 h p.i., MG132 addition 1 h after taking off the inoculum and incubation in cell culture medium; 2 h p.i., MG132 addition 2 h after taking off the inoculum and incubation in cell culture medium. All cells were lysed at 6 h p.i. and analyzed by immunoblotting using the indicated antibodies.

are present at similar, detectable levels (Fig. 3B, left panel). The Western blots of the immunoprecipitates show that NSs was able to bind both isoforms of FBXO3, whereas the ΔMx control was unable to do so (Fig. 3B, middle and right panels). These results thus confirm the findings of the proteomics study (22) and establish the F-box protein FBXO3 as a host cell interactor of RVFV NSs.

FBXO3 is important for p62 degradation and IFN antagonism by NSs. To clarify the contribution of FBXO3 to the UPS-dependent activities of NSs, we employed an siRNA knockdown approach. The Western blot analysis shown in Fig. 4A demonstrates that abrogation of FBXO3 expression had no influence on the NSs-driven destruction of PKR but prevented the degradation of p62. The degradation of p62 after infection with wt RVFV could also be seen in immunofluorescence experiments, and knockdown of FBXO3 rescued p62 levels (Fig. 4B). Moreover, in the absence of FBXO3 there is a colocalization of p62 with the typical

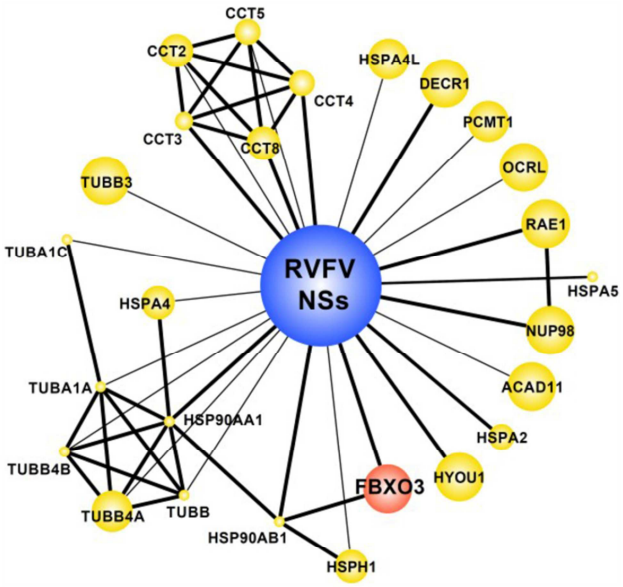

FIG 2 Host cell interactors of RVFV NSs. Interactors of RVFV NSs protein were identified by affinity purification followed by mass spectrometry (AP-MS) using RVFV NSs as bait and as published in reference 22. Network representation shows interactions between NSs and AP-MS identified proteins (preys). Known direct protein interactions between preys are also shown (22). The edge thickness represents the number of spectra identified in the RVFV NSs precipitates (1, thin edge; >1, thick edge). The size of the symbols (nodes) indirectly correlates with numbers of identifications in the published data set, i.e., big symbols show proteins uniquely identified in RVFV NSs precipitates, whereas smaller symbols indicate identification with RVFV NSs as well as other (non-NSs) viral open reading frames. Red, presence of domains suggesting involvement in ubiquitin-dependent degradation (i.e., RING or FBX domains) based on SMART domain annotations; yellow, all other proteins.

filamentous structures formed by RVFV NSs, indicating a close proximity. Real-time RT-qPCR analyses demonstrated an FBXO3 mRNA knockdown efficiency of approximately 90% (Fig. 4C, left panel). FBXO3 itself does not have a major influence on RVFV RNA synthesis (Fig. 4C, right panel) or virus replication (data not shown). Importantly, however, the abrogation of FBXO3 expression (and hence preservation of p62) increased IFN-β induction in response to wt RVFV by a factor of 25 to 30 (Fig. 5, left panel). Similarly, wt RVFV-triggered expression of the antiviral chemokine IP-10 is elevated 9- to 16-fold under conditions of FBXO3 knockdown (Fig. 5, right panel). IFN and IP-10 induction in response to the NSs-truncated Clone 13, in contrast, was not influenced by FBXO3. This confirms that the increase of IFN induction under FBXO3-depleted conditions is not an unspecific effect but is connected to NSs. Further, reducing FBXO3 levels is sufficient to partially alleviate the anti-IFN activity of NSs. These data demonstrate that the E3 ubiquitin ligase component FBXO3 is necessary for the NSs-mediated destruction of p62, whereas PKR is degraded by another pathway. The NSs-driven elimination of p62 via FBXO3 contributes to the suppression of innate immunity by RVFV.

We observed that the increased IFN induction in FBXO3-depleted cells does not impair RVFV replication (Fig. 4C, right panel). Most likely, this is because NSs still destroys PKR, one of the major IFN effectors against RVFV (Fig. 4A).

RVFV NSs removes the long isoform of FBXO3 from the nucleus. We investigated the fate of FBXO3 in cells infected with RVFV. In uninfected cells, the full-length isoform 1 of FBXO3 is concentrated in the nucleus but also present in the cytoplasm (Fig. 6A, upper panels). However, in cells infected with wt RVFV, the nuclear form is no longer detectable, whereas the cytoplasmic pool is unchanged (Fig. 6A, middle panels). This phenomenon is caused by NSs expression, since the mutant RVFV strain with the control protein ΔMx *in lieu* of NSs maintained nuclear FBXO3 (Fig. 6A, lower panels). Employing the nuclear export inhibitor leptomycin B could not rescue nuclear FBXO3/1 in RVFV-infected cells (data not shown). Moreover, applying the host cell transcription inhibitor alpha-amanitin could not mimic the effect of NSs on nuclear FBXO3/1 (data not shown). This suggests that the selective disappearance of full-length FBXO3 from the nucleus is neither caused by nuclear expulsion nor an unspecific consequence of the massive transcriptional inhibition imposed by NSs. Interestingly, the disappearance of nuclear FBXO3 does not occur in the case of the short isoform FBXO3/2 (Fig. 6B). Thus, the interaction and functional importance of FBXO3 for RVFV NSs function are reflected by a disappearance of nuclear full-length FBXO3.

Degradation of p62 is dependent on Skp1. E3 ubiquitin ligases of the SCF type typically consist of an F-box protein (which defines the substrate specificity), the linker protein Skp1, the scaffold

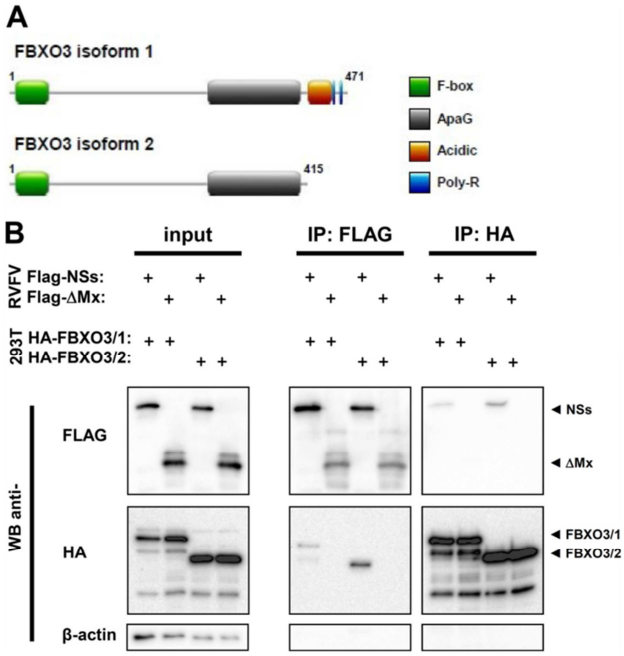

FIG 3 Interaction of FBXO3 with RVFV NSs. (A) Cartoon depicting the domain structure of FBXO3 isoforms (UniProt accession number Q9UK99), drawn by using the image creator MyDomains of the ExPASy website (45). (B) Immunoprecipitation. 293 FLP-IN TREX cells expressing SII-HA-tagged FBXO3/1 or FBXO3/2 were induced with doxycycline for 2 days and then infected with rZH-CF-NSs or rZH-NF-ΔMx (MOI of 3). Three hours p.i., MG132 was added to the medium, cells were incubated for another hour, lysed, and subjected to immunoprecipitation using the indicated antibodies.

protein cullin 1, and the docking factor Rbx1, which connects the complex to an E2 ubiquitin conjugase (29). We wanted to determine whether any of the other SCF components is involved in FBXO3-related NSs action. For this purpose, we knocked down individual SCF components using siRNA and monitored levels of p62 in infected cells. A Western blot analysis is shown in Fig. 7A. Surprisingly, knockdown of cullin 1 expression could not protect p62 from degradation by NSs, although it reduced RVFV infection to some extent. Knockdown of cullin 7, which sometimes acts as an alternative to cullin 1 (29), also had no effect, neither alone nor in combination with a cullin 1 knockdown (Fig. 7B). In contrast, siRNA knockdown of FBXO3, Rbx1, and Skp1 seemed to rescue p62 levels in wt RVFV-infected cells (Fig. 7A). However, the abrogation of Rbx1 and Skp1 expression resulted in a diminished RVFV infection. Therefore, it remained difficult to distinguish whether Rbx1 and Skp1 are indeed required for p62 degradation or whether RVFV infection is simply too inefficient for a proper NSs effect. To obtain a clearer picture, we analyzed the degradation of p62 on the single-cell level (Fig. 7C). Knockdown of any of the three basic SCF components, but especially Rbx1, had a strong impact on cell morphology. Nuclei and cells were rounded and enlarged, and the increased presence of twin nuclei may hint to possible cell division problems. Only low levels of NSs were detectable. Nonetheless, in cells deficient in cullin 1 or Rbx1, expression of NSs resulted in a disappearance of the p62 signal. In cells deficient in Skp1, by contrast, NSs-positive cells also exhibited a p62 signal. Thus, only Skp1 (but neither cullin 1, nor cullin 7, nor Rbx1) appears to be essential for p62 degradation by NSs.

In summary, our collective data demonstrate that the NSs of RVFV drives the degradation of the general transcription factor p62 by means of the F-box protein FBXO3 and the linker protein Skp1. The rapid destruction of p62 substantially contributes to the block in IFN and cytokine induction observed in wt RVFV-infected host cells.

DISCUSSION

RVFV is an eminent pathogen for humans and animals alike. The major virulence factor of RVFV is the nonstructural protein NSs, a strong suppressor of the innate immune responses. NSs is a multifunctional protein that recruits the transcriptional repressor SAP30 to the IFN promoter (15), depletes the general transcription factor TFIIH from its subunit p44 (16), and degrades the TFIIH subunit p62 (16, 21) and the antiviral effector PKR (25, 28). The aim of our study was to identify the host cell factors that are engaged by NSs. Our data show that one aspect of destructive NSs action, the degradation of the TFIIH subunit p62, is mediated by the F-box protein FBXO3.

FBXO3 knockdown experiments demonstrated that the pro-

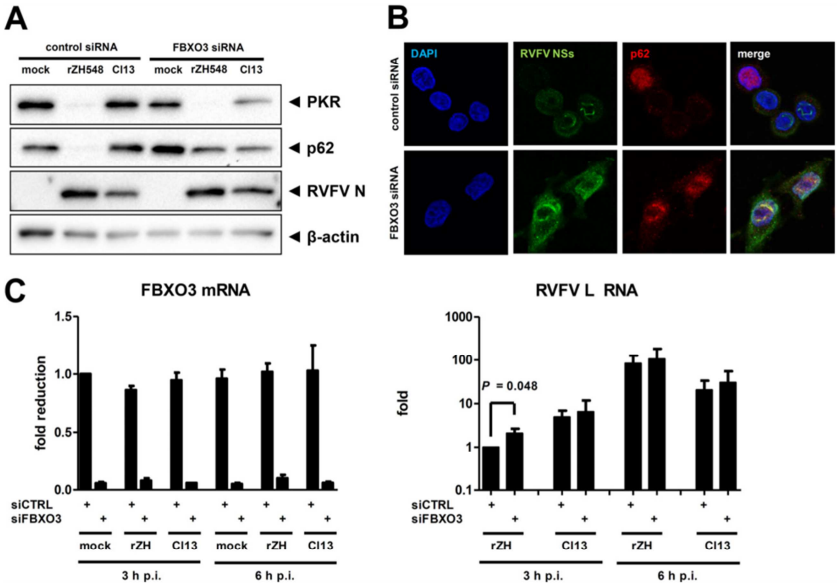

FIG 4 Effect of FBXO3 on p62 degradation by RVFV NSs. (A) Western blot analysis of knockdown cells. Human A549 cells were treated with siRNA directed against the FBXO3 mRNA or with a control siRNA. Cells were then infected with wt RVFV (rZH548) or Clone 13 (Cl13) at an MOI of 10 and 6 h later analyzed for the presence of PKR, p62, RVFV N, and β-actin using Western blot analysis. (B) Immunofluorescence analysis. siRNA knockdown of FBXO3 mRNA was achieved in HeLa cells as described for panel A. Cells were infected for 6 h with a recombinant RVFV expressing Flag-tagged NSs (rZH-CF-NSs), and the presence of p62 and Flag-RVFV NSs was analyzed 6 h later using appropriate antibodies. DAPI was used for counterstaining the nuclei. (C) Real-time RT-PCR of the knockdown cells shown in panel A. Cells were treated and infected as described for panel A and analyzed for the presence of RNAs for FBXO3 (left panel) and RVFV L (right panel) at 3 and 6 h postinfection. Mean values and standard deviations of 3 independent experiments are shown. A two-tailed, paired *t* test using log-transformed data was used to compare the siRNA pairs.

tection of p62 from NSs action partially relieved RVFV-mediated IFN suppression. To our knowledge, this is the first example of an NSs-interacting host cell partner that was positively demonstrated to be essential for NSs action. The study on the p44 host cell partner of NSs deduced its conclusions exclusively on the interaction data and on *in vitro* assays (16). The study on the SAP30 partner of NSs additionally demonstrated a correlation between the inability of the NSs Δ210-230 mutant to interact with SAP30 and the inability to inhibit IFN induction (15). Meanwhile, however, it is known that most mutations of NSs lead to a complete loss of

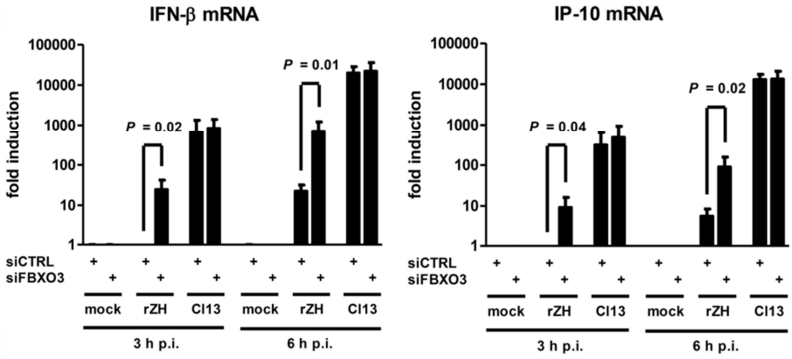

FIG 5 Effect of FBXO3 on IFN suppression by RVFV NSs. Real-time RT-PCR of knockdown cells shown in Fig. 4A and C, analyzed for the presence of IFN-β mRNA and IP-10 mRNA at 3 and 6 h postinfection. A two-tailed, paired *t* test using log-transformed data was used to compare the siRNA pairs.

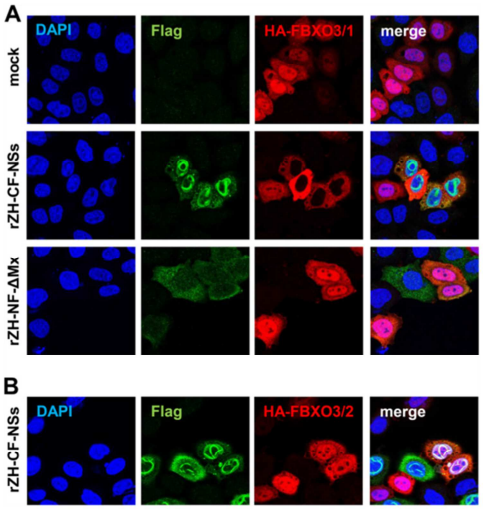

FIG 6 Influence of RVFV NSs on FBXO3 isoforms. (A) Long isoform FBXO3/1. HeLa cells were transfected with 0.5 μg of cDNA expression construct pcDNA3.1-3xHA-FBXO3/1. After overnight incubation, cells were infected at an MOI of 10 with recombinant RVFV expressing either Flag-tagged NSs (rZH-CF-NSs) or the negative-control protein ΔMx (rZH-NF-ΔMx) or were left uninfected (mock). At 6 h p.i., cells were fixed, permeabilized, and double immunostained for the Flag (green) and the HA (red) epitopes. (B) Short isoform FBXO3/2. HeLa cells were transfected with the cDNA expression construct pcDNA3.1-3xHA-FBXO3/2 and infected and immunostained as described for panel A.

function (30). In fact, Head et al. had demonstrated that NSs mutants deleted at aa 6 to 30, 31 to 55, 56 to 80, 81 to 105, 106 to 130, 131 to 155, 156 to 180, 181 to 205, 206 to 230, 231 to 248, and 249 to 265 all were unable to inhibit IFN induction or to degrade PKR. This indicates that the null phenotype of a certain NSs mutant alone is difficult to interpret, as it may affect stability or correct folding (30). In our study, in contrast, we show that the absence of the interactor FBXO3 partially neutralizes the strong block of IFN induction imposed by wt NSs whereas the PKR degradation function of NSs remains intact. We are therefore confident that FBXO3 is a crucial and specific interactor of NSs that is engaged to degrade p62 and block IFN transcription.

Compared to the deletion of NSs from the RVFV genome, siRNA depletion of FBXO3 was approximately 1 order of magnitude less efficient in rescuing IFN induction. This incomplete restoration of IFN induction, combined with the untouched PKR degradation activity, most likely is responsible for the absence of a measurable impact of FBXO3 depletion on RVFV growth. Several reasons are possible for the residual IFN suppression under conditions of FBXO3 depletion. First, it is possible that the siRNA treatment did not completely remove FBXO3 from the cells. Second, the binding of NSs to p62 (21) (Fig. 4B) to the TFIIH subunit p44 (16) and to SAP30 (15) also contributes to IFN inhibition. Third, we showed that FBXO3 depletion does not protect from PKR degradation by NSs. Since PKR is also involved in cytokine induction (31–33), the still-intact destruction of PKR by NSs may further contribute to an incomplete recovery of IFN induction in FBXO3-depleted cells. Most likely, it is the combination of all these effects that results in the remaining IFN suppression in RVFV-infected cells devoid of FBXO3.

Our study revealed the involvement of the SCF cofactor Skp1 in p62 degradation by NSs, whereas, somewhat surprisingly we failed to assign any role to the other cofactors, cullin 1, cullin 7, or Rbx1. Since siRNA depletion does not result in a complete removal of the target protein, we cannot exclude that the residual amounts of these cofactors are sufficient for the NSs mechanism. However, in the standard model for SCF E3 ligase F-box proteins, Skp1, cullins, and Rbx1 form an equimolar, stoichiometric complex (29). Moreover, both Skp1 and cullin 1 were previously identified as interactors of FBXO3 (34). It appears hence unusual that siRNA depletion of cullin 1/cullin 7 or Rbx1 does not preserve p62 from destruction by NSs. In fact, however, there are precedents of Skp1/F-box protein-only complexes that act on their own, i.e., independently of a canonical SCF-type ubiquitin ligase (35, 36). An alternative explanation therefore could be that NSs assembles a so-called "non-SCF F-Box/Skp1 complex" to degrade p62.

FBXO3 is an E3 ubiquitin ligase component that only recently gained wider attention. An earlier study suggested an involvement in transcription regulation by p53, the master regulator of apoptosis and DNA damage responses (34). TFIIH-p62, by contrast, seems to be a target of FBXO3 only in connection with RVFV NSs, as in uninfected cells neither depletion nor overexpression of FBXO3 had any effect on p62 levels. Strikingly, a recent study revealed that FBXO3 is indirectly stabilizing TRAF (tumor necrosis factor receptor-associated factor) proteins 1 to 6 (37). TRAF proteins are essential signaling adaptors for innate, inflammatory, and adaptive immune responses (38). FBXO3, through regulation of TRAF protein stability, turned out to be a key factor for production of inflammatory cytokines (37). Thus, the NSs interactor FBXO3 plays a key role in p53-mediated host cell regulation as well as in enabling TRAF-dependent inflammatory responses. Interestingly, RVFV NSs activates p53, apoptosis, and DNA damage responses (39, 40) and downregulates inflammatory cytokines (41). With respect to TRAF regulation, however, we observed that RVFV drives TRAF disappearance in an FBXO3-independent manner (data not shown), indicating an alternative, dominant pathway of counteracting inflammation.

The nuclear pool of the long isoform FBXO3/1 is removed by NSs, whereas the shorter isoform, which lacks the C-terminal acidic and poly(R)-rich domains, is not affected. It is known that F-box proteins can fall victim to their own ubiquitination activity (42) and become degraded along with their target protein ("unstable when active" phenomenon [35]). Thus, the disappearance of FBXO3/1 along with p62 could point at the C terminus of FBXO3/1 as the effector domain of NSs action, leading also to an autocatalytic degradation of FBXO3/1. In any case, the removal of FBXO3 from the nucleus may have implications for NSs regulation, liberating NSs to pursue another activity such as, e.g., PKR degradation. Interestingly, a recent chromatin immunoprecipitation-DNA sequencing (CHIP-Seq) study revealed that RVFV NSs also downregulates the promoter of the FBXO3 gene (43). Although in our experiments mRNA levels of FBXO3 were unaffected by NSs at 6 h postinfection (p.i.), it could be speculated that NSs blocks FBXO3 gene expression for the long term, for the same reason that it removes FBXO3 protein from the nucleus. Investi-

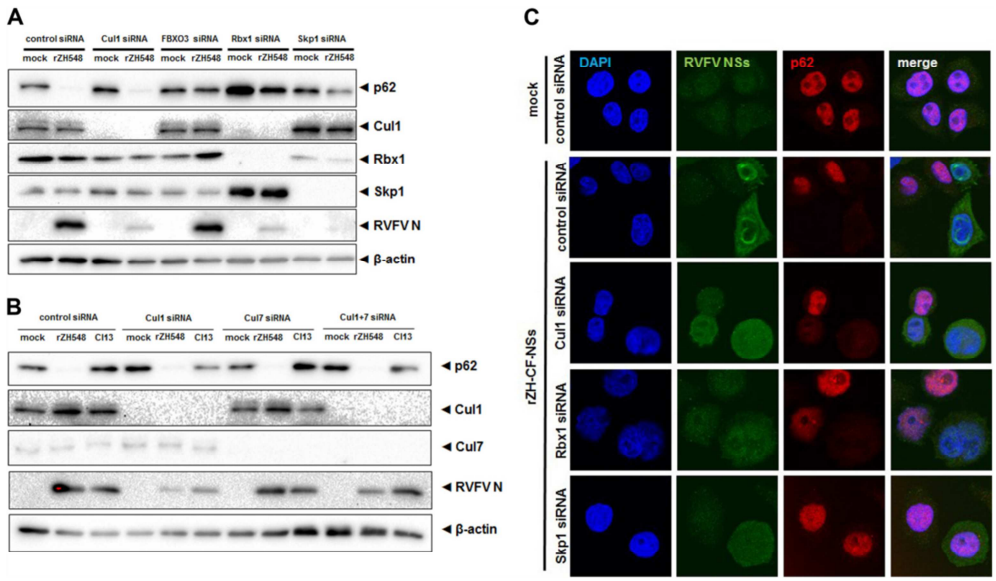

FIG 7 NSs and components of canonical SCF ubiquitin ligases. (A and B) Western blot analysis of knockdown cells. HeLa cells were treated with a control siRNA or with siRNAs directed against mRNAs of cullin 1 (Cul1), FBXO3, Rbx1, or Skp1 (A) or cullin 1 and/or cullin 7 (B). Cells were then infected with recombinant wt RVFV (rZH548) or Clone 13 (Cl13) at an MOI of 10 and analyzed 6 h later for the presence of the indicated proteins. (C) Immunofluorescence analysis. HeLa cells with siRNA knockdown of cullin 1, Rbx1, or Skp1 mRNAs were infected for 6 h with rZH-CF-NSs at an MOI of 3, and the presence of nuclear DNA, p62, and Flag-RVFV NSs was analyzed 6 h later using DAPI stain and appropriate antibodies, respectively.

gating the global consequences of FBXO3 removal could reveal novel insights into the functions of both FBXO3 and NSs.

In addition to the effects on IFN induction, host transcription, inflammatory cytokine production, p53 regulation, and PKR degradation, RVFV NSs induces chromosomal anomalies (44) and regulates many other genes involved in innate immunity, inflammation, cell adhesion, axonal guidance, development, and blood coagulation (43). Thus, NSs of RVFV is a multifunctional protein that dysregulates and damages the host at several levels. However, an NSs-truncated RVFV strain (Clone 13) kills mice even faster than the wt strain does, provided the animals are devoid of an IFN system (11). This argues for IFN antagonism (encompassing the blockade of IFN mRNA transcription and the degradation of the PKR) being the prime function of NSs, to which our newly identified host cell factor FBXO3 contributes substantially.

ACKNOWLEDGMENTS

We thank Christina Lückel for technical assistance and Eliane Meurs for kindly donating the anti-PKR antibody.

Work in our laboratories was supported by the Deutsche Forschungsgemeinschaft grants We 2616/5-2, SFB 593, and SFB 1021 to F.W., grant PI 1084/2-1 to A.P., an Alexander von Humboldt stipend to M.H., and an ERC starting grant (iViP) to A.P.

REFERENCES

1. **Bird BH, Ksiazek TG, Nichol ST, Maclachlan NJ.** 2009. Rift Valley fever virus. J. Am. Vet. Med. Assoc. **234**:883–893. http://dx.doi.org/10.2460/javma.234.7.883.
2. **Boshra H, Lorenzo G, Busquets N, Brun A.** 2011. Rift valley fever: recent insights into pathogenesis and prevention. J. Virol. **85**:6098–6105. http://dx.doi.org/10.1128/JVI.02641-10.
3. **Ikegami T, Makino S.** 2011. The pathogenesis of Rift Valley fever. Viruses **3**:493–519. http://dx.doi.org/10.3390/v3050493.
4. **WHO.** 2007. Rift Valley fever outbreak—Kenya, November 2006-January 2007. MMWR Morb. Mortal. Wkly. Rep. **56**:73–76. http://www.cdc.gov/mmwr/preview/mmwrhtml/mm5604a3.htm.
5. **Fontenille D, Traore-Lamizana M, Diallo M, Thonnon J, Digoutte JP, Zeller HG.** 1998. New vectors of Rift Valley fever in West Africa. Emerg. Infect. Dis. **4**:289–293. http://dx.doi.org/10.3201/eid0402.980218.
6. **Moutailler S, Krida G, Schaffner F, Vazeille M, Failloux AB.** 2008. Potential vectors of Rift Valley fever virus in the Mediterranean region. Vector Borne Zoonotic Dis. **8**:749–753. http://dx.doi.org/10.1089/vbz.2008.0009.
7. **Pepin M, Bouloy M, Bird BH, Kemp A, Paweska J.** 2010. Rift Valley fever virus (Bunyaviridae: Phlebovirus): an update on pathogenesis, molecular epidemiology, vectors, diagnostics and prevention. Vet. Res. **41**:61. http://dx.doi.org/10.1051/vetres/2010033.
8. **Borio L, Inglesby T, Peters CJ, Schmaljohn AL, Hughes JM, Jahrling PB, Ksiazek T, Johnson KM, Meyerhoff A, O'Toole T, Ascher MS, Bartlett J, Breman JG, Eitzen EM, Jr, Hamburg M, Hauer J, Henderson DA, Johnson RT, Kwik G, Layton M, Lillibridge S, Nabel GJ, Osterholm MT, Perl TM, Russell P, Tonat K.** 2002. Hemorrhagic fever viruses as biological weapons: medical and public health management. JAMA **287**:2391–2405. http://dx.doi.org/10.1001/jama.287.18.2391.
9. **Bouloy M, Weber F.** 2010. Molecular biology of rift valley Fever virus. Open Virol. J. **4**:8–14. http://dx.doi.org/10.2174/1874357901004020008.
10. **Billecocq A, Spiegel M, Vialat P, Kohl A, Weber F, Bouloy M, Haller O.** 2004. NSs protein of Rift Valley fever virus blocks interferon production by inhibiting host gene transcription. J. Virol. **78**:9798–9806. http://dx.doi.org/10.1128/JVI.78.18.9798-9806.2004.

11. **Bouloy M, Janzen C, Vialat P, Khun H, Pavlovic J, Huerre M, Haller O.** 2001. Genetic evidence for an interferon-antagonistic function of Rift Valley fever virus nonstructural protein NSs. J. Virol. **75:**1371–1377. http://dx.doi.org/10.1128/JVI.75.3.1371-1377.2001.
12. **Sadler AJ, Williams BR.** 2008. Interferon-inducible antiviral effectors. Nat. Rev. Immunol. **8:**559–568. http://dx.doi.org/10.1038/nri2314.
13. **Elliott RM, Weber F.** 2009. Bunyaviruses and the type I interferon system. Viruses **1:**1003–1021. http://dx.doi.org/10.3390/v1031003.
14. **Hollidge BS, Weiss SR, Soldan SS.** 2011. The role of interferon antagonist, non-structural proteins in the pathogenesis and emergence of arboviruses. Viruses **3:**629–658. http://dx.doi.org/10.3390/v3060629.
15. **Le May N, Mansuroglu Z, Leger P, Josse T, Blot G, Billecocq A, Flick R, Jacob Y, Bonnefoy E, Bouloy M.** 2008. A SAP30 complex inhibits IFN-beta expression in Rift Valley fever virus infected cells. PLoS Pathog. **4:**e13. http://dx.doi.org/10.1371/journal.ppat.0040013.
16. **Le May N, Dubaele S, De Santis LP, Billecocq A, Bouloy M, Egly JM.** 2004. TFIIH transcription factor, a target for the Rift Valley hemorrhagic fever virus. Cell **116:**541–550. http://dx.doi.org/10.1016/S0092-8674(04)00132-1.
17. **Binder M, Eberle F, Seitz S, Mucke N, Huber CM, Kiani N, Kaderali L, Lohmann V, Dalpke A, Bartenschlager R.** 2011. Molecular mechanism of signal perception and integration by the innate immune sensor retinoic acid-inducible gene-I (RIG-I). J. Biol. Chem. **286:**27278–27287. http://dx.doi.org/10.1074/jbc.M111.256974.
18. **Marcus PI, Sekellick MJ.** 1977. Defective interfering particles with covalently linked [+/−]RNA induce interferon. Nature **266:**815–819. http://dx.doi.org/10.1038/266815a0.
19. **Overby AK, Popov VL, Niedrig M, Weber F.** 2010. Tick-borne encephalitis virus delays interferon induction and hides its double-stranded RNA in intracellular membrane vesicles. J. Virol. **84:**8470–8483. http://dx.doi.org/10.1128/JVI.00176-10.
20. **Weber M, Gawanbacht A, Habjan M, Rang A, Borner C, Schmidt AM, Veitinger S, Jacob R, Devignot S, Kochs G, Garcia-Sastre A, Weber F.** 2013. Incoming RNA virus nucleocapsids containing a 5′-triphosphorylated genome activate RIG-I and antiviral signaling. Cell Host Microbe **13:**336–346. http://dx.doi.org/10.1016/j.chom.2013.01.012.
21. **Kalveram B, Lihoradova O, Ikegami T.** 2011. NSs protein of Rift Valley fever virus promotes posttranslational downregulation of the TFIIH subunit p62. J. Virol. **85:**6234–6243. http://dx.doi.org/10.1128/JVI.02255-10.
22. **Pichlmair A, Kandasamy K, Alvisi G, Mulhern O, Sacco R, Habjan M, Binder M, Stefanovic A, Eberle CA, Goncalves A, Burckstummer T, Muller AC, Fauster A, Holze C, Lindsten K, Goodbourn S, Kochs G, Weber F, Bartenschlager R, Bowie AG, Bennett KL, Colinge J, Superti-Furga G.** 2012. Viral immune modulators perturb the human molecular network by common and unique strategies. Nature **487:**486–490. http://dx.doi.org/10.1038/nature11289.
23. **Habjan M, Penski N, Spiegel M, Weber F.** 2008. T7 RNA polymerase-dependent and -independent systems for cDNA-based rescue of Rift Valley fever virus. J. Gen. Virol. **89:**2157–2166. http://dx.doi.org/10.1099/vir.0.2008/002097-0.
24. **Laurent AG, Krust B, Galabru J, Svab J, Hovanessian AG.** 1985. Monoclonal antibodies to an interferon-induced Mr 68,000 protein and their use for the detection of double-stranded RNA-dependent protein kinase in human cells. Proc. Natl. Acad. Sci. U. S. A. **82:**4341–4345. http://dx.doi.org/10.1073/pnas.82.13.4341.
25. **Habjan M, Pichlmair A, Elliott RM, Overby AK, Glatter T, Gstaiger M, Superti-Furga G, Unger H, Weber F.** 2009. NSs protein of Rift Valley fever virus induces the specific degradation of the double-stranded RNA-dependent protein kinase. J. Virol. **83:**4365–4375. http://dx.doi.org/10.1128/JVI.02148-08.
26. **Livak KJ, Schmittgen TD.** 2001. Analysis of relative gene expression data using real-time quantitative PCR and the 2(-Delta Delta C(T)) Method. Methods **25:**402–408. http://dx.doi.org/10.1006/meth.2001.1262.
27. **Bird BH, Bawiec DA, Ksiazek TG, Shoemaker TR, Nichol ST.** 2007. Highly sensitive and broadly reactive quantitative reverse transcription-PCR assay for high-throughput detection of Rift Valley fever virus. J. Clin. Microbiol. **45:**3506–3513. http://dx.doi.org/10.1128/JCM.00936-07.
28. **Ikegami T, Narayanan K, Won S, Kamitani W, Peters CJ, Makino S.** 2009. Rift Valley fever virus NSs protein promotes post-transcriptional downregulation of protein kinase PKR and inhibits eIF2alpha phosphorylation. PLoS Pathog. **5:**e1000287. http://dx.doi.org/10.1371/journal.ppat.1000287.
29. **Skaar JR, Pagan JK, Pagano M.** 2013. Mechanisms and function of substrate recruitment by F-box proteins. Nat. Rev. Mol. Cell Biol. **14:**369–381. http://dx.doi.org/10.1038/nrm3582.
30. **Head JA, Kalveram B, Ikegami T.** 2012. Functional analysis of Rift Valley fever virus NSs encoding a partial truncation. PLoS One **7:**e45730. http://dx.doi.org/10.1371/journal.pone.0045730.
31. **Garcia MA, Meurs EF, Esteban M.** 2007. The dsRNA protein kinase PKR: virus and cell control. Biochimie **89:**799–811. http://dx.doi.org/10.1016/j.biochi.2007.03.001.
32. **McAllister CS, Taghavi N, Samuel CE.** 2012. Protein kinase PKR amplification of interferon beta induction occurs through initiation factor eIF-2alpha-mediated translational control. J. Biol. Chem. **287:**36384–36392. http://dx.doi.org/10.1074/jbc.M112.390039.
33. **Onomoto K, Jogi M, Yoo JS, Narita R, Morimoto S, Takemura A, Sambhara S, Kawaguchi A, Osari S, Nagata K, Matsumiya T, Namiki H, Yoneyama M, Fujita T.** 2012. Critical role of an antiviral stress granule containing RIG-I and PKR in viral detection and innate immunity. PLoS One **7:**e43031. http://dx.doi.org/10.1371/journal.pone.0043031.
34. **Shima Y, Shima T, Chiba T, Irimura T, Pandolfi PP, Kitabayashi I.** 2008. PML activates transcription by protecting HIPK2 and p300 from SCFFbx3-mediated degradation. Mol. Cell. Biol. **28:**7126–7138. http://dx.doi.org/10.1128/MCB.00897-08.
35. **Hermand D.** 2006. F-box proteins: more than baits for the SCF? Cell Division **1:**30. http://dx.doi.org/10.1186/1747-1028-1-30.
36. **Skaar JR, D'Angiolella V, Pagan JK, Pagano M.** 2009. SnapShot: F box proteins II. Cell **137:**1358, 1358.e1. http://dx.doi.org/10.1016/j.cell.2009.05.040.
37. **Chen BB, Coon TA, Glasser JR, McVerry BJ, Zhao J, Zhao Y, Zou C, Ellis B, Sciurba FC, Zhang Y, Mallampalli RK.** 2013. A combinatorial F box protein directed pathway controls TRAF adaptor stability to regulate inflammation. Nat. Immunol. **14:**470–479. http://dx.doi.org/10.1038/ni.2565.
38. **Bradley JR, Pober JS.** 2001. Tumor necrosis factor receptor-associated factors (TRAFs). Oncogene **20:**6482–6491. http://dx.doi.org/10.1038/sj.onc.1204788.
39. **Austin D, Baer A, Lundberg L, Shafagati N, Schoonmaker A, Narayanan A, Popova T, Panthier JJ, Kashanchi F, Bailey C, Kehn-Hall K.** 2012. p53 Activation following Rift Valley fever virus infection contributes to cell death and viral production. PLoS One **7:**e36327. http://dx.doi.org/10.1371/journal.pone.0036327.
40. **Baer A, Austin D, Narayanan A, Popova T, Kainulainen M, Bailey C, Kashanchi F, Weber F, Kehn-Hall K.** 2012. Induction of DNA damage signaling upon Rift Valley fever virus infection results in cell cycle arrest and increased viral replication. J. Biol. Chem. **287:**7399–7410. http://dx.doi.org/10.1074/jbc.M111.296608.
41. **McElroy AK, Nichol ST.** 2012. Rift Valley fever virus inhibits a pro-inflammatory response in experimentally infected human monocyte derived macrophages and a pro-inflammatory cytokine response may be associated with patient survival during natural infection. Virology **422:**6–12. http://dx.doi.org/10.1016/j.virol.2011.09.023.
42. **Galan JM, Peter M.** 1999. Ubiquitin-dependent degradation of multiple F-box proteins by an autocatalytic mechanism. Proc. Natl. Acad. Sci. U. S. A. **96:**9124–9129. http://dx.doi.org/10.1073/pnas.96.16.9124.
43. **Benferhat R, Josse T, Albaud B, Gentien D, Mansuroglu Z, Marcato V, Soues S, Le Bonniec B, Bouloy M, Bonnefoy E.** 2012. Large-scale chromatin immunoprecipitation with promoter sequence microarray analysis of the interaction of the NSs protein of Rift Valley fever virus with regulatory DNA regions of the host genome. J. Virol. **86:**11333–11344. http://dx.doi.org/10.1128/JVI.01549-12.
44. **Mansuroglu Z, Josse T, Gilleron J, Billecocq A, Leger P, Bouloy M, Bonnefoy E.** 2010. Nonstructural NSs protein of Rift Valley fever virus interacts with pericentromeric DNA sequences of the host cell, inducing chromosome cohesion and segregation defects. J. Virol. **84:**928–939. http://dx.doi.org/10.1128/JVI.01165-09.
45. **Artimo P, Jonnalagedda M, Arnold K, Baratin D, Csardi G, de Castro E, Duvaud S, Flegel V, Fortier A, Gasteiger E, Grosdidier A, Hernandez C, Ioannidis V, Kuznetsov D, Liechti R, Moretti S, Mostaguir K, Redaschi N, Rossier G, Xenarios I, Stockinger H.** 2012. ExPASy: SIB bioinformatics resource portal. Nucleic Acids Res. **40:**W597–W603. http://dx.doi.org/10.1093/nar/gks400.

3 DISCUSSION

During my thesis I elucidated novel aspects in virus sensing, antiviral defense mechanisms and regulation of programmed cell death. Furthermore, I identified essential cellular factors for both, the antiviral IFN-mediated immune response and for viral immune evasion strategies.

In my main projects, I systematically delineated protein-protein interactions of 104 ISGs and focused on the binding capacity of IFIT1 to modified nucleic acid sequences. I evaluated the impact of IFIT1 binding to virus-derived 2' O-unmethylated capped RNA on the synthesis of viral encoded proteins during infection. The ISGs studied in my thesis were shown to actively influence virus replication in functional overexpression screens [69,95]. The selection of these functional relevant factors allowed me to link thousands of cellular proteins, which have not yet been known to contribute to the cellular antiviral response, to ISG proteins. I acquired AE-LC-MS/MS data and built a comprehensive ISG centric protein-protein-interaction (PPI) network, which I complemented with functional relevant data from several external sources. Subsequent system analyses revealed many unexpected interactions in the cell and could therefore extend our knowledge on the regulation of IFN signaling and to cellular viral defense programs. Furthermore, I complemented the obtained data from the proteomic analysis with targeted functional experiments to verify their importance in virus-host interactions. Therefore, I concentrated on three unexpected findings with high regulatory potential in cellular antiviral defense mechanisms. The following chapter will summarize the main findings during my thesis and will link them to current literature. Additionally, recent trends and challenges of mass spectrometry based applications in the proteomic research field will be briefly discussed.

3.1 RELEVANCE OF MAJOR FINDINGS

Innate immunity encompasses highly complex and strictly regulated cellular systems capable to deal with a variety of different foreign pathogens and intrinsic damage-associated molecular signatures as explained before. To guarantee maximal performance, the innate immune system needs to be carefully balanced in order to react fast and sensitive against potential harmful factors. However, the activity of the innate immune system also needs to be tightly controlled to prevent harmful overshooting reactions such as seen in autoimmune diseases and allergic reactions. Therefore, highly structured and self-controlled cellular regulation processes are of paramount importance for the innate immune system. During the main projects of my thesis, I identified and

characterized cellular proteins with so far unknown regulatory potential and importance for the innate immune system.

The Lectin galactoside-binding soluble 3-binding protein (LGALS3BP), also known as 90K and Mac-2 BP, showed the highest connectivity to ISGs in the protein-protein interaction network. It was also among the top hits within defense response relevant databases, suggesting a very prominent role in antiviral immunity. More than twenty years ago, LGALS3BP was studied intensively in the context of tumor progression and inflammation in breast cancer and was described as a potential bio-marker which correlates with bad prognosis for metastasis and survival of breast cancer patients [347–350]. Elevated levels of the secreted form of LGALS3BP in the blood of HIV patients also pointed towards its central role in the context of virus infections [351–354]. Recent studies revealed evolutional-conserved antiviral properties of intracellular LGALS3BP against distinct lentivirus strains including HIV-1 [355–357]. However, in contrast to its antiviral activity against lentiviruses, the observed data shown here clearly support a predominant pro-viral function of intracellular localized LGALS3BP. The observed pro-viral function is in line with results of a comprehensive meta-analysis that includes several independent genome wide siRNA depletion screens in the context of FluAV replication [107]. Functional experiments as part of my thesis showed increased expression levels of several ISGs in response to LGALS3BP depletion. This provides evidence for a negative regulatory function of LGALS3BP in the IFN-response, which was recently supported by results observed in the context of Sendai virus (SeV) infection [358]. Both, the antiviral activity against HIV and its function to potently suppress virus-induced activation of the interferon system at the same time, point towards a dual function of LGALS3BP in virus infection. Interestingly, proteomics data presented here clearly show that depletion of LGALS3BP in uninfected cells leads to an instantaneous expression of ISGs. This finding serves as breeding ground for speculations regarding the molecular mechanism that could potentially account for this negative regulatory function. I identified a surprisingly high number of different ISGs by AE-LC-MS/MS analyses that interact with LGALS3BP. Among these interactions is the Interferon Regulatory Factor 2 protein (IRF2). IRF2 acts as transcriptional repressor and antagonist of IRF1, a central mediator within the type I IFN signaling cascade which has also been linked to ISRE-dependent activation of gene-expression [95,351,359]. Interestingly, LGALS3BP is capable to control stability of specific proteins post transcriptionally [360]. It remains highly speculative, if IRF2 levels are affected by LGALS3BP in cells. Interestingly, an overexpression study of ISGs clearly showed reduced IRES promotor activation by IRF2 expression comparable to known negative regulators of the IFN system such as USP18 and SOCS1 [94]. Although the exact molecular mechanism still remains obscure, the interaction and

functional data derived from this work together with results from recent literature and databases refers to a negative regulatory function of LGALS3BP through IRF2. This points towards a novel molecular mechanism of LGALS3BP that helps to properly balance the response of the IFN-induced cellular defense system. Future experiments that focus on the LGALS3BP interactor IRF2 might not only provide molecular details of paramount importance for the understanding of its diverse functions in the innate immune system, but might also be helpful to understand the exact function of LGALS3BP in cancer progression and metastasis.

Another major finding of my thesis is the highly specific association of the ISG ANXA2R with members of the CCR4-NOT complex. The evolutionary conserved CCR4-NOT complex is a central cellular unit that regulates mRNA levels. Violation of the CCR4-NOT complex function causes severe abnormalities in the embryonic development and cytoskeletal organization in flies [361–363]. CCR4-NOT complex members were recently identified as tumor suppressors in Drosophila melanogaster eye cancer models and identification of somatic mutations in different CCR4-NOT complex members in T-cell acute lymphoblastic leukemia (T-ALL) patients underline the importance of its function in humans [364–367]. Activity of the CCR4-NOT complex affects immune system relevant processes at different levels such as the degradation of transcripts from MHC class II and different cytokine-genes [368,369]. Consequently, depletion of CCR4-NOT complex members results in increased levels of cytokines and ISGs, which consequences in more pronounced defense responses as for example in plants [370–372]. Interestingly, the CCR4-NOT complex acts post-transcriptionally by degrading mRNAs. This process commonly necessitates supportive cellular factors that guide the complex to its target transcripts [369,373]. However, the interaction of the IFN stimulated gene ANXA2R with the CCR4-NOT complex causes the trans-localization and local depletion of the CCR4-NOT complex from the cytosol to perinuclear compartments. Analysis of ANXA2R expressing cells compared to cells that lack CNOT1, a central component of the CCR4-NOT complex, results in highly similar proteome profiles, which underpins the functional relevance of the ANXA2R mediated CCR4-NOT depletion. This supports a transcript stabilizing function of the defense-response-derived mRNA by ANXA2R expression and explains the strong antiviral effect of ANXA2R expression against a broad range of different viruses [94,95,373]. Interestingly, expression of ANXA2R also results in increased apoptosis [374]. An intriguing, but highly speculative working model could be that ANXA2R facilitates the expression of cytokines and antivirally acting proteins in order to boost the defense response against viruses before suicide of the infected cell. Additional experiments would be required to elucidate the relevance of ANXA2R and the caused local depletion of the CCR4-NOT complex in the cytosol during virus infection. Further

investigations of the immunomodulatory function of ANXA2R might be important for a better understanding of posttranscriptional regulation strategies, which affect the innate immune system. These posttranscriptional regulation strategies might be of high relevance for a balanced immune system [375].

I used the data generated in this thesis to study the P2Y purinoceptor 6 (P2RY6). The P2RY6 gene encodes for a plasma membrane localized G protein-coupled purine sensing transmembrane receptor with known functions in DAMP sensing and inflammation response [376–378]. Binding of its ligand results in the production of cAMP, activation of protein kinases, inositol trisphosphate generation and intracellular Ca^{2+} release [379]. AE-LC-MS/MS analysis indicates an involvement of P2RY6 in NF-kB activation through the TRAF6 dependent non-canonical signaling pathway. Inhibition experiments of TRAF6 confirmed a predominant role of this pathway in the NF-kB activation by P2RY6, which was not known so far. This uncovered a potential chemical inhibitor class capable to block P2RY6 mediated pro-inflammatory signaling.

Taken together, the results presented in my thesis cover several central aspects in virus-host interactions. The assessed data act as a valuable resource for a broad research community and is capable to provide countless entry points for hypothesis-driven experiments that illuminate different aspects of the innate immune system. Additionally, the datasets cover interactions of pan- but also highly virus-specific antiviral acting ISGs. Systematic analysis of interactors from ISGs that affect specific virus classes might even allow the identification of cellular proteins and processes that are essential for the replication of single virus species. These essential factors could potentially be of value for targeted therapeutic treatments.

3.2 TRENDS IN APPLICATIONS OF MASS SPECTROMETRY BASED PROTEOMICS IN VIRUS-HOST INTERACTIONS AND INNATE IMMUNITY

Identification of interactions between virus-derived molecular patterns and host proteins is still the main application of mass spectrometry based proteomics in the virus-host interaction field. However, improvements in sample preparation methods, recent advances in mass spectrometry hardware as well as novel software algorithms allow highly comprehensive analysis strategies, which are capable to unravel the virus-host interplay at different levels. This includes protein profiling, analysis of signal transduction and identification of posttranslational modifications, which commonly occur in virus-infected cells. As outlined in the introduction, viruses are masters of manipulating their hosts. The interest in the dynamic evaluation during infections led to study designs capable to resolve time-dependent protein changes through sophisticated models. Common available quantitative approaches such as NGS-based methods do exclusively cover alterations during infection on the mRNA level, which are only partially predictive for the proteome at a given time [380–383]. However, quantitative data of the proteome are especially important in the context of virus infections, as viruses often highjack central components of the protein degradation system of the host cell or code for their own ubiquitin conjugating enzymes to remodel the proteome for their own benefit. Such post-transcriptional changes are of central importance for virus-mediated immune evasion strategies and essential to understand infection progression [384–387]. Hence, complex time-resolved mass spectrometry based study designs such as SILAC pulse chase experiments or the application of click-able amino acids, which incorporate into the newly synthesized proteins in cells over time, represent promising approaches to study viruses and their effects on the turnover of the host's proteome [388–390]. Alternatively, integrated omics analyses that compare virus-induced transcriptome- and proteome-changes will shed light on the alteration of mRNA- and protein-levels during virus infection. In the future, further integrative study designs will be required to pioneer novel ways in this complex research field and to successfully link mass spectrometry based proteomics data with clinical data and functional genomics methods to better understand virus caused diseases.

3.3 CHALLENGES IN MASS SPECTROMETRY BASED PROTEOMIC INTERACTION APPLICATIONS

Almost 20 years ago, knowledge derived from the human genome sequencing project has raised high expectations and hopes to identify disease causing genomic factors. However, in most cases these hopes were premature and success dragged behind these high expectations. This discrepancy is caused by the nature of many diseases, which manifest not only on the bases of a single genomic alteration but additionally necessitate further alterations to establish their characteristic phenotype. Among additional genomic alterations, such as mutations, this can also result from epigenetic changes, unbalanced inflammatory processes or exposure to toxic substances and foreign species, such as in infections. These environmentally caused perturbations are often hard to grasp by genomic approaches alone. However, they commonly cause specific traces in the proteome of the affected cells, which can be monitored and studied by several unbiased mass spectrometry based approaches. Recent studies showed, that proteome changes correlate well with disease phenotypes and, in many cases, even outperform genomic- and transcriptomic-based approaches [266,391,392]. Hence, mass spectrometry based proteomics serves as a powerful technology to comprehensively evaluate diseases caused by molecular alterations. It is capable to precisely reflect protein expression, posttranslational modification and molecular interactions and is suitable to answer complex scientific questions in both, basic research and clinical settings.

Bottom-up proteomics can explore disease-related molecular findings directly on the level of the main executing units in the cell by evaluating several thousand qualitative and quantitative proteomic parameters per analysis. This makes it especially suitable for applications in basic research. Most proteomic data presented in this thesis were derived from extensive AE-LC-MS/MS experiments and provide profound information about the physical association between proteins in the cell. Traditionally, AE- and AP-LC-MS/MS analyses require ectopic expression and affinity tags fused to the protein of interest to successfully enrich and identify associated proteins and to decipher dynamic processes in protein-complex formation [393]. However, AP-LC-MS/MS based studies often accumulate a high number of false-positive findings, which often results in misinterpretation of the acquired interaction data [394]. Fusion of an affinity tag can enhance false-negative and false-positive rates through disruption of the protein function, protein mislocalization in the cell, destabilization of true interactions and the identification of proteins with high affinity to the used molecular tag [395,396]. Furthermore, ectopic expression of the protein of interest can massively influence the cellular proteome and cause the accumulation of false-positive interactors in

case of insufficient cut-off criteria or unsuitable normalization strategies [397]. Therefore, validation and optimization of AP-LC-MS/MS workflows with subsequent statistical analysis are required to guarantee high quality PPI data [398,399]. Alternative mass spectrometry based approaches that elucidate PPIs include antibody-based capture techniques (CO-IP-MS/MS) and proximity-dependent based approaches [400,401]. CO-IP-MS/MS allows to identify protein interactions of primary cells and tissue under physiological conditions. However, availability, affinity and specificity of the used antibody need to be carefully evaluated. In addition, binding conditions for every antibody requires time consuming optimization, which limits its application to less comprehensive PPI studies. Commonly, cell lysis and buffer conditions significantly affect sensitivity and specificity of AP- and CO-IP-MS/MS workflows, which often leads to loss of low affine or transient interactions.

Proximity-dependent approaches such as BioID or APEX rely on the fusion of enzymes to the protein of interest. These fused enzymes represent modified biotin ligases and peroxidases [402,403]. Both approaches result in covalently attached biotin derivatives at proteins in close proximity of the modified protein [400]. This enables the identification of low affine and transient interactions. Furthermore, it accounts for intracellular compartmentation and localization of the protein of interest as the covalent attachment of biotin appears within the intact living cell [404]. However, the large labeling radius of the BioID and APEX based method allows protein modification even in the absence of a direct physical interaction. Hence, biotinylated proteins do not exclusively represent true, physically associated interactors but could simple represent proteins that are localized in close proximity to the protein of interest within the cell. Consequently, identified proteins are not necessarily true interactors. Furthermore, proximity-dependent approaches require genomic modifications to fuse the enzyme to the protein of interest. This limits its application to suitable cell-culture models most of the time [404].

An alternative method represents size-exclusion chromatography coupled to mass spectrometry (SEC-MS), an approach that deduces PPI information on the basis of co-eluting protein profiles. Interestingly, no tagging or enzyme fusion is required and it can be performed with almost any tissue or cell. Additionally, this method acquires PPI information of several thousand proteins in one single experiment. This allows to obtain an unbiased global picture of interactions within the studied cells or tissue. However, its resolution is limited by the separation efficiency of the used analytical size-exclusion column and the number of obtained fractions. Hence, most protocols resolve comparably high molecular weight complexes and are less suitable to elucidate interactions of small complexes and transient interactions. Additionally, SEC-MS requires gentle lysis conditions

to preserve native structures and intact complexes. This gentle lysis conditions are less suitable to study transmembrane and DNA-associated protein complexes. Furthermore, gentle lysis conditions can cause interaction artifacts between proteins and complexes that would never get in close proximity within the intact cell, a clear disadvantage compared to proximity labelling based approaches. However, a recent study performed chemical protein crosslinking in the cell prior SEC-MS, a strategy that helps to overcome these limitations [405]. Further adaptations of this method such as its combination with data-independent acquisition strategies might even increase its applicability in the future [406].

During my thesis I used AE-LC-MS/MS to elucidate interactions of cellular proteins to different modified nucleotide sequences. This resulted in the identification of IFIT1 as binder of 2'O-unmethylated capped RNA. However, mass spectrometry based proteomics can also identify protein-DNA interactions and serves as an unbiased method to determine transcription factor binding [407,408]. In combination with Chromatin Immuno Precipitation DNA-Sequencing (ChIP-seq) methods, it represents a powerful tool to study the dynamics of transcription factor binding during signaling events in the cell [409].

Another constantly increasing application represents the chemical proteomics field. It focuses on the interaction of small molecules to their targets in the cell. Prominent examples include the kinobead technology used to identify drugable kinases. Another innovative approach to characterize drug-binding in cells is thermal proteome profiling [410,411]. It relies on the ligand-induced conformational stabilization of the drug-protein complex, which commonly results in a higher tolerance against heat and causes a shift of its thermal stability profile. This shift can be used to detect specific and unspecific binding substances in cells [412].

Recently, chemical crosslinking has become a popular tool to deliver structural information from complex biological samples in solution [413]. Emerging methods in this challenging research field use collision energy cleavable chemical cross linkers to provide detailed information about the orientation of protein domains and individual proteins within multimeric protein complexes. This approach serves valuable information that complements other protein structure analysis technologies, such as Cryo Electron Microscopy and X-ray based protein structure determination, or acts as stand-alone technology that provides structural information of complex samples in solution [268].

Additionally, recent advances in mass spectrometry based proteomics paves the way towards its clinical application. High demands on reproducibility, sensitivity, specificity and robustness for clinical applications necessitate highly structured and controlled protocols to guarantee the required

performance. Major applications in the future encompass not only the identification of potential biomarkers that are specific for disease phenotypes but also include applications in therapy companion diagnostic, monitoring of prognostic markers and identification of therapeutic targets for personalized precision medicine.

Multivariate diseases are difficult to grasp by traditional diagnostic techniques that commonly rely on the analysis of a single or a low number of disease associated factors. In contrast, unbiased proteome analysis of patient samples can provide information about several thousand proteins in one application. This information can be of high value for disease classification and for the subsequent therapy decision-making process. Furthermore, the data can be used to identify so far unknown protein signatures that are specific for the disease and its progression. Analysis of different kinds of body fluids, such as blood plasma, urine or liquor from the central nerve system can be analyzed in highly robust workflows without the risk to lose valuable morphological information [414–417]. Such samples can be obtained directly by non- or low-invasive methods and allow a regular evaluation of disease status, if required.

Some multiplexed quantitative mRNA diagnostic tests for example already found their way into routine diagnostics. Examples represent quantitative mRNA-based multiplex tests which predict the benefit of chemotherapy on top of an adjuvant endocrine therapy in early stage breast cancer [418,419]. Comparable tests by mass spectrometry based proteomic approaches could cover more cellular factors directly at the protein expression level and might even increase precision of such predictive tests.

Among the most promising clinical applications of mass spectrometry are applications in the immunopeptidomics field. In immunopeptidomics, mass spectrometry is used to identify immunotherapy relevant tumor-associated MHC presented neoantigens at the surface of tumor cells. These presented tumor specific neoantigens are used to train and activate the patient's immune system against the tumor. Interestingly, evaluation of somatic mutations by genome analysis alone is insufficient to predict the immunogenic potential of the tumor as only the MHC molecule presented peptide variants at the cell surface trigger the desired immune response. Hence, the direct identification of the tumor′s immunopeptidome by mass spectrometry is the method of choice for such highly specific personalized immunotherapeutic strategies [420]. Commonly, a combination of both, genome and immunopeptidome based workflows are used to identify potential immunotherapy targets [421].

Remaining future challenges for proteomics in routine clinical applications are the high demands on robustness, sensitivity and precision of the technology. Additionally, proteomic workflows need

to provide sufficient sample throughput, short sample preparation time and reduced running costs to compete with already established technology platforms in routine diagnostic settings [422]. Furthermore, standardization and homogenization of methods and protocols that limits intra- and inter-laboratory variations need to be considered to guarantee comparable results from different diagnostic sites [423–425].

4 LITERATURE

1. Matsuzaki, Y. *et al.* Neutralizing Epitopes and Residues Mediating the Potential Antigenic Drift of the Hemagglutinin-Esterase Protein of Influenza C Virus. *Viruses* **10**; 10.3390/v10080417 (2018).
2. Dingens, A. S., Haddox, H. K., Overbaugh, J. & Bloom, J. D. Comprehensive Mapping of HIV-1 Escape from a Broadly Neutralizing Antibody. *Cell host & microbe* **21,** 777-787.e4; 10.1016/j.chom.2017.05.003 (2017).
3. Yip, T.-F., Selim, A. S. M., Lian, I. & Lee, S. M.-Y. Advancements in Host-Based Interventions for Influenza Treatment. *Frontiers in immunology* **9,** 1547; 10.3389/fimmu.2018.01547 (2018).
4. Maughan, A. & Ogbuagu, O. Pegylated interferon alpha 2a for the treatment of hepatitis C virus infection. *Expert opinion on drug metabolism & toxicology* **14,** 219–227; 10.1080/17425255.2018.1421173 (2018).
5. Wu, J. Y. J. *et al.* Influence of psychiatric diagnosis on treatment uptake and interferon side effects in patients with hepatitis C. *Journal of gastroenterology and hepatology* **29,** 1258–1264 (2014).
6. Hotchkiss, R. S., Monneret, G. & Payen, D. Sepsis-induced immunosuppression: from cellular dysfunctions to immunotherapy. *Nature reviews. Immunology* **13,** 862–874; 10.1038/nri3552 (2013).
7. Iwasaki, A. & Medzhitov, R. Control of adaptive immunity by the innate immune system. *Nature immunology* **16,** 343–353; 10.1038/ni.3123 (2015).
8. Amulic, B., Cazalet, C., Hayes, G. L., Metzler, K. D. & Zychlinsky, A. Neutrophil function: from mechanisms to disease. *Annual review of immunology* **30,** 459–489; 10.1146/annurev-immunol-020711-074942 (2012).
9. Auffray, C. *et al.* Monitoring of blood vessels and tissues by a population of monocytes with patrolling behavior. *Science (New York, N.Y.)* **317,** 666–670; 10.1126/science.1142883 (2007).
10. Porcheray, F. *et al.* Macrophage activation switching: an asset for the resolution of inflammation. *Clinical and experimental immunology* **142,** 481–489; 10.1111/j.1365-2249.2005.02934.x (2005).
11. Mellman, I. Dendritic cells: master regulators of the immune response. *Cancer immunology research* **1,** 145–149; 10.1158/2326-6066.CIR-13-0102 (2013).
12. Mitchell, D., Chintala, S. & Dey, M. Plasmacytoid dendritic cell in immunity and cancer. *Journal of neuroimmunology* **322,** 63–73; 10.1016/j.jneuroim.2018.06.012 (2018).
13. Andrews, D. M., Scalzo, A. A., Yokoyama, W. M., Smyth, M. J. & Degli-Esposti, M. A. Functional interactions between dendritic cells and NK cells during viral infection. *Nature immunology* **4,** 175–181; 10.1038/ni880 (2003).
14. Vivier, E., Tomasello, E., Baratin, M., Walzer, T. & Ugolini, S. Functions of natural killer cells. *Nature immunology* **9,** 503–510; 10.1038/ni1582 (2008).
15. Diefenbach, A. & Raulet, D. H. Strategies for target cell recognition by natural killer cells. *Immunological reviews* **181,** 170–184 (2001).
16. Moretta, A. *et al.* Activating receptors and coreceptors involved in human natural killer cell-mediated cytolysis. *Annual review of immunology* **19,** 197–223; 10.1146/annurev.immunol.19.1.197 (2001).

17. Lanier, L. L. NK cell receptors. *Annual review of immunology* **16,** 359–393; 10.1146/annurev.immunol.16.1.359 (1998).
18. Clark, R. & Kupper, T. Old meets new: the interaction between innate and adaptive immunity. *The Journal of investigative dermatology* **125,** 629–637; 10.1111/j.0022-202X.2005.23856.x (2005).
19. Gebhardt, A., Laudenbach, B. T. & Pichlmair, A. Discrimination of Self and Non-Self Ribonucleic Acids. *Journal of interferon & cytokine research : the official journal of the International Society for Interferon and Cytokine Research* **37,** 184–197; 10.1089/jir.2016.0092 (2017).
20. Habjan, M. & Pichlmair, A. Cytoplasmic sensing of viral nucleic acids. *Current opinion in virology* **11,** 31–37; 10.1016/j.coviro.2015.01.012 (2015).
21. Pichlmair, A. *et al.* RIG-I-mediated antiviral responses to single-stranded RNA bearing 5'-phosphates. *Science (New York, N.Y.)* **314,** 997–1001; 10.1126/science.1132998 (2006).
22. Hornung, V. *et al.* 5'-Triphosphate RNA is the ligand for RIG-I. *Science (New York, N.Y.)* **314,** 994–997; 10.1126/science.1132505 (2006).
23. Aregger, M. & Cowling, V. H. Regulation of mRNA capping in the cell cycle. *RNA biology* **14,** 11–14; 10.1080/15476286.2016.1251540 (2017).
24. Pichlmair, A. & Reis e Sousa, C. Innate recognition of viruses. *Immunity* **27,** 370–383; 10.1016/j.immuni.2007.08.012 (2007).
25. Hoffmann, H.-H., Schneider, W. M. & Rice, C. M. Interferons and viruses: an evolutionary arms race of molecular interactions. *Trends in immunology* **36,** 124–138; 10.1016/j.it.2015.01.004 (2015).
26. Pathinayake, P. S., Hsu, A. C.-Y. & Wark, P. A. B. Innate Immunity and Immune Evasion by Enterovirus 71. *Viruses* **7,** 6613–6630; 10.3390/v7122961 (2015).
27. Takeuchi, O. & Akira, S. Pattern recognition receptors and inflammation. *Cell* **140,** 805–820; 10.1016/j.cell.2010.01.022 (2010).
28. Broz, P. & Monack, D. M. Newly described pattern recognition receptors team up against intracellular pathogens. *Nature reviews. Immunology* **13,** 551–565; 10.1038/nri3479 (2013).
29. Fernandes-Alnemri, T., Yu, J.-W., Datta, P., Wu, J. & Alnemri, E. S. AIM2 activates the inflammasome and cell death in response to cytoplasmic DNA. *Nature* **458,** 509–513; 10.1038/nature07710 (2009).
30. Hornung, V. *et al.* AIM2 recognizes cytosolic dsDNA and forms a caspase-1-activating inflammasome with ASC. *Nature* **458,** 514–518; 10.1038/nature07725 (2009).
31. Allen, I. C. *et al.* The NLRP3 inflammasome mediates in vivo innate immunity to influenza A virus through recognition of viral RNA. *Immunity* **30,** 556–565; 10.1016/j.immuni.2009.02.005 (2009).
32. Thomas, P. G. *et al.* The intracellular sensor NLRP3 mediates key innate and healing responses to influenza A virus via the regulation of caspase-1. *Immunity* **30,** 566–575; 10.1016/j.immuni.2009.02.006 (2009).
33. Harijith, A., Ebenezer, D. L. & Natarajan, V. Reactive oxygen species at the crossroads of inflammasome and inflammation. *Frontiers in physiology* **5,** 352; 10.3389/fphys.2014.00352 (2014).
34. Lin, R.-J. *et al.* Distinct antiviral roles for human 2',5'-oligoadenylate synthetase family members against dengue virus infection. *Journal of immunology (Baltimore, Md. : 1950)* **183,** 8035–8043; 10.4049/jimmunol.0902728 (2009).
35. Kristiansen, H., Gad, H. H., Eskildsen-Larsen, S., Despres, P. & Hartmann, R. The oligoadenylate synthetase family: an ancient protein family with multiple antiviral activities.

Journal of interferon & cytokine research : the official journal of the International Society for Interferon and Cytokine Research **31,** 41–47; 10.1089/jir.2010.0107 (2011).

36. McAllister, C. S., Taghavi, N. & Samuel, C. E. Protein kinase PKR amplification of interferon β induction occurs through initiation factor eIF-2α-mediated translational control. *The Journal of biological chemistry* **287,** 36384–36392; 10.1074/jbc.M112.390039 (2012).
37. Hornung, V. SnapShot: nucleic acid immune sensors, part 1. *Immunity* **41,** 868, 868.e1; 10.1016/j.immuni.2014.10.005 (2014).
38. Hornung, V. SnapShot: Nucleic acid immune sensors, part 2. *Immunity* **41,** 1066-1066.e1; 10.1016/j.immuni.2014.10.006 (2014).
39. Balka, K. R. & Nardo, D. de. Understanding early TLR signaling through the Myddosome. *Journal of leukocyte biology* **105,** 339–351; 10.1002/JLB.MR0318-096R (2019).
40. Gack, M. U. *et al.* TRIM25 RING-finger E3 ubiquitin ligase is essential for RIG-I-mediated antiviral activity. *Nature* **446,** 916–920; 10.1038/nature05732 (2007).
41. Berke, I. C., Yu, X., Modis, Y. & Egelman, E. H. MDA5 assembles into a polar helical filament on dsRNA. *Proceedings of the National Academy of Sciences of the United States of America* **109,** 18437–18441; 10.1073/pnas.1212186109 (2012).
42. Peisley, A. *et al.* Cooperative assembly and dynamic disassembly of MDA5 filaments for viral dsRNA recognition. *Proceedings of the National Academy of Sciences of the United States of America* **108,** 21010–21015; 10.1073/pnas.1113651108 (2011).
43. Wu, B. *et al.* Structural basis for dsRNA recognition, filament formation, and antiviral signal activation by MDA5. *Cell* **152,** 276–289; 10.1016/j.cell.2012.11.048 (2013).
44. Uchikawa, E. *et al.* Structural Analysis of dsRNA Binding to Anti-viral Pattern Recognition Receptors LGP2 and MDA5. *Molecular cell* **62,** 586–602; 10.1016/j.molcel.2016.04.021 (2016).
45. Ablasser, A. *et al.* cGAS produces a 2'-5'-linked cyclic dinucleotide second messenger that activates STING. *Nature* **498,** 380–384; 10.1038/nature12306 (2013).
46. Ablasser, A. *et al.* Cell intrinsic immunity spreads to bystander cells via the intercellular transfer of cGAMP. *Nature* **503,** 530–534; 10.1038/nature12640 (2013).
47. Mogensen, T. H. Pathogen recognition and inflammatory signaling in innate immune defenses. *Clinical microbiology reviews* **22,** 240-73, Table of Contents; 10.1128/CMR.00046-08 (2009).
48. Goto, R. *et al.* Isolation of a cDNA clone from the B-G subregion of the chicken histocompatibility (B) complex. *Immunogenetics* **27,** 102–109 (1988).
49. Cekic, C. & Linden, J. Purinergic regulation of the immune system. *Nature reviews. Immunology* **16,** 177–192; 10.1038/nri.2016.4 (2016).
50. Akdis, M. *et al.* Interleukins, from 1 to 37, and interferon-γ: receptors, functions, and roles in diseases. *The Journal of allergy and clinical immunology* **127,** 701-21.e1-70; 10.1016/j.jaci.2010.11.050 (2011).
51. Zheng, C., Zhou, X.-W. & Wang, J.-Z. The dual roles of cytokines in Alzheimer's disease: update on interleukins, TNF-α, TGF-β and IFN-γ. *Translational neurodegeneration* **5,** 7; 10.1186/s40035-016-0054-4 (2016).
52. Hayden, M. S. & Ghosh, S. Shared principles in NF-kappaB signaling. *Cell* **132,** 344–362; 10.1016/j.cell.2008.01.020 (2008).
53. Sun, S.-C. The non-canonical NF-κB pathway in immunity and inflammation. *Nature reviews. Immunology* **17,** 545–558; 10.1038/nri.2017.52 (2017).

54. Gerondakis, S., Fulford, T. S., Messina, N. L. & Grumont, R. J. NF-κB control of T cell development. *Nature immunology* **15,** 15–25; 10.1038/ni.2785 (2014).
55. Dejardin, E. *et al.* The lymphotoxin-beta receptor induces different patterns of gene expression via two NF-kappaB pathways. *Immunity* **17,** 525–535 (2002).
56. Claudio, E., Brown, K., Park, S., Wang, H. & Siebenlist, U. BAFF-induced NEMO-independent processing of NF-kappa B2 in maturing B cells. *Nature immunology* **3,** 958–965; 10.1038/ni842 (2002).
57. Coope, H. J. *et al.* CD40 regulates the processing of NF-kappaB2 p100 to p52. *The EMBO journal* **21,** 5375–5385 (2002).
58. Bradley, J. R. & Pober, J. S. Tumor necrosis factor receptor-associated factors (TRAFs). *Oncogene* **20,** 6482–6491; 10.1038/sj.onc.1204788 (2001).
59. Palomino, D. C. T. & Marti, L. C. Chemokines and immunity. *Einstein (Sao Paulo, Brazil)* **13,** 469–473; 10.1590/S1679-45082015RB3438 (2015).
60. Stark, G. R. & Darnell, J. E. The JAK-STAT pathway at twenty. *Immunity* **36,** 503–514; 10.1016/j.immuni.2012.03.013 (2012).
61. Taniguchi, T. & Takaoka, A. A weak signal for strong responses: interferon-alpha/beta revisited. *Nature reviews. Molecular cell biology* **2,** 378–386; 10.1038/35073080 (2001).
62. Pestka, S., Krause, C. D. & Walter, M. R. Interferons, interferon-like cytokines, and their receptors. *Immunological reviews* **202,** 8–32; 10.1111/j.0105-2896.2004.00204.x (2004).
63. Ivashkiv, L. B. & Donlin, L. T. Regulation of type I interferon responses. *Nature reviews. Immunology* **14,** 36–49; 10.1038/nri3581 (2014).
64. Decker, T., Müller, M. & Stockinger, S. The yin and yang of type I interferon activity in bacterial infection. *Nature reviews. Immunology* **5,** 675–687; 10.1038/nri1684 (2005).
65. Platanias, L. C. Mechanisms of type-I- and type-II-interferon-mediated signalling. *Nature reviews. Immunology* **5,** 375–386; 10.1038/nri1604 (2005).
66. Schneider, W. M., Chevillotte, M. D. & Rice, C. M. Interferon-stimulated genes: a complex web of host defenses. *Annual review of immunology* **32,** 513–545; 10.1146/annurev-immunol-032713-120231 (2014).
67. Marcello, T. *et al.* Interferons alpha and lambda inhibit hepatitis C virus replication with distinct signal transduction and gene regulation kinetics. *Gastroenterology* **131,** 1887–1898; 10.1053/j.gastro.2006.09.052 (2006).
68. Bolen, C. R., Ding, S., Robek, M. D. & Kleinstein, S. H. Dynamic expression profiling of type I and type III interferon-stimulated hepatocytes reveals a stable hierarchy of gene expression. *Hepatology (Baltimore, Md.)* **59,** 1262–1272; 10.1002/hep.26657 (2014).
69. Schoggins, J. W. *et al.* A diverse range of gene products are effectors of the type I interferon antiviral response. *Nature* **472,** 481–485; 10.1038/nature09907 (2011).
70. Wu, J. & Chen, Z. J. Innate immune sensing and signaling of cytosolic nucleic acids. *Annual review of immunology* **32,** 461–488; 10.1146/annurev-immunol-032713-120156 (2014).
71. Kochs, G. & Haller, O. GTP-bound human MxA protein interacts with the nucleocapsids of Thogoto virus (Orthomyxoviridae). *The Journal of biological chemistry* **274,** 4370–4376; 10.1074/jbc.274.7.4370 (1999).
72. Haller, O., Gao, S., Malsburg, A. von der, Daumke, O. & Kochs, G. Dynamin-like MxA GTPase: structural insights into oligomerization and implications for antiviral activity. *The Journal of biological chemistry* **285,** 28419–28424; 10.1074/jbc.R110.145839 (2010).

73. Graf, L. *et al.* Effects of allelic variations in the human myxovirus resistance protein A on its antiviral activity. *The Journal of biological chemistry* **293,** 3056–3072; 10.1074/jbc.M117.812784 (2018).
74. Kane, M. *et al.* MX2 is an interferon-induced inhibitor of HIV-1 infection. *Nature* **502,** 563–566; 10.1038/nature12653 (2013).
75. Goujon, C. *et al.* Human MX2 is an interferon-induced post-entry inhibitor of HIV-1 infection. *Nature* **502,** 559–562; 10.1038/nature12542 (2013).
76. Crameri, M. *et al.* MxB is an interferon-induced restriction factor of human herpesviruses. *Nature communications* **9,** 1980; 10.1038/s41467-018-04379-2 (2018).
77. Schilling, M. *et al.* Human MxB Protein Is a Pan-herpesvirus Restriction Factor. *Journal of virology* **92**; 10.1128/JVI.01056-18 (2018).
78. Fensterl, V. *et al.* Interferon-induced Ifit2/ISG54 protects mice from lethal VSV neuropathogenesis. *PLoS pathogens* **8,** e1002712; 10.1371/journal.ppat.1002712 (2012).
79. Pichlmair, A. *et al.* IFIT1 is an antiviral protein that recognizes 5'-triphosphate RNA. *Nature immunology* **12,** 624–630; 10.1038/ni.2048 (2011).
80. Raychoudhuri, A. *et al.* ISG56 and IFITM1 proteins inhibit hepatitis C virus replication. *Journal of virology* **85,** 12881–12889; 10.1128/JVI.05633-11 (2011).
81. Hui, D. J., Bhasker, C. R., Merrick, W. C. & Sen, G. C. Viral stress-inducible protein p56 inhibits translation by blocking the interaction of eIF3 with the ternary complex eIF2.GTP.Met-tRNAi. *The Journal of biological chemistry* **278,** 39477–39482; 10.1074/jbc.M305038200 (2003).
82. Guo, J., Peters, K. L. & Sen, G. C. Induction of the human protein P56 by interferon, double-stranded RNA, or virus infection. *Virology* **267,** 209–219; 10.1006/viro.1999.0135 (2000).
83. Diamond, M. S. & Farzan, M. The broad-spectrum antiviral functions of IFIT and IFITM proteins. *Nature reviews. Immunology* **13,** 46–57; 10.1038/nri3344 (2013).
84. Saikia, P., Fensterl, V. & Sen, G. C. The inhibitory action of P56 on select functions of E1 mediates interferon's effect on human papillomavirus DNA replication. *Journal of virology* **84,** 13036–13039; 10.1128/JVI.01194-10 (2010).
85. Terenzi, F., Saikia, P. & Sen, G. C. Interferon-inducible protein, P56, inhibits HPV DNA replication by binding to the viral protein E1. *The EMBO journal* **27,** 3311–3321; 10.1038/emboj.2008.241 (2008).
86. Helbig, K. J. & Beard, M. R. The role of viperin in the innate antiviral response. *Journal of molecular biology* **426,** 1210–1219; 10.1016/j.jmb.2013.10.019 (2014).
87. Nasr, N. *et al.* HIV-1 infection of human macrophages directly induces viperin which inhibits viral production. *Blood* **120,** 778–788; 10.1182/blood-2012-01-407395 (2012).
88. Wang, X., Hinson, E. R. & Cresswell, P. The interferon-inducible protein viperin inhibits influenza virus release by perturbing lipid rafts. *Cell host & microbe* **2,** 96–105; 10.1016/j.chom.2007.06.009 (2007).
89. Wang, S. *et al.* Viperin inhibits hepatitis C virus replication by interfering with binding of NS5A to host protein hVAP-33. *The Journal of general virology* **93,** 83–92; 10.1099/vir.0.033860-0 (2012).
90. Helbig, K. J. *et al.* The antiviral protein viperin inhibits hepatitis C virus replication via interaction with nonstructural protein 5A. *Hepatology (Baltimore, Md.)* **54,** 1506–1517; 10.1002/hep.24542 (2011).

91. Neil, S. J. D., Zang, T. & Bieniasz, P. D. Tetherin inhibits retrovirus release and is antagonized by HIV-1 Vpu. *Nature* **451,** 425–430; 10.1038/nature06553 (2008).
92. Galão, R. P., Le Tortorec, A., Pickering, S., Kueck, T. & Neil, S. J. D. Innate sensing of HIV-1 assembly by Tetherin induces NF κ B-dependent proinflammatory responses. *Cell host & microbe* **12,** 633–644; 10.1016/j.chom.2012.10.007 (2012).
93. Feng, J. *et al.* Interferon-Stimulated Gene (ISG)-Expression Screening Reveals the Specific Antibunyaviral Activity of ISG20. *Journal of virology* **92**; 10.1128/JVI.02140-17 (2018).
94. Kane, M. *et al.* Identification of Interferon-Stimulated Genes with Antiretroviral Activity. *Cell host & microbe* **20,** 392–405; 10.1016/j.chom.2016.08.005 (2016).
95. Schoggins, J. W. *et al.* Pan-viral specificity of IFN-induced genes reveals new roles for cGAS in innate immunity. *Nature* **505,** 691–695; 10.1038/nature12862 (2014).
96. Meuwissen, M. E. C. *et al.* Human USP18 deficiency underlies type 1 interferonopathy leading to severe pseudo-TORCH syndrome. *The Journal of experimental medicine* **213,** 1163–1174; 10.1084/jem.20151529 (2016).
97. Malakhov, M. P., Malakhova, O. A., Kim, K. I., Ritchie, K. J. & Zhang, D.-E. UBP43 (USP18) specifically removes ISG15 from conjugated proteins. *The Journal of biological chemistry* **277,** 9976–9981; 10.1074/jbc.M109078200 (2002).
98. Basters, A., Knobeloch, K.-P. & Fritz, G. USP18 - a multifunctional component in the interferon response. *Bioscience reports* **38**; 10.1042/BSR20180250 (2018).
99. Malakhova, O. A. *et al.* UBP43 is a novel regulator of interferon signaling independent of its ISG15 isopeptidase activity. *The EMBO journal* **25,** 2358–2367; 10.1038/sj.emboj.7601149 (2006).
100. Suttle, C. A. Marine viruses--major players in the global ecosystem. *Nature reviews. Microbiology* **5,** 801–812; 10.1038/nrmicro1750 (2007).
101. Shives, K. D., Tyler, K. L. & Beckham, J. D. Molecular mechanisms of neuroinflammation and injury during acute viral encephalitis. *Journal of neuroimmunology* **308,** 102–111; 10.1016/j.jneuroim.2017.03.006 (2017).
102. Ihekweazu, C. & Abubakar, I. Tackling viral haemorrhagic fever in Africa. *Lancet (London, England)* **390,** 2612–2614; 10.1016/S0140-6736(17)32475-3 (2017).
103. Eccles, R. Understanding the symptoms of the common cold and influenza. *The Lancet. Infectious diseases* **5,** 718–725; 10.1016/S1473-3099(05)70270-X (2005).
104. McBride, A. A. The Promise of Proteomics in the Study of Oncogenic Viruses. *Molecular & cellular proteomics : MCP* **16,** S65-S74; 10.1074/mcp.O116.065201 (2017).
105. *Pandemic Influenza Preparedness and Response: A WHO Guidance Document* (Geneva, 2009).
106. Pérez Velasco, R. *et al.* Systematic review of economic evaluations of preparedness strategies and interventions against influenza pandemics. *PloS one* **7,** e30333; 10.1371/journal.pone.0030333 (2012).
107. Tripathi, S. *et al.* Meta- and Orthogonal Integration of Influenza "OMICs" Data Defines a Role for UBR4 in Virus Budding. *Cell host & microbe* **18,** 723–735; 10.1016/j.chom.2015.11.002 (2015).
108. Pillay, S. & Carette, J. E. Hunting Viral Receptors Using Haploid Cells. *Annual review of virology* **2,** 219–239; 10.1146/annurev-virology-100114-055119 (2015).
109. Smith, A. E. & Helenius, A. How viruses enter animal cells. *Science (New York, N.Y.)* **304,** 237–242; 10.1126/science.1094823 (2004).
110. Hao, L. *et al.* Drosophila RNAi screen identifies host genes important for influenza virus replication. *Nature* **454,** 890–893; 10.1038/nature07151 (2008).

111. Chatel-Chaix, L. & Bartenschlager, R. Dengue virus- and hepatitis C virus-induced replication and assembly compartments: the enemy inside--caught in the web. *Journal of virology* **88,** 5907–5911; 10.1128/JVI.03404-13 (2014).
112. den Boon, J. A., Diaz, A. & Ahlquist, P. Cytoplasmic viral replication complexes. *Cell host & microbe* **8,** 77–85; 10.1016/j.chom.2010.06.010 (2010).
113. Mühlberger, E. Filovirus replication and transcription. *Future virology* **2,** 205–215; 10.2217/17460794.2.2.205 (2007).
114. Nakano, K. & Watanabe, T. HTLV-1 Rex: the courier of viral messages making use of the host vehicle. *Frontiers in microbiology* **3,** 330; 10.3389/fmicb.2012.00330 (2012).
115. Mole, S., Milligan, S. G. & Graham, S. V. Human papillomavirus type 16 E2 protein transcriptionally activates the promoter of a key cellular splicing factor, SF2/ASF. *Journal of virology* **83,** 357–367; 10.1128/JVI.01414-08 (2009).
116. Toth, Z. & Stamminger, T. The human cytomegalovirus regulatory protein UL69 and its effect on mRNA export. *Frontiers in bioscience : a journal and virtual library* **13,** 2939–2949 (2008).
117. Balvay, L., Soto Rifo, R., Ricci, E. P., Decimo, D. & Ohlmann, T. Structural and functional diversity of viral IRESes. *Biochimica et biophysica acta* **1789,** 542–557; 10.1016/j.bbagrm.2009.07.005 (2009).
118. Decroly, E., Ferron, F., Lescar, J. & Canard, B. Conventional and unconventional mechanisms for capping viral mRNA. *Nature reviews. Microbiology* **10,** 51–65; 10.1038/nrmicro2675 (2011).
119. Aviner, R. & Frydman, J. Proteostasis in Viral Infection: Unfolding the Complex Virus-Chaperone Interplay. *Cold Spring Harbor perspectives in biology*; 10.1101/cshperspect.a034090 (2019).
120. Khachatoorian, R. & French, S. W. Chaperones in hepatitis C virus infection. *World journal of hepatology* **8,** 9–35; 10.4254/wjh.v8.i1.9 (2016).
121. Xiao, A., Wong, J. & Luo, H. Viral interaction with molecular chaperones: role in regulating viral infection. *Archives of virology* **155,** 1021–1031; 10.1007/s00705-010-0691-3 (2010).
122. Fernández de Castro, I., Tenorio, R. & Risco, C. Virus assembly factories in a lipid world. *Current opinion in virology* **18,** 20–26; 10.1016/j.coviro.2016.02.009 (2016).
123. Bozzacco, L. *et al.* Chaperone-Assisted Protein Folding Is Critical for Yellow Fever Virus NS3/4A Cleavage and Replication. *Journal of virology* **90,** 3212–3228; 10.1128/JVI.03077-15 (2016).
124. Chen, B. J. & Lamb, R. A. Mechanisms for enveloped virus budding: can some viruses do without an ESCRT? *Virology* **372,** 221–232; 10.1016/j.virol.2007.11.008 (2008).
125. Rossman, J. S., Jing, X., Leser, G. P. & Lamb, R. A. Influenza virus M2 protein mediates ESCRT-independent membrane scission. *Cell* **142,** 902–913; 10.1016/j.cell.2010.08.029 (2010).
126. Vardi, A. *et al.* Viral glycosphingolipids induce lytic infection and cell death in marine phytoplankton. *Science (New York, N.Y.)* **326,** 861–865; 10.1126/science.1177322 (2009).
127. Tollefson, A. E. *et al.* The adenovirus death protein (E3-11.6K) is required at very late stages of infection for efficient cell lysis and release of adenovirus from infected cells. *Journal of virology* **70,** 2296–2306 (1996).
128. McDonald, B. & Martin-Serrano, J. No strings attached: the ESCRT machinery in viral budding and cytokinesis. *Journal of cell science* **122,** 2167–2177; 10.1242/jcs.028308 (2009).

129. Mukhopadhyay, S., Kuhn, R. J. & Rossmann, M. G. A structural perspective of the flavivirus life cycle. *Nature reviews. Microbiology* **3,** 13–22; 10.1038/nrmicro1067 (2005).
130. Welsch, S. *et al.* Composition and three-dimensional architecture of the dengue virus replication and assembly sites. *Cell host & microbe* **5,** 365–375; 10.1016/j.chom.2009.03.007 (2009).
131. Melancon, J. M., Luna, R. E., Foster, T. P. & Kousoulas, K. G. Herpes simplex virus type 1 gK is required for gB-mediated virus-induced cell fusion, while neither gB and gK nor gB and UL20p function redundantly in virion de-envelopment. *Journal of virology* **79,** 299–313; 10.1128/JVI.79.1.299-313.2005 (2005).
132. Pichlmair, A. *et al.* Viral immune modulators perturb the human molecular network by common and unique strategies. *Nature* **487,** 486–490; 10.1038/nature11289 (2012).
133. Yi, Z., Chen, J., Kozlowski, M. & Yuan, Z. Innate detection of hepatitis B and C virus and viral inhibition of the response. *Cellular microbiology* **17,** 1295–1303; 10.1111/cmi.12489 (2015).
134. Engel, P. & Angulo, A. Viral immunomodulatory proteins: usurping host genes as a survival strategy. *Advances in experimental medicine and biology* **738,** 256–276; 10.1007/978-1-4614-1680-7_15 (2012).
135. Davidson, S. Treating Influenza Infection, From Now and Into the Future. *Frontiers in immunology* **9,** 1946; 10.3389/fimmu.2018.01946 (2018).
136. Wensing, A. M. *et al.* 2017 Update of the Drug Resistance Mutations in HIV-1. *Topics in antiviral medicine* **24,** 132–133 (2017).
137. Webster, R. G. & Govorkova, E. A. Continuing challenges in influenza. *Annals of the New York Academy of Sciences* **1323,** 115–139; 10.1111/nyas.12462 (2014).
138. Gaschen, B. *et al.* Diversity considerations in HIV-1 vaccine selection. *Science (New York, N.Y.)* **296,** 2354–2360; 10.1126/science.1070441 (2002).
139. Dauber, B., Schneider, J. & Wolff, T. Double-stranded RNA binding of influenza B virus nonstructural NS1 protein inhibits protein kinase R but is not essential to antagonize production of alpha/beta interferon. *Journal of virology* **80,** 11667–11677; 10.1128/JVI.01142-06 (2006).
140. Lu, Y., Wambach, M., Katze, M. G. & Krug, R. M. Binding of the influenza virus NS1 protein to double-stranded RNA inhibits the activation of the protein kinase that phosphorylates the elF-2 translation initiation factor. *Virology* **214,** 222–228 (1995).
141. Kainulainen, M., Lau, S., Samuel, C. E., Hornung, V. & Weber, F. NSs Virulence Factor of Rift Valley Fever Virus Engages the F-Box Proteins FBXW11 and β -TRCP1 To Degrade the Antiviral Protein Kinase PKR. *Journal of virology* **90,** 6140–6147; 10.1128/JVI.00016-16 (2016).
142. Habjan, M. *et al.* NSs protein of rift valley fever virus induces the specific degradation of the double-stranded RNA-dependent protein kinase. *Journal of virology* **83,** 4365–4375; 10.1128/JVI.02148-08 (2009).
143. Hakki, M., Marshall, E. E., Niro, K. L. de & Geballe, A. P. Binding and nuclear relocalization of protein kinase R by human cytomegalovirus TRS1. *Journal of virology* **80,** 11817–11826; 10.1128/JVI.00957-06 (2006).
144. Perdiguero, B. & Esteban, M. The interferon system and vaccinia virus evasion mechanisms. *Journal of interferon & cytokine research : the official journal of the International Society for Interferon and Cytokine Research* **29,** 581–598; 10.1089/jir.2009.0073 (2009).

145. Chen, S. *et al.* Flaviviridae virus nonstructural proteins 5 and 5A mediate viral immune evasion and are promising targets in drug development. *Pharmacology &therapeutics* **190,** 1–14; 10.1016/j.pharmthera.2018.05.004 (2018).

146. Davies, M. V., Chang, H. W., Jacobs, B. L. & Kaufman, R. J. The E3L and K3L vaccinia virus gene products stimulate translation through inhibition of the double-stranded RNA-dependent protein kinase by different mechanisms. *Journal of virology* **67,** 1688–1692 (1993).

147. Yue, Z. & Shatkin, A. J. Double-stranded RNA-dependent protein kinase (PKR) is regulated by reovirus structural proteins. *Virology* **234,** 364–371; 10.1006/viro.1997.8664 (1997).

148. Xing, J., Ly, H. & Liang, Y. The Z proteins of pathogenic but not nonpathogenic arenaviruses inhibit RIG-I-like receptor-dependent interferon production. *Journal of virology* **89,** 2944–2955; 10.1128/JVI.03349-14 (2015).

149. Ling, Z., Tran, K. C. & Teng, M. N. Human respiratory syncytial virus nonstructural protein NS2 antagonizes the activation of beta interferon transcription by interacting with RIG-I. *Journal of virology* **83,** 3734–3742; 10.1128/JVI.02434-08 (2009).

150. Gack, M. U. *et al.* Influenza A virus NS1 targets the ubiquitin ligase TRIM25 to evade recognition by the host viral RNA sensor RIG-I. *Cell host &microbe* **5,** 439–449; 10.1016/j.chom.2009.04.006 (2009).

151. Horner, S. M. Insights into antiviral innate immunity revealed by studying hepatitis C virus. *Cytokine* **74,** 190–197; 10.1016/j.cyto.2015.03.007 (2015).

152. Leung, L. W. *et al.* Ebolavirus VP35 suppresses IFN production from conventional but not plasmacytoid dendritic cells. *Immunology and cell biology* **89,** 792–802; 10.1038/icb.2010.169 (2011).

153. Varga, Z. T. *et al.* The influenza virus protein PB1-F2 inhibits the induction of type I interferon at the level of the MAVS adaptor protein. *PLoS pathogens* **7,** e1002067; 10.1371/journal.ppat.1002067 (2011).

154. Wei, C. *et al.* The hepatitis B virus X protein disrupts innate immunity by downregulating mitochondrial antiviral signaling protein. *Journal of immunology (Baltimore, Md. : 1950)* **185,** 1158–1168; 10.4049/jimmunol.0903874 (2010).

155. Yang, Y. *et al.* Disruption of innate immunity due to mitochondrial targeting of a picornaviral protease precursor. *Proceedings of the National Academy of Sciences of the United States of America* **104,** 7253–7258; 10.1073/pnas.0611506104 (2007).

156. Wang, J.-T. *et al.* Epstein-Barr virus BGLF4 kinase suppresses the interferon regulatory factor 3 signaling pathway. *Journal of virology* **83,** 1856–1869; 10.1128/JVI.01099-08 (2009).

157. Arnold, M. M., Barro, M. & Patton, J. T. Rotavirus NSP1 mediates degradation of interferon regulatory factors through targeting of the dimerization domain. *Journal of virology* **87,** 9813–9821; 10.1128/JVI.01146-13 (2013).

158. Qu, L. *et al.* Disruption of TLR3 signaling due to cleavage of TRIF by the hepatitis A virus protease-polymerase processing intermediate, 3CD. *PLoS pathogens* **7,** e1002169; 10.1371/journal.ppat.1002169 (2011).

159. Stack, J. & Bowie, A. G. Poxviral protein A46 antagonizes Toll-like receptor 4 signaling by targeting BB loop motifs in Toll-IL-1 receptor adaptor proteins to disrupt receptor:adaptor interactions. *The Journal of biological chemistry* **287,** 22672–22682; 10.1074/jbc.M112.349225 (2012).

160. Ma, Z. & Damania, B. The cGAS-STING Defense Pathway and Its Counteraction by Viruses. *Cell host &microbe* **19,** 150–158; 10.1016/j.chom.2016.01.010 (2016).

161. Kaminskyy, V. & Zhivotovsky, B. To kill or be killed: how viruses interact with the cell death machinery. *Journal of internal medicine* **267,** 473–482; 10.1111/j.1365-2796.2010.02222.x (2010).

162. Stürzl, M. *et al.* Expression of K13/v-FLIP gene of human herpesvirus 8 and apoptosis in Kaposi's sarcoma spindle cells. *Journal of the National Cancer Institute* **91,** 1725–1733; 10.1093/jnci/91.20.1725 (1999).

163. Glykofrydes, D. *et al.* Herpesvirus saimiri vFLIP provides an antiapoptotic function but is not essential for viral replication, transformation, or pathogenicity. *Journal of virology* **74,** 11919–11927; 10.1128/jvi.74.24.11919-11927.2000 (2000).

164. Cheng, E. H. *et al.* A Bcl-2 homolog encoded by Kaposi sarcoma-associated virus, human herpesvirus 8, inhibits apoptosis but does not heterodimerize with Bax or Bak. *Proceedings of the National Academy of Sciences of the United States of America* **94,** 690–694; 10.1073/pnas.94.2.690 (1997).

165. Chiou, S. K., Tseng, C. C., Rao, L. & White, E. Functional complementation of the adenovirus E1B 19-kilodalton protein with Bcl-2 in the inhibition of apoptosis in infected cells. *Journal of virology* **68,** 6553–6566 (1994).

166. Postigo, A. & Way, M. The vaccinia virus-encoded Bcl-2 homologues do not act as direct Bax inhibitors. *Journal of virology* **86,** 203–213; 10.1128/JVI.05817-11 (2012).

167. Skaletskaya, A. *et al.* A cytomegalovirus-encoded inhibitor of apoptosis that suppresses caspase-8 activation. *Proceedings of the National Academy of Sciences of the United States of America* **98,** 7829–7834; 10.1073/pnas.141108798 (2001).

168. Turner, S. J., Silke, J., Kenshole, B. & Ruby, J. Characterization of the ectromelia virus serpin, SPI-2. *The Journal of general virology* **81,** 2425–2430; 10.1099/0022-1317-81-10-2425 (2000).

169. Dobbelstein, M. & Shenk, T. Protection against apoptosis by the vaccinia virus SPI-2 (B13R) gene product. *Journal of virology* **70,** 6479–6485 (1996).

170. Wang, H.-W., Sharp, T. V., Koumi, A., Koentges, G. & Boshoff, C. Characterization of an anti-apoptotic glycoprotein encoded by Kaposi's sarcoma-associated herpesvirus which resembles a spliced variant of human survivin. *The EMBO journal* **21,** 2602–2615; 10.1093/emboj/21.11.2602 (2002).

171. Zhai, D. *et al.* Vaccinia virus protein F1L is a caspase-9 inhibitor. *The Journal of biological chemistry* **285,** 5569–5580; 10.1074/jbc.M109.078113 (2010).

172. Nie, Z., Bren, G. D., Rizza, S. A. & Badley, A. D. HIV Protease Cleavage of Procaspase 8 is Necessary for Death of HIV-Infected Cells. *The open virology journal* **2,** 1–7; 10.2174/1874357900802010001 (2008).

173. Prikhod'ko, G. G., Prikhod'ko, E. A., Pletnev, A. G. & Cohen, J. I. Langat flavivirus protease NS3 binds caspase-8 and induces apoptosis. *Journal of virology* **76,** 5701–5710; 10.1128/jvi.76.11.5701-5710.2002 (2002).

174. Thierry, F. & Demeret, C. Direct activation of caspase 8 by the proapoptotic E2 protein of HPV18 independent of adaptor proteins. *Cell death and differentiation* **15,** 1356–1363; 10.1038/cdd.2008.53 (2008).

175. Cho, Y. S. *et al.* Phosphorylation-driven assembly of the RIP1-RIP3 complex regulates programmed necrosis and virus-induced inflammation. *Cell* **137,** 1112–1123; 10.1016/j.cell.2009.05.037 (2009).

176. Huang, Z. *et al.* RIP1/RIP3 binding to HSV-1 ICP6 initiates necroptosis to restrict virus propagation in mice. *Cell host & microbe* **17,** 229–242; 10.1016/j.chom.2015.01.002 (2015).

177. Camini, F. C., da Silva Caetano, C. C., Almeida, L. T. & Brito Magalhães, C. L. de. Implications of oxidative stress on viral pathogenesis. *Archives of virology* **162,** 907–917; 10.1007/s00705-016-3187-y (2017).

178. Reshi, M. L., Su, Y.-C. & Hong, J.-R. RNA Viruses: ROS-Mediated Cell Death. *International journal of cell biology* **2014,** 467452; 10.1155/2014/467452 (2014).

179. Lin, X. *et al.* The Influenza Virus H5N1 Infection Can Induce ROS Production for Viral Replication and Host Cell Death in A549 Cells Modulated by Human Cu/Zn Superoxide Dismutase (SOD1) Overexpression. *Viruses* **8**; 10.3390/v8010013 (2016).

180. Tait, S. W., Reid, E. B., Greaves, D. R., Wileman, T. E. & Powell, P. P. Mechanism of inactivation of NF-kappa B by a viral homologue of I kappa b alpha. Signal-induced release of i kappa b alpha results in binding of the viral homologue to NF-kappa B. *The Journal of biological chemistry* **275,** 34656–34664; 10.1074/jbc.M000320200 (2000).

181. Zheng, H. *et al.* Torque teno virus (SANBAN isolate) ORF2 protein suppresses NF-kappaB pathways via interaction with IkappaB kinases. *Journal of virology* **81,** 11917–11924; 10.1128/JVI.01101-07 (2007).

182. Valentine, R. *et al.* Epstein-Barr virus-encoded EBNA1 inhibits the canonical NF-kappaB pathway in carcinoma cells by inhibiting IKK phosphorylation. *Molecular cancer* **9,** 1; 10.1186/1476-4598-9-1 (2010).

183. Graff, J. W., Ettayebi, K. & Hardy, M. E. Rotavirus NSP1 inhibits NFkappaB activation by inducing proteasome-dependent degradation of beta-TrCP: a novel mechanism of IFN antagonism. *PLoS pathogens* **5,** e1000280; 10.1371/journal.ppat.1000280 (2009).

184. Goodkin, M. L., Ting, A. T. & Blaho, J. A. NF-kappaB is required for apoptosis prevention during herpes simplex virus type 1 infection. *Journal of virology* **77,** 7261–7280; 10.1128/jvi.77.13.7261-7280.2003 (2003).

185. Hargett, D., Rice, S. & Bachenheimer, S. L. Herpes simplex virus type 1 ICP27-dependent activation of NF-kappaB. *Journal of virology* **80,** 10565–10578; 10.1128/JVI.01119-06 (2006).

186. Sun, S. C. & Ballard, D. W. Persistent activation of NF-kappaB by the tax transforming protein of HTLV-1: hijacking cellular IkappaB kinases. *Oncogene* **18,** 6948–6958; 10.1038/sj.onc.1203220 (1999).

187. Li, Q., Means, R., Lang, S. & Jung, J. U. Downregulation of gamma interferon receptor 1 by Kaposi's sarcoma-associated herpesvirus K3 and K5. *Journal of virology* **81,** 2117–2127; 10.1128/JVI.01961-06 (2007).

188. Geiger, T. R. & Martin, J. M. The Epstein-Barr virus-encoded LMP-1 oncoprotein negatively affects Tyk2 phosphorylation and interferon signaling in human B cells. *Journal of virology* **80,** 11638–11650; 10.1128/JVI.01570-06 (2006).

189. Lin, R.-J., Chang, B.-L., Yu, H.-P., Liao, C.-L. & Lin, Y.-L. Blocking of interferon-induced Jak-Stat signaling by Japanese encephalitis virus NS5 through a protein tyrosine phosphatase-mediated mechanism. *Journal of virology* **80,** 5908–5918; 10.1128/JVI.02714-05 (2006).

190. Valmas, C. *et al.* Marburg virus evades interferon responses by a mechanism distinct from ebola virus. *PLoS pathogens* **6,** e1000721; 10.1371/journal.ppat.1000721 (2010).

191. Weihua, X. *et al.* The polyoma virus T antigen interferes with interferon-inducible gene expression. *Proceedings of the National Academy of Sciences of the United States of America* **95,** 1085–1090; 10.1073/pnas.95.3.1085 (1998).

192. Garcin, D., Marq, J.-B., Strahle, L., Le Mercier, P. & Kolakofsky, D. All four Sendai Virus C proteins bind Stat1, but only the larger forms also induce its mono-ubiquitination and degradation. *Virology* **295,** 256–265; 10.1006/viro.2001.1342 (2002).

193. Hong, S., Mehta, K. P. & Laimins, L. A. Suppression of STAT-1 expression by human papillomaviruses is necessary for differentiation-dependent genome amplification and plasmid maintenance. *Journal of virology* **85,** 9486–9494; 10.1128/JVI.05007-11 (2011).

194. Stuart, J. H., Sumner, R. P., Lu, Y., Snowden, J. S. & Smith, G. L. Vaccinia Virus Protein C6 Inhibits Type I IFN Signalling in the Nucleus and Binds to the Transactivation Domain of STAT2. *PLoS pathogens* **12,** e1005955; 10.1371/journal.ppat.1005955 (2016).

195. Wiltzer, L. *et al.* Interaction of rabies virus P-protein with STAT proteins is critical to lethal rabies disease. *The Journal of infectious diseases* **209,** 1744–1753; 10.1093/infdis/jit829 (2014).

196. Xu, W. *et al.* Ebola virus VP24 targets a unique NLS binding site on karyopherin alpha 5 to selectively compete with nuclear import of phosphorylated STAT1. *Cell host &microbe* **16,** 187–200; 10.1016/j.chom.2014.07.008 (2014).

197. Bussey, K. A. & Brinkmann, M. M. Strategies for immune evasion by human tumor viruses. *Current opinion in virology* **32,** 30–39; 10.1016/j.coviro.2018.08.015 (2018).

198. Christiaansen, A., Varga, S. M. & Spencer, J. V. Viral manipulation of the host immune response. *Current opinion in immunology* **36,** 54–60; 10.1016/j.coi.2015.06.012 (2015).

199. Yang, F. Post-translational Modification Control of HBV Biological Processes. *Frontiers in microbiology* **9,** 2661; 10.3389/fmicb.2018.02661 (2018).

200. Thomas, D. *et al.* Inhibition of RNA polymerase II phosphorylation by a viral interferon antagonist. *The Journal of biological chemistry* **279,** 31471–31477; 10.1074/jbc.M400938200 (2004).

201. Kalveram, B., Lihoradova, O. & Ikegami, T. NSs protein of rift valley fever virus promotes posttranslational downregulation of the TFIIH subunit p62. *Journal of virology* **85,** 6234–6243; 10.1128/JVI.02255-10 (2011).

202. Di Valentin, E. *et al.* Varicella-zoster virus IE63 protein represses the basal transcription machinery by disorganizing the pre-initiation complex. *Biological chemistry* **386,** 255–267; 10.1515/BC.2005.031 (2005).

203. Vreede, F. T. & Fodor, E. The role of the influenza virus RNA polymerase in host shut-off. *Virulence* **1,** 436–439; 10.4161/viru.1.5.12967 (2010).

204. Hsu, A. C.-Y. Influenza Virus: A Master Tactician in Innate Immune Evasion and Novel Therapeutic Interventions. *Frontiers in immunology* **9,** 743; 10.3389/fimmu.2018.00743 (2018).

205. Hatada, E. & Fukuda, R. Binding of influenza A virus NS1 protein to dsRNA in vitro. *The Journal of general virology* **73 (Pt 12),** 3325–3329; 10.1099/0022-1317-73-12-3325 (1992).

206. Zhao, M., Wang, L. & Li, S. Influenza A Virus-Host Protein Interactions Control Viral Pathogenesis. *International journal of molecular sciences* **18**; 10.3390/ijms18081673 (2017).

207. Silverman, A. J. & Desnoyers, O. The hypothalamic magnocellular neurosecretory system of the guinea pig. III. Ultrastructure of the fetal neural lobe. *The American journal of anatomy* **145,** 499–515; 10.1002/aja.1001450408 (1976).

208. Nemeroff, M. E., Barabino, S. M., Li, Y., Keller, W. & Krug, R. M. Influenza virus NS1 protein interacts with the cellular 30 kDa subunit of CPSF and inhibits 3'end formation of cellular pre-mRNAs. *Molecular cell* **1,** 991–1000 (1998).

209. Bercovich-Kinori, A. *et al.* A systematic view on influenza induced host shutoff. *eLife* **5**; 10.7554/eLife.18311 (2016).

210. Poon, L. L., Pritlove, D. C., Fodor, E. & Brownlee, G. G. Direct evidence that the poly(A) tail of influenza A virus mRNA is synthesized by reiterative copying of a U track in the virion RNA template. *Journal of virology* **73,** 3473–3476 (1999).

211. Aranda, M. & Maule, A. Virus-induced host gene shutoff in animals and plants. *Virology* **243,** 261–267; 10.1006/viro.1998.9032 (1998).

212. Castelló, A., Izquierdo, J. M., Welnowska, E. & Carrasco, L. RNA nuclear export is blocked by poliovirus 2A protease and is concomitant with nucleoporin cleavage. *Journal of cell science* **122,** 3799–3809; 10.1242/jcs.055988 (2009).

213. Ghildyal, R. *et al.* Rhinovirus 3C protease can localize in the nucleus and alter active and passive nucleocytoplasmic transport. *Journal of virology* **83,** 7349–7352; 10.1128/JVI.01748-08 (2009).

214. Ren, Y., Seo, H.-S., Blobel, G. & Hoelz, A. Structural and functional analysis of the interaction between the nucleoporin Nup98 and the mRNA export factor Rae1. *Proceedings of the National Academy of Sciences of the United States of America* **107,** 10406–10411; 10.1073/pnas.1005389107 (2010).

215. Faria, P. A. *et al.* VSV disrupts the Rae1/mrnp41 mRNA nuclear export pathway. *Molecular cell* **17,** 93–102; 10.1016/j.molcel.2004.11.023 (2005).

216. Kobbe, C. von *et al.* Vesicular stomatitis virus matrix protein inhibits host cell gene expression by targeting the nucleoporin Nup98. *Molecular cell* **6,** 1243–1252 (2000).

217. Bryant, H. E., Wadd, S. E., Lamond, A. I., Silverstein, S. J. & Clements, J. B. Herpes simplex virus IE63 (ICP27) protein interacts with spliceosome-associated protein 145 and inhibits splicing prior to the first catalytic step. *Journal of virology* **75,** 4376–4385; 10.1128/JVI.75.9.4376-4385.2001 (2001).

218. Malik, P. *et al.* Herpes simplex virus ICP27 protein directly interacts with the nuclear pore complex through Nup62, inhibiting host nucleocytoplasmic transport pathways. *The Journal of biological chemistry* **287,** 12277–12292; 10.1074/jbc.M111.331777 (2012).

219. Nojima, T. *et al.* Herpesvirus protein ICP27 switches PML isoform by altering mRNA splicing. *Nucleic acids research* **37,** 6515–6527; 10.1093/nar/gkp633 (2009).

220. Hashizume, C. *et al.* Human immunodeficiency virus type 1 Vpr interacts with spliceosomal protein SAP145 to mediate cellular pre-mRNA splicing inhibition. *Microbes and infection* **9,** 490–497; 10.1016/j.micinf.2007.01.013 (2007).

221. Richner, J. M. *et al.* Global mRNA degradation during lytic gammaherpesvirus infection contributes to establishment of viral latency. *PLoS pathogens* **7,** e1002150; 10.1371/journal.ppat.1002150 (2011).

222. Rowe, M. *et al.* Host shutoff during productive Epstein-Barr virus infection is mediated by BGLF5 and may contribute to immune evasion. *Proceedings of the National Academy of Sciences of the United States of America* **104,** 3366–3371; 10.1073/pnas.0611128104 (2007).

223. Saffran, H. A., Read, G. S. & Smiley, J. R. Evidence for translational regulation by the herpes simplex virus virion host shutoff protein. *Journal of virology* **84,** 6041–6049; 10.1128/JVI.01819-09 (2010).

224. Walsh, D. & Mohr, I. Viral subversion of the host protein synthesis machinery. *Nature reviews. Microbiology* **9,** 860–875; 10.1038/nrmicro2655 (2011).

225. Sonenberg, N. & Hinnebusch, A. G. Regulation of translation initiation in eukaryotes: mechanisms and biological targets. *Cell* **136,** 731–745; 10.1016/j.cell.2009.01.042 (2009).

226. Moral-López, P., Alvarez, E., Redondo, N., Skern, T. & Carrasco, L. L protease from foot and mouth disease virus confers eIF2-independent translation for mRNAs bearing picornavirus IRES. *FEBS letters* **588,** 4053–4059; 10.1016/j.febslet.2014.09.030 (2014).

227. Kahvejian, A., Svitkin, Y. V., Sukarieh, R., M'Boutchou, M.-N. & Sonenberg, N. Mammalian poly(A)-binding protein is a eukaryotic translation initiation factor, which acts via multiple mechanisms. *Genes & development* **19,** 104–113; 10.1101/gad.1262905 (2005).

228. Kuyumcu-Martinez, N. M., Joachims, M. & Lloyd, R. E. Efficient cleavage of ribosome-associated poly(A)-binding protein by enterovirus 3C protease. *Journal of virology* **76,** 2062–2074; 10.1128/jvi.76.5.2062-2074.2002 (2002).

229. Rivera, C. I. & Lloyd, R. E. Modulation of enteroviral proteinase cleavage of poly(A)-binding protein (PABP) by conformation and PABP-associated factors. *Virology* **375,** 59–72; 10.1016/j.virol.2008.02.002 (2008).

230. Rodríguez Pulido, M., Serrano, P., Sáiz, M. & Martínez-Salas, E. Foot-and-mouth disease virus infection induces proteolytic cleavage of PTB, eIF3a,b, and PABP RNA-binding proteins. *Virology* **364,** 466–474; 10.1016/j.virol.2007.03.013 (2007).

231. Breyne, S. de, Bonderoff, J. M., Chumakov, K. M., Lloyd, R. E. & Hellen, C. U. T. Cleavage of eukaryotic initiation factor eIF5B by enterovirus 3C proteases. *Virology* **378,** 118–122; 10.1016/j.virol.2008.05.019 (2008).

232. Reuther, P. *et al.* Generation of a variety of stable Influenza A reporter viruses by genetic engineering of the NS gene segment. *Scientific reports* **5,** 11346; 10.1038/srep11346 (2015).

233. Ploss, A. *et al.* Human occludin is a hepatitis C virus entry factor required for infection of mouse cells. *Nature* **457,** 882–886; 10.1038/nature07684 (2009).

234. Saeed, M. *et al.* SEC14L2 enables pan-genotype HCV replication in cell culture. *Nature* **524,** 471–475; 10.1038/nature14899 (2015).

235. Evans, M. J. *et al.* Claudin-1 is a hepatitis C virus co-receptor required for a late step in entry. *Nature* **446,** 801–805; 10.1038/nature05654 (2007).

236. Yoneyama, M. *et al.* The RNA helicase RIG-I has an essential function in double-stranded RNA-induced innate antiviral responses. *Nature immunology* **5,** 730–737; 10.1038/ni1087 (2004).

237. Brass, A. L. *et al.* Identification of host proteins required for HIV infection through a functional genomic screen. *Science (New York, N.Y.)* **319,** 921–926; 10.1126/science.1152725 (2008).

238. Zhu, J. *et al.* Comprehensive identification of host modulators of HIV-1 replication using multiple orthologous RNAi reagents. *Cell reports* **9,** 752–766; 10.1016/j.celrep.2014.09.031 (2014).

239. Tai, A. W. *et al.* A functional genomic screen identifies cellular cofactors of hepatitis C virus replication. *Cell host &microbe* **5,** 298–307; 10.1016/j.chom.2009.02.001 (2009).

240. Hackett, B. A. *et al.* RNASEK is required for internalization of diverse acid-dependent viruses. *Proceedings of the National Academy of Sciences of the United States of America* **112,** 7797–7802; 10.1073/pnas.1424098112 (2015).

241. Panda, D. & Cherry, S. Cell-based genomic screening: elucidating virus-host interactions. *Current opinion in virology* **2,** 784–792; 10.1016/j.coviro.2012.10.007 (2012).

242. Stukalov, A. & Pichlmair, A. Gambling with Flu: "All in" to Maximize Reward. *Cell host & microbe* **18,** 643–645; 10.1016/j.chom.2015.11.010 (2015).

243. Lupberger, J. *et al.* EGFR and EphA2 are host factors for hepatitis C virus entry and possible targets for antiviral therapy. *Nature medicine* **17,** 589–595; 10.1038/nm.2341 (2011).

244. Puschnik, A. S., Majzoub, K., Ooi, Y. S. & Carette, J. E. A CRISPR toolbox to study virus-host interactions. *Nature reviews. Microbiology* **15,** 351–364; 10.1038/nrmicro.2017.29 (2017).

245. Carette, J. E. *et al.* Haploid genetic screens in human cells identify host factors used by pathogens. *Science (New York, N.Y.)* **326,** 1231–1235; 10.1126/science.1178955 (2009).

246. Carette, J. E. *et al.* Ebola virus entry requires the cholesterol transporter Niemann-Pick C1. *Nature* **477,** 340–343; 10.1038/nature10348 (2011).

247. Jae, L. T. *et al.* Deciphering the glycosylome of dystroglycanopathies using haploid screens for lassa virus entry. *Science (New York, N.Y.)* **340,** 479–483; 10.1126/science.1233675 (2013).

248. Pillay, S. *et al.* An essential receptor for adeno-associated virus infection. *Nature* **530,** 108–112; 10.1038/nature16465 (2016).

249. Riblett, A. M. *et al.* A Haploid Genetic Screen Identifies Heparan Sulfate Proteoglycans Supporting Rift Valley Fever Virus Infection. *Journal of virology* **90,** 1414–1423; 10.1128/JVI.02055-15 (2016).

250. Sagi, I. *et al.* Derivation and differentiation of haploid human embryonic stem cells. *Nature* **532,** 107–111; 10.1038/nature17408 (2016).

251. Li, Y. & Shuai, L. A versatile genetic tool: haploid cells. *Stem cell research &therapy* **8,** 197; 10.1186/s13287-017-0657-4 (2017).

252. Le Cong *et al.* Multiplex genome engineering using CRISPR/Cas systems. *Science (New York, N.Y.)* **339,** 819–823; 10.1126/science.1231143 (2013).

253. Jinek, M. *et al.* A programmable dual-RNA-guided DNA endonuclease in adaptive bacterial immunity. *Science (New York, N.Y.)* **337,** 816–821; 10.1126/science.1225829 (2012).

254. Jinek, M. *et al.* RNA-programmed genome editing in human cells. *eLife* **2,** e00471; 10.7554/eLife.00471 (2013).

255. Ma, H. *et al.* A CRISPR-Based Screen Identifies Genes Essential for West-Nile-Virus-Induced Cell Death. *Cell reports* **12,** 673–683; 10.1016/j.celrep.2015.06.049 (2015).

256. Marceau, C. D. *et al.* Genetic dissection of Flaviviridae host factors through genome-scale CRISPR screens. *Nature* **535,** 159–163; 10.1038/nature18631 (2016).

257. Savidis, G. *et al.* Identification of Zika Virus and Dengue Virus Dependency Factors using Functional Genomics. *Cell reports* **16,** 232–246; 10.1016/j.celrep.2016.06.028 (2016).

258. Zhang, R. *et al.* A CRISPR screen defines a signal peptide processing pathway required by flaviviruses. *Nature* **535,** 164–168; 10.1038/nature18625 (2016).

259. Orchard, R. C. *et al.* Discovery of a proteinaceous cellular receptor for a norovirus. *Science (New York, N.Y.)* **353,** 933–936; 10.1126/science.aaf1220 (2016).

260. Park, R. J. *et al.* A genome-wide CRISPR screen identifies a restricted set of HIV host dependency factors. *Nature genetics* **49,** 193–203; 10.1038/ng.3741 (2017).

261. Parnas, O. *et al.* A Genome-wide CRISPR Screen in Primary Immune Cells to Dissect Regulatory Networks. *Cell* **162,** 675–686; 10.1016/j.cell.2015.06.059 (2015).

262. Fenn, J. B., Mann, M., Meng, C. K., Wong, S. F. & Whitehouse, C. M. Electrospray ionization for mass spectrometry of large biomolecules. *Science (New York, N.Y.)* **246,** 64–71 (1989).

263. Karas, M. & Hillenkamp, F. Laser desorption ionization of proteins with molecular masses exceeding 10,000 daltons. *Analytical chemistry* **60,** 2299–2301 (1988).

264. Lander, E. S. *et al.* Initial sequencing and analysis of the human genome. *Nature* **409,** 860–921; 10.1038/35057062 (2001).

265. Venter, J. C. *et al.* The sequence of the human genome. *Science (New York, N.Y.)* **291,** 1304–1351; 10.1126/science.1058040 (2001).

266. Grabowski, P., Kustatscher, G. & Rappsilber, J. Epigenetic Variability Confounds Transcriptome but Not Proteome Profiling for Coexpression-based Gene Function

Prediction. *Molecular &cellular proteomics : MCP* **17,** 2082–2090; 10.1074/mcp.RA118.000935 (2018).

267. Aebersold, R. & Mann, M. Mass-spectrometric exploration of proteome structure and function. *Nature* **537,** 347–355; 10.1038/nature19949 (2016).
268. Klykov, O. *et al.* Efficient and robust proteome-wide approaches for cross-linking mass spectrometry. *Nature protocols* **13,** 2964–2990; 10.1038/s41596-018-0074-x (2018).
269. Schilling, O. & Overall, C. M. Proteomic discovery of protease substrates. *Current opinion in chemical biology* **11,** 36–45; 10.1016/j.cbpa.2006.11.037 (2007).
270. Harper, J. W. & Bennett, E. J. Proteome complexity and the forces that drive proteome imbalance. *Nature* **537,** 328–338; 10.1038/nature19947 (2016).
271. Bennike, T., Birkelund, S., Stensballe, A. & Andersen, V. Biomarkers in inflammatory bowel diseases: current status and proteomics identification strategies. *World journal of gastroenterology* **20,** 3231–3244; 10.3748/wjg.v20.i12.3231 (2014).
272. Scheltema, R. A. *et al.* The Q Exactive HF, a Benchtop mass spectrometer with a pre-filter, high-performance quadrupole and an ultra-high-field Orbitrap analyzer. *Molecular &cellular proteomics : MCP* **13,** 3698–3708; 10.1074/mcp.M114.043489 (2014).
273. León, I. R., Schwämmle, V., Jensen, O. N. & Sprenger, R. R. Quantitative assessment of in-solution digestion efficiency identifies optimal protocols for unbiased protein analysis. *Molecular &cellular proteomics : MCP* **12,** 2992–3005; 10.1074/mcp.M112.025585 (2013).
274. Waas, M. *et al.* Combine and conquer: surfactants, solvents, and chaotropes for robust mass spectrometry based analyses of membrane proteins. *Analytical chemistry* **86,** 1551–1559; 10.1021/ac403185a (2014).
275. Rogers, J. C. & Bomgarden, R. D. Sample Preparation for Mass Spectrometry-Based Proteomics; from Proteomes to Peptides. *Advances in experimental medicine and biology* **919,** 43–62; 10.1007/978-3-319-41448-5_3 (2016).
276. Seddon, A. M., Curnow, P. & Booth, P. J. Membrane proteins, lipids and detergents: not just a soap opera. *Biochimica et biophysica acta* **1666,** 105–117; 10.1016/j.bbamem.2004.04.011 (2004).
277. Sechi, S. & Chait, B. T. Modification of cysteine residues by alkylation. A tool in peptide mapping and protein identification. *Analytical chemistry* **70,** 5150–5158 (1998).
278. Olsen, J. V., Ong, S.-E. & Mann, M. Trypsin cleaves exclusively C-terminal to arginine and lysine residues. *Molecular &cellular proteomics : MCP* **3,** 608–614; 10.1074/mcp.T400003-MCP200 (2004).
279. Sielaff, M. *et al.* Evaluation of FASP, SP3, and iST Protocols for Proteomic Sample Preparation in the Low Microgram Range. *Journal of proteome research* **16,** 4060–4072; 10.1021/acs.jproteome.7b00433 (2017).
280. Ishihama, Y., Rappsilber, J. & Mann, M. Modular stop and go extraction tips with stacked disks for parallel and multidimensional Peptide fractionation in proteomics. *Journal of proteome research* **5,** 988–994; 10.1021/pr050385q (2006).
281. Bantscheff, M., Schirle, M., Sweetman, G., Rick, J. & Kuster, B. Quantitative mass spectrometry in proteomics: a critical review. *Analytical and bioanalytical chemistry* **389,** 1017–1031; 10.1007/s00216-007-1486-6 (2007).
282. Michalski, A., Cox, J. & Mann, M. More than 100,000 detectable peptide species elute in single shotgun proteomics runs but the majority is inaccessible to data-dependent LC-MS/MS. *Journal of proteome research* **10,** 1785–1793; 10.1021/pr101060v (2011).

283. Schirle, M., Heurtier, M.-A. & Kuster, B. Profiling core proteomes of human cell lines by one-dimensional PAGE and liquid chromatography-tandem mass spectrometry. *Molecular & cellular proteomics : MCP* **2,** 1297–1305; 10.1074/mcp.M300087-MCP200 (2003).

284. Rabilloud, T., Chevallet, M., Luche, S. & Lelong, C. Two-dimensional gel electrophoresis in proteomics: Past, present and future. *Journal of proteomics* **73,** 2064–2077; 10.1016/j.jprot.2010.05.016 (2010).

285. Blue, L. E. *et al.* Recent advances in capillary ultrahigh pressure liquid chromatography. *Journal of chromatography. A* **1523,** 17–39; 10.1016/j.chroma.2017.05.039 (2017).

286. Broeckhoven, K. & Desmet, G. Considerations for the use of ultra-high pressures in liquid chromatography for 2.1mm inner diameter columns. *Journal of chromatography. A* **1523,** 183–192; 10.1016/j.chroma.2017.07.040 (2017).

287. Helmueller, S. C., Poe, D. P. & Kaczmarski, K. Adiabatic packed column supercritical fluid chromatography using a dual-zone still-air column heater. *Journal of chromatography. A* **1535,** 141–153; 10.1016/j.chroma.2018.01.004 (2018).

288. Steen, H. & Mann, M. The ABC's (and XYZ's) of peptide sequencing. *Nature reviews. Molecular cell biology* **5,** 699–711; 10.1038/nrm1468 (2004).

289. Haag, A. M. Mass Analyzers and Mass Spectrometers. *Advances in experimental medicine and biology* **919,** 157–169; 10.1007/978-3-319-41448-5_7 (2016).

290. Kelstrup, C. D. *et al.* Performance Evaluation of the Q Exactive HF-X for Shotgun Proteomics. *Journal of proteome research* **17,** 727–738; 10.1021/acs.jproteome.7b00602 (2018).

291. Biemann, K. Mass spectrometry of peptides and proteins. *Annual review of biochemistry* **61,** 977–1010; 10.1146/annurev.bi.61.070192.004553 (1992).

292. Roepstorff, P. & Fohlman, J. Proposal for a common nomenclature for sequence ions in mass spectra of peptides. *Biomedical mass spectrometry* **11,** 601; 10.1002/bms.1200111109 (1984).

293. Burlet, O., Orkiszewski, R. S., Ballard, K. D. & Gaskell, S. J. Charge promotion of low-energy fragmentations of peptide ions. *Rapid communications in mass spectrometry : RCM* **6,** 658–662; 10.1002/rcm.1290061106 (1992).

294. Mikesh, L. M. *et al.* The utility of ETD mass spectrometry in proteomic analysis. *Biochimica et biophysica acta* **1764,** 1811–1822; 10.1016/j.bbapap.2006.10.003 (2006).

295. Espadas, G., Borràs, E., Chiva, C. & Sabidó, E. Evaluation of different peptide fragmentation types and mass analyzers in data-dependent methods using an Orbitrap Fusion Lumos Tribrid mass spectrometer. *Proteomics* **17**; 10.1002/pmic.201600416 (2017).

296. Richards, A. L. *et al.* One-hour proteome analysis in yeast. *Nature protocols* **10,** 701–714; 10.1038/nprot.2015.040 (2015).

297. Schwartz, J. C., Senko, M. W. & Syka, J. E. P. A two-dimensional quadrupole ion trap mass spectrometer. *Journal of the American Society for Mass Spectrometry* **13,** 659–669; 10.1016/S1044-0305(02)00384-7 (2002).

298. Bogdanov, B. & Smith, R. D. Proteomics by FTICR mass spectrometry: top down and bottom up. *Mass spectrometry reviews* **24,** 168–200; 10.1002/mas.20015 (2005).

299. Marshall, A. G., Hendrickson, C. L. & Jackson, G. S. Fourier transform ion cyclotron resonance mass spectrometry: a primer. *Mass spectrometry reviews* **17,** 1–35; 10.1002/(SICI)1098-2787(1998)17:1<1::AID-MAS1>3.0.CO;2-K (1998).

300. Scigelova, M., Hornshaw, M., Giannakopulos, A. & Makarov, A. Fourier transform mass spectrometry. *Molecular &cellular proteomics : MCP* **10,** M111.009431; 10.1074/mcp.M111.009431 (2011).

301. Hu, Q. *et al.* The Orbitrap: a new mass spectrometer. *Journal of mass spectrometry : JMS* **40,** 430–443; 10.1002/jms.856 (2005).
302. Matthiesen, R. Methods, algorithms and tools in computational proteomics: a practical point of view. *Proteomics* **7,** 2815–2832; 10.1002/pmic.200700116 (2007).
303. Cox, J. *et al.* Andromeda: a peptide search engine integrated into the MaxQuant environment. *Journal of proteome research* **10,** 1794–1805; 10.1021/pr101065j (2011).
304. Perkins, D. N., Pappin, D. J., Creasy, D. M. & Cottrell, J. S. Probability-based protein identification by searching sequence databases using mass spectrometry data. *Electrophoresis* **20,** 3551–3567; 10.1002/(SICI)1522-2683(19991201)20:18<3551::AID-ELPS3551>3.0.CO;2-2 (1999).
305. Tyanova, S., Temu, T. & Cox, J. The MaxQuant computational platform for mass spectrometry-based shotgun proteomics. *Nature protocols* **11,** 2301–2319; 10.1038/nprot.2016.136 (2016).
306. Cox, J. & Mann, M. MaxQuant enables high peptide identification rates, individualized p.p.b.-range mass accuracies and proteome-wide protein quantification. *Nature biotechnology* **26,** 1367–1372; 10.1038/nbt.1511 (2008).
307. Gonzalez-Galarza, F. F. *et al.* A critical appraisal of techniques, software packages, and standards for quantitative proteomic analysis. *Omics : a journal of integrative biology* **16,** 431–442; 10.1089/omi.2012.0022 (2012).
308. Ong, S.-E. & Mann, M. Mass spectrometry-based proteomics turns quantitative. *Nature chemical biology* **1,** 252–262; 10.1038/nchembio736 (2005).
309. Bantscheff, M., Lemeer, S., Savitski, M. M. & Kuster, B. Quantitative mass spectrometry in proteomics: critical review update from 2007 to the present. *Analytical and bioanalytical chemistry* **404,** 939–965; 10.1007/s00216-012-6203-4 (2012).
310. Cox, J. *et al.* A practical guide to the MaxQuant computational platform for SILAC-based quantitative proteomics. *Nature protocols* **4,** 698–705; 10.1038/nprot.2009.36 (2009).
311. Ong, S.-E., Kratchmarova, I. & Mann, M. Properties of 13C-substituted arginine in stable isotope labeling by amino acids in cell culture (SILAC). *Journal of proteome research* **2,** 173–181 (2003).
312. Geiger, T. *et al.* Use of stable isotope labeling by amino acids in cell culture as a spike-in standard in quantitative proteomics. *Nature protocols* **6,** 147–157; 10.1038/nprot.2010.192 (2011).
313. Hanke, S., Besir, H., Oesterhelt, D. & Mann, M. Absolute SILAC for accurate quantitation of proteins in complex mixtures down to the attomole level. *Journal of proteome research* **7,** 1118–1130; 10.1021/pr7007175 (2008).
314. Schmidt, A., Kellermann, J. & Lottspeich, F. A novel strategy for quantitative proteomics using isotope-coded protein labels. *Proteomics* **5,** 4–15; 10.1002/pmic.200400873 (2005).
315. Ross, P. L. *et al.* Multiplexed protein quantitation in Saccharomyces cerevisiae using amine-reactive isobaric tagging reagents. *Molecular &cellular proteomics : MCP* **3,** 1154–1169; 10.1074/mcp.M400129-MCP200 (2004).
316. Chen, Y., Wang, F., Xu, F. & Yang, T. Mass Spectrometry-Based Protein Quantification. *Advances in experimental medicine and biology* **919,** 255–279; 10.1007/978-3-319-41448-5_15 (2016).
317. Karp, N. A. *et al.* Addressing accuracy and precision issues in iTRAQ quantitation. *Molecular &cellular proteomics : MCP* **9,** 1885–1897; 10.1074/mcp.M900628-MCP200 (2010).

318. Ting, L., Rad, R., Gygi, S. P. & Haas, W. MS3 eliminates ratio distortion in isobaric multiplexed quantitative proteomics. *Nature methods* **8,** 937–940; 10.1038/nmeth.1714 (2011).
319. Venable, J. D., Dong, M.-Q., Wohlschlegel, J., Dillin, A. & Yates, J. R. Automated approach for quantitative analysis of complex peptide mixtures from tandem mass spectra. *Nature methods* **1,** 39–45; 10.1038/nmeth705 (2004).
320. Liu, H., Sadygov, R. G. & Yates, J. R. A model for random sampling and estimation of relative protein abundance in shotgun proteomics. *Analytical chemistry* **76,** 4193–4201; 10.1021/ac0498563 (2004).
321. Cox, J. *et al.* Accurate proteome-wide label-free quantification by delayed normalization and maximal peptide ratio extraction, termed MaxLFQ. *Molecular &cellular proteomics : MCP* **13,** 2513–2526; 10.1074/mcp.M113.031591 (2014).
322. Lai, X., Wang, L. & Witzmann, F. A. Issues and applications in label-free quantitative mass spectrometry. *International journal of proteomics* **2013,** 756039; 10.1155/2013/756039 (2013).
323. Lu, P., Vogel, C., Wang, R., Yao, X. & Marcotte, E. M. Absolute protein expression profiling estimates the relative contributions of transcriptional and translational regulation. *Nature biotechnology* **25,** 117–124; 10.1038/nbt1270 (2007).
324. Schwanhäusser, B. *et al.* Global quantification of mammalian gene expression control. *Nature* **473,** 337–342; 10.1038/nature10098 (2011).
325. Wiśniewski, J. R., Hein, M. Y., Cox, J. & Mann, M. A "Proteomic Ruler" for Protein Copy Number and Concentration Estimation without Spike-in Standards*. *Molecular &cellular proteomics : MCP* **13,** 3497–3506; 10.1074/mcp.M113.037309 (2014).
326. Simon, P. F. *et al.* Highly Pathogenic H5N1 and Novel H7N9 Influenza A Viruses Induce More Profound Proteomic Host Responses than Seasonal and Pandemic H1N1 Strains. *Journal of proteome research* **14,** 4511–4523; 10.1021/acs.jproteome.5b00196 (2015).
327. Nightingale, K. *et al.* High-Definition Analysis of Host Protein Stability during Human Cytomegalovirus Infection Reveals Antiviral Factors and Viral Evasion Mechanisms. *Cell host &microbe* **24,** 447-460.e11; 10.1016/j.chom.2018.07.011 (2018).
328. Diamond, D. L. *et al.* Temporal proteome and lipidome profiles reveal hepatitis C virus-associated reprogramming of hepatocellular metabolism and bioenergetics. *PLoS pathogens* **6,** e1000719; 10.1371/journal.ppat.1000719 (2010).
329. Horvatić, A. *et al.* High-throughput proteomics and the fight against pathogens. *Molecular bioSystems* **12,** 2373–2384; 10.1039/c6mb00223d (2016).
330. Jean Beltran, P. M., Federspiel, J. D., Sheng, X. & Cristea, I. M. Proteomics and integrative omic approaches for understanding host-pathogen interactions and infectious diseases. *Molecular systems biology* **13,** 922; 10.15252/msb.20167062 (2017).
331. Meissner, F. & Mann, M. Quantitative shotgun proteomics: considerations for a high-quality workflow in immunology. *Nature immunology* **15,** 112–117; 10.1038/ni.2781 (2014).
332. Meissner, F., Scheltema, R. A., Mollenkopf, H.-J. & Mann, M. Direct proteomic quantification of the secretome of activated immune cells. *Science (New York, N.Y.)* **340,** 475–478; 10.1126/science.1232578 (2013).
333. Rieckmann, J. C. *et al.* Social network architecture of human immune cells unveiled by quantitative proteomics. *Nature immunology* **18,** 583–593; 10.1038/ni.3693 (2017).
334. Karniely, S. *et al.* Human Cytomegalovirus Infection Upregulates the Mitochondrial Transcription and Translation Machineries. *mBio* **7,** e00029; 10.1128/mBio.00029-16 (2016).

335. Ly, T. *et al.* Proteome-wide analysis of protein abundance and turnover remodelling during oncogenic transformation of human breast epithelial cells. *Wellcome open research* **3,** 51; 10.12688/wellcomeopenres.14392.1 (2018).

336. Schwanhäusser, B., Gossen, M., Dittmar, G. & Selbach, M. Global analysis of cellular protein translation by pulsed SILAC. *Proteomics* **9,** 205–209; 10.1002/pmic.200800275 (2009).

337. An, J. *et al.* pSILAC mass spectrometry reveals ZFP91 as IMiD-dependent substrate of the CRL4CRBN ubiquitin ligase. *Nature communications* **8,** 15398; 10.1038/ncomms15398 (2017).

338. Jovanovic, M. *et al.* Dynamic profiling of the protein life cycle in response to pathogens. *Science (New York, N.Y.)* **347,** 1259038; 10.1126/science.1259038 (2015).

339. Schwanhäusser, B., Wolf, J., Selbach, M. & Busse, D. Synthesis and degradation jointly determine the responsiveness of the cellular proteome. *BioEssays : news and reviews in molecular, cellular and developmental biology* **35,** 597–601; 10.1002/bies.201300017 (2013).

340. Menneteau, T. *et al.* Mass Spectrometry-based Absolute Quantification of 20S Proteasome Status for Controlled Ex-vivo Expansion of Human Adipose-derived Mesenchymal Stromal/Stem Cells. *Molecular & cellular proteomics : MCP* **18,** 744–759; 10.1074/mcp.RA118.000958 (2019).

341. Jäger, S. *et al.* Global landscape of HIV-human protein complexes. *Nature* **481,** 365–370; 10.1038/nature10719 (2011).

342. Davis, Z. H. *et al.* Global mapping of herpesvirus-host protein complexes reveals a transcription strategy for late genes. *Molecular cell* **57,** 349–360; 10.1016/j.molcel.2014.11.026 (2015).

343. Abbas, Y. M., Pichlmair, A., Górna, M. W., Superti-Furga, G. & Nagar, B. Structural basis for viral 5'-PPP-RNA recognition by human IFIT proteins. *Nature* **494,** 60–64; 10.1038/nature11783 (2013).

344. Keilhauer, E. C., Hein, M. Y. & Mann, M. Accurate protein complex retrieval by affinity enrichment mass spectrometry (AE-MS) rather than affinity purification mass spectrometry (AP-MS). *Molecular & cellular proteomics : MCP* **14,** 120–135; 10.1074/mcp.M114.041012 (2015).

345. Scaturro, P. *et al.* An orthogonal proteomic survey uncovers novel Zika virus host factors. *Nature* **561,** 253–257; 10.1038/s41586-018-0484-5 (2018).

346. Coyaud, E. *et al.* Global Interactomics Uncovers Extensive Organellar Targeting by Zika Virus. *Molecular & cellular proteomics : MCP* **17,** 2242–2255; 10.1074/mcp.TIR118.000800 (2018).

347. Fusco, O. *et al.* 90K (MAC-2 BP) gene expression in breast cancer and evidence for the production of 90K by peripheral-blood mononuclear cells. *International journal of cancer* **79,** 23–26 (1998).

348. Iacobelli, S., Arnò, E., D'Orazio, A. & Coletti, G. Detection of antigens recognized by a novel monoclonal antibody in tissue and serum from patients with breast cancer. *Cancer research* **46,** 3005–3010 (1986).

349. Ullrich, A. *et al.* The secreted tumor-associated antigen 90K is a potent immune stimulator. *The Journal of biological chemistry* **269,** 18401–18407 (1994).

350. Woodman, N. *et al.* Two E-selectin ligands, BST-2 and LGALS3BP, predict metastasis and poor survival of ER-negative breast cancer. *International journal of oncology* **49,** 265–275; 10.3892/ijo.2016.3521 (2016).

351. Natoli, C. *et al.* 90K protein: a new predictor marker of disease progression in human immunodeficiency virus infection. *Journal of acquired immune deficiency syndromes* **6,** 370–375 (1993).
352. Natoli, C., Iacobelli, S. & Ghinelli, F. Unusually high level of a tumor-associated antigen in the serum of human immunodeficiency virus-seropositive individuals. *The Journal of infectious diseases* **164,** 616–617; 10.1093/infdis/164.3.616 (1991).
353. Longo, G. *et al.* Prognostic value of a novel circulating serum 90K antigen in HIV-infected haemophilia patients. *British journal of haematology* **85,** 207–209 (1993).
354. Dorrucci, M. *et al.* Longitudinal analysis of the 90K glycoprotein in the Italian HIV-seroconversion study: temporal trend and predictability of the maturity of HIV infection. *Journal of biological regulators and homeostatic agents* **18,** 18–25 (2004).
355. Lodermeyer, V. *et al.* The Antiviral Activity of the Cellular Glycoprotein LGALS3BP/90K Is Species Specific. *Journal of virology* **92**; 10.1128/JVI.00226-18 (2018).
356. Lodermeyer, V. *et al.* 90K, an interferon-stimulated gene product, reduces the infectivity of HIV-1. *Retrovirology* **10,** 111; 10.1186/1742-4690-10-111 (2013).
357. Wang, Q., Zhang, X., Han, Y., Wang, X. & Gao, G. M2BP inhibits HIV-1 virion production in a vimentin filaments-dependent manner. *Scientific reports* **6,** 32736; 10.1038/srep32736 (2016).
358. Zhou, M.-T. *et al.* Quantitative Proteomics Reveals the Roles of Peroxisome-associated Proteins in Antiviral Innate Immune Responses. *Molecular &cellular proteomics : MCP* **14,** 2535–2549; 10.1074/mcp.M115.048413 (2015).
359. Oshima, S. *et al.* Interferon regulatory factor 1 (IRF-1) and IRF-2 distinctively up-regulate gene expression and production of interleukin-7 in human intestinal epithelial cells. *Molecular and cellular biology* **24,** 6298–6310; 10.1128/MCB.24.14.6298-6310.2004 (2004).
360. Park, S.-Y. *et al.* Glycoprotein 90K Promotes E-Cadherin Degradation in a Cell Density-Dependent Manner via Dissociation of E-Cadherin-p120-Catenin Complex. *International journal of molecular sciences* **18**; 10.3390/ijms18122601 (2017).
361. Chicoine, J. *et al.* Bicaudal-C recruits CCR4-NOT deadenylase to target mRNAs and regulates oogenesis, cytoskeletal organization, and its own expression. *Developmental cell* **13,** 691–704; 10.1016/j.devcel.2007.10.002 (2007).
362. Pavanello, L., Hall, B., Airhihen, B. & Winkler, G. S. The central region of CNOT1 and CNOT9 stimulates deadenylation by the Ccr4-Not nuclease module. *The Biochemical journal* **475,** 3437–3450; 10.1042/BCJ20180456 (2018).
363. Temme, C., Zaessinger, S., Meyer, S., Simonelig, M. & Wahle, E. A complex containing the CCR4 and CAF1 proteins is involved in mRNA deadenylation in Drosophila. *The EMBO journal* **23,** 2862–2871; 10.1038/sj.emboj.7600273 (2004).
364. Chen, Y. *et al.* A DDX6-CNOT1 complex and W-binding pockets in CNOT9 reveal direct links between miRNA target recognition and silencing. *Molecular cell* **54,** 737–750; 10.1016/j.molcel.2014.03.034 (2014).
365. Inoue, T. *et al.* CNOT3 contributes to early B cell development by controlling Igh rearrangement and p53 mRNA stability. *The Journal of experimental medicine* **212,** 1465–1479; 10.1084/jem.20150384 (2015).
366. Keersmaecker, K. de *et al.* Exome sequencing identifies mutation in CNOT3 and ribosomal genes RPL5 and RPL10 in T-cell acute lymphoblastic leukemia. *Nature genetics* **45,** 186–190; 10.1038/ng.2508 (2013).

367. Vicente, C. *et al.* The CCR4-NOT complex is a tumor suppressor in Drosophila melanogaster eye cancer models. *Journal of hematology & oncology* **11,** 108; 10.1186/s13045-018-0650-0 (2018).
368. Rodríguez-Gil, A. *et al.* The CCR4-NOT complex contributes to repression of Major Histocompatibility Complex class II transcription. *Scientific reports* **7,** 3547; 10.1038/s41598-017-03708-7 (2017).
369. Leppek, K. *et al.* Roquin promotes constitutive mRNA decay via a conserved class of stem-loop recognition motifs. *Cell* **153,** 869–881; 10.1016/j.cell.2013.04.016 (2013).
370. Okamura, Y., Makita, N., Hizukuri, Y. & Hayashi, Y. Genome-wide siRNA screening in mouse bone marrow-derived macrophages revealed that knockdown of ribosomal proteins suppresses IL-10 and enhances TNF-α production. *Journal of clinical and experimental hematopathology : JCEH* **58,** 87–94; 10.3960/jslrt.17036 (2018).
371. Sarowar, S. *et al.* Capsicum annuum CCR4-associated factor CaCAF1 is necessary for plant development and defence response. *The Plant journal : for cell and molecular biology* **51,** 792–802; 10.1111/j.1365-313X.2007.03174.x (2007).
372. Chapat, C. *et al.* hCAF1/CNOT7 regulates interferon signalling by targeting STAT1. *The EMBO journal* **32,** 688–700; 10.1038/emboj.2013.11 (2013).
373. Yamaji, M. *et al.* DND1 maintains germline stem cells via recruitment of the CCR4-NOT complex to target mRNAs. *Nature* **543,** 568–572; 10.1038/nature21690 (2017).
374. Xiong, Y. *et al.* Annexin II receptor induces apoptosis independent of Annexin II. *Apoptosis : an international journal on programmed cell death* **18,** 925–939; 10.1007/s10495-013-0846-2 (2013).
375. Toubi, E. & Vadasz, Z. Innate immune-responses and their role in driving autoimmunity. *Autoimmunity reviews* **18,** 306–311; 10.1016/j.autrev.2018.10.005 (2019).
376. Khine, A. A. *et al.* Human neutrophil peptides induce interleukin-8 production through the P2Y6 signaling pathway. *Blood* **107,** 2936–2942; 10.1182/blood-2005-06-2314 (2006).
377. Ferrari, D., Idzko, M., Müller, T., Manservigi, R. & Marconi, P. Purinergic Signaling: A New Pharmacological Target Against Viruses? *Trends in pharmacological sciences* **39,** 926–936; 10.1016/j.tips.2018.09.004 (2018).
378. Bar, I. *et al.* Knockout mice reveal a role for P2Y6 receptor in macrophages, endothelial cells, and vascular smooth muscle cells. *Molecular pharmacology* **74,** 777–784; 10.1124/mol.108.046904 (2008).
379. Nakano, M. *et al.* UDP/P2Y6 receptor signaling regulates IgE-dependent degranulation in human basophils. *Allergology international : official journal of the Japanese Society of Allergology* **66,** 574–580; 10.1016/j.alit.2017.02.014 (2017).
380. Borirak, O. *et al.* Time-series analysis of the transcriptome and proteome of Escherichia coli upon glucose repression. *Biochimica et biophysica acta* **1854,** 1269–1279; 10.1016/j.bbapap.2015.05.017 (2015).
381. Ji, Z., Zeng, Y., Liang, Y., Qian, Q. & Yang, C. Proteomic dissection of the rice-Fusarium fujikuroi interaction and the correlation between the proteome and transcriptome under disease stress. *BMC genomics* **20,** 91; 10.1186/s12864-019-5435-5 (2019).
382. Lemée, J.-M. *et al.* Integration of transcriptome and proteome profiles in glioblastoma: looking for the missing link. *BMC Molecular Biology* **19**; 10.1186/s12867-018-0115-6 (2018).
383. Sun, N. *et al.* Quantitative proteome and transcriptome analysis of the archaeon Thermoplasma acidophilum cultured under aerobic and anaerobic conditions. *Journal of proteome research* **9,** 4839–4850; 10.1021/pr100567u (2010).

384. Yan, J. *et al.* HIV-1 Vpr Reprograms CLR4DCAF1 E3 Ubiquitin Ligase to Antagonize Exonuclease 1-Mediated Restriction of HIV-1 Infection. *mBio* **9**; 10.1128/mBio.01732-18 (2018).
385. Su, X. *et al.* Jembrana disease virus Vif antagonizes the inhibition of bovine APOBEC3 proteins through ubiquitin-mediate protein degradation. *Virology* **519,** 53–63; 10.1016/j.virol.2018.03.028 (2018).
386. Liu, X.-J. *et al.* Human cytomegalovirus IE1 downregulates Hes1 in neural progenitor cells as a potential E3 ubiquitin ligase. *PLoS pathogens* **13,** e1006542; 10.1371/journal.ppat.1006542 (2017).
387. Davis, K. A. & Patton, J. T. Shutdown of interferon signaling by a viral-hijacked E3 ubiquitin ligase. *Microbial Cell* **4,** 387–389; 10.15698/mic2017.11.600.
388. Mathieson, T. *et al.* Systematic analysis of protein turnover in primary cells. *Nature communications* **9,** 689; 10.1038/s41467-018-03106-1 (2018).
389. Savitski, M. M. *et al.* Multiplexed Proteome Dynamics Profiling Reveals Mechanisms Controlling Protein Homeostasis. *Cell* **173,** 260-274.e25; 10.1016/j.cell.2018.02.030 (2018).
390. Zecha, J. *et al.* Peptide Level Turnover Measurements Enable the Study of Proteoform Dynamics. *Molecular &cellular proteomics : MCP* **17,** 974–992; 10.1074/mcp.RA118.000583 (2018).
391. Kustatscher, G., Grabowski, P. & Rappsilber, J. Pervasive coexpression of spatially proximal genes is buffered at the protein level. *Molecular systems biology* **13,** 937; 10.15252/msb.20177548 (2017).
392. Wang, J. *et al.* Proteome Profiling Outperforms Transcriptome Profiling for Coexpression Based Gene Function Prediction. *Molecular &cellular proteomics : MCP* **16,** 121–134; 10.1074/mcp.M116.060301 (2017).
393. Gingras, A.-C., Gstaiger, M., Raught, B. & Aebersold, R. Analysis of protein complexes using mass spectrometry. *Nature reviews. Molecular cell biology* **8,** 645–654; 10.1038/nrm2208 (2007).
394. Meysman, P. *et al.* Protein complex analysis: From raw protein lists to protein interaction networks. *Mass spectrometry reviews* **36,** 600–614; 10.1002/mas.21485 (2017).
395. Gingras, A.-C., Aebersold, R. & Raught, B. Advances in protein complex analysis using mass spectrometry. *The Journal of physiology* **563,** 11–21; 10.1113/jphysiol.2004.080440 (2005).
396. Lavallée-Adam, M., Cloutier, P., Coulombe, B. & Blanchette, M. Modeling contaminants in AP-MS/MS experiments. *Journal of proteome research* **10,** 886–895; 10.1021/pr100795z (2011).
397. Hubner, N. C. & Mann, M. Extracting gene function from protein-protein interactions using Quantitative BAC InteraCtomics (QUBIC). *Methods (San Diego, Calif.)* **53,** 453–459; 10.1016/j.ymeth.2010.12.016 (2011).
398. Eyckerman, S. *et al.* Intelligent Mixing of Proteomes for Elimination of False Positives in Affinity Purification-Mass Spectrometry. *Journal of proteome research* **15,** 3929–3937; 10.1021/acs.jproteome.6b00517 (2016).
399. Titeca, K. *et al.* sfinx: an R package for the elimination of false positives from affinity purification-mass spectrometry datasets. *Bioinformatics (Oxford, England)* **33,** 1902–1904; 10.1093/bioinformatics/btx076 (2017).
400. Roux, K. J., Kim, D. I. & Burke, B. BioID: a screen for protein-protein interactions. *Current protocols in protein science* **74,** Unit 19.23; 10.1002/0471140864.ps1923s74 (2013).

401. Myers, S. A. *et al.* Discovery of proteins associated with a predefined genomic locus via dCas9-APEX-mediated proximity labeling. *Nature methods* **15,** 437–439; 10.1038/s41592-018-0007-1 (2018).

402. Lobingier, B. T. *et al.* An Approach to Spatiotemporally Resolve Protein Interaction Networks in Living Cells. *Cell* **169,** 350-360.e12; 10.1016/j.cell.2017.03.022 (2017).

403. Roux, K. J., Kim, D. I., Raida, M. & Burke, B. A promiscuous biotin ligase fusion protein identifies proximal and interacting proteins in mammalian cells. *The Journal of cell biology* **196,** 801–810; 10.1083/jcb.201112098 (2012).

404. Gingras, A.-C., Abe, K. T. & Raught, B. Getting to know the neighborhood: using proximity-dependent biotinylation to characterize protein complexes and map organelles. *Current opinion in chemical biology* **48,** 44–54; 10.1016/j.cbpa.2018.10.017 (2019).

405. Larance, M. *et al.* Global Membrane Protein Interactome Analysis using In vivo Crosslinking and Mass Spectrometry-based Protein Correlation Profiling. *Molecular &cellular proteomics : MCP* **15,** 2476–2490; 10.1074/mcp.O115.055467 (2016).

406. Heusel, M. *et al.* Complex-centric proteome profiling by SEC-SWATH-MS. *Molecular systems biology* **15,** e8438; 10.15252/msb.20188438 (2019).

407. Makowski, M. M. *et al.* Global profiling of protein-DNA and protein-nucleosome binding affinities using quantitative mass spectrometry. *Nature communications* **9,** 1653; 10.1038/s41467-018-04084-0 (2018).

408. Hubner, N. C., Nguyen, L. N., Hornig, N. C. & Stunnenberg, H. G. A quantitative proteomics tool to identify DNA-protein interactions in primary cells or blood. *Journal of proteome research* **14,** 1315–1329; 10.1021/pr5009515 (2015).

409. Guillen-Ahlers, H., Shortreed, M. R., Smith, L. M. & Olivier, M. Advanced methods for the analysis of chromatin-associated proteins. *Physiological genomics* **46,** 441–447; 10.1152/physiolgenomics.00041.2014 (2014).

410. Bantscheff, M. *et al.* Quantitative chemical proteomics reveals mechanisms of action of clinical ABL kinase inhibitors. *Nature biotechnology* **25,** 1035–1044; 10.1038/nbt1328 (2007).

411. Dziekan, J. M. *et al.* Identifying purine nucleoside phosphorylase as the target of quinine using cellular thermal shift assay. *Science translational medicine* **11**; 10.1126/scitranslmed.aau3174 (2019).

412. Franken, H. *et al.* Thermal proteome profiling for unbiased identification of direct and indirect drug targets using multiplexed quantitative mass spectrometry. *Nature protocols* **10,** 1567–1593; 10.1038/nprot.2015.101 (2015).

413. Benda, C. *et al.* Structural model of a CRISPR RNA-silencing complex reveals the RNA-target cleavage activity in Cmr4. *Molecular cell* **56,** 43–54; 10.1016/j.molcel.2014.09.002 (2014).

414. Zhao, M. *et al.* A Comparative Proteomics Analysis of Five Body Fluids: Plasma, Urine, Cerebrospinal Fluid, Amniotic Fluid, and Saliva. *Proteomics. Clinical applications* **12,** e1800008; 10.1002/prca.201800008 (2018).

415. Marimuthu, A. *et al.* A Comprehensive Map of the Human Urinary Proteome. *Journal of proteome research* **10,** 2734–2743; 10.1021/pr2003038 (2011).

416. Lygirou, V., Makridakis, M. & Vlahou, A. Biological sample collection for clinical proteomics: existing SOPs. *Methods in molecular biology (Clifton, N.J.)* **1243,** 3–27; 10.1007/978-1-4939-1872-0_1 (2015).

417. Geyer, P. E. *et al.* Plasma Proteome Profiling to Assess Human Health and Disease. *Cell systems* **2,** 185–195; 10.1016/j.cels.2016.02.015 (2016).

418. Peláez-García, A. *et al.* Comparison of risk classification between EndoPredict and MammaPrint in ER-positive/HER2-negative primary invasive breast cancer. *PloS one* **12,** e0183452; 10.1371/journal.pone.0183452 (2017).

419. Buus, R. *et al.* Comparison of EndoPredict and EPclin With Oncotype DX Recurrence Score for Prediction of Risk of Distant Recurrence After Endocrine Therapy. *Journal of the National Cancer Institute* **108**; 10.1093/jnci/djw149 (2016).

420. Ternette, N. & Purcell, A. W. Immunopeptidomics Special Issue. *Proteomics* **18,** e1800145; 10.1002/pmic.201800145 (2018).

421. Chong, C. *et al.* High-throughput and Sensitive Immunopeptidomics Platform Reveals Profound Interferon γ -Mediated Remodeling of the Human Leukocyte Antigen (HLA) Ligandome. *Molecular & cellular proteomics : MCP* **17,** 533–548; 10.1074/mcp.TIR117.000383 (2018).

422. Panis, C., Pizzatti, L., Souza, G. F. & Abdelhay, E. Clinical proteomics in cancer: Where we are. *Cancer letters* **382,** 231–239; 10.1016/j.canlet.2016.08.014 (2016).

423. Varjosalo, M. *et al.* Interlaboratory reproducibility of large-scale human protein-complex analysis by standardized AP-MS. *Nature methods* **10,** 307–314; 10.1038/nmeth.2400 (2013).

424. Kennedy, J. J. *et al.* Demonstrating the feasibility of large-scale development of standardized assays to quantify human proteins. *Nature methods* **11,** 149–155; 10.1038/nmeth.2763 (2014).

425. Abbatiello, S. E. *et al.* Large-Scale Interlaboratory Study to Develop, Analytically Validate and Apply Highly Multiplexed, Quantitative Peptide Assays to Measure Cancer-Relevant Proteins in Plasma*. *Molecular & cellular proteomics : MCP* **14,** 2357–2374; 10.1074/mcp.M114.047050 (2015).

ACKNOWLEDGEMENTS

First I would like to thank my supervisor Prof. Dr. Andreas Pichlmair for the opportunity to work in his lab. It was a thrilling time where I could put my scientific interest into practice. I want to thank you especially for your forward-looking mentality, for your unshakable optimism, for your open-door mentality and for providing all the resources in the lab. This made it possible for me to work on such complex resource expensive topics, which I really enjoyed. My special thank goes to my doctoral advisor Prof. Matthias Mann for providing such an outstanding research environment at his department at the MPI. I always felt welcome and supported there. I am sure that many of my projects would not have been doable without the input and support from different sites of the department. Therefore, I want to take the chance to thank all people that I got to know during my time in the Mann department. It was really a pleasure to work, to discuss and to have fun with you! Especially, I want to thank Felix Meissner for his help and fruitful discussions, Alison Dalfovo and Theresa Schneider for the great administrative support and of course Korbinian Mayr and Igor Paron for keeping the mass spectrometers running. I had a lot of fun and learned a lot from you.

In particular, I want to thank all members of the Innate Immunity Lab for fruitful discussions, collaborations, support and help. Especially I would like to thank Matthias Habjan and Alexey Stukalov, which I both highly appreciate for their intellectual knowledge, constructive criticism and practical help within different projects.

Furthermore, I want to thank the members of my Defense- and TAC committee for their time and support (Prof. Matthias Mann, Prof. Dr. Andreas Pichlmair, Prof. Karl-Klaus Conzelmann, Dr. Andreas Bergthaler, Prof. Klaus Förstemann, PD Dr. Dietmar Martin, Prof. Karl-Peter Hopfner).

Dear Mom and Dad, I can't thank you enough for all your support during my life. You made me to the person who I am! I am very grateful that you sensitized me for the important values in life. Thank you for being such great role models.

Dear Nikolas, you're the best brother in the world. You encourage me to look over the edge of the plate from time to time. Thank you for the countless discussion, crazy ideas and nice moments.

My deepest gratitude goes to my ~~girlfriend~~ ~~fiancée~~ wife Karin. Thank you for your support during my PhD, for your patience, your love and simply for being who you are. You manage to put a smile on my lips every day.